Study of acoustic cavitation near metal surfaces contaminated by uranium

Ran Ji

THÈSE POUR OBTENIR LE GRADE DE DOCTEUR DE L'UNIVERSITÉ DE MONTPELLIER

En Chimie Séparative - Matériaux et Procédés

École doctorale Sciences Chimiques Balard (ED 459)

Unité de recherche Institut de Chimie Séparative de Marcoule (UMR 5257)

Study of Acoustic Cavitation near Metal Surfaces Contaminated by Uranium

Présentée par Ran JI

Le 13 novembre 2018

Sous la direction de Sergueï NIKITENKO

Devant le jury composé de

[Jean-François DUFÊCHE, Prof, Université Montpellier]	[Président]
[Jean-Yves HIHN, Prof, Université de Franche-Comté]	[Rapporteur]
[Laurie BARTHE, MCF, INP Toulouse]	[Rapporteur]
[Sergueï NIKITENKO, DR, CNRS Montpellier]	[Directeur de Thèse]
[Claire LE NAOUR, CR, Université Paris Saclay]	[Examinateur]
[Micheline DRAYE, Prof, Université Savoie Mont Blanc]	[Examinateur]
[Rachel PFLIEGER, CR, CEA Marcoule]	[Encadrant]
[Matthieu VIROT, CR, CEA Marcoule]	[Encadrant]
[Pascal PILUSO, CR, CEA Cadarache]	[Invité]

UNIVERSITÉ DE MONTPELLIER

"The unity of inner *knowledge and action"*

[Wang Yangming]

Acknowledgements

The doctoral study of the past three years has greatly enriched my experience in academic and personal life. I would like to express my gratitude to my supervisors, colleagues, friends and family. Without their advice, assistance and support, the present work would not have been accomplished. I am also very grateful to all the jury members of my thesis defense for their comments and suggestions.

First and foremost, I would like to give my appreciation to my supervisor: Dr. Sergey Nikitenko, and my co-supervisors: Dr. Rachel Pflieger and Dr. Matthieu Virot. I am very fortunate and grateful to have such an opportunity to work on this topic under their guidance. Each of my publications and presentations has their invaluable contributions on countless discussions and encouragements. Without their insight and in-depth knowledge, this work could never have reached its present form.

I would like to thank my colleague Dr. Tony Chave for his patience in explaining the use of laboratory equipment and the meaning of many French words. I owe my thanks to Dr. Renaud Podor, Dr. Joseph Lautru and Xavier le Goff, who helped me with SEM, EDX analysis and 3D reconstruction measurements.

I appreciate all the people I met at ICSM during the past few years. It is a pleasure to work with them in such a good atmosphere. I am especially grateful to Danwen Qin, Elodie Dalodiere, Laurénanne Parizot, Témim Ouerhani and Laura Bonato for their kind help, friendship and amusement. We have had a lot of good times together, especially the countless and delicious dinners with Danwen (the best Chinese cuisine master in Avignon).

Finally, my ultimate and special thanks must be attributed to my mother, my father and my girlfriend, for their love, unconditional support and unwavering confidence.

Résumé

Le démantèlement des réacteurs et usines de l'industrie nucléaire produit un grand volume de matériaux métalliques contaminés. Parmi ceux-ci, les alliages à base de magnésium issus des réacteurs UNGG sont connus pour être des métaux hautement réactifs présentant un risque élevé de corrosion et pouvant générer de l'hydrogène gazeux qui peut causer de graves dommages pendant le stockage. Afin de réduire le volume d'effluents radioactifs générés et de déclasser les déchets nucléaires, la sonochimie peut être considérée comme une alternative efficace pour la décontamination des surfaces métalliques. La sonochimie traite des effets des ondes ultrasonores sur les réactions chimiques en solution. Les effets observés en sonochimie proviennent du phénomène de cavitation acoustique, qui comprend la nucléation, croissance et effondrement implosif et rapide de microbulles remplies de gaz et de vapeur de solvant. Des espèces excitées ainsi que des radicaux peuvent être générés lors de son implosion. Le plasma formé au cœur de la bulle permet l'émission de lumière se propageant de l'UV au proche IR (sonoluminescence). Lorsque l'effondrement des bulles a lieu à proximité d'une surface solide étendue, la formation d'ondes de choc violentes et de micro-jets dirigés vers la surface contribue fortement au nettoyage, à la dépassivation et à la décontamination de surfaces métalliques.

Cette étude cible la décontamination de surfaces métalliques à base de magnésium sous irradiation ultrasonore. Après une synthèse bibliographique permettant de faire un état de l'art sur le traitement de surfaces métalliques par ultrasons de puissance, les outils expérimentaux et techniques analytiques utilisés dans ce travail sont décrits. La partie résultats et discussion est ensuite présentée selon trois chapitres distincts visant : 1) une étude fondamentale de sonoluminescence à 100 kHz permettant la caractérisation du phénomène de cavitation acoustique à proximité de surfaces solides étendues ; 2) l'étude de la structuration de surfaces de Mg sous irradiation ultrasonore ; 3) le traitement ultrasonore de surfaces métalliques radioactives contaminées au laboratoire avec de l'uranium naturel.

Ce travail met en évidence le fort impact de la fréquence ultrasonore sur l'activité sonochimique, sa distribution spatiale et sur les effets générés sur des échantillons de magnésium. Une répartition spatiale homogène de l'activité sonochimique est observée aux fréquences ≥ 100 kHz. Les résultats confirment que l'effondrement asymétrique des bulles est susceptible de se produire à proximité des surfaces solides étendues. La formation d'une structure allongée semblable à une balle de golf est observée pour des fréquences comprises entre 100 et 362 kHz. De telles architectures résultent de la dissolution sonochimique contrôlée de la surface de Mg. Il est probable que la nucléation hétérogène assurée par la création de défauts sous ultrasons combiné à la libération de gaz H_2 soient à l'origine de cette structuration. Les essais réalisés sur un alliage Mg-Zr montrent un comportement similaire permettant de simuler le comportement d'une gaine de réacteur UNGG. La décontamination rapide et totale de ces

différents matériaux est observée en milieu oxalique dilué à 20 °C. Un faible et lent processus de recontamination des matériaux à base de Mg est observé du fait de l'adsorption d'uranyle par la brucite formée sur les surfaces. Les essais réalisés sur des échantillons à géométrie complexe permettent également de souligner le fort potentiel de la sonochimie pour la décontamination efficace de surfaces à base de Mg.

Abstract

The dismantling of UNGG reactors produces large volumes of contaminated metallic materials. Among these, magnesium-based alloys which are known as highly reactive metals, have a high risk of corrosion and can generate hydrogen gas that can cause serious damages during storage. In order to reduce the volume of generated radioactive effluents and downgrade nuclear wastes, sonochemistry can be considered as an original and efficient alternative for metallic surface decontamination. Sonochemistry deals with the effects of ultrasound waves on chemical reactions in solution. The effects observed in sonochemistry originate from the acoustic cavitation phenomenon, which is the nucleation, growth and rapid implosive collapse of gas and vapor filled microbubbles. Excited species and radicals can be generated in the formed plasma and light (sonoluminescence) is emitted. When the bubble collapse takes place in the vicinity of a solid surface, it produces violent shock waves and microjets directed towards the surface. These physical effects strongly contribute in ultrasonic cleaning, surface depassivation and decontamination.

This study focuses on the decontamination of magnesium metal surfaces under ultrasonic irradiation. After a bibliographic synthesis making a state of the art on the treatment of metallic surfaces by ultrasonic power, the experimental tools and analytical techniques used in this work are described. The results and discussion section are then presented in three separate chapters: 1) a fundamental 100 kHz sonoluminescence study for the characterization of the acoustic cavitation phenomenon in solution and near extended solid surfaces; 2) a study of the structuring of Mg-based surfaces under ultrasonic irradiation; 3) Ultrasonic treatment of radioactive metal surfaces contaminated in the laboratory with natural uranium.

This work highlights the strong impact of ultrasonic frequency on sonochemical activity, its spatial distribution and the effects generated on magnesium samples. A homogeneous spatial distribution of sonochemical activity is observed at frequencies ≥ 100 kHz. The results confirm that asymmetrical bubble collapse is likely to occur near extended solid surfaces. The formation of an elongated structure similar to a golf ball is observed for frequencies between 100 and 362 kHz. Such architectures result from controlled sonochemical dissolution of the Mg surface. It is likely that the heterogeneous nucleation provided by the creation of ultrasonic flaws combined with the release of H_2 gas is at the origin of this structuring. The tests carried out on a Mg-Zr alloy show a similar behavior making it possible to simulate the behavior of a UNGG reactor cladding. Rapid and total decontamination of these different materials is observed in dilute oxalic medium at 20 ℃. A low and slow recontamination process of Mg-based materials is observed due to uranyl adsorption by brucite formed on the surfaces. Tests on samples with complex geometry also highlight the high potential of sonochemistry for effective decontamination of Mg-based surfaces.

Foreword

The work presented in this thesis manuscript has been the subject of several scientific communications detailed hereinafter:

Award

Best oral presentation award from the Asia-Oceania Sonochemical Society (AOSS-3), Structuration of Magnesium Surface by Acoustic Cavitation, September 14th to 16th **2017**, Kattankulathur, Chennai, India.

Publications

R. Ji, R. Pflieger, M. Virot, and S. I. Nikitenko, Multibubble Sonochemistry and Sonoluminescence at 100 kHz: The Missing Link between Low- and High-Frequency Ultrasound *The Journal of Physical Chemistry B* 122 **(2018)** 6989–6994.

R. Ji, M. Virot, R. Pflieger, R. Podor, X. Le Goff, S. I. Nikitenko, Controlled "Golf Ball Shape" Structuring of Mg Surface under Acoustic Cavitation *Ultrasonics Sonochemistry* 40 **(2017)** 30-40.

Communications (talks)

Acoustic Cavitation at Intermediate Frequency (100 kHz) Ultrasound, 16th Meeting of the European Society of Sonochemistry (ESS 16th), April 15th to 19th **2018**, Besançon, France.

Structuration of Magnesium Surface by Acoustic Cavitation, 3rd Asia - Oceania Sonochemical Society conference (AOSS-3rd), September 14th to 16th **2017**, Kattankulathur, Chennai, India.

Structuration of Magnesium Surface by Acoustic Cavitation, Journées Scientifiques Ultrasons et Procédés (JSUP IV), July 4th to 5th **2017**, Toulouse, France.

Poster presentations

R. Ji, M. Virot, R. Pflieger, S. I. Nikitenko, Mg Surface Decontamination by Power Ultrasound in Aqueous Solution, Journées scientifiques de Marcoule, **2018**, Bagnols sur Cèze, France.

R. Ji, M. Virot, R. Pflieger, S. I. Nikitenko, Structuration of Magnesium Surface by Acoustic Cavitation, Journées scientifiques de Marcoule, **2017**, Bagnols sur Cèze, France.

R. Ji, M. Virot, R. Pflieger, S. I. Nikitenko, Acoustic Cavitation near Metal Surfaces Contaminated with Radionuclides, XVèmes Journées Nationales de Radiochimie et de Chimie Nucléaire, September 8th to 9th **2016**, Nice, France.

R. Ji, M. Virot, R. Pflieger, S. I. Nikitenko, Acoustic Cavitation near Metal Surfaces Contaminated with Radionuclides, Journées scientifiques de Marcoule, **2016**, Bagnols sur Cèze, France.

Contents

Table of figures

List of tables

Introduction

The natural uranium graphite-gas (UNGG) reactors were the first generation of nuclear reactors developed in France. They used graphite moderator, gas (air or carbon dioxide) coolant and natural uranium metal as fuel. Since 1956, in total 9 UNGG reactors have been built and put into operation in France. Until the last unit at Bugey was decommissioned in 1994, a large amount of nuclear wastes of various kinds, including spent fuel, graphite bricks, radioactive gases and metal structural wastes, have been generated during commission and dismantling processes of UNGG reactors. Among the radioactive metal wastes, large quantities of magnesium alloy, which has been used as fuel cladding tubes and plugs, are temporarily stored at La Hague and Marcoule, and wait for conditioning and transportation to long-term disposals. The large amounts of Mg cladding wastes take a huge volume of storage and present a risk of radioactive leakage, as well as great costs of conditioning and disposal.[1] Moreover, as an active metal, Mg is easily corroded and can produce hydrogen gas, which can result in the risk of radioactive material leakage during long-term storage of these UNGG cladding wastes.[2] As a result, it is necessary to reduce the volume of these cladding wastes by removing radioactive contaminants on their surfaces, thereby reducing their radiation level to a lower storage category or even to allow them to be unconditionally released or reused. One of the potentially efficient approaches for the decontamination of the UNGG Mg alloy cladding wastes is ultrasonic cleaning.

Ultrasound has been applied as a cleaning tool since the 1950s. Compared to other conventional cleaning methods, ultrasonic cleaning has the advantages of not being limited by complex shapes, fewer process stages, use of less or non-hazardous aqueous solutions, a wider range of substrate surfaces to be treated and milder operating conditions.[3] In fact, it is not the ultrasound wave itself, but the acoustic cavitation phenomenon which interacts with treated surfaces in a liquid medium and removes contaminants. Acoustic cavitation results from the nucleation, growth and rapid implosive collapse of gas and vapor filled microbubbles in liquids exposed to an ultrasonic wave. In the vicinity of a solid boundary, the bubble collapse produces violent shock waves and micro-jets directed towards the substrate surface. Thanks to the combination of the in-situ generation of chemically active species with the enhancement of mass transfer by acoustic streaming on the treated surface, an efficient cleaning by power ultrasound can be achieved. However, though ultrasonic cleaning has been widely studied and used in various fields, the behavior of cavitation in liquid in the presence of a solid boundary is still unclear. Meanwhile, the impacts of cavitation on metal surfaces and the ultrasonic cleaning efficiency on radioactive materials are of great interest in material science and for the nuclear industry.

The manuscript is outlined in the following 6 chapters:

The first chapter is a literature review. In this part the general principles of acoustic cavitation, including sonochemistry and sonoluminescence, and some application examples of ultrasonic modification and cleaning of solid surfaces are reported. Besides, the conceptions of UNGG reactors and current state of storage of Mg cladding wastes in France, as well as some examples of ultrasonic decontamination are described later.

The second chapter is devoted to the description of the experimental techniques and methods. The sample surfaces and experimental set-ups used in this study are described in detail, as well as the corresponding characterization tools.

Chapter III aims to determine the effect of ultrasonic frequency on sonochemical activity and sonoluminescence intensity, especially in the range of the less studied intermediate frequency (100 kHz). It also allows to identify cavitation bubble activity and distribution in the presence of a solid surface in liquid, including the cavitation behavior at different distances to the surface and in different acoustic standing wave fields induced by the reflection on the surface. This study is accomplished by chemical measurements (H_2O_2 yields and sonochemiluminescence of luminol) and spectroscopic probes (multibubble sonoluminescence of OH*, NH*, Na* and continuum).

Investigations on how sonication affects extended Mg and Mg-Zr alloy surfaces are presented in chapter IV. The evolution of surfaces treated at different ultrasonic frequencies in different solutions is characterized by surface roughness, morphology, dissolution rate, hydrogen generation rate and evolution of chemical composition. The formation of an original and unprecedented golf-ball shape microstructure on Mg based sample surfaces sonicated at ultrasonic frequencies in the range of 100 to 345 kHz is discussed in detail. The way it affects surface properties is studied via roughness and wettability measurements.

Chapter V is dedicated to the assessment of the efficiency of ultrasonic decontamination of metal surfaces contaminated by natural uranium to simulate real UNGG cladding materials. It considers samples of Mg, Mg-Zr alloy, non-irradiated UNGG cladding fragments and stainless steel.

Finally, general conclusions and perspectives for a future work are given.

This study has been carried out at Marcoule Institute for Separation Chemistry (ICSM) and was supported by the Division of Nuclear Energy (DEN) of the French Alternative Energies and Atomic Energy Commission (CEA).

Chapter I. Bibliography

I.1 Ultrasound and sonochemistry

I.1.1 Ultrasound

Ultrasound is the inaudible sound wave with frequency above 16 kHz, higher than the upper limit of human hearing range. In nature, animals like bats and dolphins, echolocate quarries or obstacles by producing ultrasound. For human beings, the first research about the effects of ultrasound or cavitation was done by Thornycroft and Barnaby, when they were trying to explain the observation of submarine propeller erosion in 1895.[3] And the first purposeful application of ultrasound was developed by Langevin in 1917. Again for submarine, Langevin had designed an underwater detector, which can emit ultrasonic waves in water and collect echoes form certain objects to identify their distances. Such device is now well known under the name of sonar.[3-5]

There are several basic properties of ultrasound: frequency f and acoustic power P_{ac}, the latter includes acoustic power density $P_{ac,V}$ and power intensity I_{ac}.

I.1.1.1 Ultrasonic frequency

The ultrasound frequency f (Hz) is given by:

$$f = c/\lambda \tag{I-1}$$

Where c (m s^{-1}) is the ultrasound wave velocity in a considered medium and λ (m) is the wavelength of the ultrasound.

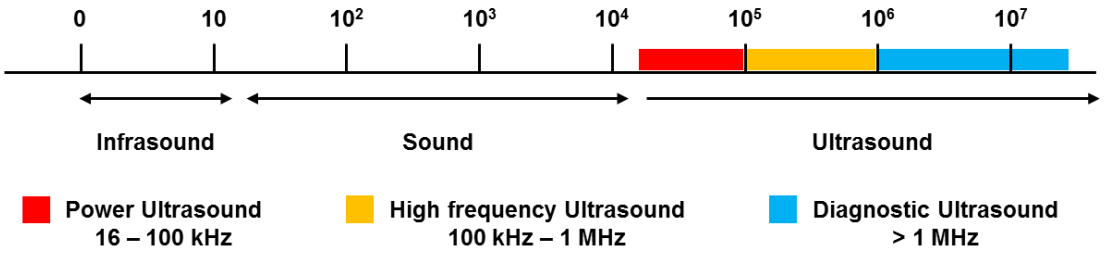

Figure I-1 Ultrasound frequency category.[3]

According to its frequency, ultrasound can be divided into three frequency domains, namely power ultrasound (16 – 100 kHz), high frequency ultrasound (100 kHz or sometimes 200 kHz – 1 MHz), and diagnostic ultrasound (> 1 MHz), as presented in **Figure I-1**. Power ultrasound and high frequency ultrasound are widely applied in ultrasonic cleaning and sonochemistry, where chemical and physical effects caused by acoustic cavitation bubbles are desired.[6]

I.1.1.2 Acoustic power

The absorbed acoustic power P_{ac} (W) is the power transmitted to the medium by ultrasound. Normally for better controlling and comparing between different experimental conditions, parameters such as acoustic power density $P_{ac,V}$ (W mL^{-1}) and acoustic power intensity I_{ac} (W cm^{-2}) are used.

$$P_{ac,V} = \frac{P_{ac}}{V} \tag{I-2}$$

Where V (mL) is the volume of irradiated liquid.

$$I_{ac} = \frac{P_{ac}}{S} \tag{I-3}$$

Where S (cm^2) is the area normal to the direction of ultrasonic wave propagation, e.g. for a horn type ultrasonic transducer tip, S is the surface of the probe tip.

Based on ultrasonic intensity, ultrasound can also be classified into power ultrasound and diagnostic ultrasound. The acoustic intensity of power ultrasound should be higher than a certain intensity to produce violent acoustic cavitation collapse, which is known as the Blake threshold.[7] The Blake threshold is closely related to ultrasonic frequency, for example: 0.49 W cm^{-2} at 20 kHz, 0.88 W cm^{-2} at 140 kHz and 3 W cm^{-2} at 1 MHz.[8] Thus for non-destructive medical imaging at a frequency over 1 MHz, acoustic power intensity is limited to 1 W cm^{-2} or less to avoid cavitation.

By changing the ultrasonic frequency or acoustic power, the effect of ultrasound can be completely different. Fundamentally, the ultrasonic effect difference arises from changes in the behavior of acoustic cavitation.

I.1.2 Acoustic cavitation

Acoustic cavitation is the process of the formation, growth and implosive collapse of bubbles in liquids irradiated by ultrasound, accompanied by a series of physical and chemical phenomena and effects: sonoluminescence, sonochemiluminescence, generation of excited species and radicals, formation of H_2O_2, shock waves, microjets, micro-streaming and etc.[9]

I.1.2.1 Cavitation mechanism

When a liquid is exposed to ultrasound, alternating rarefaction and compression cycles are propagated by the ultrasonic waves, as shown in **Figure I-2**. In compression cycles, liquid molecules are pressed together by a locally positive force. In rarefaction phase, it is in the opposite that a negative force draws the liquid molecules apart. In fact, this force comes from the difference between ambient pressure in liquid and acoustic pressure from ultrasonic wave. And in rarefaction phase, if the local acoustic pressure

is larger than ambient pressure, a negative force can be produced. When this negative force exceeds the liquid tensile strength in the rarefaction phase, tiny gas or vapor filled bubbles appear. For a pure degassed liquid, its tensile strength is too strong to easily form bubbles. However, in real situations, there are usually inhomogeneities such as dissolved gases in liquid, which can reduce the tensile strength and play as nuclei of bubbles.[6, 10]

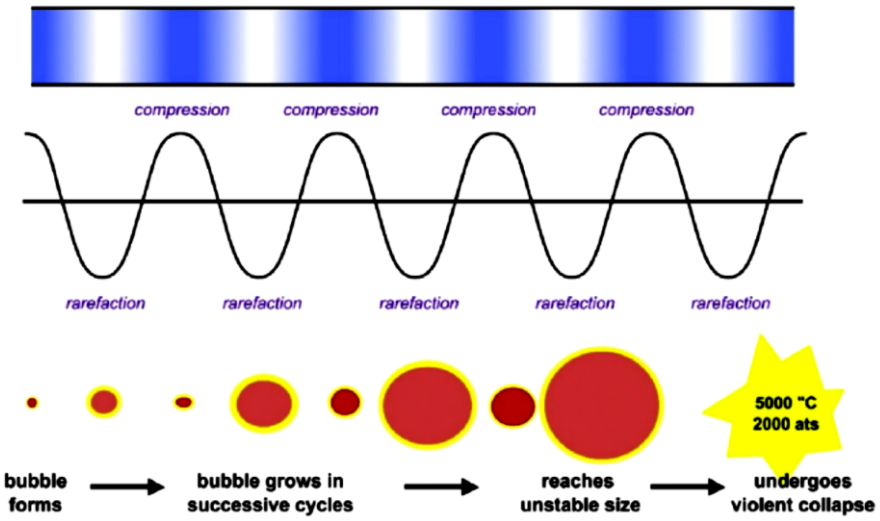

Figure I-2 Acoustic cavitation generation and collapse.[11]

These bubbles continue to expand in rarefaction phase, until their sizes arrive to the maximum when the pressure on the bubble wall is no more negative. If the bubble oscillates between rarefaction and compression phases for several cycles around an equilibrium radius, this process is called stable cavitation. Since there is no significant change in bubble size, stable cavitation does not strongly involve in physical or chemical effects of ultrasound. However, if the bubble exists for only a few cycles and grows rapidly to a maximum size (tens or hundreds times the initial bubble diameter) with a following violent implosion, transient cavitation happens. Extreme temperature and pressure are created during the implosion in a transient cavitation bubble, which leads to obvious physical and chemical effects: sonoluminescence light emission and sonochemical reactions. Besides, stable cavitation can resolve itself into transient cavitation. After the collapse of transient cavitation bubbles, the generated daughter bubbles can also perform as nuclei of stable cavitation. There are some bubbles exhibiting both stable and transient cavitation characteristics, such as bubbles with a long lifetime as well as strong physical/chemical effects.[9, 10, 12]

I.1.2.2 Cavitation mathematical model

Rayleigh's mathematical formulation was the first basic model formulated for the collapse of an empty cavitation bubble.[13] If one assumes that the cavity is an adiabatic bubble filled with an ideal gas, Rayleigh-Plesset equation can be expressed as:[4]

$$R\ddot{R} + \frac{3}{2}\dot{R}^2 = \frac{\left(P_0 + \frac{2\sigma}{R_0}\right)\left(\frac{R_0}{R}\right)^{3\gamma} - \frac{2\sigma}{R} - \frac{4\mu\dot{R}}{R} - p_\infty}{\rho} \quad \text{(I-4)}$$

Where R is the radius of the cavitation bubble, one and two dots are the first and second order time derivatives of bubble radius, R_0 is the bubble radius at equilibrium, P_0 is the hydrostatic (ambient) pressure, p_∞ is the liquid pressure in the bulk of liquid, γ is the specific heat ratio of the gas in bubble, σ is the surface tension, μ is the liquid viscosity and ρ is the density of the liquid.

However, due to the complexity and instability of the collapse of bubbles (especially in multibubble systems), there were more dynamical equations and numerical analysis developed from Rayleigh-Plesset equation.[14]

I.1.2.3 Hot spot theory

A widely accepted theory to explain most cavitation effects is the hot spot theory.[9, 12, 15] According to the first law of thermodynamics:

$$\Delta U = Q - W \quad \text{(I-5)}$$

With ΔU the change in internal energy of a closed system, Q the heat transferred to the system and W the work done by the system

When compressing a gas:

$$W = p\Delta V \quad \text{(I-6)}$$

Where p is the pressure and ΔV is the volume change (negative). Compression introduces energy to the system. In a very simple approximation, one may consider an adiabatic system during the bubble violent collapse, because the temperature increase of the gas inside a bubble is too fast for an important heat transport to happen ($Q \cong 0$). A localized transient hot spot is created in the bubble, with an average gas temperature and pressure up to 5,000 K and 500 atm, and a fast cooling rate of 10^9 to 10^{10} K s^{-1}.[16-18] This hot spot is believed to be the origin of sonoluminescence and sonochemistry.[12, 19]

I.1.2.4 Non-equilibrium model

It was recently shown that the hot spot theory is not sufficient to take into account the complex conditions in cavitation: quasi-adiabatic bubble compression, water vapor at the bubble wall, intrabubble chemical reactions and gas molecules ionization. Therefore, a non-equilibrium model has been developed. As presented in **Table I-1**, spectroscopic studies of OH ($A^2\Sigma^+$-$X^2\Pi$), NH ($A^3\Pi$-$X^3\Sigma^-$) and C_2 Swan bands emissions from multibubble system in aqueous solutions proved evidence for non-equilibrium plasma formation inside the collapsing bubbles.[20, 21] Such non-equilibrium plasma cannot

be characterized by a single gas temperature, but by multiple temperatures of different particles and degrees of freedom in the plasma: electron (T_e), vibrational (T_v), rotational (T_r) and translational (T_0) temperatures. These temperatures in a plasma far from thermodynamic equilibrium follow the inequality $T_e > T_v > T_r \approx T_0$.[22]

Table I-1 Rovibronic temperatures estimated from the simulations of molecular emissions in sonoluminescence spectra from aqueous solutions.[18, 21, 23]

Solution	Gas	Ultrasonic frequency (kHz)	Transition	T_v (K)	T_r (K)	Reference
Benzene 10^{-3} M	Ar	20	C_2 Swan ($d^3\Pi_g$–$a^3\Pi_u$)	4300 ± 200	-	[18]
tert-butanol 0.05-0.4 M	Ar	20	C_2 Swan ($d^3\Pi_g$–$a^3\Pi_u$)	6300 ± 1000	4800 ± 1000	[23]
tert-butanol $1 \cdot 10^{-3} – 5 \cdot 10^{-3}$ M	Ar	204 / 362 / 613	C_2 Swan ($d^3\Pi_g$–$a^3\Pi_u$)	5800 / 8000 / 5000 (± 1000)	5800 / 4000 / 4000 (± 1000)	
tert-butanol 0.12 M	Xe	20	C_2 Swan ($d^3\Pi_g$–$a^3\Pi_u$)	14000 ± 1000	2500 ± 1000	
Ammonia 0.1 M	Ar	20	OH ($A^2\Sigma^+$-$X^2\Pi$)	9000 ± 1000	5000 ± 500	[21]
			NH ($A^3\Pi$-$X^3\Sigma^-$)	7000 ± 1000	4000 ± 500	
Ammonia 0.1 M	Ar	359	OH ($A^2\Sigma^+$-$X^2\Pi$)	13000 ± 2000	6000 ± 1000	
			NH ($A^3\Pi$-$X^3\Sigma^-$)	10000 ± 1000	2200 ± 500	

I.1.2.5 Microjet

As presented in **Figure I-3**, when acoustic cavitation occurs close to a solid boundary, a micro-jet is formed towards the wall.[14, 24] It also happen when neighbour bubbles are close enough to each other.[19, 25]

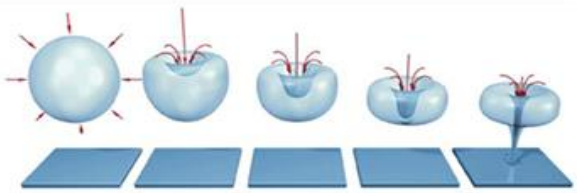

Figure I-3 Micro-jet formation.[26]

To explain this process, the concept of impulse is significant. Impulse I is the inertia of the liquid moving towards a solid boundary close to the cavitation bubbles:[14]

$$I = uM \tag{I-7}$$

Where u is the speed of the centre of the bubble perpendicular to the substrate surface and M is the added mass of the bubble. This mass is based on the assumption that some liquid is carried by the moving bubble, thus leading to a virtual addition of the bubble mass. M can be expressed as:

$$M = c\rho V \tag{I-8}$$

Where c is the added mass coefficient, ρ is the liquid density and V is the volume of the bubble.

So the impulse can also be expressed as:

$$\mathrm{I} = \mathrm{uc\rho V} \tag{I-9}$$

In the absence of any external force, the impulse remains nearly constant with the bubble approaching to the substrate. With the sharp shrinking of the bubble volume V during collapse, the speed of the bubble u increases dramatically. When the velocity u gets too large that the spherical bubble cannot undertake the large external pressure difference from the high velocity, a liquid inrush enters the bubble from the side away of the substrate and pierces the other side of the bubble, targeting to the surface.[24, 27] Such so called micro-jets can achieve a velocity of several hundreds meters per second [28].

I.1.2.6 Shock wave

Shock wave is another strong acoustic phenomenon occurring during the collapse of cavitation bubbles. Extremely rapid compression and the enormous pressure inside bubble at the collapse moment produce a shock wave faster than the sound velocity in liquid.[8] **Figure I-4** shows the propagation of a shock

wave from a trapped sonoluminescing bubble driven by low frequency ultrasound. The tiny black spot in the center is the acoustic bubble and the ring is the shock wave.[29]

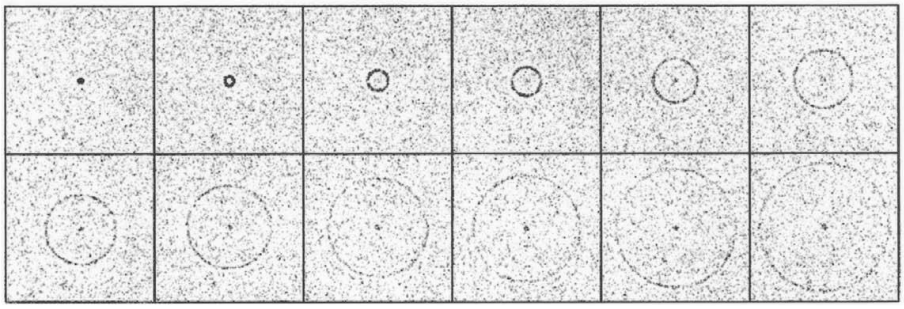

Figure I-4 Shock wave from a trapped sonoluminescing bubble produced by ultrasound at 21.4 kHz, pressure amplitude of 132 kPa, frame interval 30 ns.[29]

The high velocity (1,000 to 4,000 m s^{-1}) and pressure (GPa) of the shock wave make it destructive, though it is a very localized impact due to the fast attenuation of wave energy in the medium.[30, 31]

For both micro-jet and shock wave occuring in the vicinity of a solid boundary, an important parameter to be considered is the stand-off distance γ:[32, 33]

$$\gamma = \frac{L}{R_{max}} \tag{I-10}$$

Where L is the distance between solid substrate and bubble center, and R_{max} is the bubble radius at its maximum expansion.

Obvious effects from micro-jets and shock waves on a solid surface can be observed only with a stand-off distance $\gamma \leq 2$.[34, 35] These two phenomena are considered to be the principle mechanisms responsible for surface damage, modification and cleaning.

I.1.2.7 Acoustic streaming

In an intense ultrasonic field, the acoustic wave propagation is attenuated due to the liquid viscosity.[36] This attenuation produces a gradient of radiation pressure in liquid, which generates a steady motion of fluid, hence an acoustic streaming.[8, 36] Two different types of acoustic streaming exist: i) Eckart streaming in the bulk of a liquid, which accelerates fluid in the direction of acoustic traveling wave propagation; ii) vortex-like Rayleigh streaming at the solid boundary due to the local viscous stress.[8, 37] Acoustic streaming can significantly enhance convective heat exchange in an irradiated liquid and accelerate the mass transfer in a heterogeneous system, thus increases sonochemical reaction rate and ultrasonic cleaning efficiency.[38, 39]

When near a small bubble or particle, a similar but localized fluid motion caused by viscous dissipation happens at a small length scale, named microstreaming.[8] It is a typically circulation flow with a velocity

of several millimeters per second.[40] Microstreaming can also change the processes of heat and mass diffusion of cavitation bubbles, thus alter the phenomenon of sonochemistry and sonoluminescence.[40]

I.1.3 Sonochemistry

In general, sonochemistry is the use of acoustic cavitation to achieve chemical reactions or chemical process. From a historical point of view, Richards and Loomis first reported the chemical effects of power ultrasound in 1927.[41] Sonochemistry is different from the other conventional chemical processes, due to its special cavitation bubble collapse: extreme local temperature and pressure with exceptional cooling rate. By applying ultrasound, high energy chemical interactions can be generated in mild conditions. The applications of sonochemistry are diverse in the domains of chemical synthesis, catalysis, material science (nanomaterial and biomaterial) etc. Depending on the reaction environment, ultrasonic chemical effects can be categorized into homogeneous sonochemistry of liquid systems and heterogeneous sonochemistry at liquid-liquid or liquid-solid interfaces.[3, 4, 9, 42, 43]

I.1.3.1 Homogeneous sonochemistry

The use of ultrasound in aqueous solutions results in the production of different intermediates such as $H^{\cdot}$, $HO^{\cdot}$, $HO_2^{\cdot}$ and of primary products such as H_2 and H_2O_2. Reactions (I-11) to (I-18) present the sonolysis of water in the presence of argon and oxygen:[4, 44]

$$H_2O \overset{)))}{\rightarrow} H^{\cdot} + HO^{\cdot} \quad \text{(I-11)}$$

$$H^{\cdot} + HO^{\cdot} \rightarrow H_2O \quad \text{(I-12)}$$

$$2H^{\cdot} \rightarrow H_2 \quad \text{(I-13)}$$

$$2\,HO^{\cdot} \rightarrow H_2O_2 \quad \text{(I-14)}$$

$$H^{\cdot} + O_2 \rightarrow HO_2^{\cdot} \quad \text{(I-15)}$$

$$H^{\cdot} + HO_2^{\cdot} \rightarrow H_2O_2 \quad \text{(I-16)}$$

$$2HO_2^{\cdot} \rightarrow H_2O_2 + O_2 \quad \text{(I-17)}$$

$$H_2O + HO^{\cdot} \rightarrow H_2O_2 + H^{\cdot} \quad \text{(I-18)}$$

If the cavitation energy is high enough, for example in the case of Ar saturated water exposed to high frequency ultrasound, the dissociation of diatomic gas or volatile molecules, such as oxygen and nitrogen, can happen at bubble collapse:[45, 46]

$$O_2 \overset{)))}{\rightarrow} 2O^{\cdot} \quad \text{(I-19)}$$

$$N_2 \overset{)))}{\rightarrow} 2N^{\cdot} \quad \text{(I-20)}$$

The produced oxygen and nitrogen radicals can react with radicals and molecules:

$$O^{\cdot} + H_2O \rightarrow 2HO^{\cdot} \quad \text{(I-21)}$$

$$O^{\cdot} + H^{\cdot} \rightarrow HO^{\cdot} \quad \text{(I-22)}$$

$$N^{\cdot} + H^{\cdot} \rightarrow NH^{\cdot} \quad \text{(I-23)}$$

$$N^{\cdot} + HO^{\cdot} \rightarrow NOH^{\cdot} \quad \text{(I-24)}$$

The key of sonochemical reactions is the radicals formed during sonolysis of water. For example, $HO^{\cdot}$ and H_2O_2 are strong oxidants which can react with solutes in the liquid surrounding the cavitation bubbles. Meantime, it is found that an artificial introduction of cavitation nuclei is important for an efficient homogeneous sonochemical process.[9]

I.1.3.2 Heterogeneous sonochemistry

Thanks to the mechanical effects of cavitation bubble collapse, sonochemistry in heterogeneous systems is more efficient than in homogeneous systems and has been widely studied and applied for decades. Micro-jets, shock waves and micro-streaming strongly enhance the mass transfer and significantly accelerate the chemical reactions in the heterogeneous systems.[4, 9, 47, 48]

In liquid-liquid system, power ultrasound can form very fine emulsions, which is applied to increase the combustion efficiency of petrol, and decrease the so-produced pollution as well.[49]

At liquid-solid interfaces, the erosion and deformation from micro-jets and shock waves is obvious.[50] This property is widely used for ultrasonic cleaning and decontamination.[3, 51] Other studies and applications in the fields of solid catalysts, material crystallization and electrochemistry also present the enhancements and benefits of ultrasound in chemical process.[52-55]

More detail investigations and applications of power ultrasound in heterogeneous system will be discussed later.

I.1.4 Sonoluminescence

The light emitted from liquid irradiated by ultrasound is called sonoluminescence (SL) or sonochemiluminescence (SCL). The difference between SL and SCL is the origin of light emission: SL is light emitted directly by the acoustic cavitation bubbles, as shown in **Figure I-5**, while SCL is

chemiluminescence from chemical reactions, e.g. luminol with oxidants ($HO^{\cdot}$ and H_2O_2) created by cavitation.[8] Cavitation bubbles can have both activities of sonochemistry and SL, but it is believed that SL bubbles are larger than sonochemical bubbles at certain ultrasonic frequency and power conditions.[56, 57]

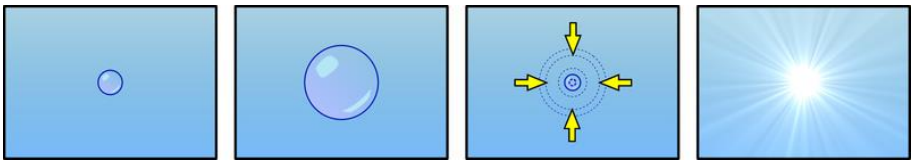

Figure I-5 Sonoluminescence generation from a cavitation bubble.[58]

SL was first observed by Frenzel and Schultes in 1934.[9] The mechanism of SL is still unclear, though different theories tried to explain it.[31, 42] One of the hypotheses is that the origin of SL is the chemiluminescence from the plasma inside collapsing bubbles, which is similar to a flame plasma.[12] Such plasma is created during the compression cycle or the implosion moment, when the intrabubble gas temperature is extremely high. At such high temperature, gas and volatile molecules insides bubbles can be degraded and excited.[17, 18] However, recent studies revealed non-equilibrium plasma as SL source in cavitation, which indicates multiple temperatures characterization of SL emissions: lifetime of this plasma is not long enough to allow equilibration.[22]

There are two types of SL: multibubble sonoluminescence (MBSL) and single-bubble sonoluminescence (SBSL).[8, 9] In general conditions of liquid exposed to ultrasound, MBSL can be observed with large numbers of interacting cavitation bubbles and bubble clusters.[59, 60] SBSL is from a specially produced stable cavitation bubble in a standing wave of an ultrasonically irradiated and degassed liquid.[61] Both MBSL and SBSL spectra in water present continuum emissions, which are originated of Bremsstrahlung (electron-atom or electron-ion Bremsstrahlung) and radiative recombination (electron-ion or $H^{\cdot}$-$HO^{\cdot}$ radical recombination).[8, 62] For MBSL in water, a peak around 310 nm is present in spectra from excited radical of $HO^{\cdot}$.[9, 62, 63] Emission lines of some nonvolatile metal ions such as Na and K were also reported in MBSL spectra in aqueous solutions of NaCl and KCl respectively (see **Figure I-6**).[62, 64, 65] But for SBSL, only in some typical solutions such as sulfuric acid (Ar, Xe dissolved) or at very low acoustic pressure in water, emission lines of gas molecules like Ar, Xe or $HO^{\cdot}$ radicals can be observed.[8, 66]

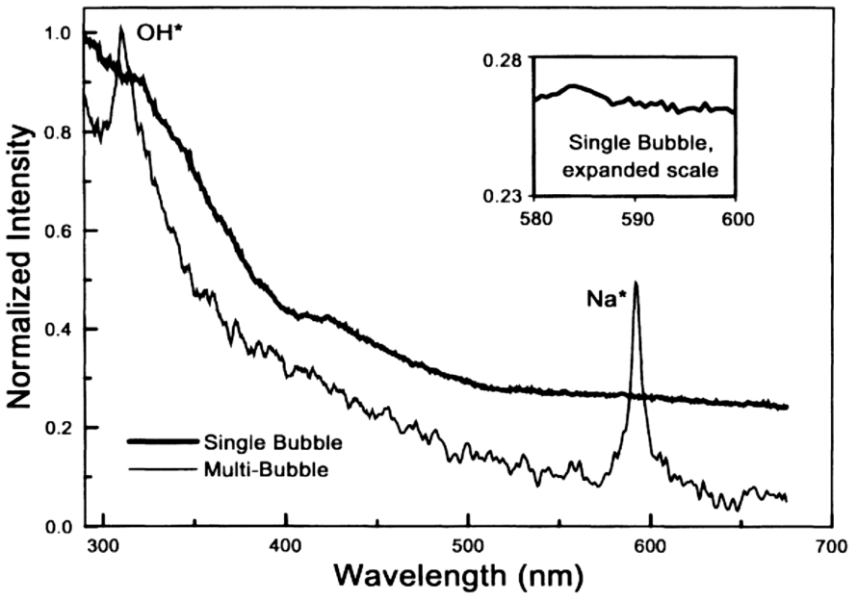

Figure I-6 Comparison of MBSL and SBSL spectra in 1 M NaCl solution.[62]

The disparity of MBSL and SBSL spectra most probably arises from the symmetry of cavitation compression and collapse.[8, 9, 62] For SBSL, the stable bubble compression cycle and collapse are almost spherical, which means that much less nonvolatile particles can enter bubbles, but a featureless emission exists in bubbles.[61] This makes it difficult to characterize the intrabubble conditions in a single bubble. Xu and Suslick observed strong emission from excited $HO^{\cdot}$ radicals in a single bubble produced in Ar saturated phosphoric acid irradiated by 20 kHz ultrasound and provided an estimated rovibronic temperature of almost 10,000 K.[67] For MBSL in phosphoric acid solution saturated by helium, the same group observed two distinct spectroscopic temperatures of $HO^{\cdot}$ (4000 K) and $PO^{\cdot}$ (9500 K) emissions, indicates both symmetrical and asymmetrical collapses occur in irradiated solution.[68] The unstable transient bubbles and the interaction between bubbles in bubble cloud lead to the asymmetrical collapses.[59, 62, 66] Those asymmetrical collapses can introduce ions, atoms and molecules directly into bubbles by jetting and misting (small droplets).[66] Thus emissions from excited-state injected ions, atoms and radicals are observed in MBSL spectra, especially the nonvolatile metal radicals (Na, K). At the same time, the estimated temperature of the non-spherical bubbles is lower than that of the spherical ones, due to the energy transfer by excitation and dissociation of the injected particles.[69, 70]

The SL spectroscopy provides an indirect but efficient way to determine the intrabubble conditions.[22, 58, 63] The presence of diatomic or polyatomic gas and molecules in irradiated liquid can lead to specific emission bands in MBSL spectra, and the corresponding rotational and vibrational temperatures can be estimated by modelling these emissions.[45]

I.1.5 Dependence of sonochemistry and sonoluminescence on various factors

I.1.5.1 Ultrasonic frequency

Frequency of ultrasound strongly affects the initial growth and the population (number, size and distribution) of cavitation bubbles, especially the SL and sonochemical active bubbles.[56, 57] Generally, more nucleation and production of bubbles occur in high frequency acoustic field. The mean diameter of cavitation bubbles and its radius distribution range decreases with an increase in ultrasonic frequency (**Figure I-7**), thus a higher surface-to-volume ratio for mass transfer.[56, 71, 72] Meanwhile, in a high frequency ultrasonic field, acoustic streaming drives bubbles away from the transducer by radiation force, which leads to a relatively homogeneous distribution of acoustic field compared to low frequency ultrasound.[73] So considering the size, cycle duration and stability of cavitation bubble and collapse violence, low frequency ultrasound generates predominantly transient cavitation, whereas in high frequency acoustic field stable cavitation is majority.[74, 75]

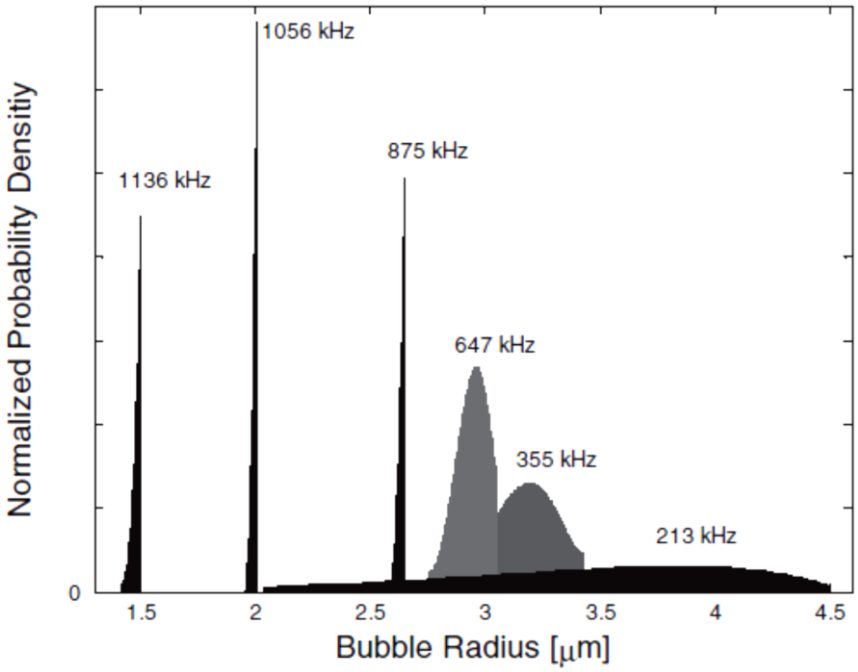

Figure I-7 Size distribution of chemically active bubbles at different ultrasonic frequencies in 0.01 M luminol solution saturated by air.[56]

These changes of cavitation bubble population induced by frequency difference are ultimately reflected in sonochemistry and SL. A strong but not linear correlation between frequency and sonochemical activity or efficiency was previously found in different works.[74, 76-80] An important mechanical or physical effect is expected from low frequency ultrasound, while in high frequency acoustic field, the radical or chemical effect dominates the degradation or oxidation reactions.[81, 82] Such opposite tendency

has been proved by Protenlanger and Heusinger [81] and Petrier et al.[80] The former found the strongest degradation of dextranes by the mechanical effect of ultrasound at 35 kHz than at frequencies over 500 kHz, while the latter observed an enhanced oxidation of iodide ions due to the more significant chemical effect at 514 kHz than at 20 kHz. For each application, no matter in homogeneous or in heterogeneous system, an optimal ultrasonic frequency exists. Under certain conditions, a combination of both chemical and physical effects of ultrasound can significantly enhance the sonochemical reaction rate. For example, in homogeneous system, the most efficient ultrasonic frequency for formation of H_2O_2 in water was found around 360 kHz.[45, 74] In heterogeneous system, 40 kHz produced a better modification of polystyrene surface in the frequency range from 20 kHz to 1 MHz,[82] and for synthesis of gold nanoparticles, 213 kHz acoustic cavitation was found to be the most efficient from 20 kHz to 1 MHz.[77] Such trend of optimum frequency also depends on acoustic power.[83]

In the case of MBSL, from a theoretical point of view, SL intensity is strongly linked to the maximum gas temperature T_{max} reached during bubble collapse, which highly depends on ultrasonic frequency.[31] On the other hand, the number of active cavitation bubbles was believed to increase with ultrasonic frequency, contributing to an enhancement of MBSL intensity.[74] As a result of these multiple effects, the mechanism of frequency effect on sonoluminescence intensity is still unclear. Kanthale et al. observed in the sonolysis of degassed water at a given acoustic power (exceeding Blake threshold), that the SL intensity measured by a photomultiplier tube decreased with an increase in ultrasonic frequency, in the order 213 > 355 > 647 > 1056 kHz.[78] But the first low-resolution MBSL spectra obtained by Beckett and Hua demonstrated an optimum frequency (358 kHz) for the maximum MBSL intensity in Ar saturated water.[74] A similar trend was confirmed by Pflieger et al.: a much stronger MBSL emission in water saturated by Ar was observed at 362 kHz than at 20 kHz, and an enhancement of MBSL intensity in the presence of Ar/20%O_2 gas mixture happened at 362 kHz.[84]

Nevertheless, from both theoretical calculations and experimental observations, high frequency acoustic cavitation mainly shows the emission from plasma continuum, while both plasma continuum and intense lines of excited radicals ($HO^{\cdot}$) or nonvolatile ions (Na) are present in low frequency MBSL spectra.[45, 84-86]

I.1.5.2 Acoustic power

By changing acoustic power, the acoustic pressure in liquid will be changed.[42] Generally, no matter at what frequency, an increase in acoustic power can increase acoustic pressure amplitude in liquid. As a result, in between the upper and lower threshold of acoustic pressure amplitude, the temperature of bubble collapse and the number of active bubbles also increase, thus improve the sonochemical yield and the SL intensity.[44] When the pressure exceeds the upper threshold, a further increase in power will lead to the opposite impact, which is explained by the formation of bubble clusters in the irradiated solution.[56, 78, 85, 87] An optimum acoustic intensity or power density was observed for sonochemical

reactions in H_2O_2 yield,[78] oxidation of iodide,[88] decomposition of carbonyl[89] and corrosion of stainless steel.[83] As for sonoluminescence, the enhancement by increasing acoustic power is found to be much stronger than for sonochemistry,[78] and similarly to H_2O_2 yield, a maximum in SL intensity exists,[90-92] though sometimes it cannot be detected due to the amplifier limitation.[85] It was also noticed that an increase in acoustic power decreases the ratio of sodium line emission against continuum emission in the sonolysis of a NaCl aqueous solution.[85] As a result, it is critical to select a proper acoustic power for specific research or application.

I.1.5.3 Irradiated liquid

Cavitation is favored in liquids with low viscosity, low surface tension and high vapor pressure.[4, 6, 42] A high acoustic pressure is needed for cavitation bubble nucleation and growth in a liquid with high viscosity and high surface tension. Bubble stability, which is very important for SBSL, can be increased in a higher viscosity liquid, such as sulfuric acid.[44] By changing the liquid from basic to acid solution as well as the evolution of liquid pH during sonolysis may also influence sonochemical reaction rate [44] and SL quenching.[93]

I.1.5.4 Dissolved gas

Dissolved gases in an ultrasonically irradiated liquid play as nucleation sites of cavitation, as well as the important composition of gas phase in acoustic bubbles.[4, 6] Gases having higher solubility can increase the size and number of cavitation bubbles, but lower the violence of bubble collapse as more gas molecules diffuse into bubbles.[4, 6, 44] The heat specific ratio and thermal conductivity of the dissolved gas, as well as the number of atoms in the gas molecule (monatomic or polyatomic) and gas ionization potential, can also affect acoustic bubble collapse and intrabubble conditions, hence sonochemistry activity and sonoluminescence intensity.[23, 63, 65, 84, 94] Considering their properties for violent collapses, noble gases like argon and xenon are widely used in studies of sonochemistry and sonoluminescence.[44]

To compensate the degassing effect of sonication, continuous gas bubbling is usually used in experiments in order to facilitate cavitation. By studying the impact of the gas inlet position on sonochemical activity, Pflieger et al. showed that it is a combined effects of dissolved gas concentration and number of cavitation nuclei (introduced by continuous gas bubbling) that control the extent of sonochemical reactions.[95]

Some other investigations in a gas mixture like Ar/O_2 or Ar/N_2 found an optimum mix content for sonochemical reactions (H_2O_2 yield) and SL intensity.[4, 44-46, 84] These observations indicate that a certain content of diatomic gases in monoatomic gases can accelerate the generation and recombination of free radicals during aqueous solution sonolysis.[4, 44]

I.1.5.5 Ambient temperature and pressure

Increasing ambient temperature reduces the cavitation threshold, but lowers the collapse violence at the same time.[4, 44] As a result, unlike most of the chemical processes, in a sonochemical system, a higher temperature leads to a slower reaction rate and a dimmer SL intensity. This effect is much pronounced if the reactant is more volatile, since vapor diffusion into bubble becomes easier under high temperature.[6, 44]

High ambient pressure reduces the liquid vapor pressure thus cavitation becomes more difficult. As long as the acoustic pressure exceeds the threshold of the high ambient pressure, cavitation collapse intensity can be enhanced, thus increasing sonochemical activity and SL intensity.[4, 6]

I.1.5.6 Transducer type

Based on the inverse piezoelectric effect, an ultrasonic transducer converts AC electric energy into the vibration of a piezoelectric material and then propagates sound wave into contacted media.[8] According to the geometric shape, two types of transducer are used: horn and plate.

A horn type transducer is normally designed to generate low frequency ultrasonic waves, which primarily produce transient bubbles with large size and violent collapse in a local conical zone adjoining the horn tip. However, due to the agglomeration of dense bubbles at the horn tip, an attenuation of the cavitation efficiency exists.[44, 96] Moreover, the diameter of horn tip can influence the sonochemical activity. Enterzari and Kruus [97] observed an increase of iodide oxidation rate with the increasing horn tip size, and explained it by an increasing number of bubbles and less bubble coalescence or agglomeration. However, the contrary trend with H_2O_2 yield in sonolyzed water was found by Nikitenko et al.[98] and explained by the different acoustic power intensity. An optimum horn tip diameter might exist for specific applications.

A plate type transducer, on the contrary, can be designed for both low- and high-frequency ultrasound. For a low-frequency plate transducer, usually a standing wave is formed and active acoustic bubbles are mainly trapped at the pressure antinodes.[44] For a high-frequency plate transducer, the standing wave is attenuated by acoustic streaming. Therefore, traveling wave becomes dominant in the liquid at high frequency, which drives bubbles towards the liquid surface. Hence a large cavitation active region is expected.[44, 99] Simultaneously, the traveling wave produced by a high-frequency transducer also hinders bubble clusters formation and enhances the mass transfer in the irradiated liquid.[100]

I.1.5.7 Reflection from a liquid surface or a solid plate

A free liquid surface or a reflective solid plate in the reactor can affect cavitation activity by modifying the wave predominance distributed in irradiated liquid.[101-103] At low acoustic power, a free liquid surface can reflect ultrasonic wave efficiently, which can generate a resonant standing wave in liquid if

the distance between liquid surface and the transducer plate equals to an odd multiple of $\lambda/4$ (**Figure I-8**).[72] Such standing wave can influence cavitation activity and distribution for both sonochemistry and SL.[8, 44, 104] When the acoustic power increases, vibration of the liquid surface becomes strong, hence such standing wave resonance becomes unstable and weak.[104] But if a rigid solid exists in the liquid and acts as a reflective plate, the standing wave pattern can become more dominant and stable, which significantly impacts SL and SCL intensity and distribution in liquid.[44]

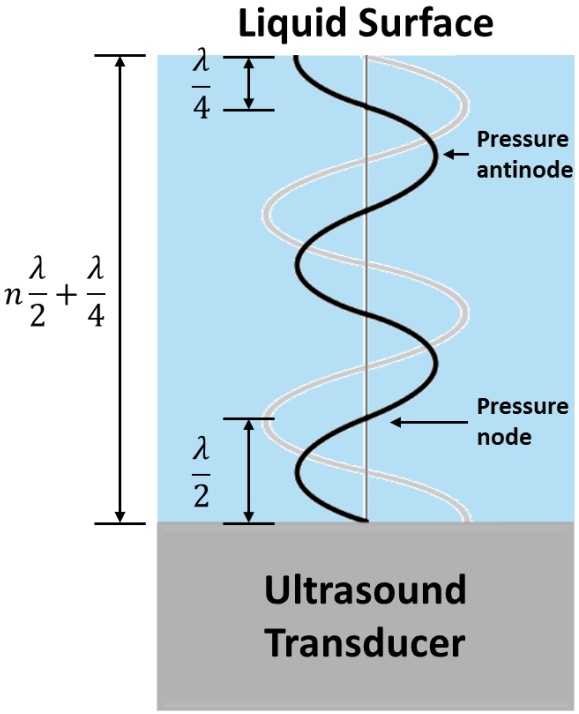

Figure I-8 Schema of a resonant standing wave: pressure variation (black) and displacement variation (grey).

I.1.5.8 Reactor geometry

Different types of ultrasonic reactors have been designed for various studies and applications. Thangavadivel et al.[102] observed the dependence between sonochemical efficiency and the diameter ratio of a reactor to a 200 kHz transducer, and found a maximal sonochemical yield at the ratio equals 1.45. Kim et al. revealed that a bottom plate attached to the ultrasonic transducer at 334 kHz is more efficient for energy transfer if their dimensions are close.[105] Other previous studies did not found obvious effect on sonochemical activity by changing the diameter of ultrasonic reactor or vessel.[44, 98]

I.1.5.9 Mechanical stirring

An in-situ mechanical stirring is often applied during experiments, which can introduce an artificial flow in the acoustic field. This addition of fluid motions can either increase or decrease active cavitation activity and distribution in liquid, dependent on applied ultrasonic frequency, power, stirring speed,

reactor configuration etc.[44] Previously, Bussemaker and Zhang observed an increase of H_2O_2 yield with increasing stirring speed at low frequency ultrasound (40 kHz), because the agitation flow prevents bubble coalescence.[106] At high frequencies, a traveling wave is already present in the irradiated liquid. Based on the sonication conditions, an artificial stirring can impact it in a positive or negative way. Bussemaker and Zhang found a decrease of sonochemical activity and SCL distribution in high-frequency acoustic fields (376, 995 and 1179 kHz) at low power in the presence of mechanical stirring, and explained it by the agitation distortion of acoustic wave propagation and standing wave formation.[106] However, a higher sonochemical activity was observed at high frequencies (204 and 613 kHz) with an agitation speed of 370 rpm, besides a more homogeneous active bubble distribution in liquid irradiated, by Pflieger et al.[84] Therefore, depending on sonication conditions, the mechanical stirring, the size and position of stirrer and its speed should be carefully selected if possible for a better application.[44]

I.1.5.10 Ultrasonic duration

By controlling the ultrasonic treatment duration, sonochemical reaction rate and ultrasonic cleaning effect can be influenced. Mahbubul et al. obtained a more stable and lower viscosity nanofluid by extending the ultrasonic treatment duration over 90 minutes. [105] Another group of Kaltsa et al. also found that by increasing sonication time, more stable emulsions with smaller size oil droplets can be produced.[107] Other studies of extraction efficiency,[108] catalytic reaction rate,[109] surface modification and structuration [42, 110] also proved the importance to control the duration of ultrasound in order to obtain an effective treatment.

I.2 Ultrasonic modification and cleaning of solid surfaces

As described before, it has been proved that within a short distance between a collapsing bubble and a solid substrate, the combined impact of microjets and shockwaves from the bubble collapse, besides the extreme local temperature and pressure, can strongly modify the physical morphology and chemical composition of the substrate surface.[50] On the one hand, this effect may induce unwanted erosion damages on surfaces, such as the erosion of ship propellers and turbine blades. On the other hand, it can be an efficient method for surface cleaning and for special functional surfaces formation to meet industrial requirements. Macro- and micro-scale applications of power ultrasound devoted to the modification and cleaning of extended surfaces, e.g. organic polymers, inorganic solids or metallic alloys, have been developed for over 50 years already.[3, 4, 42, 50, 111] Compared to other conventional techniques, ultrasonic surface modification and cleaning have the advantages of easier access to narrow areas, fewer process stages, use of less or non-hazardous aqueous solutions, a wider range of substrate surfaces to be treated and milder operating conditions.[3]

I.2.1 Ultrasonic modification of solid surfaces

I.2.1.1 Polymer

Polymers like acrylonitrile butadiene styrene (ABS), polyvinyl chloride (PVC) and polyethylene initially have an inert surface, which is hard for adhesion or coating. In order to improve their functionality, polymer surfaces usually have to be modified to increase the roughness and wettability, so that compounds like dyes, metal ions and hydrophilic monomers can be grafted to the treated surfaces.[111] To achieve a better adhesion, power ultrasound can be joined with conventional wet chemical treatments to significantly accelerate the polymer material surface functionalization process: (1) microjets increase the roughness, thus expanding the contact surface; (2) locally high temperatures and pressures reached by collapsing bubbles break chains and bonds on surfaces; (3) generated radicals may chemically oxidize material surfaces.[3] The chemical etching of ABS surface was compared by Zhao et al. in the presence or absence of power ultrasound.[110] **Figure I-9** illustrates the stronger and faster surface roughness increase observed under ultrasound irradiation in comparison to conventional etching in the presence of chromic acid. Generally, the sonochemical enhancement of polymer surface coating properties depends on the type of polymer substrates, the initial polymer surface condition, the processing solution, the operation temperature, and the ultrasound properties including the frequency, saturating atmosphere and applied power intensity. For example, it was observed that for sonochemical surface modification of a polymer named Noryl (polyphenylene/polyester) in water, a much higher weight loss and a more significant change of surface morphology were observed at 20 kHz ultrasound, than at 40 kHz and at high frequencies (582, 863 and 1142 kHz). Besides, an obvious increase of sonicated polymeric surface oxidation in the order from 20 kHz to 863 kHz indicated a stronger sonochemical effect by high-frequency ultrasound.[82]

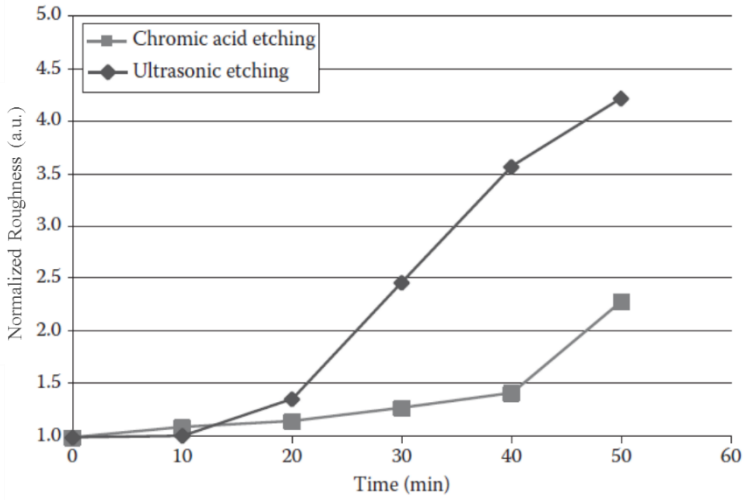

Figure I-9 Surface roughness of ABS versus etching time in the presence and absence of ultrasound.[110]

I.2.1.2 Inorganic solids

For layered inorganic solids, such as sulfides and oxides (ZrS_2, TaS_2, MoS_2, MoO_3, V_2O_5), adsorption of organic, organometallic and inorganic compounds between their layered microstructure may significantly change their catalytic, electronic and optical properties. Such materials have been highly used for the preparation of batteries, lubricants and catalysts.[112] To produce these materials, routine synthetic techniques normally require long treatment duration and high operational temperature. When combined with high-intensity ultrasound, the intercalation rate of molecules into layered inorganic solids was found to be dramatically improved.[111, 112] Suslick et al. examined the effect of 20 kHz ultrasound with high intensity (20 $W.cm^{-2}$) on inorganic solids of TaS_2, MoO_3, and found strong erosion with solid particle size reduction from 60 to 5 μm, and also significant aggregation of inorganic particles after 30 minutes sonication.

Some hard inorganic surfaces such as ceramics and glasses may also be modified under ultrasound irradiation in order to modify the physico-chemical properties of their surfaces. Virot et al. studied the effect of acoustic cavitation at the water-glass interface with two different types of glass materials: soda lime and fused silica.[32] Their experimental results clearly indicated that glass surface sonicated by 20 kHz ultrasound was not only eroded physically as illustrated in **Figure I-10**. Chemical analyses of the post-sonicated solutions evidenced an acceleration of the leaching of the glass material components during sonication. Similar strong erosion effects were previously observed by Cobley and Mason on ceramic surface materials sonicated in pure water.[113] The same group also found that ceramic surface modification level does not correspond to their glass transition temperatures (T_g) or their surface chemical composition, which means that chemical attack is not as important as the physical damages for such ceramic/glass material surfaces.[114]

Figure I-10 Erosion of fused silica glass sonicated 180 min in distilled water at 25 ℃ by 20 kHz ultrasound at 49 $W.cm^{-2}$.[32]

I.2.1.3 Metals and metallic alloys

For metals and their alloys, ultrasound irradiation has been widely applied for surface structuration, crystallization, finishing, coating, etc.[50] Several authors showed that sonication processing allows metal

surfaces to be highly functionalized with a superhydrophobic feature, to show excellent electrostatic properties, to possess a good adhesion for anticorrosion coating, or to exhibit metal hydride layers for hydrogen-storage.[50, 115-117]

Chiu et al. has identified three stages of surface roughness evolution for metal alloys based on stainless steel, titanium and copper.[113] They initially observed an almost linear increase of the roughness, followed by its slight decrease in a second stage, until a stable roughness is observed in a final stage. This evolution is well correlated to the acoustic cavitation erosion periods of incubation, acceleration and maximum saturation observed by other authors, for instance for aluminum and glass materials.[32, 118]

Due to the ductility and reactivity of some metallic materials, both physical and chemical effects of acoustic cavitation may play a predominant role during surface modifications.[50, 119] Microjets and shock waves resulting from the cavitation bubble collapses may directly deform metallic surface. For instance, Verdan et al. have done series of ultrasonic tests with aluminum, copper, silver and zinc surfaces at 20 kHz in water.[120] They found that on the surface after a very short sonication time, pits and craters are the most common microscopic deformation structures observed (see **Figure I-11**). At the same time, similar increasing trend of surface roughness with the sonication duration was observed for each examined metal, for example aluminum surface roughness raised from an initial 5 µm to about 30 µm after 4 minutes treatment. These ultrasonically modified metal surfaces can be used in industry to enhance coating adherence for specific applications.[120]

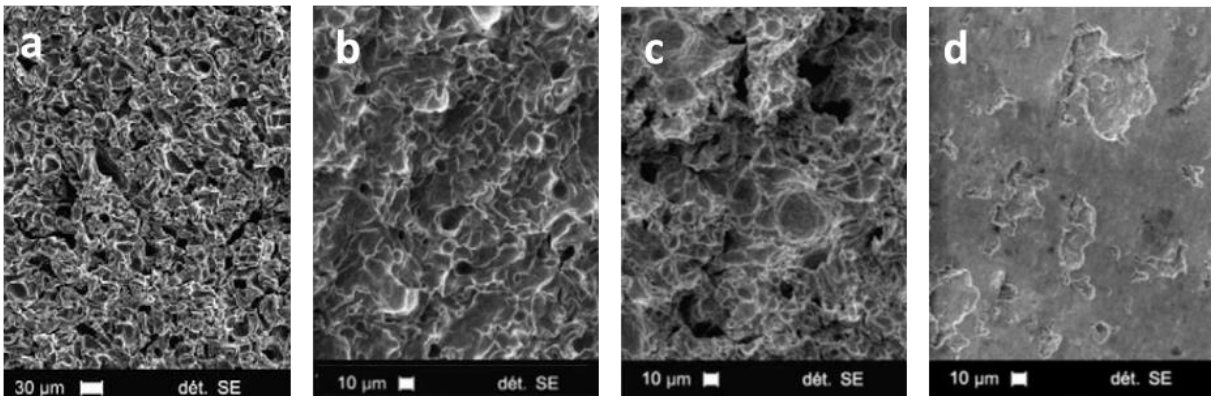

Figure I-11 SEM images of metallic surfaces sonicated at 20 kHz in pure water (40 ℃, 40 W.cm^{-2}): (a) Al sonicated during 4 min; (b) Cu sonicated during 10 min; (c) Ag sonicated during 10 min and (d) Zn sonicated during 10 min.[120]

Meanwhile, some results suggested that for low melting point metals, the high bubble collapsing temperatures may locally melt some surface compounds and then recrystallize them due to fast cooling rates[50]. A smaller grain size and a refined surface structure can be expected during recrystallization processes. Even if the temperature reached during bubble collapses is not high enough to melt metallic

surfaces, the stressed induced solid-state diffusion may also result in the formation of a porous structure at the metal surface.[121] For example, the formation of mesoporous structures on different metallic surfaces was noticed by Skorb et al. They applied low frequency ultrasound (20 kHz) at high power intensity (57 and 200 $W.cm^{-2}$) to material of aluminum, magnesium, stainless steel in water and titanium surfaces in 5 M sodium hydroxide solution respectively. As presented in **Figure I-12**, highly modified surfaces with similar porous structures on these 4 different metals were produced after 15 to 40 minutes sonication, which represented a strong hydrophilic property.[115, 122] Such specific nanostructures can potentially be applied for the development of superhydrophilic or superhydrophobic surfaces, which are of great interest in the fields of automotive, aerospace and biomaterial.[115, 122]

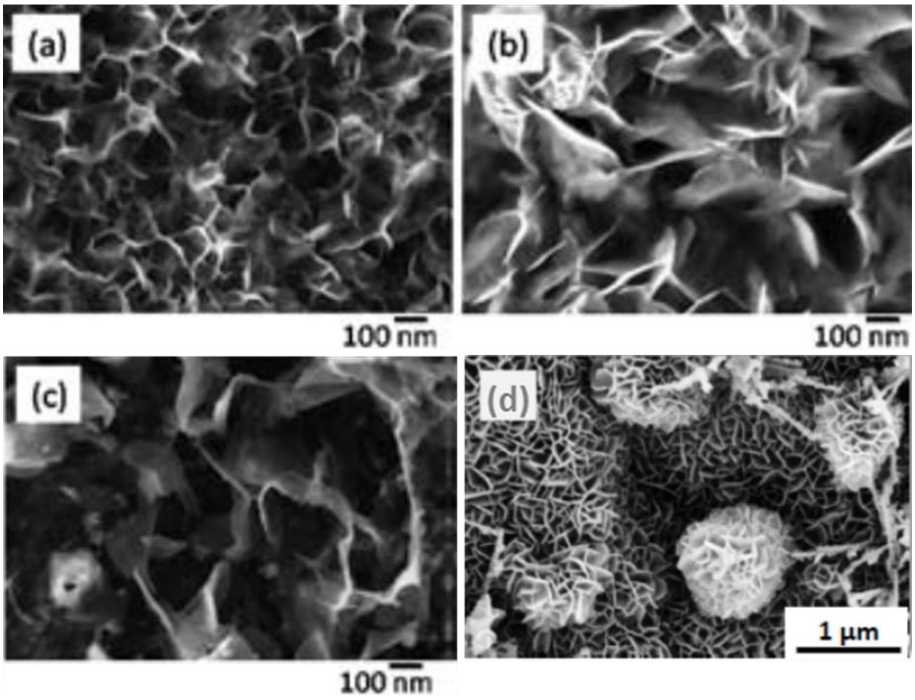

Figure I-12 SEM images of metallic surfaces sonicated at 20 kHz in pure water (65 ℃, 57 $W.cm^{-2}$): (a) Al; (b) Mg alloys; (c) stainless steel; and (d) in 5 M NaOH solution (60 ℃, maximum 200 $W.cm^{-2}$) Ti.[115, 122]

In addition, the sonochemical reactions triggered in heterogeneous systems can also lead to the formation of new phases at metal surfaces. Reactive radicals produced during bubble collapses may react with the unprotected surface through oxidative or reductive processes.[50, 117] For example, a sponge-like structure, composed of porous metal stabilized by an oxide layer, was observed by Skorb et al. with chemically reactive metal particles, including Zn, Mg, Al and their alloys, sonicated at 20 kHz in water. Such novel metal sponges are of great interest to form nanocomposites, nanocatalysts and corrosion-resistant surfaces for applications in material science, chemistry and biomedical science.[123] However, the ultrasonic aid on the formation of these mesoporous structures is not evident, since similar oxide microstructures was observed with various metals (Mg, Al, Ni) after hot water treatment (75 ℃).[124]

I.2.2 Ultrasonic cleaning of solid surfaces

Ultrasound has been applied as a tool for surface cleaning since 1950s.[125] Nowadays, it is widely used in daily life (glasses, watches and jewelry washing), electronics (cleaning of printed circuit boards), optics (decontamination of optical instruments), pharmaceutical industry (cleaning of medicine bottles), laboratory (descaling of experimental devices), machinery (removal of corrosion layers), metal industry (cleaning of metal wires) and many other fields.[125, 126]

Cleaning or removal of dirt and contaminants from the target surfaces can be accomplished by either chemical dissolution by solvents or physical erosion by external forces.[127] In case of ultrasonic cleaning, two primary factors drive the cleaning process in both physical and chemical approaches: i) the non-symmetric collapse in the vicinity of a solid surface, which can directly damage the adhered dirt and contaminants; ii) the acoustic streaming in ultrasonic field, which can reduce the thickness of hydrodynamic boundary on the surface and enhance the mass transfer at the interface of contaminant and solvent.[51]

The biggest advantage of ultrasonic cleaning is that it has much less limit of the shape and size of objects and it can easily get access to small cavities and blind spaces in treated materials that are not accessible for other conventional cleaning approaches. As described before, cavitation bubble size is inversely related to ultrasonic frequency. As a result, depending on the size of contaminants, different frequencies are applied in ultrasonic cleaning as presented in **Figure I-13**.

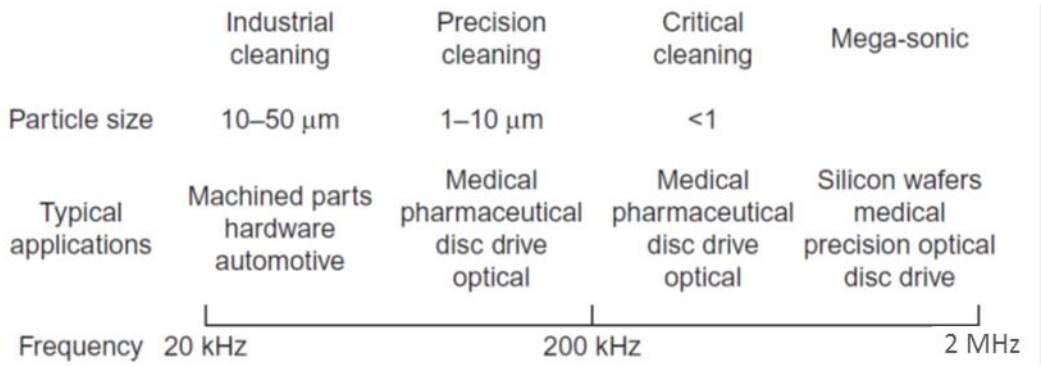

Figure I-13 Ultrasonic cleaning application as a function of frequency.[127]

In general, most ultrasonic cleaning systems are based on frequency from approximately 20 to 200 kHz.[127] Approximately, 20 to 40 kHz is suitable for industrial machine metals cleaning, while frequencies of 60 to 80 kHz are often used for more precise cleaning applications. Intermediate to high frequency (100 to 200 kHz) ultrasonic systems are introduced for very delicate parts cleaning, such as medical and optical instruments. Some systems also provide the option of multiple frequencies within a single ultrasonic cleaning tank. In semiconductor production, megasonic cleaning is used in order to minimize the cavitation damage on the fragile silicon wafers (see **Figure I-14**).[128]

Megasonic cleaning has a range from 350 kHz to 2 MHz, which is efficient in removal of sub-micron particles.[51] In contrast with conventional ultrasonic cleaning at low frequency, where surface cleaning is from both physical and chemical effects from cavitation, at megasonic frequencies fluid motion (acoustic streaming and micro streaming) is dominant in decontamination.[127] As a result, contaminants on surface are swept and cleaned by shear forces of the megasonic fluid flow, which will not attack the substrates. However, megasonic cleaning is not suitable for complex structures or in blind corners.[128]

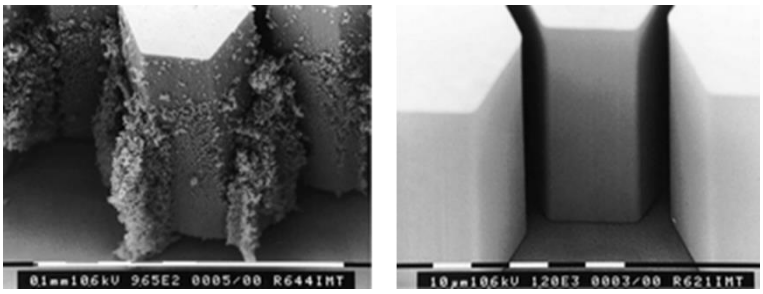

Figure I-14 Cleaning of microstructures with high aspect ratio: without (left) and with megasonics (right).[129]

After several decades of progress in both theory and application technology, various ultrasonic cleaning systems have been developed to meet the different cleaning purposes of solid surfaces with different sizes, geometries, chemical compositions and physical properties. These systems include high frequency ultrasonic cleaning, focused ultrasonic cleaning, multi-frequency ultrasonic cleaning and sweep frequency ultrasonic cleaning.[130]

Besides, in addition to these specially designed cleaning systems and equipment, the control of the operational conditions (including the ultrasonic frequency, intensity, temperature, detergent solution and surfactant, etc.) is essential for an efficient cleaning of material surfaces. Usually, a combination of ultrasound with other thermal or chemical cleaning techniques is also attractive for a better cleaning result.[51, 131]

I.3 Decontamination of UNGG radioactive structure materials

I.3.1 UNGG reactors

I.3.1.1 UNGG reactor development history in France

After the Second World War, France decided to develop its own capability of nuclear power, both in military and civilian fields. However, even with sufficient deposits of uranium ore, the lack of industrial scale facilities for enrichment of uranium limited the available possibility of choice for French government at that time. To skip the step of enrichment and to directly apply natural uranium in nuclear

reactors, moderators characterized with a small absorption cross-section and a large scattering cross-section were essential. Though heavy water was the best candidate as a moderator, its production technology was not mastered by France yet. To meet these limitations, purified graphite, as a mature developed industrial product, replaced heavy water to be the neutron moderator. It has a low neutron capture cross-section and good mechanical resistance to neutron flux and temperature. Carbon dioxide was chosen as the coolant due to its good properties for heat transfer and neutron cross section, as well as its easy access, cheap price and chemical stability with graphite, cladding material and uranium fuel.[132]

As soon as the design of such a gas-cooled nuclear reactor was decided, the construction of the natural uranium graphite-gas (UNGG) reactors in France started rapidly. In total, 9 UNGG reactors were built in France as located in **Figure I-15** and 1 in Spain (Vandellos unit 1). The first three UNGG reactors (G1, G2 and G3) were built in Marcoule by CEA between 1956 and 1960, in order to supply plutonium for the manufacture of nuclear weapons. Then six other reactors were commissioned between 1963 and 1972 for the thermal and electrical power generation. **Table I-2** summarizes the basic characteristics of those 9 reactors.

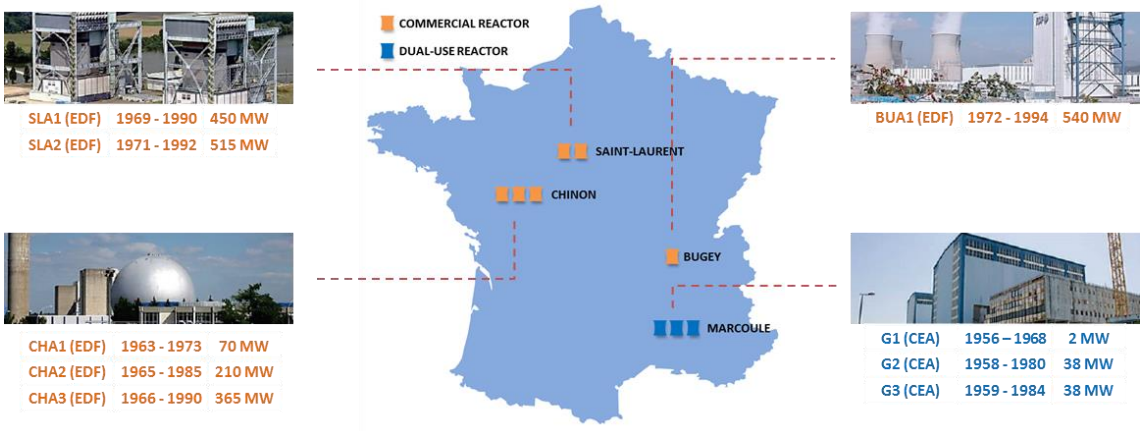

Figure I-15 Location of the 9 French UNGG reactors.[132]

Table I-2 Characteristics of the 9 UNGG reactors implemented in France.[132, 133]

UNGG reactor	**G1**	**G2**	**G3**	**CHA1**	**CHA2**	**CHA3**	**SLA1**	**SLA2**	**BUA1**
Site	Marcoule			Chinon			St-Laurent-des-Eaux		Bugey
Manager	CEA			EDF					
Commission time	01/1956 10/1968	07/1958 02/1980	06/1959 06/1984	06/1963 04/1973	02/1965 06/1985	08/1966 06/1990	03/1969 04/1990	08/1971 04/1992	04/1972 05/1994
Thermal power	46	250	250	300	850	1560	1650	1700	1920
Electrical power	2	38	38	70	210	365	480	515	540
Graphite mass (t)	1200	1300	1300	1120	1650	2350	2572	2440	2039
Operation temp. (℃)	30-230	140-400		150-360	190-290	240-410	230-430	240-440	220-530
Piling mode	horizontal			vertical					
Coolant	Air	CO_2							
Pressure (bar)	1	15		25	26		27	29	43
Gas flow	Longitudinal			upward			downward		
Heat exchanger	non-integrated			non-integrated			integrated		
Cladding nature	Mg-Zr alloy								

I.3.1.2 Principle of nuclear fission in UNGG reactors

In a thermal nuclear reactor, such as UNGG units, fission reactions occur between neutrons and fissile material such as ^{233}U, ^{235}U, ^{239}Pu and ^{241}Pu. And ^{235}U is the most common and used nuclear fuel. Each fission reaction leads to the creation of two fission fragments which are ejected at a high speed, and may locally warm up the fuel matrix. Electricity is converted from thermal energy generated by fission

reactions in nuclear reactors. In the nuclear fission reaction of ^{235}U, approximately 2.3 high-energy neutrons (with an average energy of 2.1 MeV) are produced and continuously interact with other ^{235}U isotopes to maintain the chain reaction (I-25). A parallel phenomenon of activation of ^{238}U produces plutonium (I-26), which can be used for military applications and MOX fuel fabrication. The created neutrons arising from nuclear fissions have a very high energy/speed. However, nuclear fission reactions of ^{235}U has a much higher effective cross-section with neutrons at low energy (0.025 eV), so called thermal neutrons. Hence a neutron moderator is necessary to slow down those fast neutrons to thermal level and therefore maintain the chain reaction.[132]

$$^{235}_{92}\mathrm{U} + {}^{1}_{0}n \rightarrow {}^{236}_{92}U \rightarrow FP_1 + FP_2 + k\,{}^{1}_{0}n \qquad \text{(I-25)}$$

$$^{238}_{92}\mathrm{U} + {}^{1}_{0}n \rightarrow {}^{239}_{92}U + \gamma \rightarrow {}^{239}_{93}Np + {}^{0}_{-1}e + \overline{\upsilon} \rightarrow {}^{239}_{94}Pu + {}^{0}_{-1}e + \overline{\upsilon} \qquad \text{(I-26)}$$

With, n, the neutron, FP_1 and FP_2, the fission products ($^{85}_{36}Kr$, $^{80}_{38}Sr$, $^{89}_{43}Tc$, $^{128}_{53}I$, $^{137}_{55}Cs$, etc.), k, the average number of emitted fast neutrons ($k \cong 2.3$).

To maintain the critical state in a thermal reactor, the multiplication factor *k* should be equal to 1, which means that a steady state is observed for the neutron population. The latter is function of the rate of neutron production (due to fission processes) and the rate of neutron losses (due to non-fission absorption mechanisms and leakage from the system). Therefore, a proper distance between ^{235}U isotopes (fuel concentration) in fuel, an efficient moderator in the reactor and an appropriate distribution of absorption material (control rods) are essential conditions for nuclear chain reaction to happen and be maintained. Furthermore, a coolant flow (liquid or gas) with good thermal specific capacity is also important for heat transfer. Combining all of these factors, different types of nuclear power plant were designed and developed for civil and military applications. One of the initial and important nuclear power plant designed for the development of nuclear industry in France was the UNGG reactor.[134]

I.3.1.3 UNGG reactor conception

UNGG is the first generation of nuclear reactors in France. These reactors used metallic natural uranium (0.7% ^{235}U) as fuel, graphite as moderator and gas as coolant for their operation. Presented in **Figure I-16**, a UNGG reactor (type SLA2) consists of four main elements:[132]

- The reactor core contains the metallic natural uranium fuel, the graphite moderator and the control rods. The entire reactor core is confined inside a steel reactor vessel acting as a heat insulator.
- The primary circuit, which contains the heat-transfer coolant, a gas composed of over 97% volume CO_2 (except air for the first reactor G1). The role of heat transfer is provided by the gas which allows transporting the heat produced by the nuclear chain reactions to the heat exchanger between the primary and secondary circuit. The earlier units in Marcoule and Chinon had heat

exchangers outside the reactor vessel. Later units (Saint-Laurent, Bugey and Vandellos) moved the heat exchangers into the vessel. These first two elements are placed in a concrete building used as a radiation shield.

- The secondary circuit contains the water that drives the movement of the turbines. The water is heated and converted into steam in the heat exchanger in contact with the primary circuit. The steam is then used to drive the turbine connected to the alternator which allows the production of electricity.
- The water vapor of the secondary circuit is condensed by a cooling circuit connected to a source of cold water from a river or a sea.

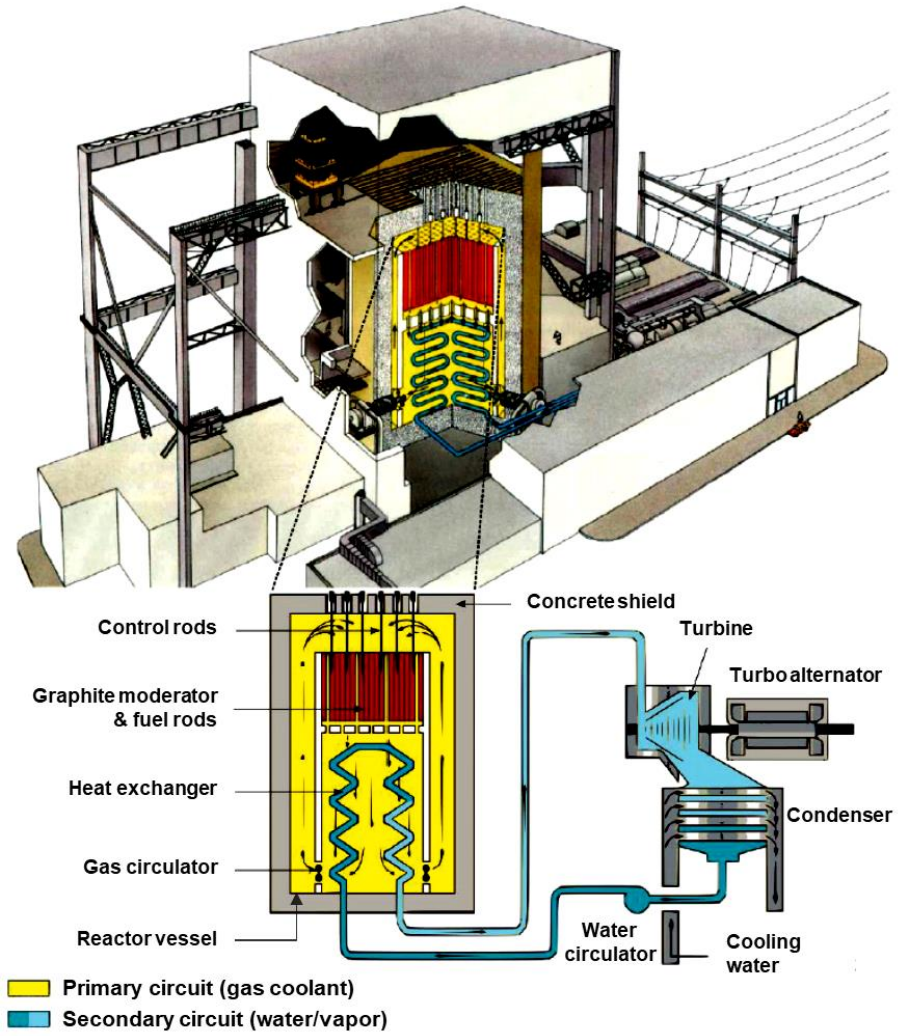

Figure I-16 Scheme of a UNGG reactor (type SLA2).[132]

As the main components of the reactor core, the fuel, the moderator and the coolant were specially optimized for UNGG reactor's specific technology and configuration.

I.3.1.3.1 Fuel element

The fuel tube used in UNGG reactor of SLA2 is shown as an example in **Figure I-17**. Considering the low ^{235}U concentration of unenriched natural uranium, UNGG fuel was packed in the form of thin cylinders of metallic natural uranium to provide a sufficient ^{235}U density for the maintenance of the chain reaction in the reactor core. Natural metallic uranium fuel was then introduced into Mg-Zr (~0.5 wt.% Zr) alloy cladding tube sealed with two Mg-Mn (~1.2 wt.% Mn) plug ends before being inserted in a graphite shell.[132] The fins structure present on the outside part of the cladding allows turbulence of the coolant gas and expands the heat transfer surface between fuel and gas. The fuel tubes were replaced during the operation at a rate of about 2 to 3 channels per day.[134]

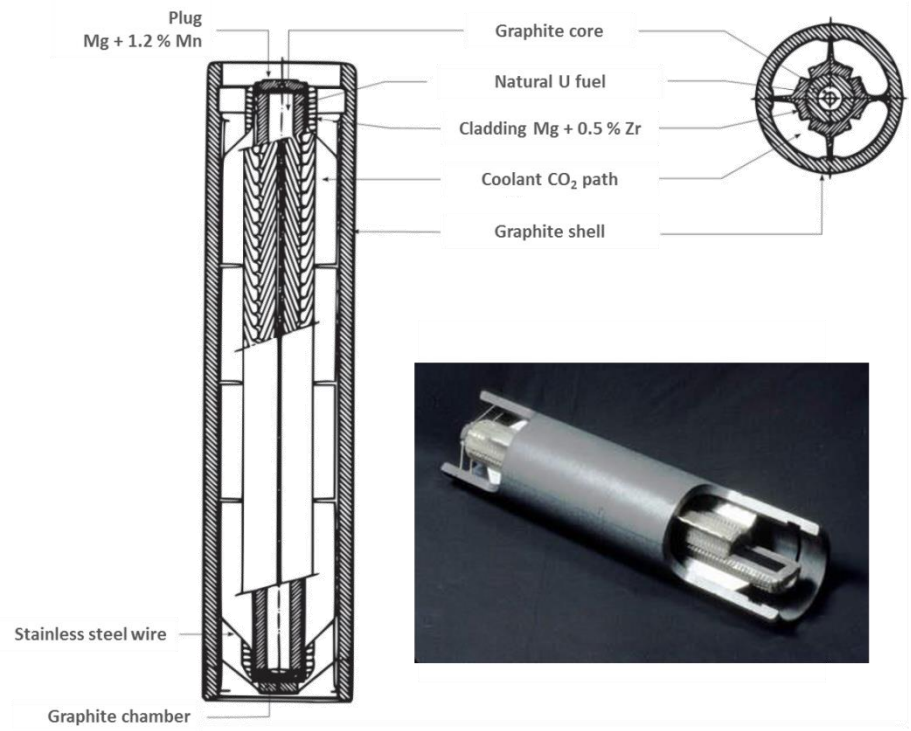

Figure I-17 Scheme of a UNGG fuel tube (type SLA2).[132, 135]

In fact, during the development of UNGG reactors, an evolution of fuel element can be seen in **Figure I-18**. The early fuel elements (G1, G2 and G3) were designed as simple bars with longitudinal fin structures on the outside of their claddings, and were loaded in a horizontal direction in reactors. With the change in operation conditions and the improvement of power generation capacity in the later-built reactors, obvious modifications of dimensions and shapes of fuel elements are observed. The later additions of graphite core and shell, as well as the chevron fin structures, optimized the fission yield, mechanical resistance and heat exchange inside reactors. The fuel loading mode also became vertical for the later EDF reactors.[133]

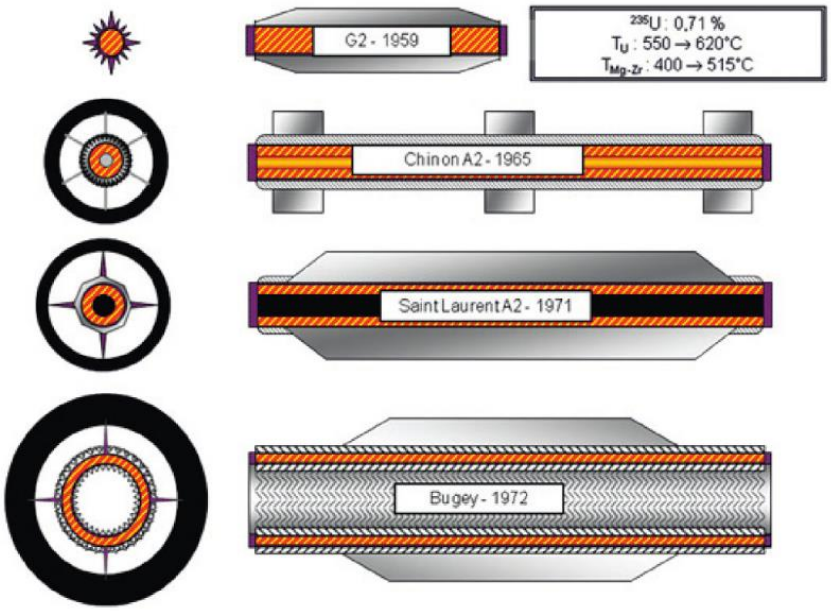

Figure I-18 UNGG fuel element evolution.[136]

I.3.1.3.2 Moderator

The primary function of a moderator is to slow down the fast neutrons into thermal neutrons, thus allowing effective chain reactions. Owing to its low neutron absorption cross-section and good mechanical resistance in the environment of strong radiation and high temperature in reactor core, graphite was used as moderator in forms of piles for UNGG reactors, which consisted of large number of arranged graphite bricks. According to different reactors, the geometries of graphite bricks (hollow or hexagonal) evolved with the shape of the fuel elements. The early reactors of CEA (G1, G2 and G3) had horizontal channel moderator piles, while the later ones belonging to EDF had vertical channel piles.[133]

An example of graphite piles in construction for a UNGG reactor (type CHA3) is illustrated in **Figure I-19**.a. One piece of graphite brick (type SLA2) is presented as an example in **Figure I-19**.c. Fuel tubes (**Figure I-19**.b) or control rods can be inserted in the cylindrical channels of the graphite bricks. The moderator cannot be replaced during the operating of the reactor. Thus its lifetime (between 10 and 24 years) is the same as that of the reactor. Due to the poor neutron slow-down efficiency of graphite, the volume of moderator should be sufficiently large in order to achieve significant power levels. After decades of service, different radionuclides were present in the moderation graphite, coming from the neutron activation of impurities, fragments of the fuel and the fission products of uranium. The most common radionuclides are short-lived ^{3}H, ^{60}Co, ^{133}Ba and ^{137}Cs, and long-lived ^{14}C and ^{36}Cl (half-life period > 31 years).[133]

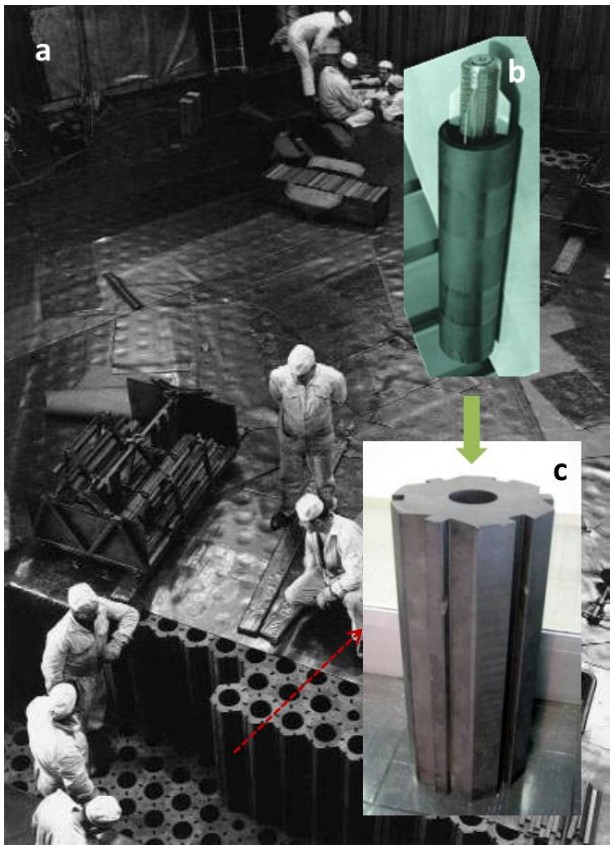

Figure I-19 a) UNGG graphite pile in construction (CHA3, 1965);[133] b) UNGG fuel tube;[2] c) UNGG graphite brick (type SLA2).[137]

I.3.1.3.3 Coolant

The coolant is used to transfer the core heat emitted by the fission reactions to the heat exchangers. The first UNGG reactor (G1 in Marcoule) was cooled with air. Starting from the second unit (G2 in Marcoule), the coolant was changed to a gas mainly composed of CO_2, due to the increasing operational temperature from 300 to 400 ℃. The gas composition is detailed in **Table I-3**. Such a CO_2-based coolant represents a good corrosion inhibition with Mg alloys even at the temperature as high as 500 ℃. On the contrary in air above 350 ℃, the corrosion rate of Mg-based material can dramatically increase.[138]

Table I-3 Composition of the coolant gas used in a UNGG reactor (SLA1 and SLA2).[132]

CO_2	CO	CH_4	O_2	H_2	H_2O
97.43 % vol	2.50 % vol	500 ppm	500 ppm	100 ppm	5 – 100 ppm

I.3.1.4 End of UNGG reactor development

During the development of UNGG reactor and the construction of EDF reactors for commercial services, the French nuclear industry developed its own uranium enrichment capacity with the commissioning of

the enrichment plant in Pierrelatte in 1964. Therefore, EDF modified its research strategy towards Light Water Reactors (LWR), using light water as both moderator and coolant. It became widely agreed that LWR was much more efficient and economic than UNGG reactors, since the upper power limit of a UNGG reactor was restricted by the volume of graphite moderator and in turn the high capital cost. As a result, in 1968, the last designed UNGG power plant in Fessenheim was abandoned during its construction. Since then, the safer and more economical LWRs have occupied the nuclear industry in France and in the world.[132, 134]

I.3.2 Nuclear reactor cladding material: Mg-Zr alloy and stainless steel

I.3.2.1 Nuclear fuel cladding

In a reactor core, the first and important barrier to avoid the radioactive elements of fuel and its fission products entering the primary circuit and environment is the fuel cladding. Considering that the cladding is exposed to the most severe conditions in a reactor during operation, cladding material selections are restricted. Multiple prerequisites should be taken into account: high neutron transparency, good neutron radiation resistance, sufficient maximum service temperature, acceptable melting temperature, excellent thermal conductivity, low thermal expansion, good creep resistance, suitable mechanical strength, high corrosion resistance, stable chemical compatibility with fuel materials, coolant, moderator and fissile products, etc. The neutron capture cross-section versus melting temperature for different elements is present in **Figure I-20**.[139, 140] The low neutron absorption of magnesium combined to its other intrinsic properties allowed this metal to be considered as an appropriate base for the nuclear fuel cladding alloys in the first generation of reactors.

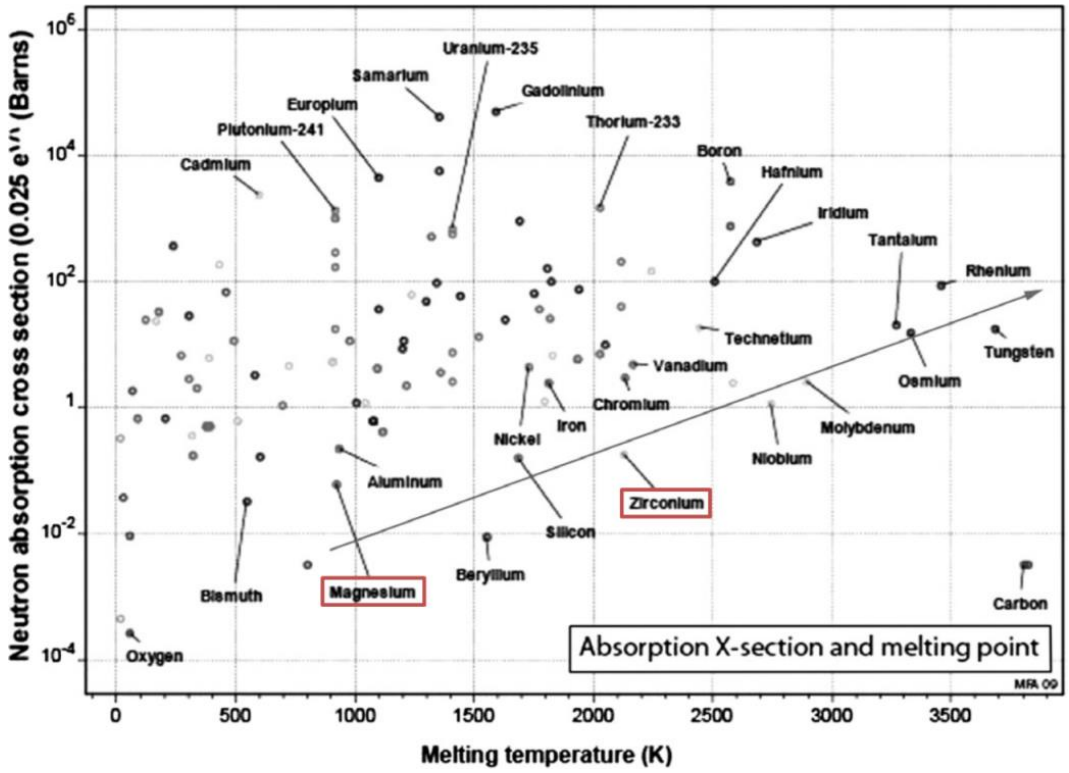

Figure I-20 Element melting temperatures versus neutron absorption cross-sections.[139]

I.3.2.2 Mg alloys cladding

I.3.2.2.1 Mg and its alloys

Magnesium, as the fourth most abundant element in the Earth (13 % mass of our planet after iron, oxygen and silicon), makes itself easy access and cheap for industrial applications.[141] Pure Mg is a shiny grey metal, with a low density of 1.738 kg.m^{-3} at 20 ℃.[142] Crystalline Mg exhibits a hexagonal structure with a c/a ratio equals to 1.623 (parameters of mesh a = 0.32093 nm and c = 0.52099 nm). With a low melting point at 650 ℃ and a low boiling point at 1090 ℃ under atmospheric pressure, Mg is very ductile with temperature increase and can be readily casted and welded.[143, 144] As one of the second column (alkaline earth metals) of the periodic table, Mg is very reactive both in air and aqueous medium even at room temperature. When coupled or precipitated with other metallic elements, Mg can be damaged even more strongly by galvanic corrosion. Nevertheless, such corrosion of Mg can be slowed down or stopped by the formation of a protective film of oxide or hydroxide on the Mg surface.[142]

Considering the high chemical reactivity, as well as the low mechanical properties and flammability of pure Mg, this metal is commonly alloyed with other metallic elements including aluminum, zinc, cerium, silver, thorium, yttrium or zirconium. Mg alloys normally have good flowability due to their high fluidity in the liquid state and their machinability is also excellent. However, these alloys can have a high microporosity as well as a large grain size resulting from fabrication processes which are detrimental to their mechanical properties. By adding zirconium elements, the grain size can be refined and the

formation of microporosities can be prevented, which significantly improves the mechanical properties of Mg alloys. In the light of the similar low neutron absorption cross-section of zirconium (see **Figure I-20**), Mg-Zr alloy was applied as the nuclear cladding material for UNGG reactors.[142, 145]

I.3.2.2.2 Mg alloys in UNGG

In fact, the first UNGG reactor G1 used commercial magnesium, and not Mg-Zr alloys, as the material for fuel cladding. Though such claddings worked properly under its operational temperature below 300 ℃ in air, some corrosion was observed after their service. At the same time, laboratory experiments had proven that in CO_2 gas environment, Mg and its alloys performed a good corrosion resistance even for temperatures around 450 ℃, which was higher than the operational temperature selected (400 ℃) for the next designed UNGG reactors (G2 and G3). In addition, most of the Mg alloys can not meet the criterions required for the new reactors excepted for Mg-Zr alloy. Thanks to their finer grain size and lower microporosity, even after long irradiations at high temperatures, Mg-Zr alloy claddings still maintained a low thermal expansion, a good creep resistance and a high mechanical strength. Hence, the decision to adopt Mg-Zr alloy as a cladding material became logical.[145] As described above, the plug ends of fuel elements were composed of Mg-Mn (~1.2 wt.%) alloys. Similar to that of Zr with Mg, a small amount of Mn can also refine Mg grains, but better than Zr.[146] Though the physical properties of Mg-Mn alloys were found not far from that of Mg-Zr alloys,[147] Mg-Mn alloys exhibit a better thermal conductivity, besides a higher strain-dependent damping,[146] which made it more suitable as cladding plugs.

With the development of nuclear reactors, a higher primary circuit temperature was required to increase the thermal efficiency of the reactors. Mg-Zr alloy operational temperature was restricted to approximately 500 ℃ due to its creep and corrosion resistance. Meanwhile, long-term storage in spent fuel pools was impossible for Mg-Zr alloy because of its high corrosion rate in water. As the LWR replaced UNGG reactors in France, there was no reason to use Mg-Zr alloys in the light water primary circuit environment. Instead, stainless steel and Zr alloys became the main fuel cladding material.[134, 139, 140]

I.3.2.2.3 Characteristic of Mg-Zr claddings after service and during storage

During the lifetime of fuel element in a core, irradiation can result in the diffusion of radioactive fission products in the inner wall of the cladding including ^{90}Sr, ^{137}Cs, ^{60}Co, ^{63}Ni, ^{239}Pu, ^{240}Pu, ^{241}Pu and ^{241}Am. This diffusion process was found as deep as 20 μm, which significantly reduced the ductility of the material. [35] To solve this problem, a graphite barrier named aquadag was coated on the inner side of UNGG cladding to keep the diffusion depth within a few microns.[2, 140]

Within the service period of fuel rods, corrosion of the Mg based cladding material can happen at the high in-core operational temperature. Considering the negligible quantity of zirconium in Mg-Zr

cladding, corrosion mainly occurred with chemically active magnesium. In air coolant, impurities such as hydrocarbons and water vapor played the main harmful role in the slow corrosion reactions with claddings, and this complicated process can be strongly accelerated with the temperature increase. For example, the maximum corrosion thickness formed on a pure Mg surface can reach 250 mm per year in dry air at 575 ℃ under atmospheric pressure, while this value was just 5 mm per year at 475 ℃. Yet, in dry CO_2 the corrosion layer formation was ignorable (< 10^{-2} mm per year for Mg-Zr alloys). The possible chemical reactions between Mg and O_2, CO_2 are listed below (reactions (I-27 to (I-31):[138]

$$1/2\,O_2 + Mg \rightarrow MgO \quad \text{(I-27)}$$

$$CO_2 + Mg \rightarrow MgO + CO \quad \text{(I-28)}$$

$$CO + Mg \rightarrow MgO + C \quad \text{(I-29)}$$

$$CO_2 + 2Mg \rightarrow 2MgO + C \quad \text{(I-30)}$$

$$CO_2 + MgO \rightarrow MgCO_3 \quad \text{(I-31)}$$

According to the (I-27) to (I-31) reactions, one can expect the formation of a thin corrosion layer enriched in MgO, $MgCO_3$ and carbon on the metal at the real operational temperature. However, the formation kinetics for these corrosion products was found to be lower with Mg-Zr alloys.[138]

Furthermore, after the operating cycle, corrosion of Mg-Zr cladding of the discharged fuel rods did not stop, but continued and even became severe during the storage in spent fuel pools and cement matrix packages.[2, 148] In fact, most of the corrosion of Mg-Zr claddings occurred after their service in reactors, producing large amounts of magnesium hydroxide and hydrogen.[149] The corrosion process of Mg in moist air or water is presented in the following reaction (I-32):[2]

$$Mg + 2H_2O \rightarrow Mg(OH)_2 + H_2 \quad \text{(I-32)}$$

The overall reaction can be expressed into the anodic and cathodic partial reactions and the formation of precipitates expressed in reactions (I-33) to (I-35):[2]

Anodic reaction: $$Mg \rightarrow Mg^{2+} + 2e^- \quad \text{(I-33)}$$

Cathodic reaction: $$2H_2O + 2e^- \rightarrow H_2 + 2OH^- \quad \text{(I-34)}$$

Precipitation: $$Mg^{2+} + 2OH^- \rightarrow Mg(OH)_2 \quad \text{(I-35)}$$

In the spent fuel pools, the temperature increase caused by the decay of the used fuel may enhance the corrosion reaction between Mg and water. Besides, the existence of chloride ions (impurities in graphite)

and the possible presence of cracks or pits at the cladding surface may significantly accelerate corrosion processes.[140, 142] Moreover, galvanic corrosions caused by the graphite coating and the noble alloy elements (Fe, Ni) may also involve damage to the Mg based claddings.[150, 151] For example in **Figure I-21**, galvanic corrosion occurs in the presence of an electrolyte, liquid of spent fuel pool in this case, and the deposited graphite and Mg substrate act as cathode and anode respectively.[2] The potential difference between anode and cathode produces a current that accelerates the dissolution of Mg on the anode side and the generation of H_2 on the cathode side.

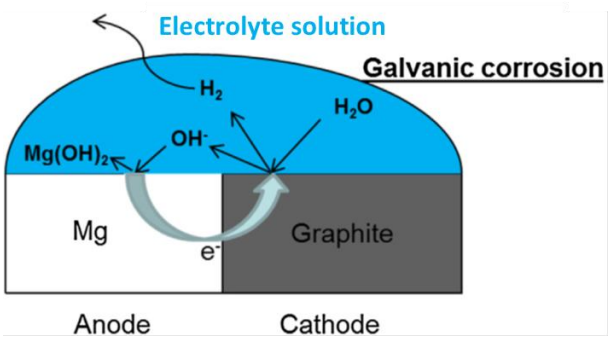

Figure I-21 Galvanic corrosion in the case of graphite deposited on Mg surface.[2]

Since cement has a high density, which can immobilize and provide a sufficient shielding of radioactive substances, besides its low cost and simple process, encapsulation of solid wastes from nuclear power plants in cement matrix packages becomes a practical method.[152-154] This method has been already applied in UK with Magnox cladding wastes for over 30 years and nowadays is also in consideration as a potential waste treatment strategy of UNGG metallic wastes in France.[2, 155] However, even in a cement matrix, Mg-Zr claddings were continuously corroded by residual water in the porosity of hydrated cement.[156] During the long-term storage, the production of hydrogen gas and the volume expansion of the mixture of cement and radioactive materials, can lead to a potential risk of radioactive leakage.[2] Though the formed passive layer of brucite on the cladding surface can somehow slow down further corrosion, the risk of gradual hydrogen accumulation cannot be neglected during long time storage.[2, 156]

I.3.2.3 Stainless steels claddings and components

Although the neutron absorption cross-section of Fe is relatively higher than that of Mg or Zr (see **Figure I-20**), better corrosion resistance coupled with excellent creep resistance to higher temperatures turned stainless steel (stainless steel) into a good candidate for fuel claddings in the early LWRs and the UK's advanced gas-cooled reactors (AGR).[139, 157] In fact, austenitic stainless steel was used as cladding material in the first LWRs. However, high neutron flux in the core of reactor can strongly damage austenitic stainless steel mechanical properties with the void swelling, radiation-induced segregation, helium embrittlement and irradiation creeping.[139] Moreover, the chemical interactions between fission

products (^{131}I) and austenitic stainless steel claddings, as well as the physical deformation and bonding at the interface of fuel pellet and inner side of cladding, can lead to an in-service failure in reactors.[139] As a result, Zr alloys soon replaced stainless steel as the main material for nuclear fuel claddings, due to its lower absorption cross section for thermal neutrons and its higher melting temperature.[139, 158]

However, in the severe accident in Fukushima, H_2 explosion due to the reaction of melting Zr alloy claddings with sea water at the accidental high temperature has brought people to reconsider the use of stainless steel as nuclear cladding material in nuclear reactors.[158, 159] At the same time, other families of stainless steel, such as ferritic/martensitic stainless steel, and the developed oxide dispersion strengthened (ODS) stainless steel alloys, are potential materials for generation IV reactors.[139]

In addition to the fuel claddings, most of the cooling pipe, heat exchanger and other components in the primary circuit of reactors have been made of stainless steel.[160] During the operation and decommissioning of LWRs in the last few decades, large amounts of those structural wastes composed of stainless steel were produced, with radioactive contaminates (mainly ^{60}Co) deposited on the metal surfaces.[160]

I.3.3 Radioactive waste and decontamination method

I.3.3.1 Radioactive waste in France

I.3.3.1.1 Radioactive waste category

During the development of the atomic energy research and the nuclear industry in the past 70 years, thousand tons of radioactive wastes, in the form of solid, liquid and gas, have been produced. From a regulatory point of view, the nuclear industry participants (EDF, ORANO and CEA in particular) are responsible for managing, treating and storing those large amounts of nuclear wastes. Meanwhile, Andra (Agence nationale pour la gestion des déchets radioactifs) is in charge to guarantee the safe management of nuclear wastes in France. According to the activity level of these wastes and the lifetime of the radionuclides contained inside, Andra's classification of the radioactive wastes is presented in **Table I-4**.

Table I-4 French radioactive waste classification.[132]

<table>
<tr><td colspan="2">Radioactive period</td><td>Very short lived
(< 100 days)</td><td>Short lived
(≤ 31 years)</td><td>Long lived
(> 31 years)</td></tr>
<tr><td rowspan="4">Activity level</td><td>Very low level (VLL)
< 100 Bq.g^{-1}</td><td rowspan="3">Natural radioactive decay on production site</td><td colspan="2">Surface storage (CIRES)
VLLW</td></tr>
<tr><td>Low level (LL)
0.1 – 100 kBq.g^{-1}</td><td rowspan="2">Surface disposal (CSA)
LILW-SL</td><td>Subsurface disposal (research ongoing)
LLW-LL</td></tr>
<tr><td>Intermediate level (IL)
0.1 – 100 MBq.g^{-1}</td><td rowspan="2">ILW-LL</td></tr>
<tr><td>High level (HL)
≥ 100 MBq.g^{-1}</td><td></td><td colspan="2">Reversible deep geological disposal (research ongoing)
HLW</td></tr>
</table>

Concerning this current study, the metal structural elements that stayed in nuclear reactors, particularly Mg-Zr alloy claddings, belong to the ILW-LL presented in **Table I-4**. Such type of wastes represents 3% of the total volume of radioactive wastes and 4 % of their whole activity in France. Depending on their nature, ILW-LL can be conditioned by cementing, asphalting or vitrification, before being packaged in stainless steel containers, and stored at their production site waiting for transportation to deep storage on site Cigéo in Bure (Meuse).

I.3.3.1.2 UNGG structural wastes statement and conditioning

Nowadays in France, the main structural wastes coming from UNGG used fuels, including the graphite shells (VLLW type) and the Mg alloy claddings (ILW-LL type), have been treated and stored in La Hague and Marcoule, waiting for their packaging and subsequent deep deposit. In La Hague, 1,905 m^3 of such structural wastes resulting from UNGG reactors are stored at Silo 115 and 130, with a total activity of 2.50 10^{17} Becquerels. In Marcoule, 1,616 tons of Mg structural wastes, including Mg-Zr (0.5 % mass) claddings and Mg-Mn (1.2-1.5 % mass) plug ends, are stored in 17 water filled silos. 1,119 tons of them are ILW-LL wastes (β/γ decay ≈ 70 MBq.g^{-1} and α decay ≈ 0.7 MBq.g^{-1}). They are in the form of bulk, or sheared into small pieces without fuel (**Figure I-22**).[1]

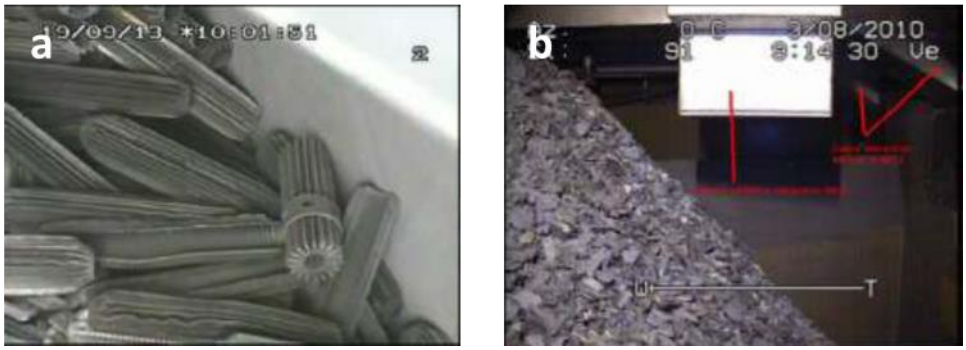

Figure I-22 Mg structural waste stored in wet silos at Marcoule: a) Entire Mg alloy claddings; b) sheared fragments.[1]

The treatment and conditioning strategy for those Mg based structural wastes are currently under study. One of the potential solutions is to encapsulate those wastes into a mineral hydraulic binder, normally Portland cement or geopolymer (aluminosilicate material). The sheared fragments are first compacted to form a pancake and placed in a stainless steel container with a volume of 223 liters. Then Portland cement or geopolymer is grouted into the container (see **Figure I-23**) before the latter is encapsulated and sent to Cigéo. Each package is planned to contain 150 kg of compacted Mg claddings, and about 7,500 of such packages are needed for all of the Mg structural waste in Marcoule.[1, 2]

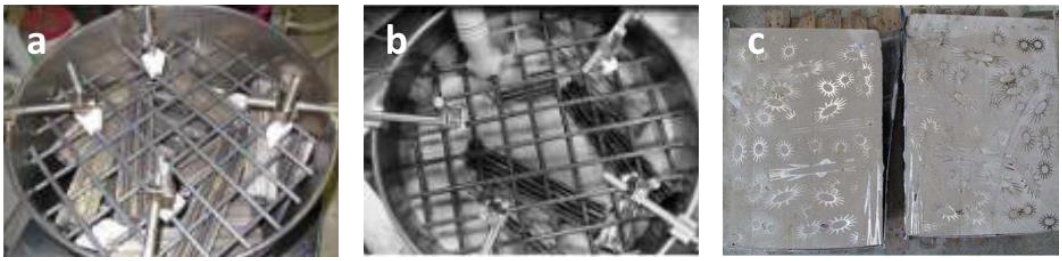

Figure I-23 Inactive simulated Mg claddings in 223 L stainless steel container: a) before grouting; b) geopolymer material grouting; c) profile view after cutting the grouted package.[1]

For such an ILW-LL package holding compacted cladding wastes from spent fuel reprocessing, the activity evolution follows a general decreasing pattern presented in **Figure I-24**. The average thermal output of an ILW-LL waste package is initially about 20 W, but decreases by a factor of 10 every 100 years.[161]

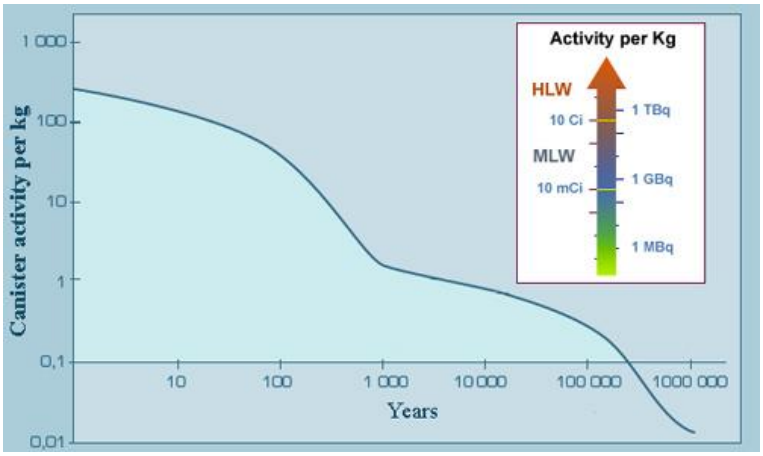

Figure I-24 Radioactivity evolution of an ILW-LL package.[161]

As mentioned before, the corrosion of Mg alloys will not stop in the cement or geopolymer material during storage. Some laboratory experiments have proven a very low release of hydrogen: less than 2 liters per package per year within Na–geopolymer package.[162] Such slow corrosion effect will be accumulated in the long storage duration and can still lead to potential leakages of radioactive wastes.[1]

For this reason, reducing the volume of Mg structural waste (or the number of ILW-LL packages) appears necessary and significant for long-term storage. Several proposals were brought forward, such as using nitric acid or carbonic acid to dissolve the Mg alloy structural components, then separating dissolved Mg and radioelements by filtration, extraction or heating processes. The final produced solid wastes, containing radioelements or Mg precipitations, would be immobilized by cementation or vitrification. However, such dissolution methods consume large amounts of solution and energy, and produce at the same time notable secondary radioactive liquid and gaseous wastes.[163, 164]

Another possible solution consists in an additional surface decontamination before packaging those Mg structural wastes. By removing the radioactive contamination on the metal surfaces, their radiation level becomes lower, so the later treatment process and storage strategy can be simplified. Some efficient decontamination methods can also limit the secondary waste volumes.

I.3.3.2 Decontamination methods

I.3.3.2.1 Definition of decontamination

Decontamination is the process which allows to remove radioactive contaminates from surfaces of components, structures or equipment in nuclear facilities, by chemical, physical and other methods. The objectives of decontamination are: to reduce the radiation exposure (dose level), to reduce the activity level to a lower category, to reduce the volume of radioactive waste for storage and to recycle or reuse components and materials.[165]

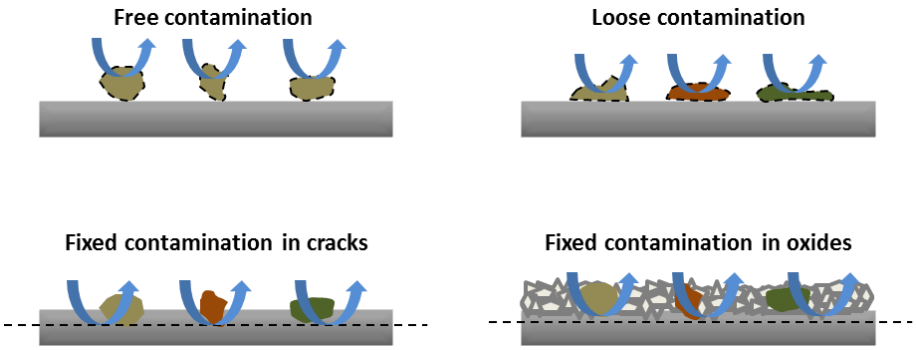

Figure I-25 Contaminates classification: free contamination, loose contamination, fixed contamination in cracks and in oxides.

In a nuclear reactor system, contaminates are the deposits of radioelements which can be neutron activated particles, dissolved compounds in coolant, leaked fuel fragments or fission products from a failure of fuel cladding. As presented in **Figure I-25**, different states of contaminates can exist: free contamination, loose contamination and fixed contamination in cracks and in oxides.[166] Both free and loose contaminates can be readily removed by simple cleaning techniques whereas fixed contamination involves deposits that adhere tightly in oxidation layer or migrate deeply in cracks. Such contaminated materials require more aggressive decontamination methods with removal of surface layers.[166] In order to remove as much radiations as possible, especially those fixed contaminates that accumulated during service and long-term storage, destructive decontamination is allowed to damage the base materials during decommissioning and waste treatment.[167]

The efficiency of decontamination is usually evaluated by a decontamination factor (DF), defined as:[167]

$$DF = \frac{initial\ activity}{residual\ activity} \tag{I-36}$$

I.3.3.2.2 Decontamination techniques

Various techniques are applied for different targets of decontamination in nuclear industry. Based on the media type, decontamination techniques can be classified into: non-chemical methods, including liquid flushing, ultrasonic cleaning, dry ice blasting, and laser cleaning; chemical methods, including gels, foams, pastes and other chemical agents; and electrochemical or electropolishing methods.[167]

However, the secondary waste is a trouble with all decontamination techniques. An efficient decontamination of solid wastes may also produce a large amount of radioactive liquid wastes. This problem is more prominent for chemical decontamination processes. As a result, it is often preferred a selection of chemical methods combined with electropolishing or ultrasound, rather than solely chemical decontamination.[166]

I.3.3.2.3 Ultrasonic decontamination

In the world, ultrasonic cleaning is one of the first and most widely used techniques for decontamination in nuclear industry.[166] It has the advantages of decontaminating a variety of objects with complex configurations and different sizes.[166] Even in a mild environment without addition of aggressive chemical agents, ultrasound can play an efficient role on the decontamination of radioactive surfaces with a controlled destructive effect on the base material. Based on the different purposes, ultrasonic decontamination effects should be different when applied in-service or in decommissioning. As described before, in-service decontamination or cleaning should be non-destructive, while decontamination for decommissioning is aimed to lower the radiation as much as possible.[166, 167]

Before- and in-service decontamination with ultrasound has been studied and applied in nuclear industry globally. For example, tests of an ultrasonic fuel-cleaning technology (UFC) were done by EPRI (USA) with reloaded Zr alloy fuel assemblies in 1999 in order to solve the problem of crud deposition on fuel rods, which can distort heat distribution in the reactor core and accelerate corrosion and failure of the rods.[167, 168] This advanced technique was developed to hold an entire fuel assembly in a cylinder canister, with 16 high-energy ultrasonic transducers of 25 kHz placed along the wall as presented in **Figure I-26**.a. After only 5 minute treatment in 40 ℃ water flow, the majority of the crud was loosened and removed efficiently by cavitation bubbles and the whole reloaded fuel assembly was well cleaned for the next fuel cycle (see **Figure I-26**.b). Due to the excellent performance in a series of tests, UFC technology has been licensed and widely applied in the United States.[168] Similar technologies for preliminary cleaning and removal of defective fuel elements and deposits on the surface of fuel rod of fuel assemblies of VVERs (Russian water-water energetic reactors) before service have also been developed in Russia (see **Figure I-27**).[169] Recently, another ultrasonic cleaning system was designed and tested in India for removal of loose contaminates present on the outer surface of nuclear fuel pins during fabrication.[170] After 5 to 30 minutes sonication by 38 kHz ultrasound in water at room temperature, 45 ℃ and 65 ℃, an efficient decontamination of fuel pins was proven.

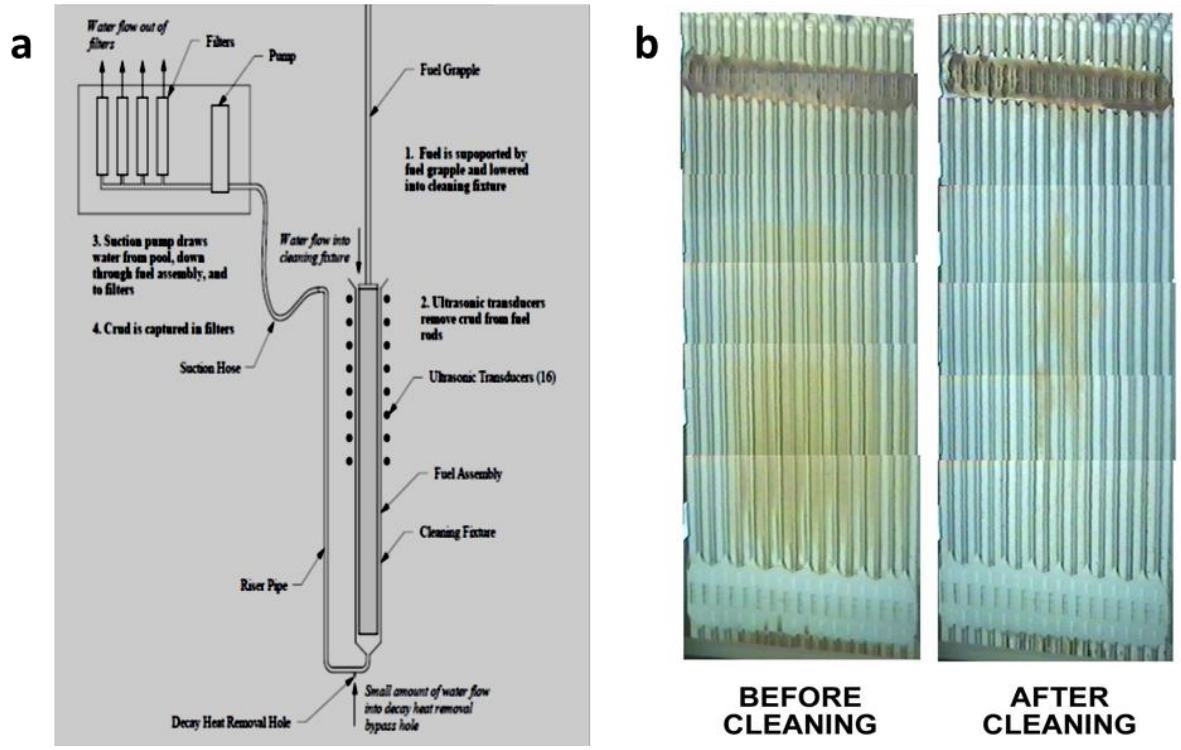

Figure I-26 a) Ultrasonic fuel-cleaning technology scheme and b) video inspection of fuel assembly from USA Callaway plant before and after cleaning.[168]

Figure I-27 Ultrasonic cleaning equipment for VVER fuel assemblies in Russia.[169]

In the case of decommissioning and nuclear waste treatment, ultrasonic decontamination also represents an important approach. From an historical point of view, ultrasonic cleaning was studied for the decontamination of nuclear radioactive components by different groups in many countries.

Between 1950 and 1960 in Springfield UK, laboratory tests on ultrasonic decontamination with a wide range of materials, such as stainless steel and Magnox cladding samples, were done at low frequencies (20 and 36 kHz) in different solutions at 25 and 70 ℃. In comparison with non-ultrasound treatment, a more effective decontamination factor was obtained for stainless steel after 2 minutes of sonication, especially in 1% sulphuric acid (487 times more than non-ultrasound). It was also found that the ultrasonic enhancement of decontamination was more important at room temperature than at 70 ℃, and that an appropriate decontamination solution should be chosen for different contaminates and substrate materials.[171]

In France, similar but more systematic studies about the ultrasonic decontamination of stainless steel, mild steel and cotton fabric were reported by Cerre et al. in 1962.[172] They examined the decontamination effects in different conditions, including ultrasonic frequency from 16.5 kHz to 3 MHz and acoustic intensity from 0.35 to 6 $W.cm^{-2}$. After 2 minutes sonication in 0.05 M sulfuric acid, an optimal decontamination result appeared at 80 kHz, 4 $W.cm^{-2}$ for stainless steel and at 22 kHz for mild steel. In the case of cotton, however, no ultrasonic aid was observed. The same group also investigated ultrasonic decontamination on contaminated copper and brass samples, and similar conclusions were made as on stainless steel.[173]

In USA, decontamination of radioactive items from a nuclear facility was implemented in an ultrasonic bath at 300 kHz in different solutions by Cortlett and Kolb in 1955. They observed an acceleration of decontamination by factors of 2 or 3 in the presence of ultrasound. Another sonication test with a contaminated heat-exchanger piping was done by Henry in 1957. He compared the decontamination effect of low- (20 kHz) and high- (300 kHz to 1 MHz) frequency ultrasound, and found sonication at 20 kHz was more efficient in removal of contaminates.[171]

In the 1990s, Borioli et al. tested decontamination effectiveness of different mechanical, chemical and electrical methods with radioactive metal scraps from three different nuclear reactors in Italy, including one Magnox reactor, one boiling water reactor and one pressurized water reactor. Ultrasonic decontamination was operated in a 40 kHz ultrasonic tank filled with water at room temperature for 60 minutes. A joint ultrasonic and chemical decontamination was also applied within a mixture of 3% hydrofluoric and 15% formic acid. Comparing to a single mechanical or chemical approach, the joint ultrasonic and chemical decontamination was much more efficient with about 85% contaminations removal.[174] In order to increase the efficiency of the reaction and shorten the treatment time, such synergy between the effect of ultrasound and the chemical effect is very common in decontamination process.[166]

Recently, development of new cleaning units has attracted more research on decontamination of nuclear wastes. For example experimental tests on the decontamination of small-size radioactive metal components were implemented in South Korea. Researchers had optimized their device by introducing

a magnetic field in a 29 kHz acoustic field. After 15 minutes treatment in this advanced device in water at 35 ℃, a higher DF was observed than conventional ultrasonic decontamination.[175]

A Russian company, Alexandra-Plus, has performed ultrasonic decontamination tests on fragments of irradiated fuel assemblies (^{137}Cs and ^{90}Sr) from decommissioned nuclear-powered submarines in their designed pilot unit MO-42 (**Figure I-28**).[169] Decontamination was operated in a low frequency tank containing acid solution at room temperature or 50 ℃. After 2 to 20 minutes treatment, it was revealed that compared to conventional decontamination, ultrasonic treatment improved decontamination efficiency with an average DF of 850 and reduced radioactive waste volume by a factor of 35.[176]

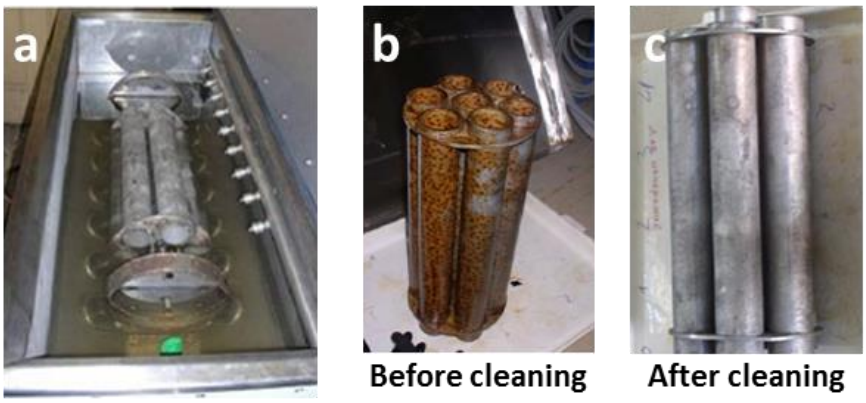

Figure I-28 a) Ultrasonic bath MO-42 for fuel assembly cladding decontamination and fuel assembly waste fragment from submarine: b) before treatment, c) after treatment.[169]

Other decontamination devices for different sizes of solid wastes or applications were developed by the same company. For example, a huge ultrasonic bath (MO-21, see **Figure I-29**) with a volume of 19 m^3 is produced at Khabarovsk, which is capable to handling large solid waste parts of up to 5 m long and 7 t weight. A remotely controlled ultrasonic device has also been developed to clean the spent fuel pool (**Figure I-29**). However, no detailed operation conditions are given in their report.[169]

Figure I-29 MO-21 ultrasonic bath (left) and a remotely controlled ultrasonic module (right).[169]

The company Sinaptec in France has designed ultrasonic/immersion baths for nuclear power plants and facilities like La Hague (see **Figure I-30**). These installations can receive nuclear metal components of

intermediate or low activity level. Objects to be decontaminated are placed in the bath filled with water or chemical agents. No detailed information about the dimension and operation conditions of these decontamination devices can be accessed.

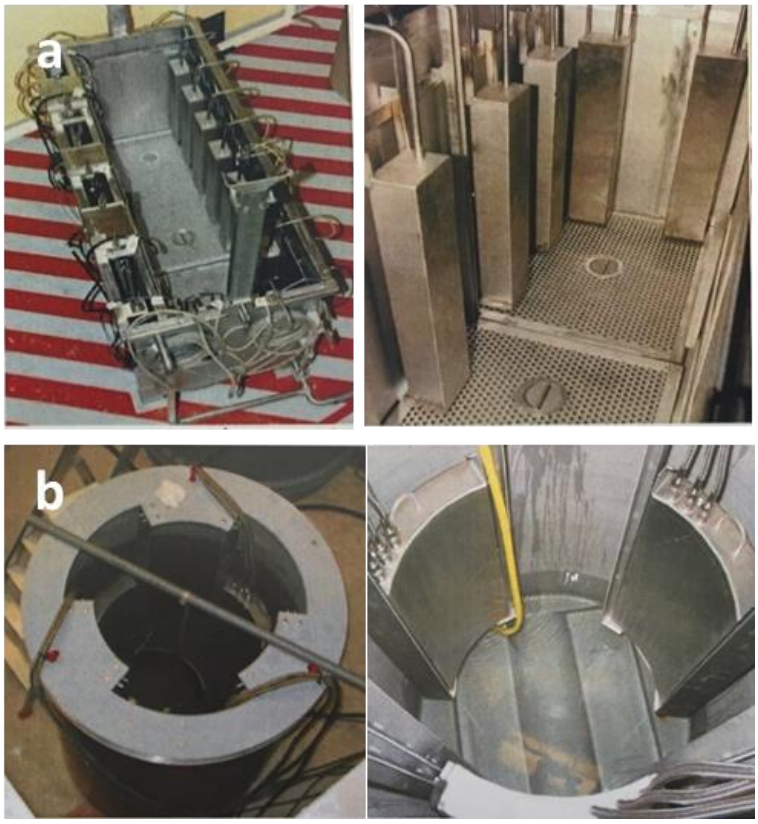

Figure I-30 Underwater ultrasonic generators in decontamination tanks at La Hague: a) type AD1-BDH and b) type R7 for dismantling of vitrification plant [courtesy of Sinaptec].

Chapter II. Materials and Methods

II.1 Materials

Magnesium (99.9% purity) and stainless steel (Fe 70.75, Cr 18.42, Ni 8.58, C 1.63, Si 0.45 and Mo 0.25 wt.%) discs with a diameter of 25 mm and a thickness of 0.5 mm were purchased from Goodfellow (UK). Magnesium/zirconium alloys (99.5/0.5 wt.%, 99.95% purity) discs with a diameter of 25 mm and a thickness of 1 mm were obtained from Neyco (France). Magnesium sheets (99.9% purity, 100 mm x 100 mm, 0.5 mm thickness) were supplied by Goodfellow. The compositions of all the received materials were analyzed and in agreement with EDX measurement. The metallic discs were used as received (without polishing or chemical pretreatment) whereas the Mg sheets were cut into small ribbons (about 45 mm x 20 mm) before bending them in a cylindrical shape to simulate materials with a complex geometry.

A genuine and non-irradiated UNGG cladding tube fragment (**Figure II-1**) was provided by DTCD department from CEA Marcoule. This material has been stored during decades and a passive layer is formed at the surface. The fragment was cut into small pieces from different sides (external fin and internal graphite parts) in order to obtain samples with a flat and homogeneous rectangular shape for treatment. The weight composition of UNGG cladding has been previously described in the literature:[162] Mg 99.49, Zr 0.49 and Mn 0.016 wt.%, which was found to be in agreement with EDX measurements. These claddings also display a graphite-based coating named “aquadag” on their internal side (black part presented in **Figure II-1**.b).[2]

For all of those samples, their surface characteristics were analyzed by different characterization techniques before and after treatment (as described later).

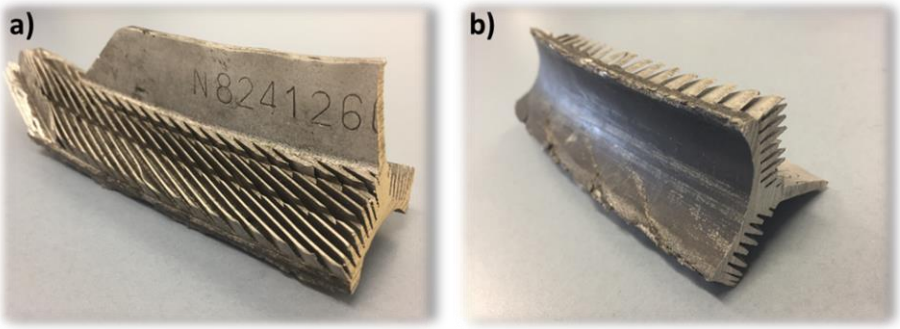

Figure II-1 UNGG cladding tube fragment used for sonication experiments. The Figure clearly shows the complexity of the sample and the chemical composition differences (inside vs. outside).

All chemicals and reagents were of analytical grade and were purchased from Sigma-Aldrich (France and Japan). Gases were provided by Air Liquide (99.9999% purity). The various solutions were prepared with milli-Q water having a resistivity higher than 18.2 MΩ.cm at 25 ℃. The two most used aqueous solutions applied in the experiments were composed of dilute oxalic acid and nitric acid, which have

been widely used in the decontamination of metal wastes during nuclear sites decommissioning, for example in chemical processes or electrochemical decontaminations.[165, 167]

II.2 Preparation of contaminated metallic surfaces

Discs of magnesium, magnesium/zirconium alloy and stainless steel, or ribbons of magnesium were contaminated with 0.1 M uranyl nitrate ($UO_2(NO_3)_2$) aqueous solutions (natural U with ^{238}U 99.27 (at.%), ^{235}U 0.72 (at.%) and ^{234}U 0.005 (at.%)).[177] Each disc was contaminated with fine droplets of approximately 10 µL which were homogeneously distributed onto the surface (Mg-Zr disc as an example in **Figure II-2**). The total volume of deposited solution reached 70 µL, corresponding to approximately 1.67 mg U. For magnesium ribbons, 5 droplets of 10 µL (1.19 mg U) were linearly distributed along the entire length of the samples with a uniform interval (**Figure II-3**.a). After contamination, the discs or ribbons were put in a fume hood for more than 12 hours to let them dry and were then calcined at 500 °C for 2 hours under an argon gas flow in a tubular oven (**Figure II-2**, heating from room temperature with a rate at 10 °C·min^{-1}). After calcination, all the contaminated samples were characterized by α spectrometry, XRD and SEM. To simulate real samples, complex geometries were simulated by bending Mg ribbons into cylindrical shapes as shown in **Figure II-3**.b.

Figure II-2 Mg-Zr disc contamination procedure.

Figure II-3 Mg ribbon contaminated with a 0.1 M $UO_2(NO_3)_2$ aqueous solution a) after heating, b) bent in the form of a cylinder to simulate a sample with a complex geometry.

II.3 Apparatus

Sonication treatments were implemented in a cylindrical homemade glass reactor (14.4 cm height and 6.2 cm inner diameter) connected to a cryostat (Huber Unistat Tango) allowing the circulation of a

cooling fluid (water/ethanol) inside its double jacket for the control of the solution temperature which was maintained at 20 °C. Several entries were designed on the cell to allow: (i) the measurement of the in-situ experimental temperature with a thermocouple inserted in the solution; (ii) the bubbling of a saturating gas which was controlled by a volumetric flowmeter (stainless steel float, 100 mL $\cdot$min^{-1}); (iii) the collection of liquid sample aliquots during experiments; (iv) the on-line analysis of the emitted gases during sonication (through a connected mass spectrometer).

For intermediate (100 kHz) and high (200, 345, 362 and 1057 kHz) frequency ultrasound, the cylindrical reactor was mounted on top of a piezoelectric transducer.[178] The transducers are made of stainless steel and were purchased from SinapTec (effective acoustic surface 88 cm^2 for 100 kHz) or ELAC Nautik (acoustic surface 25 cm^2 for the other frequencies). They were connected to a generator having a maximum electrical power of 120 W for 100 kHz (SinapTec Lab500) and 125 W (T & C Power Conversion, Inc.) for the other frequencies. For low frequency (20 kHz) ultrasound, the bottom side of the reactor was connected to a tight Teflon part which was held on a heavy and stable metallic base. Ultrasound was provided on the top of the cell with a horn type transducer (Vibracell) having a 1 cm^2 emitting surface made out of Ti_6Al_4V alloy (750 W Sonics).

Opposite to the ultrasound emission, tight Teflon stoppers were fitted with sample holders that allowed the reproducible control of the distance between the sample holder and the ultrasound transducer plate (6.5 cm) or horn tip (1.2 cm). The tightness of the set-ups was ensured by different O-rings and machined Teflon stoppers. Metallic samples were fixed onto the Teflon sample holder with microscopy carbon tabs. To avoid the accumulation of bubbles and their cushioning effect at the surface of the high frequency sonicated samples, a mechanical agitation was provided on top of the reactor by rotating the stick holding the sample. Controlled experiments were carried out in similar conditions without ultrasound. Decontamination experiments were carried out with similar devices. Complex geometry samples were sonicated in a stainless steel tea mesh filter which fits the inside of the reactor (**Figure II-5**). The duration of each experiment was comprised between 10 and 90 min. In order to follow the evolution of the sample surfaces topography, some experiments were suspended every 10 or 20 minutes for sending the surface to SEM, drop shape analyzer and alpha spectrometer (decontamination). In-situ analysis was also done with mass spectrometer and ICP-AES (Inductively Coupled Plasma Atomic Emission Spectrometry) to obtain gas generation speeds and surface dissolution rates.

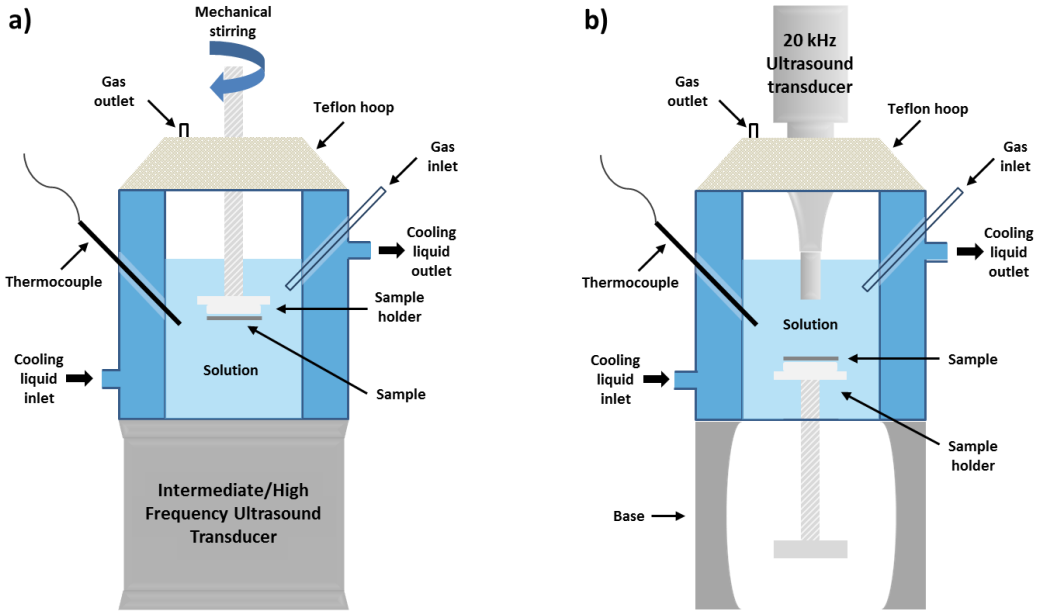

Figure II-4 Schematics of the reactors used for the sonication of the various metallic surfaces at (a) high and (b) low frequency ultrasound. Both set-ups enable the control of temperature, the sampling of solution, and the control of the sample position in the cell.

Figure II-5 Tea mesh filter used for samples with a complex geometry.

For the observation and detection of sonoluminescence and sonochemiluminescence, an equivalent sonoreactor was modified with the particular addition of a flat quartz window fitted at the middle height on one side of the reactor. The optical path passes through the quartz window, via two parabolic mirrors to the spectrometer entrance slot (SP 2356i Roper Scientific, spectral range from 230 nm up to 900 nm, gratings 150blz500, 600blz300 and 1200blz300, slit width from 0.09 mm to 0.12 mm).The reactor together with the transducer, are placed on a platform, and the detected region from window in the reactor can be adjusted by means of the micrometer screws (xyz) on the platform. The spectrometer is coupled to a CCD camera with UV coating (SPEC10-100BR Roper Scientific) cooled by liquid nitrogen. All the measurements are applied inside a black box to minimize background noise (environmental light). For surface effect investigations, a stainless steel round plate replaces the position of the low frequency

ultrasonic probe (without stirring). A schematic of the whole experimental set-up is shown in **Figure II-6**.

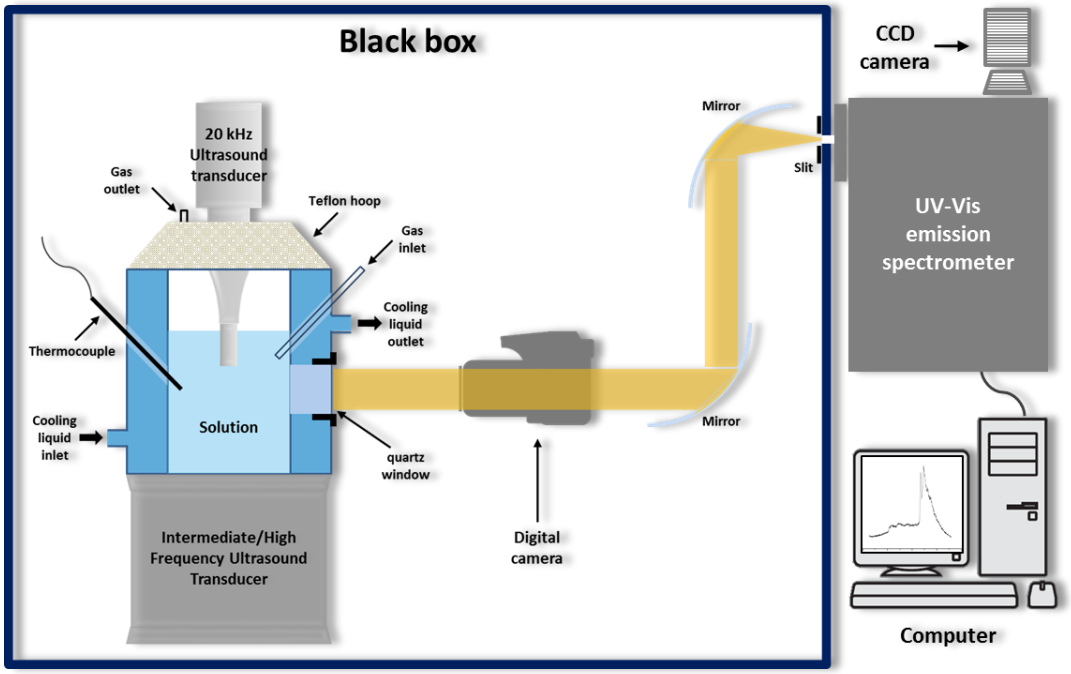

Figure II-6 Sonoluminescence and sonochemiluminescence apparatus schematic.

Spectra acquisition was done by using the spectrometer-specific Winspec software developed by the manufacturer. It allows a spectroscopic measurement from UV to the near IR. To obtain a complete sonoluminescence spectrum at certain conditions, at least 5 spectra were measured in stationary state before being averaged. The signal corresponding to the background noise was also measured at the beginning or at the end of the experiments. Then the noise was subtracted from the averaged spectrum and the resulting spectrum was corrected for the sensitivities of the CCD camera and gratings.

To take the sonoluminescence and sonochemiluminescence photos, a digital camera (Canon, EOS 100D, exposure 10-60 s, ISO 3200) was also placed in front of the quartz window. Obviously, the digital camera was removed when measuring spectra.

II.4 Calibration and characterization of the sonoreactors

II.4.1 Calorimetric method

The calorimetric method allows to quantify the energy transmitted to the fluid subjected to ultrasound in the form of heat, assuming an adiabatic system.[179] The temperature evolution of a sonicated volume of water is measured by varying the ultrasound amplitude or frequency. For selected conditions, the effective power absorbed by the media can be defined using the equation (II-1):

$$P = m\, C_p (dT/dt) \quad \text{(II-1)}$$

Where P (W) is the effectively absorbed acoustic power; m (kg) is the mass of liquid exposed to ultrasound; C_p (kJ ⸗kg^{-1} ⸗K^{-1}) is the heat capacity of the liquid under isobaric conditions (4.18 kJ ⸗kg^{-1} ⸗K^{-1} for water); and dT/dt is the slope reflecting the temperature increase of the medium over time (K s^{-1}).

The calorimetric experiments were carried out in the sonochemical reactors described in **Figure II-6** with 250 mL of milli-Q water and an empty (air filled) jacket for better heat insulation. A slow mechanical stirring (100 rpm) was added for intermediate and high frequency sonolysis systems to obtain a homogeneous temperature distribution in the reactor. Each experiment was performed during 3 minutes and was repeated three times. The temperature increase was found to be linear in the chosen experimental domain. An example of the calorimetric results observed under 100 kHz sonication is presented in **Figure II-7** and **Table II-1** (other calorimetric results are reported in Appendix A).

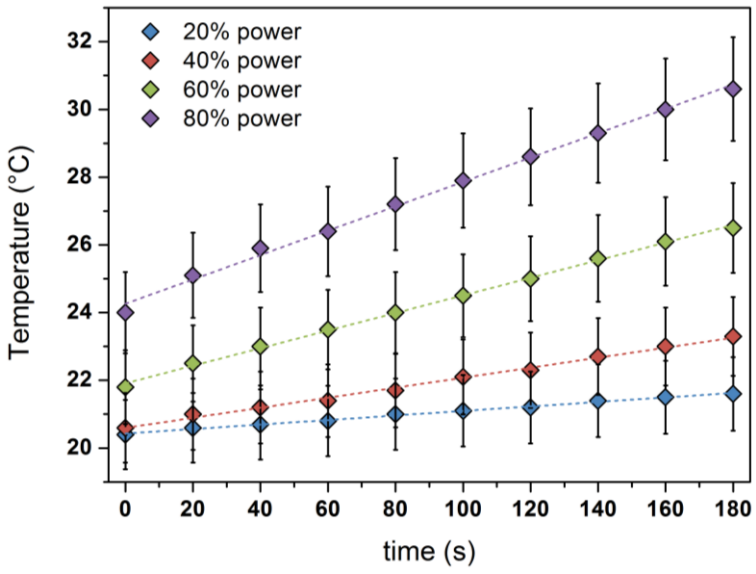

Figure II-7 Example of the temperature variation of pure water (250 mL) sonicated at 100 kHz (Ar, 100 rpm stirring).

Table II-1 Calorimetric results obtained at 100 kHz (250 mL water, Ar, stirring at 100 rpm).

Electrical power P_e (W)	Slope dT/dt (K s^{-1})	Absorbed acoustic power P_{ac}(W)	Acoustic power density $P_{ac,V}$ (W L^{-1})	Acoustic power intensity I_{ac} (W cm^{-2})
24	0.006	6.7	26.75	0.08
48	0.018	18.3	73.15	0.21
72	0.037	39.0	155.91	0.44
96	0.041	43.2	172.63	0.49

II.4.2 Formation of H_2O_2 by water sonolysis

To characterize the sonochemical activity of the used sonoreactors (**Figure II-4**) at certain conditions (ultrasound frequency, acoustic power, temperature, sparging gas, etc.), the formation rate of H_2O_2 resulting from pure water sonolysis was measured.[180] 250 mL of milli-Q water were sonicated during 180 minutes at selected conditions. During sonication, 0.5 mL of solution was sampled each 20 min, and diluted with a previously prepared $TiOSO_4$ solution (2 $\cdot 10^{-2}$ M, prepared in 0.5 M H_2SO_4).[181] The as-formed peroxotitanium(IV) complex exhibiting an orange-yellow color was then analyzed by a UV-Visible absorption spectrophotometer. The formation rate of H_2O_2 during sonication was deduced with the absorption peak standing at about 411 nm (**Figure II-8**) and the Beer-Lambert law described in equation (II-2).

$$A = \varepsilon \, l \, c \qquad \text{(II-2)}$$

Where A (unitless) is the absorbance; ε (mol^{-1} L cm^{-1}) is the molar extinction coefficient; l (cm) is the pass length of the light in the liquid container and c (mol L^{-1}) is the concentration of the measured species (here is peroxotitanium(IV) complex).

The molar extinction coefficient ε of the peroxotitanium(IV) complex was previously determined for the prepared $TiOSO_4$ solution by mixing it with a commercial H_2O_2 standard solution. An external calibration curve is shown in Appendix B.

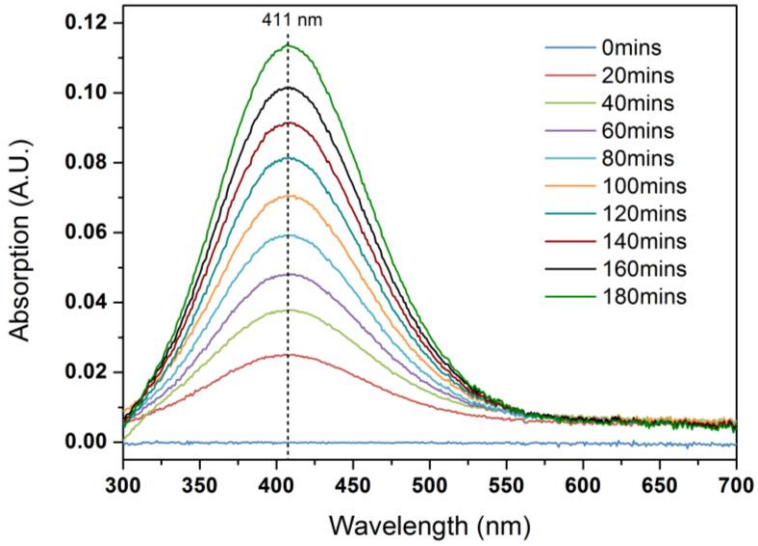

Figure II-8 UV-vis absorption spectra of the peroxotitanium(IV) complex formed by mixing sonicated pure water (100 kHz, P_{ac}= 40 W, 20 ℃, Ar, 100 rpm stirring) with $TiOSO_4$ solution.

II.5 Characterization method

Several analytical methods were used to characterize the effects of the acoustic cavitation phenomenon nearby the various solid surfaces. The used techniques, methods and procedures are described below.

II.5.1 Solid characterization

II.5.1.1 Scanning electron microscopy

Scanning electron microscopy (SEM) allows the generation of three-dimensional images of high-resolution of a sample by scanning its surface with a focused beam of electrons. Based on the interactions between electrons and atoms in the sample, SEM provides its topography, morphology and composition characteristics. A VEGA3 SEM from Tescan (France) and an environmental SEM (Quanta 200 ESEM) were used to characterize the samples and study the evolution of their surface morphology (oxide layers, deformations, secondary phases and precipitations, etc.), to realize 3D reconstructions, to analyze the sample compositions and follow the decontamination progress. Two different modes were applied in SEM depending on the studied samples:

- Secondary Electron (SE) mode: by inelastic scattering interactions between beam electrons (10 – 15 keV) and surface atoms, secondary electrons (< 50 eV) are ejected. Due to their low energy, these electrons are emitted within a few nanometers from the sample surface inducing a good image resolution and 3D appearance.
- Back-Scattered Electron (BSE) mode: by elastic scattering interactions between incidental electrons and specimen atoms, back-scattered electrons are reflected backwards with the

information of sample elements and compositions. Areas of the surface that contain atoms with a high atomic number will emit more electrons than atoms having a lower atomic number. A greater brilliance of these areas will be observed on the images. Although topographic information can be obtained using a BSE detector, its image resolution is lower than what observed in an SE image.

Energy Dispersive X-ray spectroscopy (EDX) can also be coupled with SEM. This technique allows to collect photons related to transitions of electrons from a higher to a lower level that have an energy characteristic of the atom exposed to the beam electrons. The nature and relative abundance of the chemical elements composing the samples can be defined. The concentration and distribution of chemical elements can be determined in a region of interest at the surface of a sample.[182]

II.5.1.2 3D reconstruction with MeX software

3D reconstruction MeX software (Alicona, Austria) allows to convert SEM pictures into 3D surfaces which give topographic information about the studied sample, including the profile, surface morphology, roughness, etc. 3 or 5 images were taken at the same eucentric point with different tilt angles (0 °, ±10 °, ±15 °, etc.) but with a similar working distance, magnification, brightness and contrast. 3D reconstruction of the surface was then performed by the software from those accumulated and tilted SEM images. Measurements can then be directly made on the reconstructed surfaces.

The surface roughness (R) and mass loss (ΔM) can for instance be calculated with the reconstructed surfaces by following the evolution of the topography at certain region of interest on the sample in agreement with equations (II-3) and (II-5).

$$R = \frac{\sum_{i=1}^{N} |z_i|}{N} \tag{II-3}$$

Where R (mm) is the surface roughness; N is the total number of analyzed points and $|z_i|$ (mm) is the absolute value of the height distance between the analyzed point i and the mean plane found by the software.

$$\Delta m_{i,i+1} = \rho \frac{d\pi D^2}{4} \tag{II-4}$$

$$\Delta M = \sum_{i=1} \Delta m_{i,i+1} \tag{II-5}$$

Where $\Delta m_{i,i+1}$ (g) is the estimated mass difference between two adjacent 3D reconstructions i and i+1; ρ (g mm^{-3}) is the density of material; d (mm) is the average height difference between two consecutive measurements by superimposing their 3D measurements; D (mm) is the diameter of the sample surface and ΔM (g) is the total estimated mass loss.

II.5.1.3 X-ray diffraction

X-ray diffraction (XRD) provides detailed information on the crystallographic structure and nature of the studied samples. This technique relies on X-ray diffraction when they encounter a crystal. The diffraction takes place in a precise direction for each family of lattice planes according to Bragg law:

$$2d\,sin\,\theta = n \cdot \lambda \quad \text{(II-6)}$$

Where d (nm) is the distance between two reticular planes; θ (°) is the angle of incidence of X-rays; n (unitless) is the order of reflection and λ (nm) is the wavelength of the X-ray beam (**Figure II-9**).

If the incident X-ray wavelength is similar with the spacing in a crystal, a significant diffraction appears in the pattern. The nature of the crystallographic structure for the studied samples can be identified by comparing the obtained diffraction patterns with references.[182]

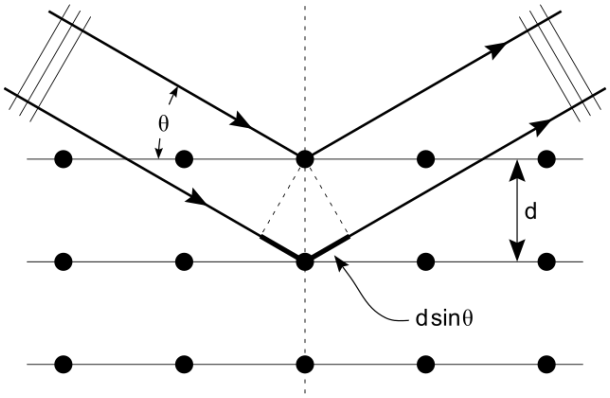

Figure II-9 X-ray diffraction.[183]

All the samples were first analyzed as received, after contamination and after treatment. For surfaces contaminated with uranium or carbon (graphite), direct measurement did not provide enough signals for crystallographic structure qualification, since the substrates were not flat and the contamination was too low. As a result, contaminants were scratched off the surfaces to form a powder suitable for XRD analysis.

II.5.1.4 Alpha spectrometry

Alpha spectroscopy was used to detect radioactive contaminants based on the alpha particles (He^{2+}) emitted in the decay process. The activity (Becquerel/sample) of the contaminated samples was characterized by alpha spectrometry (CANBERRA Model 7401) by acquiring and analyzing energy spectra with Genie 2000 software. This technique allows to identify and quantify the nature of the various radionuclides contaminating the surface of the studied samples with a low detection limit, and therefore evaluate the efficiency of the decontamination procedures used in this work. It should be noted that alpha radiation is composed of a heavy and positively charged He^{2+} nucleus that can be easily stopped by few centimeters of air or skin. Preliminary studies found that when preparing the

contaminated samples by direct evaporation and calcination, a thick layer of radioactive contaminants is deposited on the sample surface. The concentration of the uranyl solution used to contaminate the surfaces was also found to be an important parameter since the use of too concentrated solution can induce the formation of a thick and labile contamination layer. In consequence, alpha activity measurements may be misinterpreted due to the self-absorption of the created thick contamination layer on surface. In order to prevent this phenomenon, the samples were prepared in an identical and rigorous manner. Thus, the uranyl contaminants were dropped onto the metal surfaces in the form of fine droplets of similar sizes while avoiding their coalescence. Moreover, the theoretical mass of natural uranium deposited on the metallic samples made it possible to determine a theoretical activity that was confronted with the laboratory results in order to judge the efficiency of the procedure and correct the deposits and the method of treatment of results if needed.

II.5.1.5 Drop Shape Analyzer

Wettability of a solid surface is often determined by the contact angle of a liquid droplet (normally water) deposited on surface. Contact angles measured between $0\,°$ and $90\,°$ are generally correlated to hydrophilic surfaces, while contact angles measured between $90\,°$ and $180\,°$ refer to hydrophobic ones. Two principle models are applied to explain the relationship between surface roughness and wettability: Wenzel model and Cassie–Baxter model.[184]

The Wenzel's model is defined as following:[185]

$$\cos\theta^* = r\cos\theta_Y \qquad \text{(II-7)}$$

Where θ^* is the apparent or measured contact angle, θ_Y is the Young contact angle defined for an ideal flat surface, and r is the roughness ratio defined as the real area of the solid surface to the apparent or projected area. An ideal smooth surface has $r = 1$, and $r > 1$ for a rough one.

According to Wenzel's model, surface wettability is very sensitive to roughness: roughness increase leads to an intrinsically hydrophobic surface ($\theta_Y > 90°$), which becomes more hydrophobic (larger apparent contact angle θ^*), and vice versa, an intrinsically hydrophilic surface ($\theta_Y < 90°$) becomes more hydrophilic (smaller apparent contact angle θ^*).[186]

However, it is important to notice that the Wenzel model is based on the assumption that the liquid penetrates into the roughness grooves, as shown in **Figure II-10**.a. But if the liquid cannot penetrate into the roughness grooves, air will be entrapped in between the voids existing on the surface (**Figure II-10**.b). In this case, Cassie-Baxter model is used instead.[187]

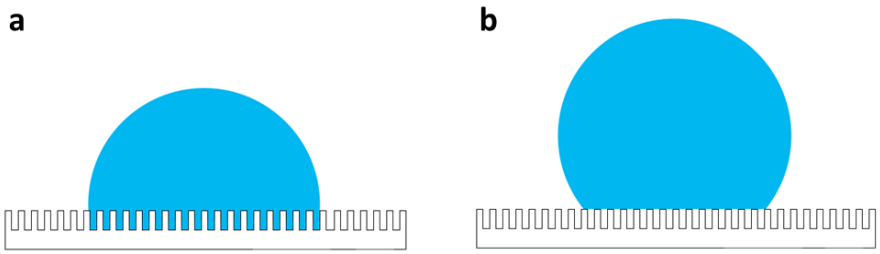

Figure II-10 Surface wetting: a) Wenzel model; b) Cassie–Baxter model.[188]

Cassie equation is used to describe the chemically heterogeneous surface. For a two-chemical-component system, it is defined as:

$$\cos\theta^* = f_1 \cos\theta_{Y1} + f_2 \cos\theta_{Y2} \quad \text{(II-8)}$$

Where f_1 and f_2 are the fraction area of the components 1 and 2 contacted with liquid ($f_1 + f_2 = 1$), and θ_{Y1} and θ_{Y2} are the Young contact angle of pure component ideal surface respectively. If the secondary component is air, as described in **Figure II-10**.b, considering the air/liquid contact angle is almost 180 °($\cos\theta_{Y2} = -1$), the equation can be written as:

$$\cos\theta^* = f_1(\cos\theta_{Y1} + 1) - 1 \quad \text{(II-9)}$$

This equation is known as the Cassie-Baxter equation. With the fraction area of the substrate material f_1 decreasing by surface roughness increasing and air trapping, apparent contact angle θ^* can be much larger than the Young contact angle θ_{Y1}. As a result, it is possible to change an instinctive hydrophilic surface into a superhydrophobic one by specially designing its surface roughness.[187]

Contact angle measurements were achieved with a Drop Shape Analyzer (DSA100S, KRÜSS). Several (n) sessile drops were formed at random position on the sample surface by dosing 5 µL of pure water with an automated syringe situated on the top of the surface. An image of each drop was recorded by a camera and transferred to the software which fits the contour of the drop shape with a geometrical model. The contact angle (θ_i) is given by the angle created between the calculated droplet shape function (shape line) and the sample surface (baseline). The given contact angle ($\overline{\theta}$) was calculated in agreement with the equation (II-10) as an average value ($n > 8$) of all the sessile drops deposited on the surface. The variability of the measured data was evaluated from the standard deviation of these droplets.

$$\overline{\theta} = \frac{\sum_{i=1}^{n} \theta_i}{n} \quad \text{(II-10)}$$

II.5.1.6 ATR-FTIR spectroscopy

Attenuated Total Reflection Fourier Transform InfraRed (ATR-FTIR) spectroscopy is a simple, fast and non-destructive chemical analytical technique. The infrared radiation interacts with crystals or

molecules in samples through series of standing waves called evanescent waves. Some of the energy of the evanescent waves is absorbed by the sample and reflected radiation is returned to the detector. The effective path length for this interaction depends on several parameters and is typically a fraction of the wavelength. This penetration depth is in the range of microns, which is ideal for sample surface analysis.[182] In our study, ATR-FTIR spectroscopy was carried out with a PerkinElmer Spectrum 100. Spectra (8 acquisitions per sample) were acquired between 4000 and 380 cm^{-1} by direct measurement of the surface without any additional treatment. All the samples were first analyzed as received, after contamination and after treatment.

II.5.1.7 Raman spectroscopy

Raman spectroscopy is a vibrational spectroscopy technique used to characterize the molecular composition and external structure of a material. By radiation of the sample with a laser beam, a molecule is excited to a (virtual) higher energy state and then returns to its original energy state with the emission of a photon with a certain energy or wavelength. When the photon released has the same energy or wavelength as the incident radiation, it is known as elastic or Rayleigh scattering. When a produced photon exhibits less energy or more energy than the incident laser radiation, it is an inelastic scattering called Stokes Raman scattering or anti-Stokes Raman scattering (**Figure II-11**). By rejecting the dominant Rayleigh scattering with a filter, the rest of the released photons are collected and analyzed by a CCD camera. The obtained Raman spectrum, as a chemical fingerprint, permits identifying molecules and chemical bonding, because different chemical bonds and symmetries correspond to different vibrational modes (energy or wavelength).[182]

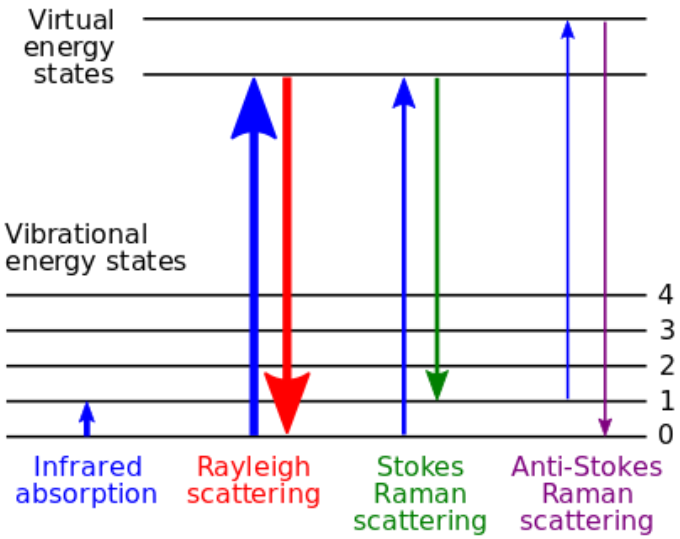

Figure II-11 Energy level diagram of Raman scattering.[189]

The Raman apparatus used in this study was a LabRAM ARAMIS Jobin-Yvon, equipped with a laser source (532 nm), and coupled with a motorized XYZ stage. An optical fiber probe is attached to the

spectrometer and allows to perform in vitro analyses. The instrument was calibrated before each set of experiments using the 520.7 cm^{-1} peak of a silicon standard. All Raman spectra were collected between 100 and 3000 cm^{-1}. All the samples were first analyzed as received, after contamination and after treatment. For surfaces contaminated with uranium or carbon (graphite), contaminant particles, besides some precipitations generated during treatment, were also deposited onto glass slides for Raman analysis.

II.5.2 Solution characterization

II.5.2.1 UV-Visible absorption spectrophotometry

UV-Visible absorption spectrophotometry consists in studying the interactions between matter and electromagnetic radiations. Different molecules absorb radiations of different wavelengths. An absorption spectrum will show a number of absorption bands corresponding to structural groups within the molecule. According to Beer-Lambert law (II-2), a quantitative determination of different analytes can be obtained. A Thermo Scientific Evolution 220 spectrophotometer was used to determine H_2O_2 formation rates during the sonolysis of water based on different sonochemical parameters as described earlier. The samples were analyzed in 1 cm quartz cuvettes.

II.5.2.2 ICP-AES

Inductively Coupled Plasma Atomic Emission Spectrometry (ICP-AES) is a chemical analysis technique based on the principle of atomic emission spectrometry. It allows precise identification and quantitative analysis of the chemical elements present in solution, with a low detection limit. During the sonication procedures, samples of approximately 1.5 mL were taken every 10 or 15 minutes. These samples were then filtered (PTFE filters, 0.2 µM) and dilute by 10 or 20 with HNO_3 at 2% by mass (0.3 M) in order to remain within the calibration range prepared beforehand (ranging from 0.5 to 15 mg L^{-1}, standards provided by SCP SCIENCE). In the context of this study, ICP-AES was used to study the release in solution of the elements Mg, Zr, and U and to determine dissolution rates (mg L^{-1} min^{-1}) of magnesium in particular.

II.5.3 Gas characterization

II.5.3.1 Mass spectrometry

Mass spectrometry (MS, Thermo Scientific, Prima BT Mass Spectrometer) was used for the analysis of gases and vapors generated during sonication. The gas sample is introduced via a stream selector and a pressure reduction system, comprised of a capillary and molecular leak that transmits a small portion of the gas into the ion source which operates under high vacuum. Using an electron emitting filament, the ionization chamber converts the sample molecules into ions which are positively charged molecules or parts of molecules. These ions are then separated according to their mass by a variable magnetic field.

The different mass ions are then quantified by the detector in accordance with the intensity of the signals at these masses.

In our study, an in-situ measurement by MS was implemented during sonication. A constant gas flow was ensured 30 minutes before and during the MS analysis. Molecular sieves (Aldrich, 3 Å) were placed between the sonoreactor gas outlet and the mass spectrometer gas inlet to trap water vapor. A multiple-ion monitoring mode was employed to follow the evolution of various gases (Ar, O_2, H_2, N_2, CO_2, H_2O, etc.) during sonication. A special attention has been given to hydrogen gas (H_2) because of its known release during the sonolysis of aqueous solutions and the reactivity of magnesium surfaces. Emitted H_2 gas was compared to an external calibration curve previously prepared with standards (Appendix C). After sonolysis, the bubbling of gas and the acquisition of the mass spectrometer continued for an extra 30 minutes or more in order to observe a return to zero for the emitted gases.

II.5.4 Cavitation characterization

II.5.4.1 Sonoluminescence and sonochemiluminescence photography

Sonoluminescence (SL) and sonochemiluminescence (SCL) emitted from the sonoreactor during sonolysis of aqueous solutions were observed by a digital camera (Canon EOS 100D) through the quartz window (**Figure II-6**). In order to get the best quality for the photos (high signal-to-noise ratio), an exposure of 10 to 60 seconds with an ISO 3200 were selected for the camera settings. All the photos were treated by ImageJ software for the results of cavitation activity field, light intensity and color (radical) distribution.

II.5.4.2 Sonoluminescence spectrometry

As shown in **Figure II-12**, the SL spectra were recorded in the range 230-900 nm using a spectrometer (SP 2356i, Roper Scientific; a triple-grating turret: 150 grooves mm^{-1} blazed at 500 nm, 600 grooves mm^{-1} and 1200 grooves mm^{-1} blazed at 300 nm) coupled to a liquid-nitrogen cooled CCD camera (SPEC10-100BR with UV coating, Roper Scientific). Optical filters were used to avoid second order light. Spectral calibration was performed using an Hg (Ar) pen-ray lamp (LSP035, LOT-Oriel). Spectra acquisition was started after reaching the steady-state temperature. Each given spectrum is an average of at least five 300 s spectra corrected by background noise and the quantum efficiencies of gratings and CCD. (Spectral calibration and quantum efficiencies of gratings and CCD are presented in Appendix D)

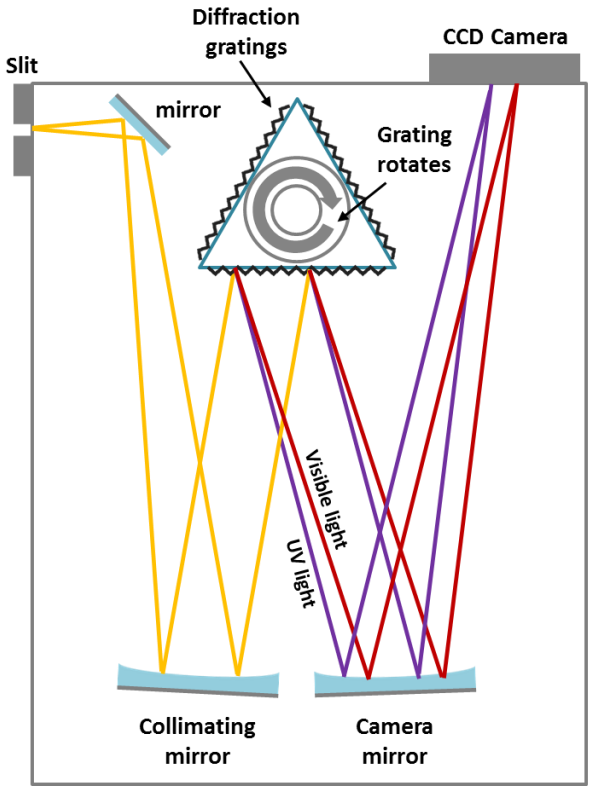

Figure II-12 SL spectrometer schematic (SP 2356i, Roper Scientific)

II.5.4.3 Specair simulations

SL spectra bear different spectral information, for example the excited molecular radical emission line positions, intensities and profiles. In this study, emissions from excited species OH ($A^2\Sigma^+$) and NH ($A^3\Pi$) were simulated by the spectroscopy code Specair 4. Each spectral band, which corresponds to a certain molecular radiation transition, is calculated and convoluted into a simulated spectrum, and then compared and fitted with the experimental multibubble SL spectrum. The simulation input parameters: vibrational (T_v) and rotational (T_r) temperatures were manually varied and optimized to fit the experimental spectrum as well as possible. A user defined measured slit function is introduced in Specair to calculate the experimental spectral resolution (150blz500 grating with a slit of 0.12 mm, FWHM= 3.9 nm; 600blz300 grating with slit of 0.05 mm, FWHM= 1.63 nm; 1200blz300 grating with a slit of 0.09 mm, FWHM= 0.30 nm and with a slit of 0.12 mm, FWHM= 0.37 nm). More detailed information about Specair simulations is given in the Appendix E.

Chapter III. Acoustic cavitation behavior at 100 kHz and in the vicinity of a solid boundary

III.1 Introduction

Conventional ultrasonic cleaning is normally based on low frequency ultrasound due to its strong mechanical effect. Increasing the ultrasonic frequency from 20 kHz to 1 MHz allows the lifetime and the average size of acoustic bubbles decrease and the chemical characteristics of cavitation become more important than its mechanical effects.[87, 190] Therefore, low and high frequencies appear almost as two different domains of acoustic cavitation. It is of great interest to identify the characteristics of cavitation at intermediate frequencies comprised between 80 and 150 kHz, which still remain poorly understood, especially their SL spectral behaviors (the only report on SL spectroscopy at an intermediate frequency of 90 kHz is that of Cairos et al.[85]).

Meantime, before the study of cavitation effect on metal surfaces and the latter ultrasonic decontamination tests, it is necessary to identify cavitation behavior in the vicinity of a solid boundary in the selected conditions.

This chapter first describes cavitation at 100 kHz in aqueous solution in comparison with low frequency (20 kHz) and high frequency (362 kHz) by different approaches: sonochemical activity (H_2O_2 yields) and spatial distribution of sonochemiluminescence (SCL photos); MBSL spatial distribution (SL photos) and spectra (OH, NH, Na* and continuum). The effects of a solid boundary (stainless steel and Mg surface) on SCL and SL are then discussed in the second part.

III.2 Sonochemistry and sonoluminescence in aqueous solution at 100 kHz

Different approaches, including sonochemical activity (H_2O_2 yields), spatial distribution of sonochemiluminescence (SCL photos), MBSL spatial distribution (SL photos) and spectra, were applied to characterize the behaviors of cavitation bubbles generated by 100 kHz ultrasound and to compare them with what observed at low- and high-frequency ultrasound. Experiments were carried out in 250 mL of distilled water or 0.01 M luminol solution (pH=11 adjusted with Na_2CO_3), saturated with Ar, Ar/(20 vol.%)O_2 or Ar/(20 vol.%)N_2.

It is known that many parameters do affect the characterizations of sonochemistry and sonoluminescence, including ultrasonic frequency, acoustic power and power intensity which condition the number of bubbles and their behaviors. An ideal investigation on the effect of ultrasonic frequency would be based on a constant number of active bubbles (SL or sonochemically active), which is impossible due to the bubble number being unknown. We have chosen to work at approximately constant absorbed acoustic power and constant solution volume (thus also approximately constant power density) and to compare chemical yields (that are independent from the acoustic power in the considered

range). The absorbed acoustic power was determined by conventional thermal probe method: P_{ac}= 33 W at 20 kHz, 40 W at 100 kHz and 43 W at 362 kHz. As a result of the distinct transducer acoustic surfaces, the power intensity equals to 33 W cm^{-2}, 0.45 W cm^{-2} and 1.6 W cm^{-2} respectively.

III.2.1 Sonochemical activity and SCL at different ultrasonic frequencies

The sonolysis of water leads to H_2O_2 formation, according to reactions (I-11) to (I-18). **Figure III-1** presents H_2O_2 yields measured under Ar and Ar/(20 vol.%)O_2 at different ultrasonic frequencies in pure water. For both gases, the maximum value occurs at 362 kHz, in agreement with the literature.[74, 191-193] Despite the much lower power intensity at 100 kHz, its corresponding H_2O_2 yields lie well in between 20 kHz and 200 kHz, which validates the choice of comparing ultrasonic frequencies at approximately constant acoustic power.

Upon addition of oxygen in the argon flow, H_2O_2 yield is enhanced for all ultrasonic frequencies as previously reported.[84] This is due to two new reaction pathways leading to H_2O_2 formation. First, oxygen molecule can scavenge $H^{\bullet}$ and form $HO_2^{\bullet}$ that recombine in H_2O_2 (reactions (I-15) and (I-17) in bibliography). This scavenging of $H^{\bullet}$ also leads to a lesser extent of H + OH recombination, resulting in a higher remaining balance of $HO^{\bullet}$ radicals. Second, the dissociation of O_2 molecules can also lead to an increase in $HO^{\bullet}$ radicals production by the recombination of O atoms with water or H atoms (reactions (I-19), (I-21) and (I-22)).

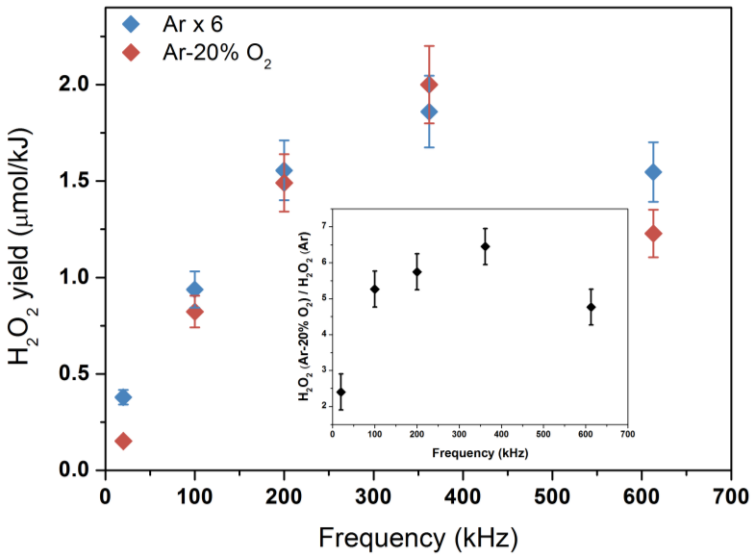

Figure III-1 H_2O_2 yields in pure water sonicated at 20 kHz (P_{ac}= 33 W), 100 kHz (P_{ac}= 40 W), 200 kHz (Pac= 45 W), 362 kHz (P_{ac}= 43 W) and 612 kHz (P_{ac}= 61 W) under 100 mL.min^{-1} Ar (blue) and Ar/(20 vol.%)O_2 (red) flow, at 18 ℃, 100 rpm mechanical stirring (except at 20 kHz); insert: ratio of H_2O_2 yields for Ar/(20 vol.%)O_2 and Ar.

The insert plot in **Figure III-1** shows the ratio of H_2O_2 yields obtained for Ar/(20 vol.%)O_2 and for Ar. This ratio is much lower at 20 kHz compared to intermediate and high frequencies, while the latter are approximately at the same level. This phenomenon is illustrated by SCL visualization in **Figure III-2**.

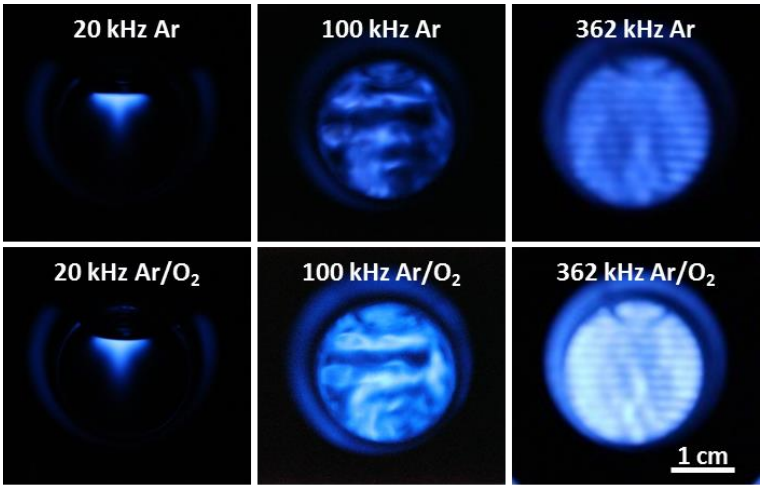

Figure III-2 Photographs of 0.01 M luminol solution (pH = 11, Na_2CO_3) submitted to 20 kHz (P_{ac}= 33 W), 100 kHz (P_{ac}= 40 W) and 362 kHz (P_{ac}= 43 W) under 100 mL.min^{-1} Ar and Ar/(20 vol.%)O_2 flow at 18 °C; exposure 10 s.

Light emission from a sonicated luminol solution arises from luminol oxidation by $OH^{\bullet}$ radicals and is thus closely correlated to H_2O_2 yields. In **Figure III-2**, the SCL pictures were taken in the same conditions as H_2O_2 monitoring. For all frequencies, SCL photos are brighter in the presence of O_2; however the change in luminosity between Ar and Ar/(20 vol.%)O_2 appears more important at 100 and 362 kHz than at 20 kHz.

This discrepancy in the effect of O_2 addition can be easily explained considering the different pathways leading to H_2O_2 formation. At all studied ultrasonic frequencies, H_2O_2 can be produced by water sonolysis and $H^{\bullet}$ scavenging with O_2. On the contrary, the extent of reaction (I-19) strongly depends on frequency. Indeed, a previous work [84] showed that 20 kHz ultrasound cannot provide enough energy to break the bond of O_2 molecule (5.15 eV) due to the less extreme conditions reached at bubble collapse, contrary to high frequency. The comparison of H_2O_2 yields under Ar and Ar/(20 vol.%)O_2 brings to light the similarity of 100 kHz with the high frequency, inasmuch as the possibility of O_2 dissociation is considered. This indicates more extreme conditions in bubbles at 100 kHz than at 20 kHz, similar to high frequency ones.

In **Figure III-2** the various SCL distributions are due to the different cavitation fields and also to the different types of apparatus. In comparison to the localized character of the low frequency cavitation field when a horn is used, at intermediate and high frequencies it is expended in the entire reactor as presented in **Figure III-3**. The nature of the saturating gas (Ar or Ar/(20 vol.%)O_2) has no effect on SCL distributions. In addition, the spacing between the bright layers at 100 and 362 kHz (~6 mm and

~1.5 mm respectively) corresponds to the half ultrasonic wavelength at each frequency (~7 mm and ~2.1 mm respectively). Previous studies [194, 195] reported similar observations at low frequency and high frequency ultrasound systems. Taking into account the saturation of pixels and the complex reactor geometry, SCL intensity of photos cannot be directly used for comparison between different frequencies. The same conclusion is also true for SL intensity, and is described later. To better understand the evolution of the sonochemical plasma with frequency and to characterize it, SL spectroscopy was implemented in our study.

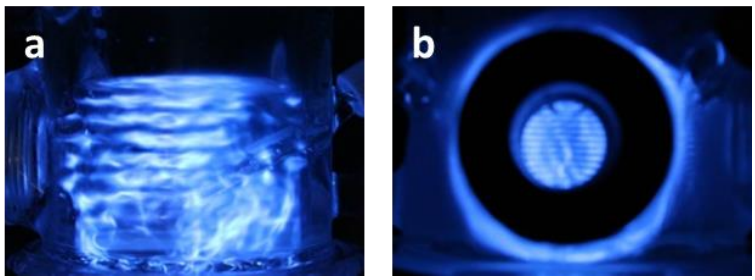

Figure III-3 Photographs of 0.01 M luminol solution (pH= 11, Na_2CO_3) submitted to a) 100 kHz (P_{ac}= 40 W) from glass wall side and b) 362 kHz (P_{ac}= 43 W) from optical window side, under 100 mL.min^{-1} Ar/(20 vol.%)O_2 flow, at 18 ℃; exposure 10 s.

III.2.2 Sonoluminescence photos and spectra at different ultrasonic frequencies

Figure III-4 presents SL photos of water sonicated at different frequencies under Ar and Ar/(20 vol.%)O_2 atmospheres. As already published [84], at 20 kHz, SL is dimmer under Ar/(20 vol.%)O_2 than under Ar, contrary to 362 kHz and 100 kHz which both exhibit a similar trend.

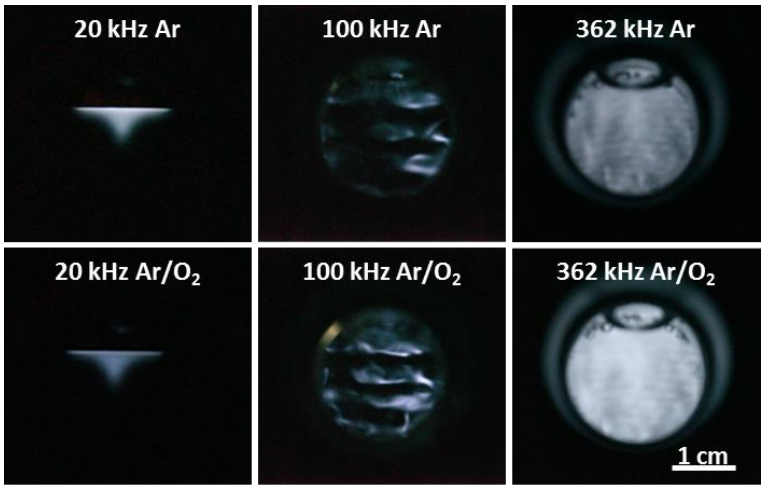

Figure III-4 Photographs of water SL at 20 kHz (P_{ac}= 33 W), 100 kHz (P_{ac}= 40 W) and 362 kHz (P_{ac}= 43 W) under 100 mL.min^{-1} Ar and Ar/(20 vol.%)O_2 flow, at 18 ℃; exposure 60 s.

To confirm this observations and to provide a quantitative comparison of SL intensity between different conditions, SL spectra were measured as shown in **Figure III-5**. All these SL spectra present a strong continuum and the molecular emission of OH ($A^2\Sigma^+$-$X^2\Pi$), with nevertheless very different relative intensities. The spectral shape of 100 kHz spectra is similar to that observed at 20 kHz with a very intense OH ($A^2\Sigma^+$-$X^2\Pi$) emission and a low continuum. On the contrary, high frequency provides a much stronger continuum comparing to OH ($A^2\Sigma^+$-$X^2\Pi$) emission. In terms of plasmachemical model of sonoluminescence, the continuum emission is usually attributed to the superposition of Bremsstrahlung, H + $OH^{\bullet}$ recombination, excited water molecule de-excitation and OH ($B^2\Sigma^+$–$A^2\Sigma$) emission.[22] Therefore, the relatively lower intensity of the continuum observed at 20 kHz most probably points out a lower electron temperature of the intrabubble plasma. This difference may be related to the water vapor fraction inside a bubble at the end of the collapse, which strongly depends on the acoustic period.[196] At lower frequencies, the longer acoustic period allows more water molecules to enter bubbles and to quench the plasma.

A second frequency-dependent difference is the impact of O_2 addition on the SL intensity: it leads to an increase at 100 kHz and 362 kHz, but to a decrease at 20 kHz (**Figure III-5**). This opposite effect of O_2 addition on SL intensity at low and high frequency ultrasound is in agreement with previously published research.[84]

This increase in continuum intensity (**Figure III-5**) at 100 kHz and 362 kHz with the addition of 20% O_2 in Ar might at first appear surprising if a classical quasi adiabatic model is considered: O_2 heat capacity ratio is lower than that of Ar, its heat conductivity is higher, and there are energy losses by vibrational excitation and dissociation of O_2 molecules. All these effects should lead to less extreme conditions. Indeed, a much dimmer SL was reported in pure O_2.[84] However, the presence of O_2 in Ar (at least for 20% O_2 in Ar) also results in the formation of a higher number of light-emitting excited species (e.g. OH*, HO_2*) and also increases the extent of H – OH recombination, that also emits light. The concentration of O_2 in Ar determines the balance between enhancement of SL by O_2 dissociation and consequent formation of excited species on the one hand and O_2 quenching effect [197] on the other hand. The balance between excited radical production and SL quenching decides the global O_2 effect on SL spectra. Thus the continuum intensity increases at high frequency ultrasound with O_2 addition and the higher the frequency, the higher the SL continuum intensity ratio (**Table III-1**). Similar O_2 content effects on SL intensity were also previously observed by Tuziuti et al. and Arakeri and Nishad.[198, 199]

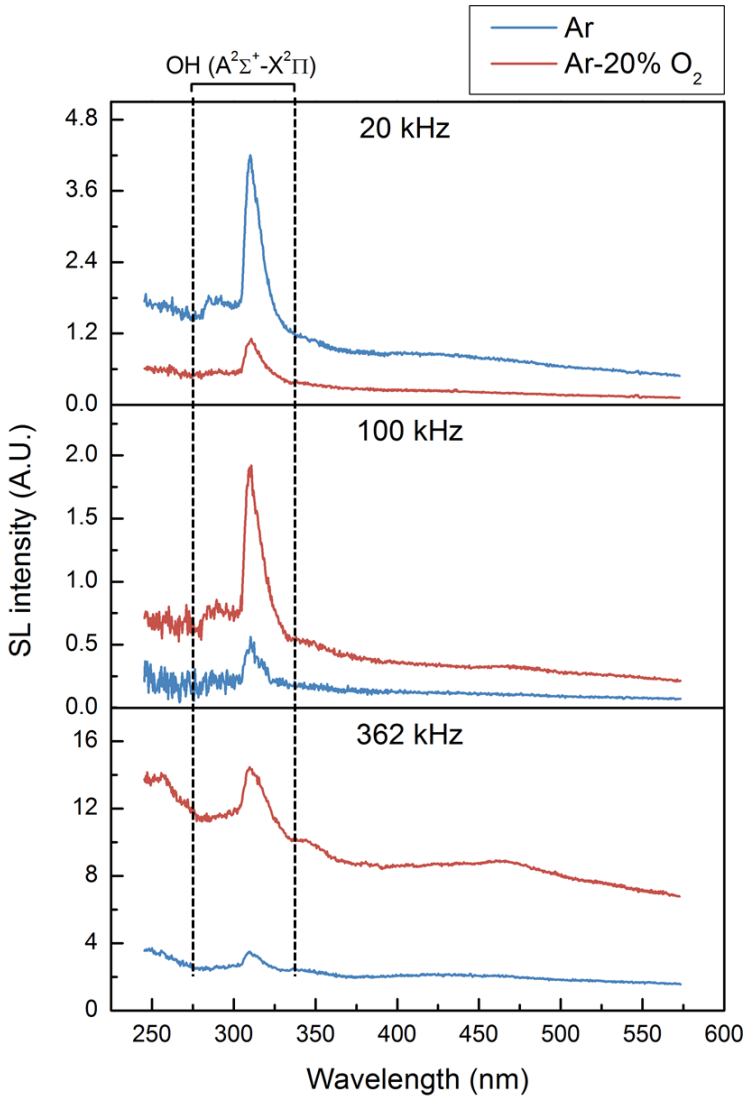

Figure III-5 SL spectra of pure water sonicated at 20 kHz (P_{ac}= 33 W), 100 kHz (P_{ac}= 40 W) and 362 kHz (P_{ac}= 43 W) under 100 mL.min^{-1} Ar and Ar/(20 vol.%)O_2 flow, at 18 ℃. The apparent broad peak around 400-475 nm at 362 kHz is an artefact due to 2nd order light emission of the strong SL UV part.

Table III-1 Ratios (between Ar-20%O_2 and Ar) of OH peak height taken at 309 nm and of SL continuum at 500 nm at different ultrasonic frequencies: 20 kHz (P_{ac}= 33 W), 100 kHz (P_{ac}= 40 W) and 362 kHz (P_{ac}= 43 W), 18 ℃.

Frequency (kHz)	OH peak ratio	Continuum ratio
20	0.24 ± 0.03	0.25 ± 0.04
100	3.5 ± 0.5	3.1 ± 0.5
362	3.4 ± 0.5	4.3 ± 0.6

To explain the different behaviors between SL and sonochemistry (H_2O_2 yield and SCL), it should be noted that not all sonochemically active bubbles do emit light.[84] SL emission occurs only if the plasma energy is high enough to form electronically excited species (radicals, molecules, ions, etc.). Obviously, the energy threshold for excited species production during the bubble collapse is much higher than that for radical formation.[56, 200] Considering for instance $OH^{\bullet}$ radicals, the presence of O_2 enhances their production and the subsequent formation of H_2O_2 whatever the frequency, as observed in **Figure III-1** and **Figure III-2**, but not all of those produced radicals are excited. The proportion of these depends on the applied acoustic frequency. The more violent the collapse, the more molecules and formed radicals can be excited, the higher SL intensity can be detected.

The intra-bubble conditions at different ultrasonic frequencies were studied by simulating spectra (**Figure III-6**) with the spectroscopic software Specair [201] to estimate vibrational (T_v) and rotational (T_r) temperatures of OH ($A^2\Sigma^+$). It is usually considered that the vibrational temperature is a lower estimate of the plasma electron temperature and the rotational temperature is a higher estimate of the translational temperature, i.e. of the gas temperature. **Table III-2** summarizes all estimated temperatures.

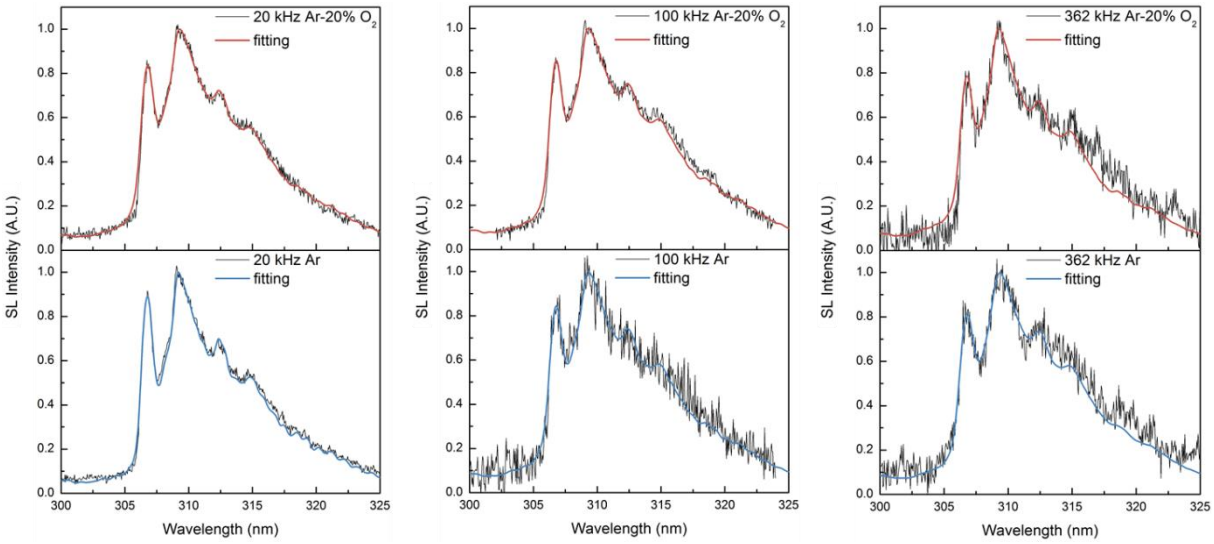

Figure III-6 Normalization of higher resolution SL spectra (after subtraction of a linear baseline) and their simulation (Specair) curves for water at 20 kHz (P_{ac}= 33 W), 100 kHz (P_{ac}= 40 W) and 362 kHz (P_{ac}= 43 W) under 100 mL.min^{-1} Ar (blue) and Ar/(20 vol.%)O_2 (red) flow, 18 ℃.

Table III-2 Estimated vibrational (T_v) and rotational (T_r) temperatures of OH ($A^2\Sigma^+$) in water sonolysis by 20 kHz (P_{ac}= 33 W), 100 kHz (P_{ac}= 40 W) and 362 kHz (P_{ac}= 43 W) under 100 mL.min^{-1} Ar and Ar/(20 vol.%)O_2 at 18 ℃.

Rovibronic Temperature	20 kHz		100 kHz		362 kHz	
	Ar	Ar/O_2	Ar	Ar/O_2	Ar	Ar/O_2
T_v (K)	5750 ± 250	6000 ± 500	6500 ± 500	7250 ± 250	8000 ± 1000	(7500 ± 500)*
T_r (K)	5250 ± 250	5000 ± 200	4750 ± 250	5200 ± 200	5250 ± 250	(3900 ± 100)*

* UV part of SL emission is partly absorbed by H_2O_2, especially at high frequency ultrasound, which leads to an underestimation of T_v and T_r

The values in **Table III-2** point out the absence of thermal equilibrium inside the collapsing bubble ($T_v > T_r$) whatever the studied conditions, in agreement with previous SL studies in aqueous solution[16, 29, 30]. According to the simulations, for both saturating gases, T_v increases with the ultrasonic frequency, while T_r seems to be independent from it and to remain around 5000 K. It is however to be stressed that these results may be somehow impacted by the fitting procedure [21] that suffers from the fact that existing spectroscopic software does not take Stark effects into account.[21] Previous works comparing low and high frequencies indicated (though they were much less accurate) more extreme intrabubble conditions at higher frequency illustrated by higher vibrational temperatures.[20], [21], [202] The present simulations highlight that OH ($A^2\Sigma^+$) rovibronic temperatures at 100 kHz lie well in between low and high frequency ultrasound.

It may look surprising that both T_v and T_r determined at 362 kHz for water saturated with Ar/(20 vol.%)O_2 are abnormally lower than for water saturated with Ar. As mentioned above, at high frequency ultrasound, H_2O_2 production and accumulation is more important, especially in the presence of O_2 in Ar. Therefore, the determined lower T_v and T_r are to be explained by an artefact due to the absorption of the cumulative H_2O_2 in solution (Appendix F).

Notwithstanding this artefact, it can be noted that *Tv* increases (though slightly) upon addition of O_2 in Ar. This difference can be explained by the existence of different OH formation pathways (reactions (I-11), (I-21) and (I-22)), each leading to a given population distribution of vibrational and rotational excited levels. It was not observed in previous works [84] due to their lower spectral resolution.

As noted above, O_2 dissociation occurs at high frequency and 100 kHz, but hardly at 20 kHz. To further study the energy available in 100 kHz cavitation bubbles and their ability to dissociate molecules, N_2

was introduced in Ar gas. Indeed, a previous work [46] showed the much higher occurrence of N_2 molecule dissociation under high frequency ultrasound compared to low frequency: the emission of NH ($A^3\Pi$-$X^3\Sigma^-$) bands was observed on SL spectra at high frequency (reactions (I-20), (I-23) and (I-24)), but not at 20 kHz. Nitrogen molecule possesses a triple bond, i.e. it has much higher bond energy than oxygen (9.79 eV against 5.15 eV for oxygen), and thus higher collapse energy is needed for its dissociation.

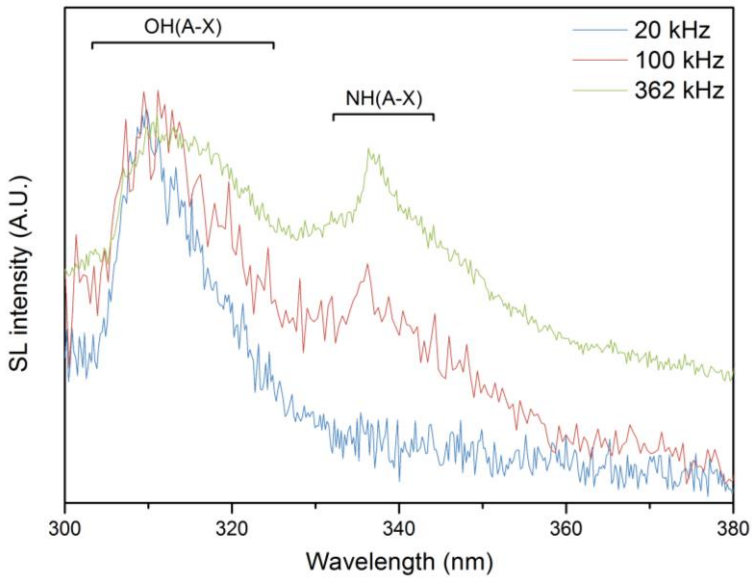

Figure III-7 SL spectra of pure water submitted to 20 kHz (blue, P_{ac}= 33 W), 100 kHz (red, P_{ac}= 40 W) and 362 kHz (green, P_{ac}= 43 W) at 18 ℃ under 100 mL.min^{-1} Ar/(20 vol.%)N_2 flow.

Figure III-7 compares the SL spectra of pure water sonicated at 20, 100 and 362 kHz under Ar/(20 vol.%)N_2 flow. NH ($A^3\Pi$-$X^3\Sigma^-$) emission appears at both the intermediate and high frequencies, indicating that electrons with an energy ≥ 9.79 eV are present in 100 kHz bubbles too. Unfortunately, the NH peak at 100 kHz is too noisy to simulate with Specair, due to the low SL intensity at this frequency.

According to the investigations above, properties of the intermediate ultrasonic frequency (100 kHz) is specific, neither the same as high frequency nor completely similar to low frequency. The chemical activity (H_2O_2 yield) of cavitation bubbles at 100 kHz presents a transitional behavior between low and high frequencies. The active cavitation zone distributes in the whole sonicated volume irradiated by 100 kHz ultrasound, similarly to high frequency and much further than at 20 kHz. The spectral shape of 100 kHz spectra is similar to that at 20 kHz. On the other hand, the intermediate-frequency ultrasound provides the dissociation of O_2 and N_2 molecules inside the bubble which is more typical for high frequency ultrasound. This faculty can be explained by the more extreme conditions reached at collapse of 100 kHz cavitation bubbles, compared to 20 kHz. And it is confirmed that at 100 kHz the estimated

rovibronic temperatures of OH ($A^2\Sigma^+$) excited radicals derived from spectroscopic simulations are higher than that at low frequency.

III.3 Sonochemistry and sonoluminescence in the vicinity of a solid boundary

In order to study the effect of a solid boundary on acoustic cavitation, in particular on sonochemiluminescence and sonoluminescence, a stainless steel plate was placed inside the reactor facing the planar transducers of 362 or 100 kHz. As described above, intermediate and high ultrasonic frequencies enable a homogeneous sonochemistry distribution also strong emissions of SL and SCL observed at 362 kHz in **Figure III-2** and **Figure III-4**, facilitate the observation of a solid boundary effect on ultrasonic cavitation. Luminol and NaCl solutions were used to characterize SCL and SL distributions and intensities in the reactor in the presence of a solid boundary. In multibubble system, considering the different types of bubble collapse, including symmetrical collapses and asymmetrical collapses during bubble coalescence, in bubble clusters and in the vicinity of a solid boundary, MBSL spectra can exhibit different shape and intensity.[67] As described in bibliography,[66] Na* emission can be observed during the sonication of NaCl aqueous solutions. This Na* emission is attributed to the asymmetrical bubble collapse, where droplet injection may happen. On the contrary, continuum and $OH^{\bullet}$ emissions are mainly resulting from the symmetrical bubble collapse.[64, 203] During sonolysis of a NaCl solution, SL intensity of excited sodium ions and continuum as presented in **Figure III-8** and the ratio between them can provide a qualitative analysis of cavitation bubble population in solution with the effect of a solid boundary.

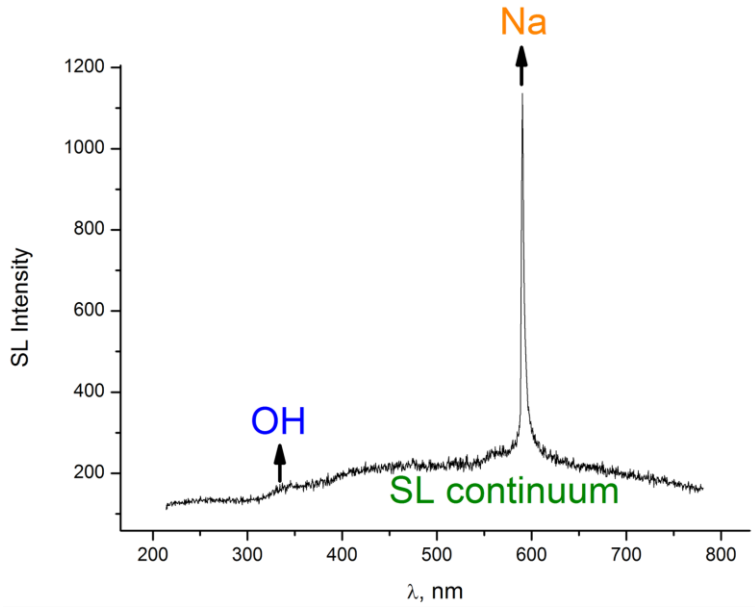

Figure III-8 SL spectra of 1 M NaCl solution sonolysis at 362 kHz (P_{ac}= 43 W) under 100 mL.min^{-1} Ar flow, 14 ℃.

The solid boundary was a stainless steel plate of 56 mm diameter (slightly smaller than the inner diameter of reactor 62 mm) and 21 mm thickness. It is thick enough to ensure a perfectly rigid reflector.[204] Two different configurations were applied in the experiments: the fixed and the mobile stainless steel plate in the reactor.

III.3.1 Fixed stainless steel plate

For the fixed condition, the distance between the stainless steel plate and the transducer plane was about 56 mm. The liquid/solid interface is materialized by a red dashed line in **Figure III-9**.

MBSL spectra of an aqueous NaCl solution sonicated at 362 kHz were collected by adjusting the screw on the platform of the reactor to allow the optical axis to move from the bottom to the top (1 to 18 mm) of the optical window (diameter = 23 mm) with a step of 0.5 or 1 mm (**Figure III-9**). Therefore, different zones in the solution (near and far from the solid surface) were detected. The light entering the SL spectrometer was limited by a slit, thus not the entire window but a short range of height (around 3 mm) was detected during operations.

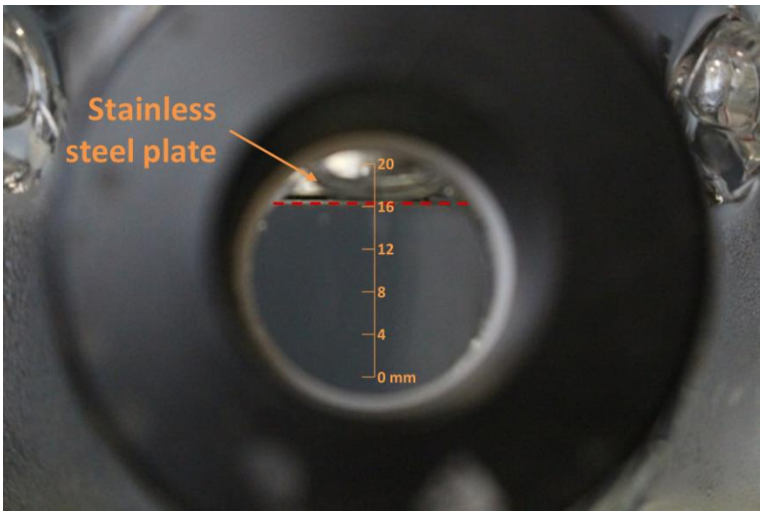

Figure III-9 Fixed stainless steel plate in the reactor

Normalized SL intensity of Na* and continuum emissions as a function of the observation position (z) are plotted in **Figure III-10** and **Figure III-11** respectively. For comparison, SL spectra were also measured in the absence of the stainless steel surface (named as free surface in the following discussion).

In the case of free surface, both Na* and continuum emissions are weak at 18 mm. The weak emissions can be attributed to the limitation of the observed range which may be out of the liquid/air interface or the interference of a big gas bubble on the top of optical window (see in **Figure III-9)**. No obvious Na* intensity difference is found between 4 and 11 mm, while a higher value of continuum appeared at 11 mm. In comparison to free surface condition, at all the observation points (except for 14.5 mm), weaker emissions of both Na* and continuum exhibit with stainless steel plate existence in solution. There are three specific zones of SL intensity evolution when moving up the observation region towards the solid boundary: i) cyclical fluctuations between 1 and 7 mm; ii) slight increase from 7 to 14.5 mm; iii) sharp decrease from 14.5 to 16 mm. In the first zone, comparably far from the stainless steel plate, SL intensity fluctuates with each cycle approximately corresponding to the half wavelength of 362 kHz ultrasound (2.1 mm). When moving gradually towards the solid boundary, a slight increase of SL intensity accompanied with fluctuations in the second zone indicates that the effect of the rigid surface became stronger. Such reflection effect, or standing wave impact, will be discussed later. From 14.5 mm, with continuous moving up of the view point, stainless steel plate starts to enter the observation range of SL spectrometer (see **Figure III-12**). Besides the big gas bubble distortion, less and less light emissions of Na* and continuum in solution are detected, which leads to the dramatic reduction of SL intensity in **Figure III-10** and **Figure III-11**.

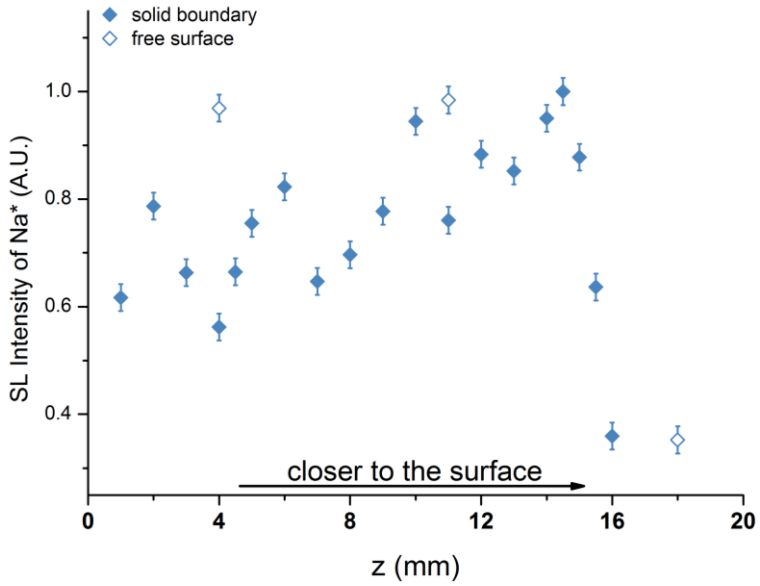

Figure III-10 SL intensity of Na* (589 nm) as a function of the observation position in the presence of a fixed stainless steel plate in 1 M NaCl solution sonicated at 362 kHz (P_{ac}= 43 W) under 100 mL.min^{-1} Ar flow, at 14 ℃.

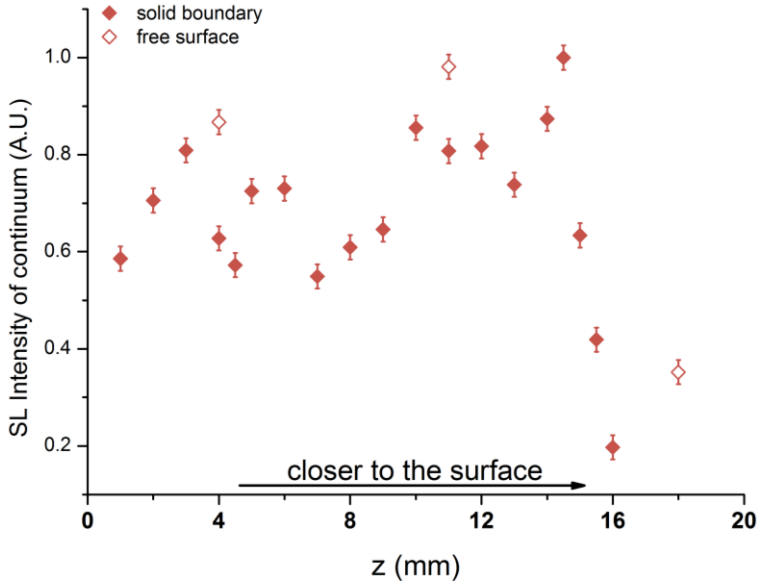

Figure III-11 SL intensity of continuum (500 nm) as a function of the observation position in the presence of a fixed stainless steel plate in 1 M NaCl solution sonicated at 362 kHz (P_{ac}= 43 W) under 100 mL.min^{-1} Ar flow, at 14 ℃.

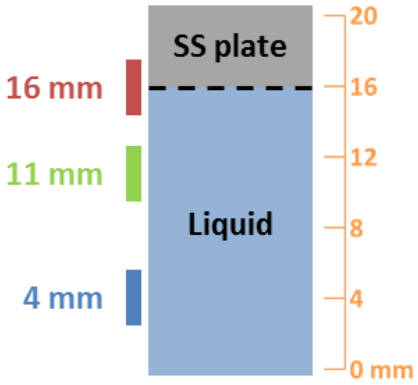

Figure III-12 Scheme of the observation positions made through the quartz window correlated to 3 different zones

Though both Na* and continuum emission intensities follow a similar trend when approaching the stainless steel plate, the ratio of Na*/continuum intensities shows a different behavior (**Figure III-13**). Without solid boundary in solution, this ratio is found to be independent from the observation position. On the contrary, in the presence of the stainless steel plate, the ratio becomes rather high when measured at the vicinity of the solid surface (15 to 16 mm). This higher ratio of Na*/continuum can be explained by the relatively higher population of asymmetrical collapses in the vicinity of the stainless steel plate, where droplet injection happen.[64, 203] However, this effect seems quite localized in a very short range (≤1.5 mm) under stainless steel plate. From 0 to 14.5 mm, the Na*/continuum ratio remains at the same level in agreement with what observed without the solid surface.

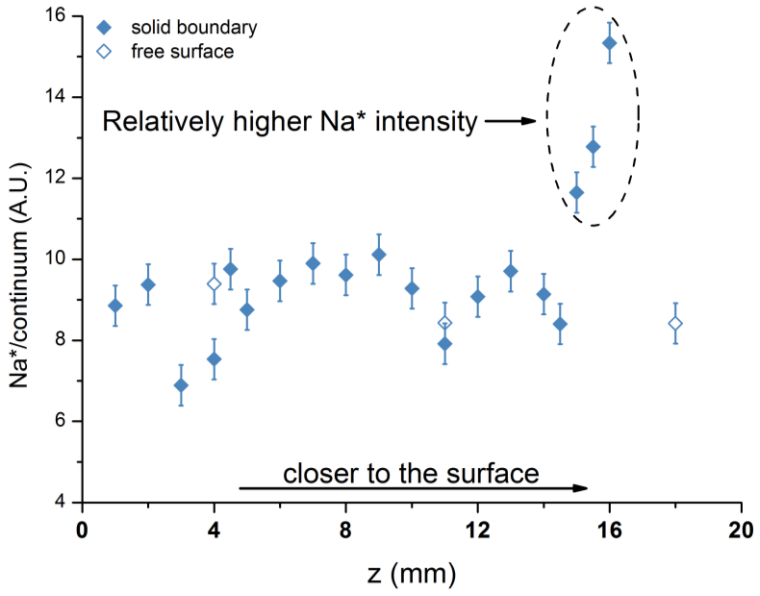

Figure III-13 SL intensity ratio between Na* (589 nm) and continuum (500 nm) emission as a function of the observation position in the presence of a fixed stainless steel plate in 1 M NaCl solution sonolysis at 362 kHz (P_{ac}= 43 W) under 100 mL.min^{-1} Ar flow, at 14 ℃.

As mentioned above, the cyclical fluctuations observed for SL intensity reveal that a standing wave is formed in the solution by the reflection of stainless steel plate. In order to verify the existence of a standing wave in the reactor, photos of SL and SCL in water and luminol solutions observed in the absence of or in the presence of a stainless steel surface are compared in **Figure III-14**. Here, 100 kHz ultrasound is used for this comparison because of its large wavelength (about 14 mm) and visible pattern stripes. The bright and dark stripes shown in **Figure III-14** confirm the presence of a standing wave in the reactor, which is found to be more obvious in the presence of the stainless steel plate. The space between bright stripes (~6 mm) is very close to the half wavelength of 100 kHz ultrasound (~7 mm). It is believed that the brighter the zone, the more intense the cavitation activity. It is clear that in the presence of a solid surface, both SL and SCL images are visually brighter. Simultaneously, SL and SCL distributions become more homogeneous in the reactor with stainless steel plate. Similar uniform SL and SCL distributions have been previously observed by Ashokkumar et al.[205] They detected that in a propanol aqueous solution submitted to 440 kHz ultrasound, a more homogeneous distribution of cavitation bubbles is generated by the reflection of a thin film placed on the liquid surface. In addition to a solid boundary, Tuziuti et al. found that with the floating of some hydrophobic Teflon particles on the free liquid surface of a luminol solution irradiated by 154 kHz ultrasound, the vibration amplitude of the liquid/air interface was reduced, leading to a more luminous light emission.[206]

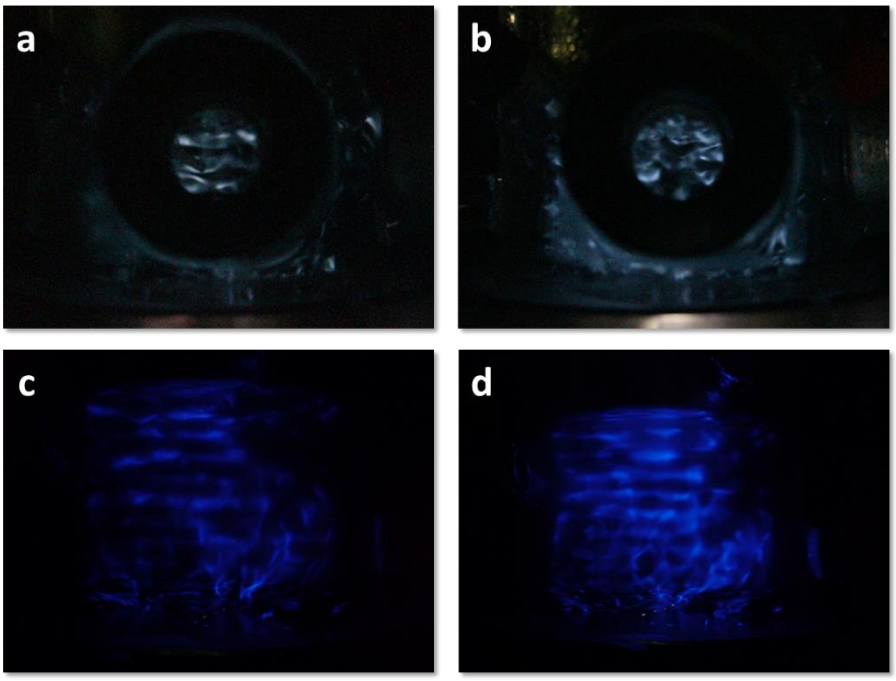

Figure III-14 Photographs of SL in pure water submitted to 100 kHz (P_{ac}= 20 W) under 110 mL.min^{-1} Ar flow, at 18 ℃, exposure 120 s: a) free surface and b) stainless steel plate (on the top of the quartz window); photographs of SCL in 0.01 M luminol solution (pH= 11, Na_2CO_3) submitted to 100 kHz (P_{ac}= 20 W) under 100 mL.min^{-1} Ar/(20 vol.%)O_2 flow, at 17 ℃, exposure 60 s) free surface and d) stainless steel plate

In fact, an ultrasonic field is a combination of both standing and traveling waves.[106] In the case of a free surface, at low acoustic intensity, the liquid/air interface can reflect the sound wave and form a standing wave. When the acoustic power increases, the instability of the liquid surface disturbs the formation of a stable standing wave, and traveling wave becomes dominant.[207] Therefore violent cavitation events mainly occur near the liquid surface, where standing wave proportion is still high.[105] Besides, the vibration of the liquid surface consumes ultrasound energy, which also reduces the pressure amplitude of the formed standing wave.[104] A solid reflector like a stainless steel plate, however, can always act as a surface stabilizer that enhances standing wave proportion in an ultrasonic field, and then increase acoustic pressure amplitude, which affects both SL and SCL.[44, 106] Since the extent of the standing wave formation should strongly depend on the distance between a reflector and the transducer, a more detailed study at different distances was implemented to investigate the effect of a solid surface on the ultrasonic field in a sonoreactor.

III.3.2 Mobile stainless steel plate and Mg disc

The distance between a solid boundary and the transducer plate can influence the ultrasonic field in solution, and in consequence, the SL and sonochemical activity.[207] In the previous study of Kauer et al. an optimum reflector position was found to enable a uniform distribution of SCL in luminol solution and of SL in NaCl solution purged with Ar irradiated by high-frequency ultrasound (≥ 580 kHz).[101] Lee and Choi also observed the sensitivity of SL and SCL intensity as a function of the distance between a stainless steel reflector and transducer plate during the sonolysis of water and luminol solution with 84 kHz ultrasound: a carefully adjusted position of the stainless steel plate was required to obtain the maximum SL and SCL emissions.[91]

In the case of a mobile stainless steel plate, the position of the surface in the reactor was adjusted by turning the screw on a rod, which was used to secure the stainless steel plate to the Teflon hoop. The screw allows 1.24 mm z deviation per revolution. The distance between the plate and the transducer was calculated based on the number of turns of the screw, and then was converted to the corresponding multiple of one quarter of the ultrasound wavelength ($\lambda/4$). Theoretically, a distance equaling to the odd multiple ($2n + 1$) of $\lambda/4$ can induce a standing wave with maximum pressure amplitude, also called a resonant mode. For the even multiple ($2n$) of $\lambda/4$, an annihilation of ultrasonic wave propagation generates the minimum acoustic pressure amplitude in irradiated solution, called anti-resonant mode.[72] For distances of non-integer multiple of $\lambda/4$, a non-resonant mode exists, with acoustic pressure standing between the maximum and minimum amplitude.

Photos of SCL in 0.01 M luminol solution and of SL in 1 M NaCl solution at different distances between the transducer plate and the reflective stainless steel plate are present in **Table III-3**. Dim and bright stripes are visually clear in both SCL and SL images in the presence of the stainless steel plate, but

exhibit blurred with free surface. This is consistent with the previous description that the solid reflector can enhance the standing wave proportion in the ultrasonic field, while the reflection at the free liquid/air surface is weakened by vibration itself. Stripes evenly space 2 mm apart, equals a half wavelength at 362 kHz (2.1 mm). According to literatures,[59, 100, 208] SL bubbles, which usually have a small size, are favored to cluster at the pressure antinodes, where is the bright space in SL images. On the other hand, the coalesced big bubbles preferentially occur at pressure nodes, where should be the dim narrow lines in the pattern. As the stainless steel plate moves closer to the transducer, the apparent SCL and SL image brightness and the spatial color distribution varied periodically. This periodic variation was again found correlated to $\lambda/4$, indicating an alternation between resonant and anti-resonant wave modes in solution. When the distance induces a resonant mode with high-pressure strong standing wave (25.5 and 29 turns), visually brighter images are obtained for both SCL and SL. On the contrary, at the anti-resonant mode, apparently dark SL and SCL images are observed. This can be explained by the lower pressure amplitude in anti-resonant mode. This phenomenon is confirmed by the observation of a similar spectral shape but more intensive SL emission at resonant mode than at non-resonant mode in the presence of stainless steel plate in NaCl solution (**Figure III-15**).

Table III-3 Photographs of SCL in 0.01 M luminol solution (pH= 11, Na_2CO_3) and SL in 1 M NaCl solution in the presence of a stainless steel plate submitted to 362 kHz (P_{ac}= 43 W) under 100 mL.min^{-1} Ar flow, at 18 ℃, exposure 20 s.

n (turn)*	free surface	25.5	26.5	28	29
D (mm)**	-	56.3	55.0	53.2	51.9
N (λ/4)***	-	53.1	51.9	50.2	49.0
Pressure mode	-	resonant	anti-resonant	anti-resonant	resonant
SCL image in 0.01 M luminol	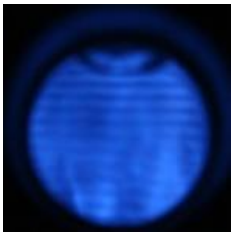	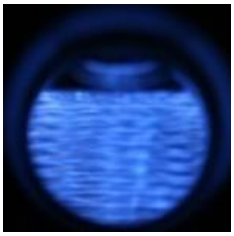	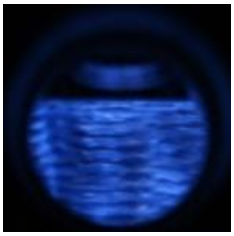	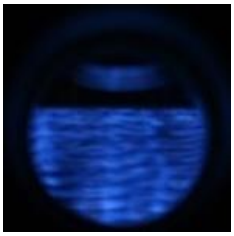	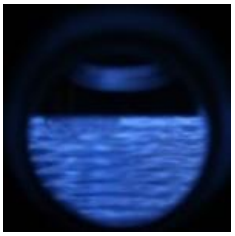
SL image in 1 M NaCl		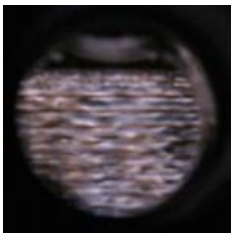		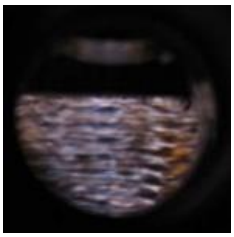	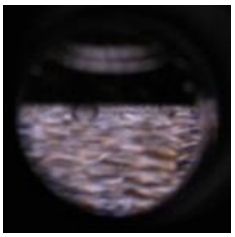

* Number of turns of the screw (1.24 mm per revolution)
** Distance between stainless steel surface and transducer plate D = 87.9-1.24 n (mm)
*** Distance in terms of λ/4 (λ = 4.2 mm)

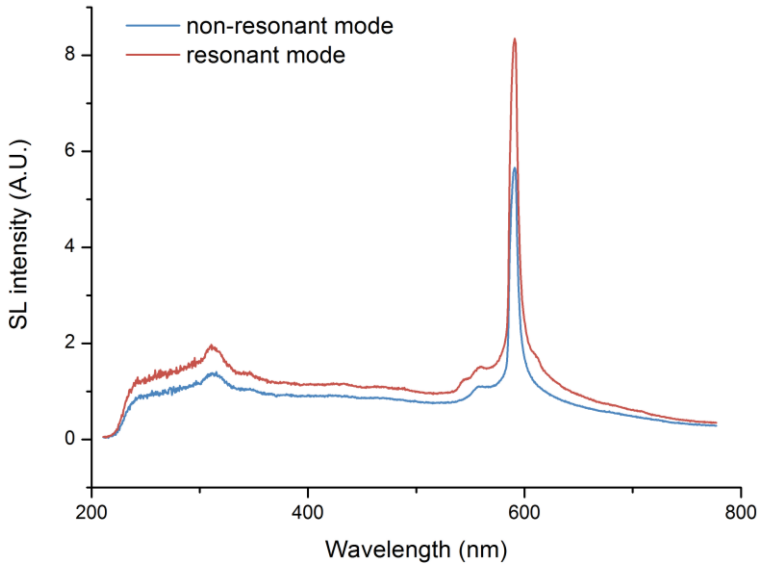

Figure III-15 SL spectra in the presence of a stainless steel plate in 1 M NaCl solution at 362 kHz (P_{ac}= 43 W) under 100 mL.min^{-1} Ar flow, 18 ℃, at resonant mode (red) and non-resonant mode (green) distances

Moreover, in SL images of resonant mode standing wave in NaCl solution, blue and white light emissions were mainly around pressure antinodes space, while the orange color mainly distributed at pressure nodes narrow lines. It is believed that two different bubble populations exist in the ultrasonic field in NaCl solution: i) sonochemically active bubbles, which emit Na* orange light; ii) sonoluminescence active bubbles, which act as sources of SL emissions, including UV and visible light, thus present white and blue colors.[64, 208] In a high pressure amplitude standing wave, stable cavitation is dominant and the small bubbles accumulate at pressure antinodes by the primary Bjerknes force, and contribute to the SL emissions.[59, 66] At the same time, secondary Bjerknes force results in bubble coalescence and clustering, and the formed big bubbles or clusters are driven to pressure nodes by the primary Bjerknes force.[59] These big size bubbles are unstable and more likely collapse asymmetrically in the vicinity of pressure nodes in solution.[64] Therefore, as described in the previous section, more Na* emission (orange) from these asymmetrical collapse appears near the pressure nodes.

However, in the anti-resonant mode, though the entire SL image brightness is significantly diminished, an apparently orange diffusion in the right area of the optical window is observed. As can be seen in **Table III-3**, big gas bubble glued on the right side below the stainless steel plate can be observed at these two anti-resonant distances. Due to the interference of the glued gas bubbles, more unstable bubbles and asymmetrical collapses occur in the right area of the reactor, leading to a heavier orange color from excited Na* emission.

To be coherent with the latter study about Mg surface sonication, Mg disc was attached to the stainless steel plate and sonicated in the same conditions. The distance between Mg disc and the transducer was recalculated by considering of the thickness of Mg disc and the stickers. Small amount of oxalic acid

(0.001 M) was added in the 1M NaCl solution, so that H_2 production existed during experiment. SCL experiment was not implemented here, since luminol is not compatible in acid environment. SL images and spectra at several selected distances are presented in **Table III-4** and **Figure III-16**.

Like stainless steel plate, compared with the free surface case, the standing wave pattern is found to be enhanced in the presence of the Mg surface. Since Mg is a chemically active material, in addition to the sonolysis of water, more hydrogen gas bubbles are expected from reaction of Mg and oxalic acid. According to the images in **Table III-4**, comparatively more bubbles are found to be glued on Mg surface during sonolysis than with the stainless steel plate, especially at the later measured position n = 25 and 26. These formed gas bubbles created a liquid/gas interface at the Mg surface. Consequently, irregular sound wave scattering or reflection from gas bubbles disturbs stable standing wave formation, which leads to a chaotic ultrasonic field with more asymmetrical collapses in solution. That is why after long time operation, the accumulated gas bubbles result in apparently more orange Na* emissions at the later measured position n = 25 than the former one at n = 30, though both distances should be in the resonant mode in the presence of a solid surface.

Table III-4 Photographs of SL in the presence of Mg surface in solution of 1 M NaCl and 0.001 M oxalic acid mixture submitted to 362 kHz (P_{ac}= 43 W) under 100 mL.min^{-1} Ar flow, at 18 ℃, exposure 20 s.

n (turn)	free surface	25	26	27.5	30
D' (mm)*	-	56.2	54.9	53.1	50.0
N' (λ/4)	-	53.0	51.8	50.0	47.1
SL image in 1 M NaCl + 0.001 M oxalic acid		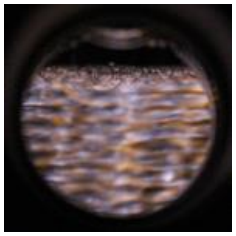	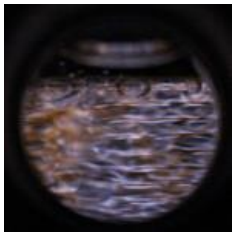	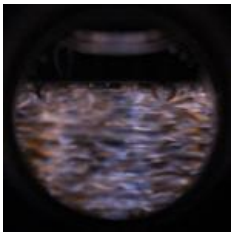	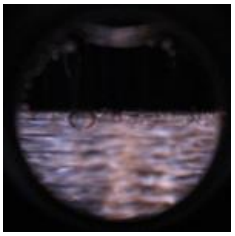

* Considering Mg disc and sticker thickness of 0.75 mm, distance between Mg surface and transducer plate D' = 87.2-1.24 n (mm)

According to **Figure III-16**, in the presence of the Mg surface in solution, it is obvious that SL intensity at the "anti-resonant" mode is much weaker than at "resonant" mode and free surface conditions. A similar spectrum with slightly weaker Na* emission than in the free surface case was observed at resonant mode. However, in consideration of the instability of the ultrasonic field, especially with the gas bubble layer reflection below the Mg surface, SL spectra can vary temporally and spatially. Since

our SL spectroscopy focuses on a localized zone of around 3 mm height and width in the middle of optical window, the obtained SL spectra may not exactly reflect the average SL intensity in the reactor. As described in the literatures, various factors such as heterogeneous dissolved gas concentration in solution,[209] gas bubbling position,[95] besides in this case interference of glued bubbles below solid boundary and irregular inner surface of the reactor, can make unpredictable difference in local SL intensity. Therefore, more precise study, for example a way to remove the glued gas bubbles, is expected in the future study.

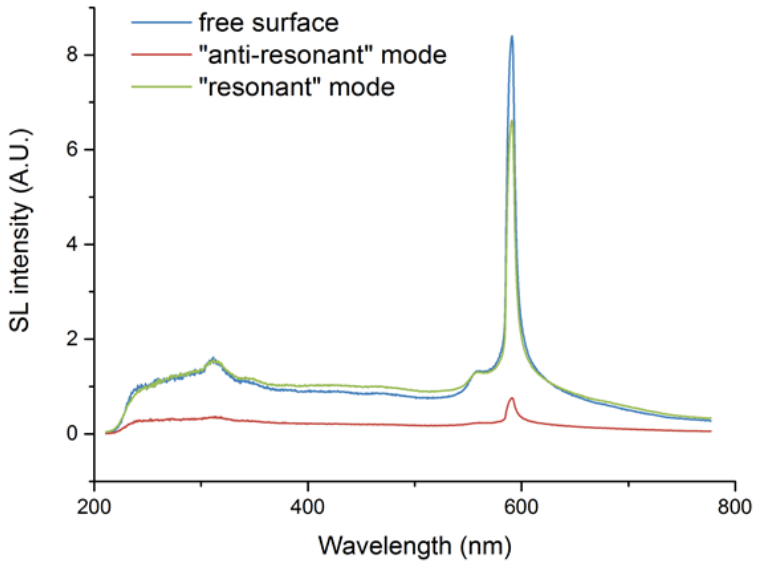

Figure III-16 SL spectra in the presence of Mg surface in the mixture solution of 1 M NaCl and 0.001 M oxalic acid at 362 kHz (P_{ac}= 43 W) under 100 mL.min^{-1} Ar flow, at 18 ℃: free surface (blue), "anti-resonant" mode (red) and "resonant" mode (green) distances

III.4 Conclusion

This chapter presents the study of sonochemistry and SL in an intermediate ultrasonic frequency (100 kHz) field and the effect of a solid boundary on SCL and SL at 100 kHz and 362 kHz.

Investigations on the sonochemistry and SL at 100 kHz find that acoustic cavitation behavior at intermediate frequency is approximately in between low and high frequency ultrasound. The H_2O_2 yield in water under Ar regularly increases with ultrasonic frequency from 20 kHz to 362 kHz. The shape of SL spectrum at 100 kHz is somewhat similar to that at 20 kHz. On the other hand, the rovibronic temperatures of OH ($A^2\Sigma^+$) radicals in the nonequilibrium sonochemical plasma produced by 100 kHz ultrasound are closer to high frequency rather than to 20 kHz. A 20% O_2 addition to Ar leads to higher H_2O_2 yields at all frequencies, and to higher SL intensity at intermediate and high frequencies. This discrepancy was traced back to their higher collapse energy that enables O_2 dissociation and subsequent formation of more excited species, while at 20 kHz O_2, mostly has a quencher effect on SL. Cavitation

bubbles at 100 kHz also share the ability of high frequency ones to dissociate N_2 molecules. Thus, from spectroscopic and chemical points of view, 100 kHz can be seen as a transition between low and high frequencies.

Afterward, according to the SCL distribution in luminol and SL intensity in NaCl solutions irradiated by ultrasound at 100 and 362 kHz in the presence of a reflective solid boundary, a strong standing wave pattern occurs in ultrasonic field which leads to a more homogeneous distribution of SCL and SL, and the correlation between the standing wave content and the distance between solid boundary and transducer is revealed. In the proximity of a fixed solid surface, a higher ratio between Na* and continuum emission intensity is observed from the MBSL spectrum of the NaCl solution. This phenomenon can be explained by the asymmetrical collapses of cavitation bubbles in the vicinity of the solid surface, which induce more Na* emission according to the droplet injection model. However, this effect seems quite localized in a very short distance ($\leq$ 1.5 mm) below the solid plate. By adjusting the position of the solid surface, clear bright dim patterns with spacing of half ultrasound wavelength ($\lambda/2$) indicate a resonant standing wave in the ultrasonic field when the distance between the reflector and the transducer equals odd multiple ($2n + 1$) of a quarter ultrasound wavelength ($\lambda/4$). SCL apparent brightness and MBSL intensity are found to be dependent on the standing wave resonance: brighter SCL photos and stronger SL emissions are observed at the resonant distances. In the case of Mg surface used as reflector in the ultrasonic field, as a result of the interference from the hydrogen bubbles that produced from the reaction between Mg surface and acid, a chaotic wave pattern is observed in the SL photos with apparently more intensive orange color. No precise conclusion can be given from the MBSL spectra because of the interference and distortion of the experimental conditions.

Future study about cavitation at intermediate frequency with other experimental probes and by simulation, and about its mechanical and chemical effects on ultrasonic cleaning and surface modification can be of great interest. Besides, the controlling of the standing wave content in a high frequency ultrasonic field and its effects on sonochemistry and SL should take more attentions and investigations.

In addition to the solid surface impacts on cavitation behaviors (SL and SCL) described above, in turn, the effect of acoustic bubble collapse on solid surfaces and the ultrasonic decontamination efficiency are investigated and discussed in the next chapters.

Chapter IV. Metallic surface structuration by ultrasound

IV.1 Introduction

As described in the previous chapter, asymmetrical bubble collapse is favored in the vicinity of a solid boundary. The generated micro-jets and shock waves participate in surface erosion and micro-deformation, fragmentation of grains, and depassivation of metallic surfaces.[32, 50, 210, 211] Most of the researches dedicated to ultrasonic surface treatment are related to cleaning or erosion and mainly focus on stainless steel, aluminum alloys and titanium,[122, 212-214] or glass and silicon wafers.[32, 215] Furthermore, most of the related studies have been carried out at low frequency ultrasound (20-60 kHz) where mechanical effects of ultrasound are generally said to be more efficient, so that high frequency domain was neglected.[120, 122, 213, 216]

This chapter focuses on the behavior of Mg based surfaces (pure Mg and Mg-Zr alloy) in aqueous solutions under ultrasonic irradiation. Several important parameters are investigated such as the ultrasonic frequency (especially intermediate and high frequencies), duration of treatment, type and concentration of solutes, mechanical stirring velocity, etc. An original approach carried out through 3D reconstruction of sonicated surfaces is used to describe the surface evolutions. The evolution of the surface morphology, wettability, and the correlation between them, besides the chemical composition of the solutions are followed and discussed. Accordingly, a mechanism is proposed for the formation of ultrasonically controlled microstructure on Mg based surfaces.

IV.2 Structuration of Mg-based material surfaces by ultrasound

IV.2.1 Characterization of native Mg surfaces

Photo and SEM image of an as-received Mg sample are presented in **Figure IV-1**. Mg samples exhibit a brownish color and a rust topography, implying the formation of an oxide layer on the native Mg surface, in agree with the literature. [217] The chemical composition of a native Mg surface analyzed by EDX is listed in **Table IV-1**.

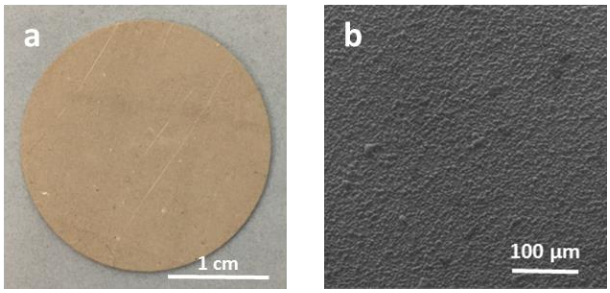

Figure IV-1 Photo and SEM observation of a native Mg surface.

Table IV-1 Chemical composition of a native Mg surface by EDX analysis.

Element	Mg	O	C
wt %	39.7 ± 3.6	44.5 ± 5.2	15.8 ± 2.7

As a reactive metal, Mg can slowly react with oxygen, water, carbon dioxide and some volatile organic compounds in air at room temperature.[217] Oxygen can directly and easily react with Mg with the formation of a thin film of MgO on the surface. Then water vapor and carbon dioxide can be adsorbed by the formed MgO film and produce $Mg(OH)_2$ and $MgCO_3$.[150, 218] This corrosion process continues with the growth of the oxide layer until it is thick enough to play as a protective layer to prevent further corrosion. Previous studies had detected a mixed layer of MgO and complex magnesium carbonates ($x(MgCO_3)$ $y(Mg(OH)_2)$ $z(H_2O)$) which exists[3] with a stable thickness of about 10 nm after 20 days exposure in air.[1] According to our EDX analyses summarized in **Table IV-1**, after long storage in the laboratory atmosphere, the native Mg surfaces seem to be covered with a thin layer of MgO and $x(MgCO_3)$ $y(Mg(OH)_2)$ $z(H_2O)$ mixtures.

Pure magnesium is a hydrophilic material exhibiting a native contact angle of about 40 °or even less.[217, 219] After long storage, the formed complex oxide layer changes the surface energy and roughness. As presented in **Figure IV-2**, a hydrophobic surface is formed on native Mg discs with a contact angle of 120 ± 4 °. The estimated roughness from 3D reconstructions, including the average roughness of profile (R_a) and the mean peak to valley height of roughness profile (R_z), equal 61.1 and 328.4 nm respectively. The contact angle value is consistent with the previous measurement of pure Mg plates stored in ambient atmosphere by Fotea et al.[217] They observed a water contact angle plateau of 113 ± 2 ° after 21 days exposure of Mg in air.

In our experiments all Mg samples were directly treated without any pre-polishing. And we assume that the characterization process just after the surface treatment is short that the new oxidation on the treated surface can be neglected.

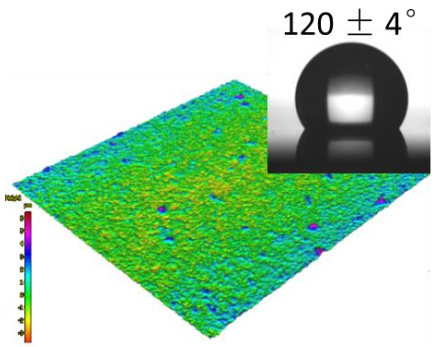

Figure IV-2 3D reconstruction of a native Mg surface (insert: image of water contact angle).

IV.2.2 Frequency effect on Mg surface sonication

Figure IV-3 compares photos of Mg surfaces treated during 1 hour in 0.01 M oxalic acid solutions at 18 ℃ under silent condition (with only stirring) and at low- (20 kHz) and high- (200 kHz and 1 MHz) frequency ultrasound. Notable differences between native Mg surface, surface treated under silent condition and sonicated surfaces can be clearly pointed out with naked eyes. Under silent condition, some dark residual areas can be observed though the majority of the brownish color disappeared. The sonicated samples are found to be much brighter whatever the experimental conditions. As a function of the applied acoustic frequency, different features are observed. The most dramatic effects are generated at low frequency ultrasound (20 kHz) with the formation of several visible pits (the bright tiny spots in **Figure IV-3**.b).

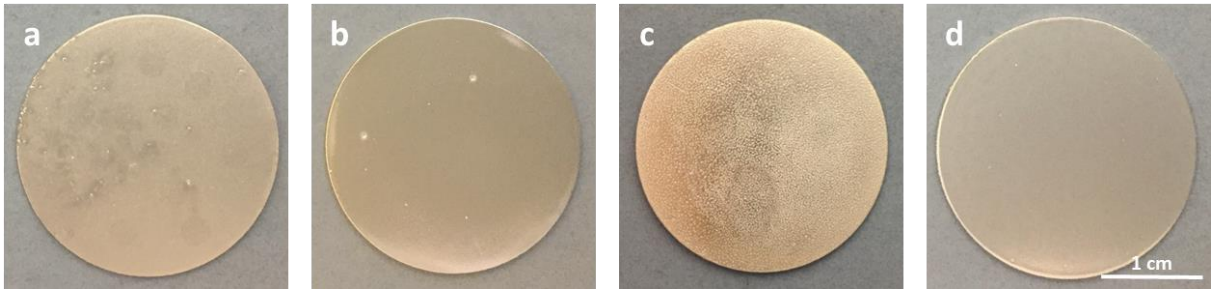

Figure IV-3 Photos of Mg surfaces treated for 1 hour in 0.01 M oxalic acid solution (Ar, 18 ℃): a) under silent condition, stirring; b) at 20 kHz, P_{ac}= 20 W; c) at 200 kHz, P_{ac}= 20 W, stirring; d) at 1 MHz P_{ac}= 40 W, stirring.

In comparison to the original material, the 200 kHz sonicated surface (0.01 M oxalic acid) is smooth and presents a homogeneous coarse appearance of visible tiny pits on the surface (**Figure IV-3**.c). The surface sonicated in 0.01 M oxalic acid at 1 MHz appears much smoother in comparison to the other samples and does not show any other particular features (**Figure IV-3**.d). These observations can be associated to a depassivation phenomenon of the magnesium surface, already reported in the literature and attributed to the acoustic cavitation generated in the vicinity of the extended surfaces.[83, 119]

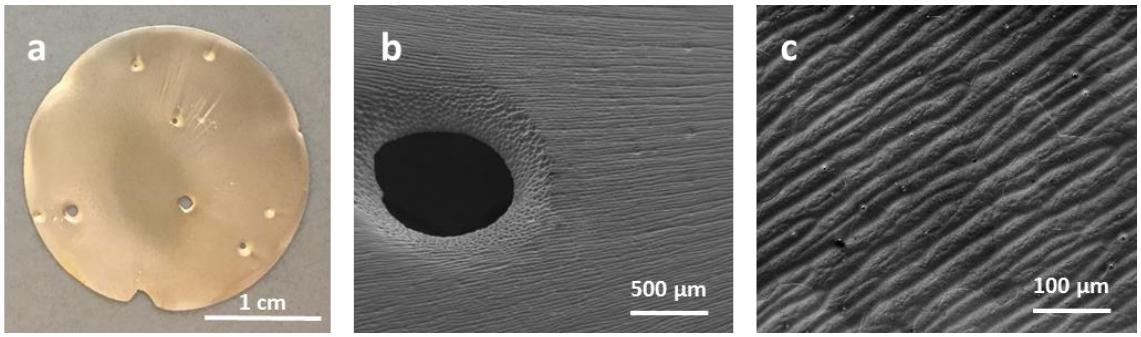

Figure IV-4 Mg surface treated at 20 kHz, P_{ac}= 20 W for 1 hour in 0.05 M oxalic acid solution (Ar, 17 ℃): a) photo; b) and c) SEM observations.

The sonication of Mg surface in a more concentrated oxalic acid solution (0.05 M) with similar other conditions leads to a higher degree of surface erosion that can be noticed in **Figure IV-4**.a. In these conditions, the surface exhibits large holes that completely cross the sample initially measuring 0.5 mm in depth.

SEM investigations related to the frequency effects on the surface are illustrated in **Figure IV-4**.b and c. and **Figure IV-5**.

Under silent condition, the stirred surface is partly devoid of the complex oxide film and exhibits a different morphology (**Figure IV-5**). The oxidation film is indeed replaced by large flakes of more than 100 µm in diameter which are heterogeneously distributed and appear very loose and fragile. In such conditions, corrosion most probably occurs from the edge of the grain boundaries with Mg material peeling off, also known as lamellar or exfoliation corrosion.[220, 221] This behavior can be related to a local oxidation of magnesium into magnesium hydroxide which is thermodynamically more stable in such conditions and is known to exhibit a higher molar volume in comparison to pure magnesium (24.9 $cm^3.mol^{-1}$ for $Mg(OH)_2$ against 14.0 $cm^3.mol^{-1}$ for pure Mg).[222] Such transformation occurring at localized areas can therefore weaken and stress the surface film and favor the departure of large flakes.[150, 221]

The 20 kHz experiment performed in 0.01 M oxalic acid shows a heterogeneous surface with the presence of small pits combined with large and polydispersed cavities (or “craters”). The craters are heterogeneously dispersed on the surface and have a size comprised between 100 and 300 µm. One of them is visible in **Figure IV-5**. If the oxalic acid concentration increases to 0.05 M, these craters are found to grow as big holes of about 1 mm diameter, as presented in **Figure IV-4**.b. It is also interesting to note that 20 kHz sonication also leads to the formation of channels and fluctuating undulations which are more obvious in 0.05 M oxalic acid solution (**Figure IV-4**.c). Such features can be attributed to the acoustic pressure field and streamings generated on the surface during sonication.[42]

In agreement with **Figure IV-5**, the experiments carried out at 1 MHz do not reveal the presence of craters on the surface which is found smoother and much more homogeneous. Similar surface topography is also observed on Mg sample treated at 665 kHz (Appendix G). Meantime, these sonication treatments at very high ultrasonic frequencies also allow the Mg material grains to be revealed.

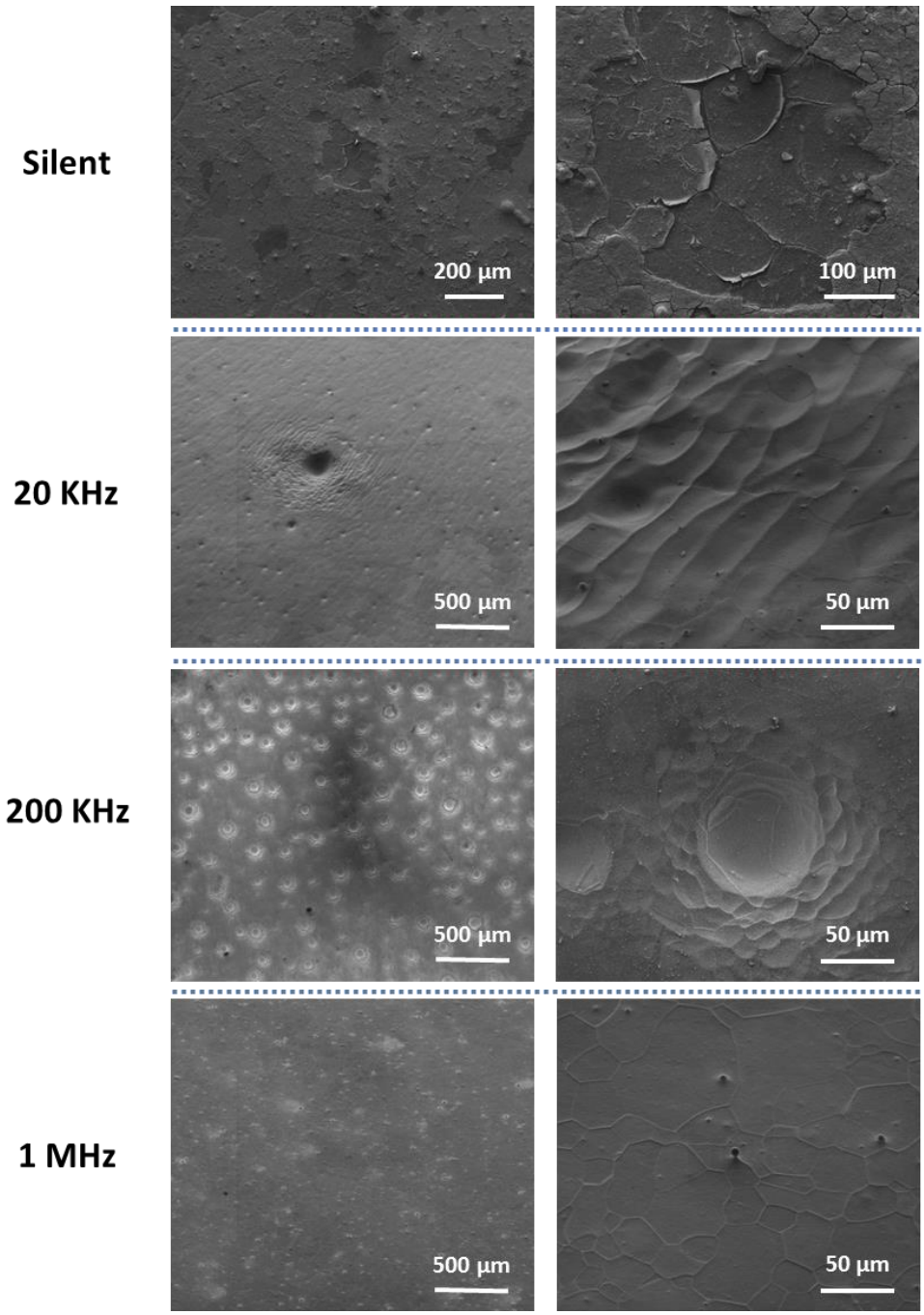

Figure IV-5 SEM observations of Mg surfaces treated for 1 hour in 0.01 M oxalic acid solution, (Ar, 18 ℃, stirring 200 rpm): under silent condition; at 20 kHz, P_{ac}= 20 W, no stirring; at 200 kHz, P_{ac}= 20 W; at 1 MHz P_{ac}= 40 W.

By contrast to the other applied ultrasonic frequencies, 200 kHz sonication leads to an unpreceded microstructure characterized by a homogeneous surface where a monodispersed distribution of craters can be noticed (**Figure IV-5**). When tilted, this surface exhibits a "golf ball" shape structuration that can be observed in **Figure IV-6**.a and b. More generally, the increase of the ultrasonic frequency from 20 kHz to 200 kHz favors the homogeneous distribution of the craters on the surface.[223] Higher

ultrasonic frequencies (≥ 665 kHz), which are known to provide smaller bubbles, does not lead to crater formation. Golf ball shape microstructures generated at 200 kHz therefore result from a fine tuning of the applied acoustic frequency coupled to an appropriate solute. Furthermore, it is important to note that the procedure allows the homogeneous structuring of a large area of material which can be of potential interest for technological surface and alloy structuring and engineering (**Figure IV-6**.a).

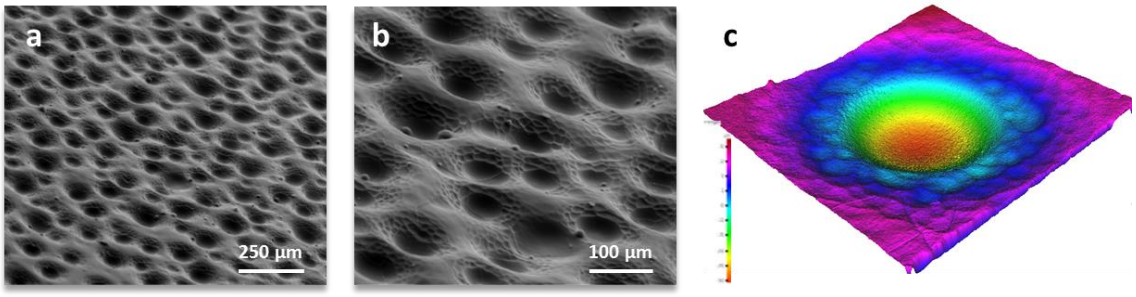

Figure IV-6 Crater structures on Mg surface treated for 1 hour in 0.01 M oxalic acid solution (Ar, 18 ℃): a) and b) SEM observation with a 65 °tilt angle at 200 kHz, P_{ac}= 20 W; c) 3D reconstruction at 100 kHz, P_{ac}= 20 W.

At the same time, we notice the presence of small particles on the surface (secondary phases). More details about the precipitation and the crater formation mechanism will be described later in this chapter.

Similar crater structures can be observed on Mg surfaces treated by 100 kHz (**Figure IV-6**.c) and 345 kHz (not shown here) ultrasound. According to **Table IV-2**, the crater diameter and depths are found to decrease with the increasing ultrasonic frequency in agreement with the decreasing resonance radius of the collapsing resonant bubbles going from 150 µm at 20 kHz to 8.7 µm at 345 kHz.[56, 223]

Table IV-2 acoustic bubble resonance radius and estimated crater size of Mg surfaces treated for 1 hour in 0.01 M oxalic acid solution (Ar, 18 ℃, stirring 100 rpm): 20 kHz, P_{ac}= 20 W; 100 kHz, P_{ac}= 20 W ; 200 kHz, P_{ac}= 20 W; 345 kHz P_{ac}= 40 W; 1 MHz, P_{ac}= 40 W.

Frequency	**20 kHz**	**100 kHz**	**200 kHz**	**345 kHz**	**1 MHz**
Bubble resonance radius (µm)[56]	150	30	15	8.7	3.0
Crater diameter (µm)	100 - 300	110 ±13	85 ±7	40 ±4	-
Crater depth (µm)	-*	60 ±7	34 ±5	18 ±4	-

* At 20 kHz, 3D reconstructions of the big craters did not allow to access to effective depth values

Figure IV-7 summarizes the reconstructed 3D surfaces with the corresponding water contact angle measurements obtained for the Mg surfaces sonicated in 0.01 M oxalic acid at different ultrasonic frequencies besides under silent condition. Their corresponding estimated roughness from 3D reconstructions are listed in **Table IV-3**.

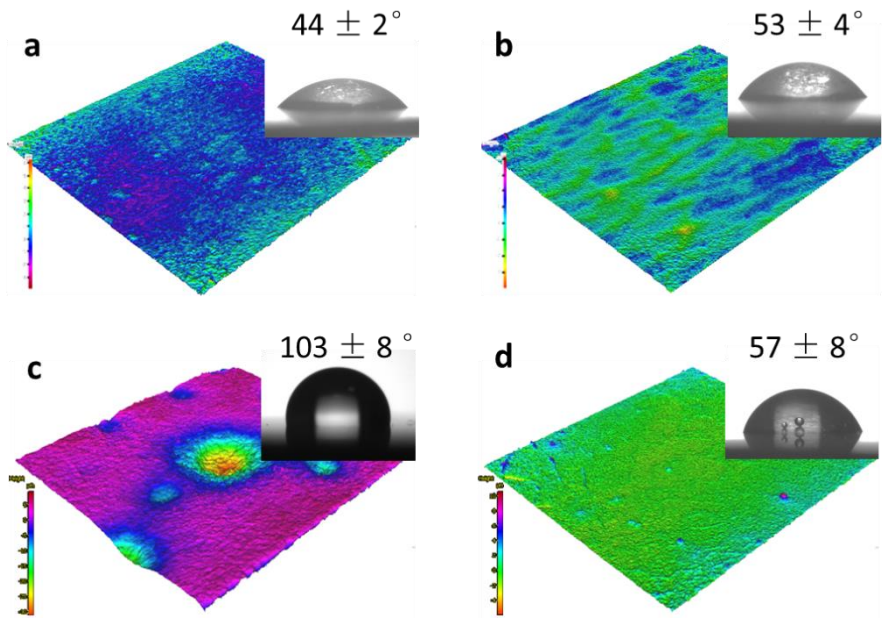

Figure IV-7 3D reconstruction of Mg surfaces treated for 1 hour in 0.01 M oxalic acid solutions, Ar, 18 ℃ stirring 200 rpm: a) under silent condition; b) 20 kHz, P_{ac}= 20 W, no stirring; c) 200 kHz, P_{ac}= 20 W, stirring; d) 1 MHz P_{ac}= 40 W, (insert: images of water contact angle).

Table IV-3 Estimated roughness for Mg surfaces treated during 1 hour in 0.01 M oxalic acid solutions (Ar, 18 ℃, stirring 100 rpm): silent condition; 20 kHz, P_{ac}= 20 W, no stirring; 100 kHz, P_{ac}= 20 W; 200 kHz, P_{ac}= 20 W; 345 kHz P_{ac}= 40 W; 1 MHz P_{ac}= 40 W.

Frequency	**Original**	**Silent**	**20 kHz**	**100 kHz**	**200 kHz**	**345 kHz**	**1 MHz**
R_a (nm)	61.1 ± 1.2	43.9 + 0.9	40.3 ± 4.1	162.3 ± 2.4	169.6 ± 3.4	211.5 ± 4.2	39.4 ± 0.8
R_z (nm)	328.4 ± 5.6	260.4 ± 4.7	185.0 ± 8.7	634.8 ± 7.8	582.7 ± 6.1	605.5 ± 5.5	257.8 ± 4.4

The contact angle values obtained on Mg samples treated under silent condition reaches 44 ± 2 °, which is lower than the original Mg surface and very close to a native Mg material without oxide layer (~ 40 °). This result is expected, considering the incomplete removal of oxide layer and the absence of formation of specific microstructures on the treated surface. However, the heterogeneous surface observed at 20 kHz (presence of fluctuating undulations, valleys, large craters and holes) also leads to a small contact angle of 53 ± 4 °. The areas surrounding the holes exhibit a lower roughness in comparison to the original material. Similar observations have been reported during the laser structuring of Mg alloy material,[186] the 20 kHz ultrasound treatment of aluminum and stainless steel in pure water,[115] and the 20 kHz sonication of titanium alloys in 5 M sodium hydroxide.[122] For surface treated at 1 MHz, the measured contact angle and roughness are very close to that obtained at 20 kHz, though the absence of surface deformations and craters leads to a much smoother and homogeneous surface.

The estimated roughness for surfaces treated under silent condition, at 20 kHz and at 1 MHz ultrasound present a high correlation with their corresponding measured contact angles. For 20 kHz sonication, the use of a more concentrated oxalic acid solution (0.05 M) involves a more dense undulation structure which can slightly increase the surface roughness to R_a= 48.2 nm and R_z= 223.6 nm, with a smaller contact angle at 45 ± 4°. This observation is in good agreement with Wenzel's model (**Figure IV-9**.b), that an increase in roughness for an intrinsically hydrophilic surface allows increasing its hydrophilicity.[186]

It is important to note that heterogeneous surface structuration observed for Mg samples treated at low frequency ultrasound may involve a larger local roughness due to the presence of big craters and holes.

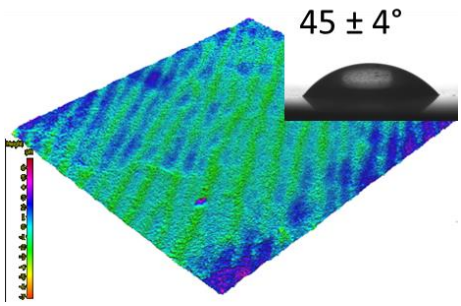

Figure IV-8 3D reconstruction of Mg surface treated at 20 kHz, P_{ac}= 20 W for 1 hour in 0.05 M oxalic acid solution (Ar, 17 ℃). The insert shows an image of water contact angle.

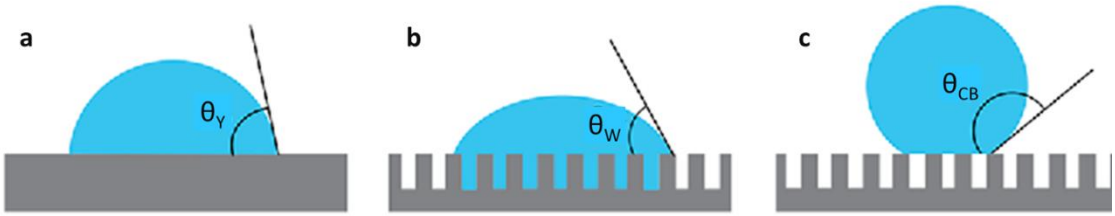

Figure IV-9 Solid surface wetting: a) Young contact angle; b) Wenzel model; c) Cassie-Baxter model.[224]

For the Mg surfaces treated at 200 kHz, the homogeneously formed craters result in higher roughness parameters as presented in **Table IV-3**, but also in a surprisingly larger contact angle (103 ± 8 °). In this case, Wenzel's model is not sufficient to explain this phenomenon. Here we assumed that the microstructures created on Mg surfaces sonicated at 200 kHz are rough enough to trap air in the craters during the contact angle measurement, which is the case of Cassie–Baxter model (**Figure IV-9**.c). As a result, the wettability of Mg surface is substantially changed from hydrophilic to hydrophobic thanks to the homogeneous distribution of the golf-ball shape craters. Similar contact angles and roughness are also observed with surfaces sonicated at 100 and 345 kHz.

Table IV-4 compares the amount of dissolved material (weight loss) for the Mg surfaces sonicated at different ultrasonic frequencies. Except for high frequency at 1 MHz, all of the results are in agreement with photos, SEM observations and 3D reconstructions. For the surface treated by 1 MHz ultrasound, the morphology change is not comparable with lower frequencies, which may be due to its weaker physical effect and the smaller bubble sizes. The notable weight loss found at 1 MHz ultrasound, which was even more than that observed at 200 kHz, probably relies on the higher used acoustic power.

Table IV-4 Weight loss of Mg surfaces treated for 1 hour in 0.01 M oxalic acid solution (Ar, 18 ℃): under silent condition; at 20 kHz, P_{ac}= 20 W; at 200 kHz, P_{ac}= 20 W, stirring; at 1 MHz P_{ac}= 40 W, stirring 200 rpm.

Frequency	**Silent**	**20 kHz**	**200 kHz**	**1 MHz**
Weight loss (%)	1.08 ± 0.04	10.12 ± 0.17	5.18 ± 0.11	6.12 ± 0.06

The special structuring of the surfaces treated at ultrasonic frequencies ranging from 100 to 345 kHz appears very interesting and has, to our knowledge, never been reported in the literature. Therefore, the following studies were carried out within this range of frequency to focus on the formation of this "golf ball" shape structure.

IV.2.3 Solutions effect on Mg surface sonication

SEM images of Mg surfaces sonicated at 200 kHz in water, 0.01 M sodium oxalate and 0.001 M oxalic acid solutions are presented in **Figure IV-10**. According to previous studies on the sonication of oxalic acid, the degradation of oxalic acid or oxalate group in solutions irradiated by ultrasound is negligible even after several hours experiment.[225, 226] In comparison to the sample sonicated in similar conditions with a higher oxalic acid concentration (0.01 M, see **Figure IV-5**), almost no depassivation effect is observed on the Mg surfaces treated in water or in 0.01 M sodium oxalate solution. A dense distribution of new phases appears on Mg sample treated in sodium oxalate which can be attributed to magnesium hydroxide precipitation considering the sodium oxalate solution should be low alkalinity (pH ≈ 8), but not magnesium oxalate precipitation due to its relatively higher solubility (solubility product constant K_{sp}= 8.6 ·10^{-5}, and for $Mg(OH)_2$ K_{sp}= 5.61 ·10^{-12}).[227, 228] This is confirmed by EDX analysis that almost no carbon is observed on the treated surface. After 1 hour sonication in the dilute 0.001 M oxalic acid solution, it is possible to observe the partial and complex removal of the oxide layer without any formation of craters. Some pits and deformations can nevertheless be noticed. Prolongation of sonication until 90 minutes leads to the formation of crater structures, which formation mechanism is described later.

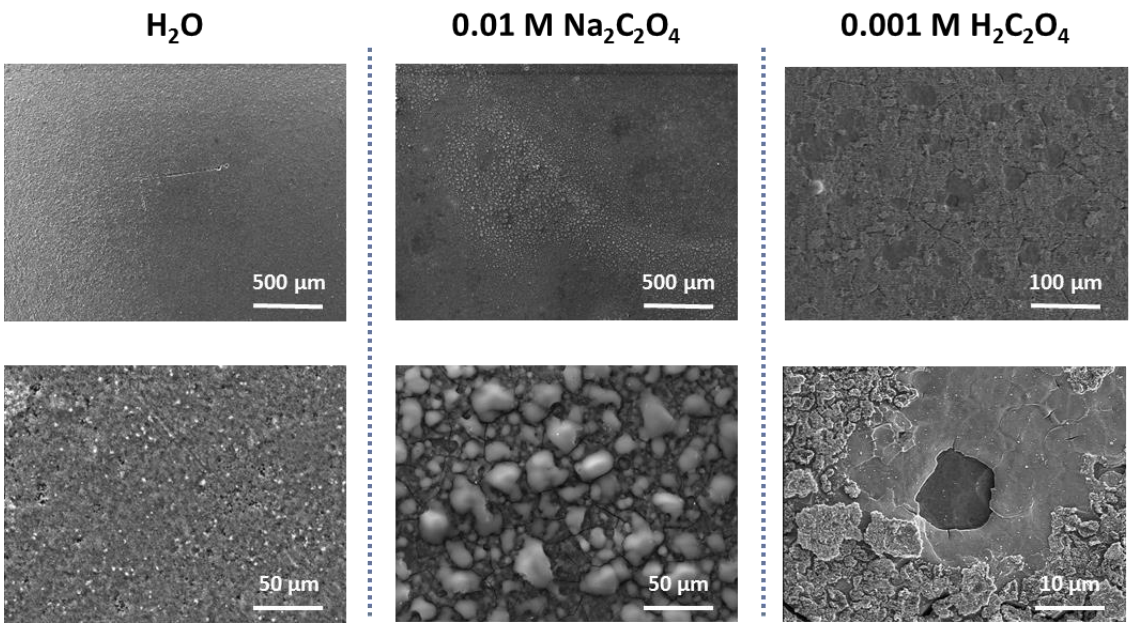

Figure IV-10 SEM observations of Mg surfaces treated at 200 kHz, P_{ac}= 20 W, stirring, Ar, 18 ℃ for 1 hour in: water, 0.01 M sodium oxalate solution and 0.001 M oxalic acid solution.

Table IV-5 compares the contact angle measurements obtained on the surfaces sonicated in the various solutions. In water and 0.01 M $Na_2C_2O_4$ solution, a slight decrease of the contact angle can be noted and attributed to the low or partial removal of the native oxide layer. For Mg surface treated in a 0.001 M oxalic acid solution, the contact angle decreases to about 20 °, which agrees with the observed depassivation of the metallic surface and what reported for pure Mg material. This huge differences between $Na_2C_2O_4$ and oxalic acid solutions should come from the presence of protons, which strongly react and remove the oxide layer on Mg surfaces. However, there is a significant discrepancy between the measured contact angles of Mg surfaces treated in the dilute 0.001 M and 0.01 M oxalic acid solutions.

Table IV-5 Water contact angles obtained for Mg surfaces treated at 200 kHz (P_{ac}= 20 W, stirring, Ar, 18 ℃) for 1 hour in water, 0.01 M sodium oxalate solution and 0.001 M oxalic acid solution.

Solution	**H_2O**	**0.01 M $Na_2C_2O_4$**	**0.001 M $H_2C_2O_4$**
Contact angle (°)	82.7 ±4	84.8 ±4	22.8 ±4

By comparing the contact angle evolution of Mg surface sonicated at 200 kHz in three different solutions (see **Figure IV-11**), the surface wettability is found to be directly correlated to the removal of the oxide layer and the formation of craters. The contact angle of the sonicated Mg surface decreases linearly and slowly in water which agrees with the very limited depassivation observed by SEM. With the departure of the oxidation layer in 0.001 M oxalic acid, Mg surface contact angle rapidly decreases to less than

40 °in 20 minutes and remains at the same level in the next 40 minutes treatment. Such strongly wetting surface can refer to strong hydrophilicity in agreement with the literature.[229] SEM images of both experiments in **Figure IV-5** and **Figure IV-10** do not present the formation of crater structures. However, in 0.01 M oxalic acid, contact angle is over 80 °after just 30 minutes sonication. This is not the same situation as in water, since in oxalic acid the oxide layer is totally removed, and at the same time an obvious distribution of craters already existed on the sonicated surface.

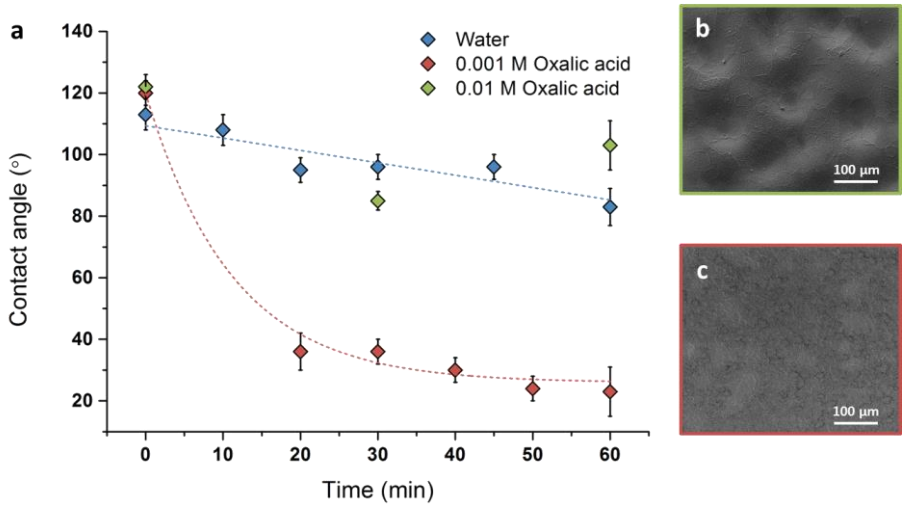

Figure IV-11 Mg surfaces treated at 200 kHz (P_{ac}= 20 W, stirring, Ar, 18 ℃) for 1 hour in water, 0.001 M and 0.01 M oxalic acid solutions: a) water contact angle evolution; SEM image of Mg surface after 30 min treatment in b) 0.01 M oxalic acid solution and c) 0.001 M oxalic acid.

These results strengthen our previous observations and hypotheses where golf-ball shape craters formed by ultrasound are assumed to strongly increase the roughness and the contact angle of Mg surface. The formation of crater structures does not only depend on acoustic cavitation, but also on acidic environment. For a much dilute acid, longer sonication duration or higher acoustic power intensity can help the production of craters.

In water the dissolution of the oxide layer and the corrosion of Mg are very weak and slow (reaction (I-32)). In oxalic acid, several chemical reactions ((IV-1) to (IV-4)) can take place due to the presence of protons:

$$MgO + 2H^+ \rightarrow Mg^{2+} + H_2O \quad \text{(IV-1)}$$

$$Mg(OH)_2 + 2H^+ \rightarrow Mg^{2+} + 2H_2O \quad \text{(IV-2)}$$

$$MgCO_3 + 2H^+ \rightarrow Mg^{2+} + H_2O + CO_2 \quad \text{(IV-3)}$$

$$Mg + 2H^+ \rightarrow Mg^{2+} + H_2 \quad \text{(IV-4)}$$

In the case of sodium oxalate solution, a weak alkaline environment is created by oxalate ligands (reactions (IV-5) and (IV-6)). At the same time, H_2O and the produced small amount of $HC_2O_4^-$ and $H_2C_2O_4$ can dissolve the complex oxide layer on Mg surface and bring Mg^{2+} into solution, which will precipitate as $Mg(OH)_2$ in the weak alkaline system (reaction (IV-7)).

$$C_2O_4^{2-} + H_2O \rightleftharpoons HC_2O_4^- + OH^- \quad \text{(IV-5)}$$

$$HC_2O_4^- + H_2O \rightleftharpoons H_2C_2O_4 + OH^- \quad \text{(IV-6)}$$

$$Mg^{2+} + 2OH^- \rightarrow Mg(OH)_2 \quad \text{(IV-7)}$$

Figure IV-12 and **Table IV-6** compare Mg dissolution and hydrogen production kinetics observed for the four different aqueous solutions sonicated at 200 kHz. In agreement with SEM investigations, Mg is found to poorly accumulate in sonicated pure water, with an initial rate of 0.8 µM.min^{-1}. This can be explained by the low solubility of $Mg(OH)_2$ (K_{sp}= 5.61 ·10^{-12}) formed in pure water.[222] The presence of 0.01 M sodium oxalate significantly enhances Mg dissolution rate which reaches 5.8 µM.min^{-1}. In comparison to pure water, this rate can be again improved (11.3 µM.min^{-1}) with the presence of protons (H^+) through the sonication of a 0.001 M oxalic acid solution thus confirming the ultrasonic dissolution of Mg material with time. A dramatic increase of the dissolution kinetics can be further observed in the presence of 0.01 M oxalic acid where the initial dissolution rate gains two orders of magnitude in comparison to pure water and reaches 76.7 µM.min^{-1}. These Mg dissolution differences confirm the strong contribution of H^+ in the microstructure formation process. Nevertheless, the contribution of oxalate ligands cannot be totally neglected in the whole mechanism as evidenced by the higher dissolution rates observed in the presence of sodium oxalate solutions in comparison to pure water.

For oxalic acid solutions, it is interesting to note an obvious slowdown of the Mg accumulation rate after 30 minutes of sonication in **Figure IV-12**. This phenomenon is easily perceptible for 0.01 M oxalic acid solution and can be related to (i) the exhaustion of protons during dissolution, or (ii) the precipitation of MgC_2O_4 which saturates the solution and the surface. According to the solubility constant for magnesium oxalate (K_{sp}= 8.6 ·10^{-5}) and the concentration of protons initially introduced, the maximal dissolution yield estimated for Mg appears limited by the concentration of protons for 0.001 M oxalic acid (24 mg.L^{-1} against 2 g.L^{-1} for Mg oxalate solubility). For higher oxalic acid concentration, both protons and magnesium oxalate precipitation can limit Mg dissolution (240 mg.L^{-1} for protons against 206 mg.L^{-1} for the solubility). However, Mg oxalate precipitates were not noticed in solution (in contrast to 0.05 M experiments) supporting a mechanism driven by H^+ consumption.

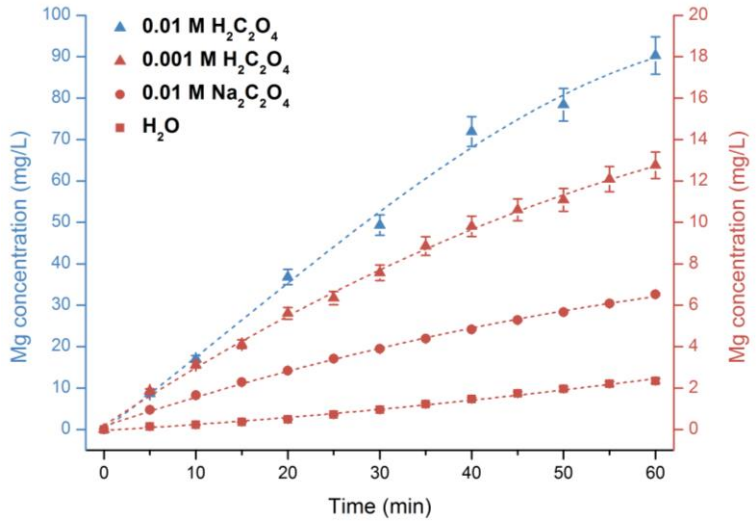

Figure IV-12 Dissolution of Mg surfaces treated at 200 kHz (P_{ac}= 20 W, stirring, Ar, 18 ℃) for 1 hour in water, 0.01 M sodium oxalate solution, 0.001 M and 0.01 M oxalic acid solutions.

It is important to note that experiments carried out at 20 kHz in 0.05 M oxalic acid results in a strong H_2 gas release (177.7 µM.min^{-1}) as well as a high concentration of solubilized Mg in solution. Furthermore, these conditions involved the formation of Mg oxalate precipitate (or glushinskite, K_{sp}= 4.83 ·10^{-6})[227] which was characterized by Raman spectroscopy and XRD measurements in **Figure IV-13** and **Figure IV-14** respectively.

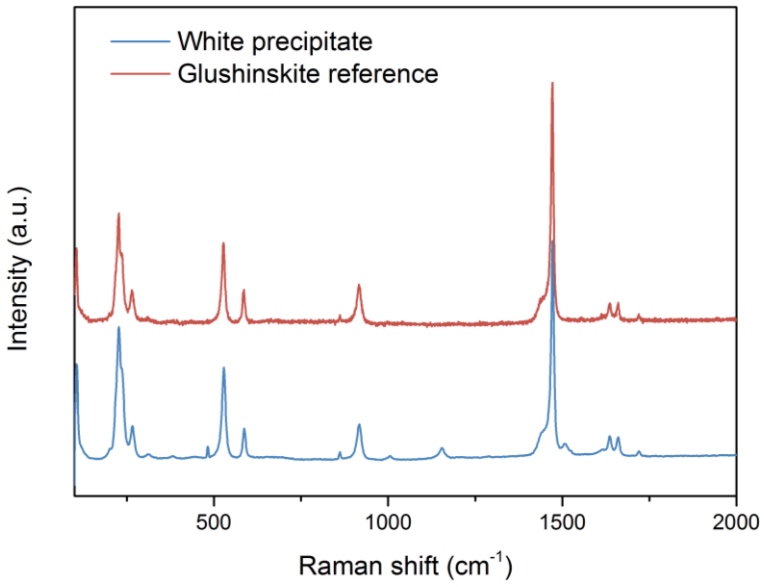

Figure IV-13 Raman spectra of the white precipitate obtained in solution after Mg surface sonication at 20 kHz, P_{ac}= 20 W for 1 hour in 0.05 M oxalic acid solution (Ar, 17 ℃) and glushinskite standard as reference

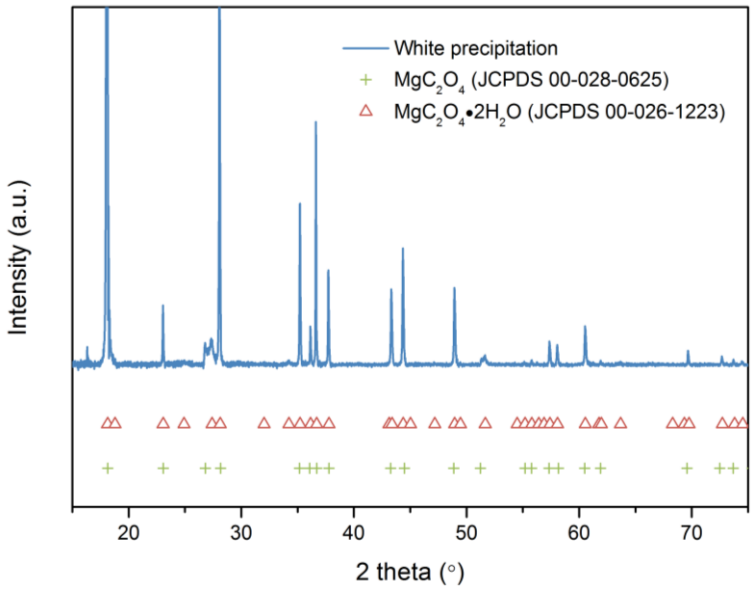

Figure IV-14 X-ray diffraction pattern of the white precipitate obtained in solution after Mg surface sonication at 20 kHz, P_{ac}= 20 W for 1 hour in 0.05 M oxalic acid solution (Ar, 17 ℃) (standard patterns of MgC_2O_4 JCPDS 00-028-0625 and MgC_2O_4•$2H_2O$ JCPDS 00-026-1223)

Furthermore, according to **Table IV-6**, on-line mass spectrometry experiments confirmed that sonication of Mg surfaces is accompanied with the generation of hydrogen (H_2) gas. The measured H_2 flow rate is observed to increase from 0.5 µM.min^{-1} in pure water to 31.7 µM.min^{-1} in 0.01 M oxalic acid solution. Generally, due to the amount of oxalate ligands and H^+ concentration addition, the increasing tendency of hydrogen gas release is correlated to Mg accumulation in solution. However, the amounts of dissolved Mg ions and released hydrogen gas for the various studied solutions do not correspond if we consider the reactions previously described ((I-33), (I-34) and (IV-4)). Hydrogen gas generation indeed represents only about half or less of the dissolved Mg amount while they should be approximately equal. This phenomenon has been already observed by other authors and has been attributed to the dissolution of hydrogen atoms in the Mg metal matrix.[230, 231] The initial oxide layer dissolution (no hydrogen production, reactions (IV-1) to (IV-3)) and the possible inevitable leakage of gas during experiments may also partly contribute to this inconsistency between Mg dissolution and hydrogen production. Nevertheless, it is important to emphasize that the kinetics of Mg ion accumulation in solutions and the evolution of hydrogen gas are correlated to the structuration progress reported for Mg surfaces. These observations confirm that the surface microstructure formations result from a controlled dissolution process driven by ultrasound.

Table IV-6 Dissolution rate and H_2 maximal formation rate of Mg surfaces treated at 200 kHz (P_{ac}= 20 W, stirring, Ar, 18 ℃) for 1 hour in water, 0.01 M sodium oxalate solution, 0.001 M and 0.01 M oxalic acid solutions.

Solution	Mg dissolution rate ($\mu M.min^{-1}$)	H_2 maximal formation rate ($\mu M.min^{-1}$)
H_2O	0.8 ±0.1	0.5 ±0.1
0.01 M $Na_2C_2O_4$	5.8 ±0.3	3.6 ±0.1
0.001 M $H_2C_2O_4$	11.3 ±0.3	5.7 ±0.2
0.01 M $H_2C_2O_4$	76.7 ±2.5	31.7 ±1.1

As a function of the experimental conditions, Mg surface dissolution is accompanied with the formation and deposition of new structures on the surface of the sample. These secondary phases can be observed in **Figure IV-15**. They exhibit a spherical shape with a diameter generally comprised from few µm to around 20 µm. The experiments showed that they can be formed whatever the dissolution conditions and appear favored with the dissolution progress and an increased concentration of oxalic acid.

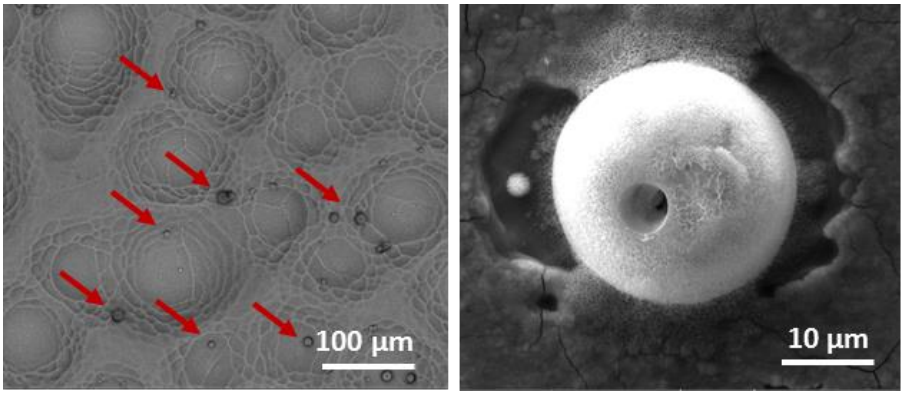

Figure IV-15 SEM observations of the secondary phases on Mg surfaces treated at 200 kHz (P_{ac}= 20 W, Ar, 18 ℃) for 1 hour in 0.01 M oxalic acid solution.

ATR-FTIR investigations carried out on a native Mg surface and other three samples sonicated at 200 kHz in pure water, sodium oxalate, and oxalic acid are summarized in **Figure IV-16**. In comparison to the original Mg sample, all of the treated surfaces exhibit a sharp IR band at 3695 cm^{-1} that can refer to the stretching band mode reported for hydroxyl groups of $Mg(OH)_2$.[232] A band standing at 1650 cm^{-1} can be observed on the three treated surfaces and can be attributed to both surface-adsorbed water, and the antisymmetric stretching vibration mode for oxalate groups.[233, 234] Furthermore, a small band observed at 1320 cm^{-1} can also be attributed to the symmetric stretching vibration of oxalate groups in

agreement with the literature.[233, 234] XRD experiments did not allow to conclude on the nature of these secondary phases present on the surface film. The entire sample showed the diffraction peaks characteristic from pure Mg.

SEM-EDX measurements performed on these secondary phases confirmed the presence of oxygen and magnesium and the absence of carbon (**Figure IV-17**). Although the presence of oxalate groups adsorbed on the Mg surface cannot be totally excluded, it is unlikely that these secondary phases be composed of magnesium oxalate. $Mg(OH)_2$ deposition on surface has been already observed by other authors and can be attributed to an alkalization effect.[150] Such phenomenon can result from the time required by species to migrate away from the surface after reaction. Mg surface can locally become more alkaline than the solution after H^+ consumption therefore resulting in the deposition of $Mg(OH)_2$ on the surface. Studies showed that local pH adjacent to the surface can be higher than 10 even in acidic solutions suggesting its formation in our conditions.[150]

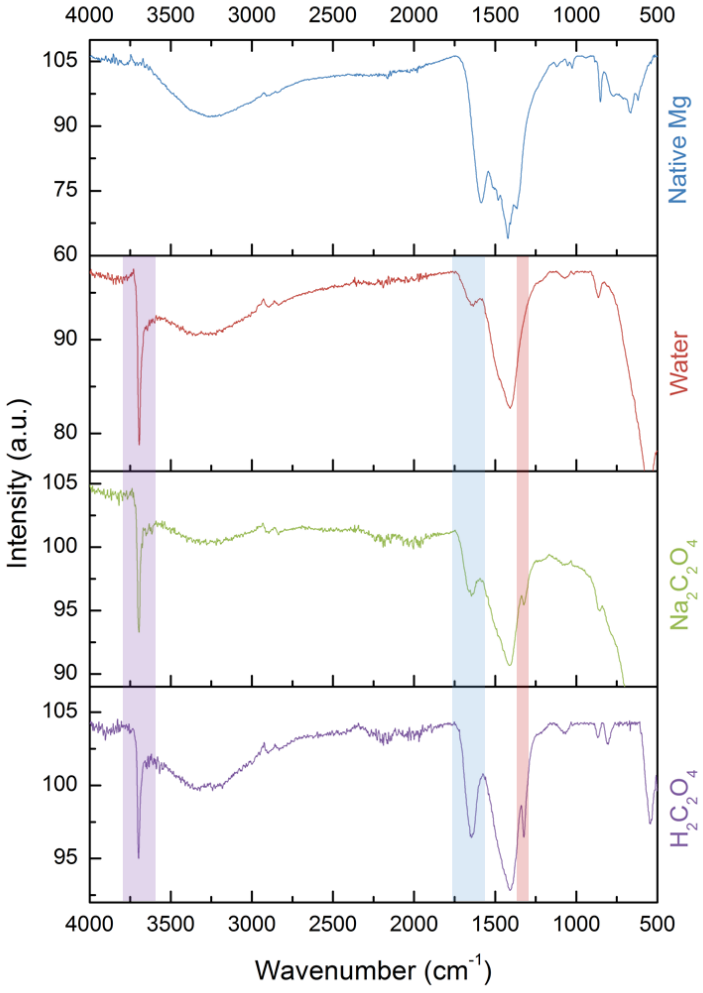

Figure IV-16 ATR-FTIR spectra of native Mg surface and of Mg surfaces treated at 200 kHz (P_{ac}= 20 W, stirring, Ar, 18 ℃) for 1 hour in water, 0.01 M sodium oxalate solution and 0.01 M oxalic acid solution.

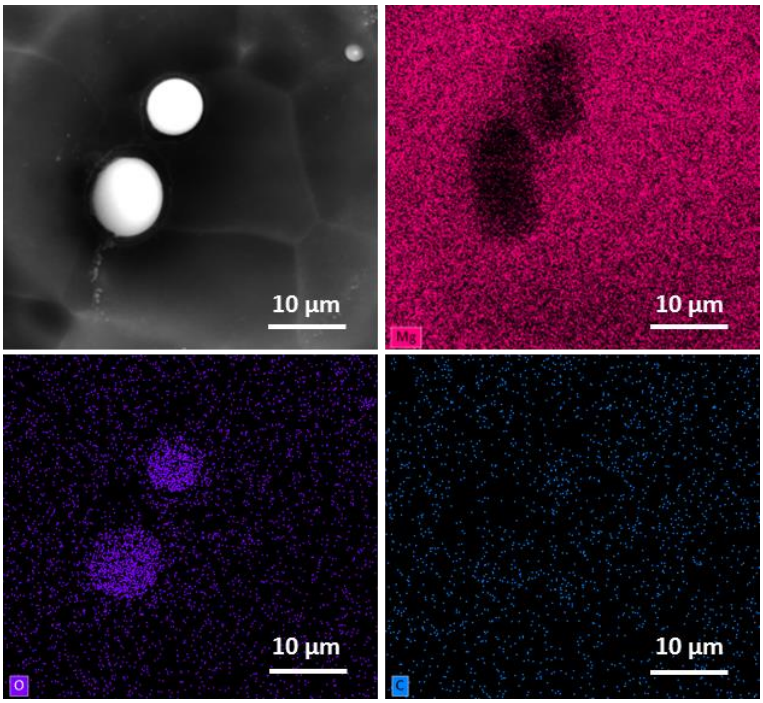

Figure IV-17 SEM-EDX analysis of secondary phases on Mg surface treated at 200 kHz (P_{ac}= 20 W for 1 hour in 0.01 M oxalic acid solution, Ar, 18 ℃). A shadowing effect can be noted on Mg map due to the position of the detector. Mg X-ray counts on the oxides are lower than bulk Mg explaining the color intensity differences for this map.

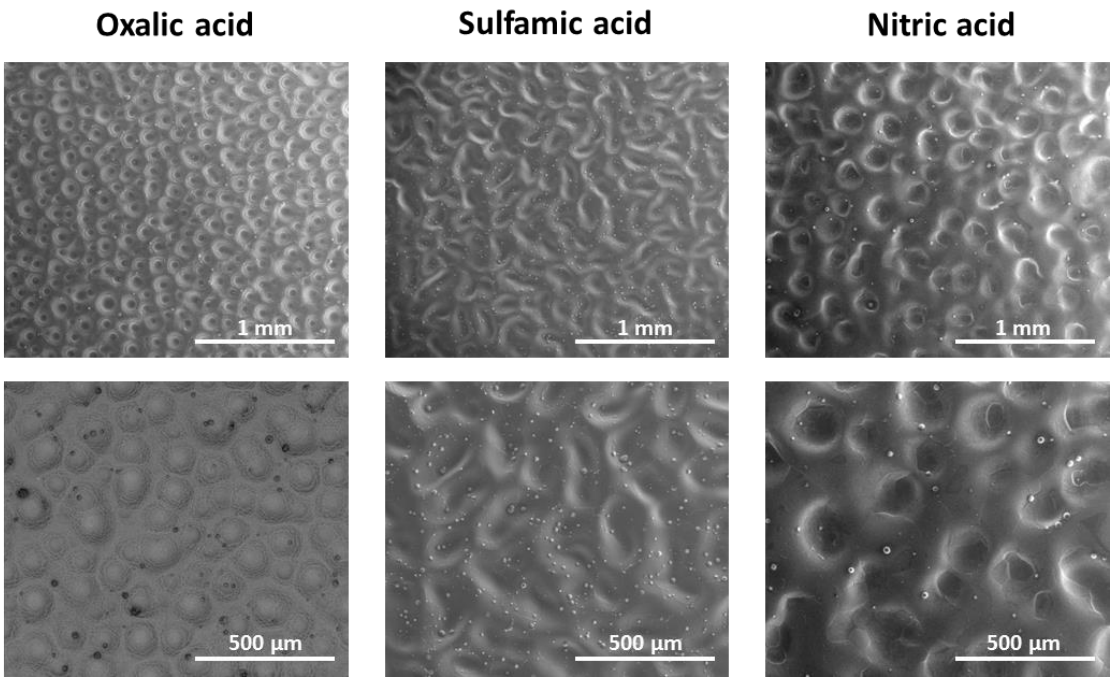

Figure IV-18 SEM observations of Mg surfaces treated at 200 kHz (P_{ac}= 20 W, stirring, Ar, 20 ℃) for 1 hour in 0.01 M oxalic, sulfamic and nitric acid solutions.

Figure IV-18 compares Mg surfaces treated by 200 kHz ultrasound during 1 h in the presence of other mineral acids. Both 0.01 M sulfamic and 0.01 M nitric acid solutions allow the formation of microstructures that can be compared to those previously described in the presence of oxalic acid. These solutions also allow the formation of craters on their surface which are nevertheless characteristic from the used mineral acid and different from what observed in oxalic acid. The nature of the counter ions appears therefore essential for the surface structuring. It is also important to note the presence of secondary phases on the surface of the various samples thus strengthening the hypothesis related to $Mg(OH)_2$ precipitation and confirming a mechanism driven by H^+ consumption.

IV.2.4 Stirring velocity effect on Mg surface sonication

In our investigation, an in-situ stirring was always applied (except for 20 kHz) to prevent the accumulation of produced gas bubbles (hydrogen) on the sample surface and favor more homogeneous sonication effects. Preliminary experiments showed the presence of bubbles during sonication that can cushion the cavitation effect and dramatically decrease the treatment efficiency. In order to identify the effect of stirring and its speed during sonication of Mg surfaces, several experiments were carried out. In **Figure IV-19**, the evolution of Mg surface dissolution in 0.01 M oxalic acid by only immersion, by 100 rpm stirring, and by sonication at 345 kHz ultrasound together with 100 rpm stirring is compared. The treatment only lasted for 30 minutes to minimize the impact of H^+ consumption.

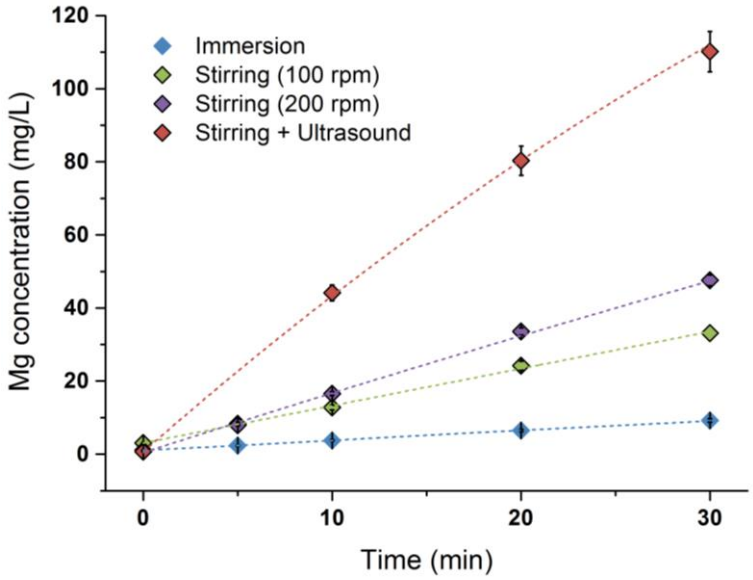

Figure IV-19 Dissolution of Mg surfaces in 0.01 M oxalic acid solution, Ar, 20 ℃ for 30 minutes by immersion, stirring (100 rpm and 200 rpm) and sonicated at 345 kHz, P_{ac}= 40 W with stirring (100 rpm).

According to **Figure IV-19**, it is obvious that Mg dissolution rate can dramatically increase in the combined presence of ultrasound and stirring. Dissolution rates follow: ultrasound + stirring > stirring > immersion. In-situ stirring accelerates Mg dissolution rate but is not as effective as ultrasound. By

increasing the stirring velocity from 100 rpm to 200 rpm, Mg dissolution rate can be slightly increased. The SCL photos of a luminol solution irradiated by 100 kHz ultrasound at different stirring speeds also confirm a more chaotic distribution of sonochemical activity at 200 rpm than at 100 rpm, which is believed to accelerate Mg dissolution (Appendix H).

IV.2.5 Evolution of Mg surfaces sonicated at 200 kHz in oxalic acid

In order to understand the mechanism of Mg surface structuration, especially the golf-ball shape crater formation process as well as the surface wettability evolution, the formation kinetics was decreased by using a more dilute (0.001 M) oxalic acid solution, a slower stirring speed of 100 rpm, and a longer sonication duration.

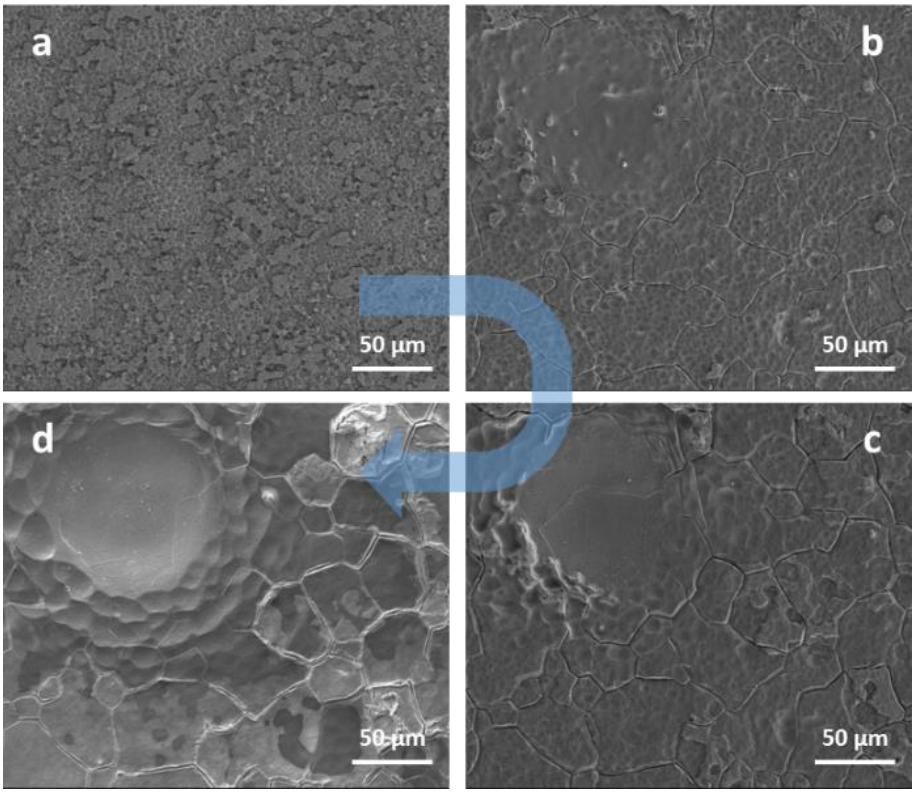

Figure IV-20 Iterative SEM observations of a crater structure formation on Mg surface treated at 100 kHz, P_{ac}= 20 W for 1.5 hours in 0.001 M oxalic acid solution (Ar, 18 ℃): a) 10 min; b) 30 min; c) 60 min and d) 90 min.

Iterative SEM pictures taken at the same position on the sample surface after ultrasound treatment intervals show the crater growth and bulk area structuring (**Figure IV-20**). In agreement with silent experiments, the microstructure evolution involves the progressive removal of the native oxide film in less than 30 min (**Figure IV-20**.a and b). After 30 min, sonication leads to grain boundary apparition superimposed with the formation of numerous intercalated tiny pits of about 5 µm forming an undulated surface typical from plastic deformation already reported in the literature.[235] By contrast to the stirred

surface under silent condition, ultrasonic corrosion is not solely occurring at grain boundaries but appears homogeneously distributed on the surface as evidenced by the presence of small corrosion pits. In **Figure IV-20**.b after 30 min treatment, it is possible to observe the outline of a crater formation with a much smoother surface in comparison to the rest of the sample. In addition, grain boundaries are far less defined inside this crater. Further sonication leads to a slight enlargement of the crater diameter as evidenced by **Figure IV-20**.c and d. Interestingly, the rest of the surface is poorly evolving suggesting that this crater is a preferential area of cavitation. This hypothesis is strengthened by the formation of smaller (5 to 20 µm) cavities surrounding the original crater after 90 minutes sonication (**Figure IV-20**.d).

At the same time, crater growth can also be accelerated by pitting corrosion, which is known as an extremely localized damage that leads to the creation of tinny pits or holes in metals. In fact, it is an autocatalytic galvanic corrosion process: a local depassivation of a small area (the exposed Mg by cavitation attack) becomes anodic and the vast areas (oxidation MgO or $Mg(OH)_2$) becomes cathodic. As presented in **Figure IV-21**, the electrochemical potential between Mg and $MgO/Mg(OH)_2$ continuously drives the galvanic corrosion, including Mg dissolution at anodes and H_2 generation besides $Mg(OH)_2$ precipitation at cathodes.[236] As a result, during this pitting process, along with cavitation, small pits are formed, which grow into large craters in the anode locations. While at the vast areas, the formed $Mg(OH)_2$ precipitation cannot remain on the surface and will dissolve in acid. Meantime the generated H_2 gas bubbles on the vast areas will also play as cavitation nuclei, which can aid the depassivation and removal of oxidation and precipitation. It is assumed that with the removal of oxidation layer on the surface, the electrical coupling between anode and cathode will become weak, thus the pitting corrosion effect will become less important.

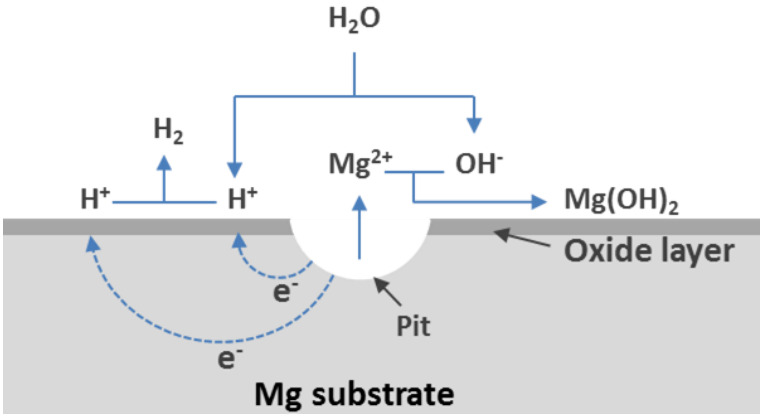

Figure IV-21 Scheme of pitting corrosion on Mg surface

Another type of crater formation mechanism can be deduced from **Figure IV-22**. Obviously, most of the deformations are located along the grain boundaries and the craters preferentially occur at the triple junctions. In this case, at beginning the grain boundaries may act as anodes and the grains as cathodes,

thus galvanic corrosion happens which involves the dissolution of Mg from the anodic grain boundaries. Those primary damages made by electrochemical erosion usually form at the vicinity of initial cracks, defects and grain boundaries, especially at the triple junctions of grain boundary where electrochemical potential is generally high.[213, 237] Meantime, those initial deformations can in turn become the nuclei of cavitation bubbles, hence enhancing the deformation and corrosion of grain boundaries and the local formation of craters, as in **Figure IV-22**.

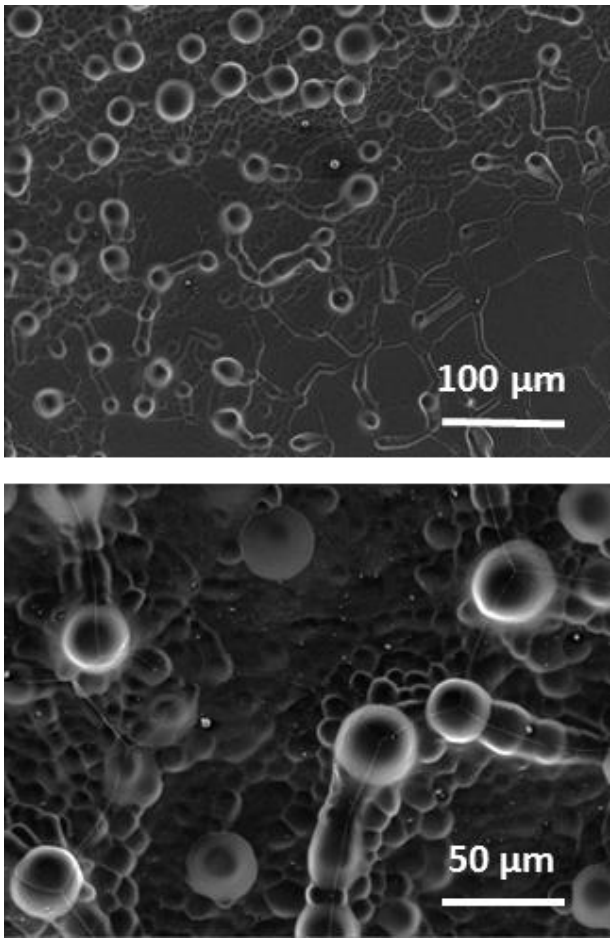

Figure IV-22 SEM observations of crater structures at grain boundaries on Mg surface treated at 345 kHz (P_{ac}= 40 W, Ar, 20 ℃) for 1 hour in 0.01 M oxalic acid solution.

In summary, the golf-ball architectures can be clearly attributed to ultrasound and its related acoustic cavitation phenomenon. The help of the initial damages from galvanic corrosion, besides the reinforcement of pitting corrosion, can also play a significant role. At the Mg/solution interface, severe transient conditions are reached during bubble collapse involving, among other phenomena, the formation of shock waves and micro-jets that have been already pointed out during erosion and structuration studies.[27, 238] Pure magnesium exhibits a hardness comprised between 44 and 260 MPa.[222] Micro-jets are likely to be formed in the vicinity of solid surfaces and then directly imping the surface with a peak pressure estimated at about 225 MPa.[239] Shock waves generated by the spherical collapse

of acoustic bubbles may have an impact pressure ranging from 1 to 10 GPa.[32, 239] These events are known to dramatically decrease diffusion layers and increase surface erosion, grain fracturation, and mass transfer. Small plastic deformations observed on the main surface can in consequence result from a combination of micro-jet impingement and chemical dissolution (such observations were not reported during Mg surface sonicated in pure water).

According to SEM investigations, the formation of the craters is assumed to result from a localized and favored dissolution area that can be attributed to heterogeneous nucleation for electrochemical corrosion and cavitation bubbles. Nucleation for electrochemical reactions always has a high electrochemical potential such as surface scratches, particles of a second phase emerging on the metal surface, dislocations and grain boundaries. Nucleation of bubbles partly coincides with that of electrochemical corrosion, and may indeed be promoted by the presence of weak points (grain boundaries), surface defects and dissolved gases at the solid/liquid interface.[50, 120, 240] Local differences in surface energy (hydrophobic/hydrophilic balance) may also play a significant role in such processes as showed for instance by Belova et al.[186, 241] Mg is a very reactive material which can release H_2 gas bubbles due to local oxidation or dissolution. Such gas generation in combination to ultrasonically-induced surface defects favors the nucleation of acoustic bubbles that may implode in turn at the vicinity of their formation sites. This phenomenon has been already noticed during the sonication of extended glass,[32] aluminum and silicon surfaces.[50, 240] All of these factors drive the initial damages and the following formation of craters on the sonicated Mg surfaces.

IV.2.6 Sonication of Mg-Zr surfaces

In addition to pure Magnesium, Mg-Zr alloys (0.5 wt.%) were studied as models or surrogates of the real Mg-Zr cladding material. Same experimental conditions as that of Mg surfaces were selected for Mg-Zr surfaces except the ultrasonic frequency: 345 kHz. Considering the similar surface structuration and dissolution rates for 200 and 345 kHz in the sonication of Mg samples, we believed that the discrepancy caused by different frequencies is insignificant in this range.

IV.2.6.1 Characterization of native Mg-Zr surface

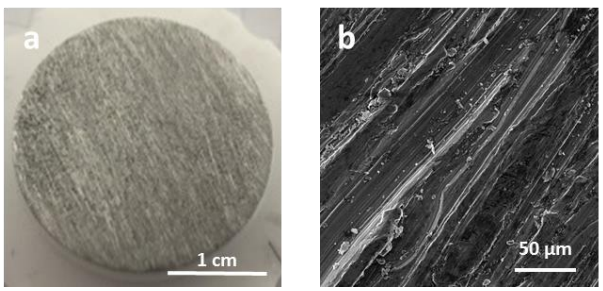

Figure IV-23 Photo and SEM observation of a native Mg-Zr surface.

The native Mg-Zr samples show a homogeneous distribution of initial oriented scratches on their surface (**Figure IV-23**) which can be attributed to material fabrication process. The metallic silver color is indicative of a low oxidation of Mg-Zr surface. The chemical composition of a native Mg-Zr surface analyzed by EDX is listed in **Table IV-7**.

Table IV-7 Chemical composition of a native Mg-Zr surface by EDX analysis.

Element	**Mg**	**Zr**	**O**	**C**
wt %	85.3 ±4.6	-	13.2 ±2.0	1.5 ±0.3

In contrast to pure Mg, EDX analysis of Mg-Zr surface exhibits a higher magnesium and lower oxygen content which is consistent with its apparent lower oxidation. Addition of Zr in Mg alloys can significantly refine the grain size, and as a result, improve the corrosion resistance. [41] At the same time, all of the Mg-Zr samples were stored in sealed plastic bags which can also slowdown surface corrosion.[217] Zirconium element was not detected in these samples most probably because of its very low amount coupled to the sensitivity of EDX detector.

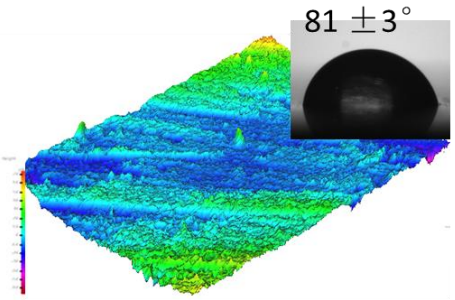

Figure IV-24 3D reconstruction of a native Mg-Zr surface (insert: image of water contact angle).

Without the existence of a thin oxide layer, surface roughness of Mg-Zr samples mainly presents initial scratches resulting in a much higher roughness (R_a= 271.2 nm and R_z= 1.31 µm) than what observed for pure Mg (Ra= 61.1 nm and R_z= 328.4 nm). The contact angle of Mg-Zr surface is small with a value of 81 ±3 °(against 120 ±4 °for pure Mg).

IV.2.6.2 Mg-Zr surface sonication at 345 kHz in oxalic acid

Similarly to pure Mg samples, Mg-Zr surfaces were sonicated (345 kHz, P_{ac}= 40 W) in 0.01 M oxalic acid. The photo and SEM pictures presented in **Figure IV-25** show the formation of an dense distribution of craters (30 to 40 µm diameter) in these conditions. According to 3D reconstruction (**Figure IV-26**), the denser craters on the sonicated Mg-Zr surfaces leads to a much higher roughness (Ra= 370.9 nm and Rz= 1.79 µm) in comparison to the sonicated pure Mg (Ra= 211.5 nm and Rz= 605.5 nm). According to Cassie–Baxter model, a higher roughness brings a larger contact angle, which is consistent with the difference observed between the sonicated Mg (about 100 °) and Mg-Zr surfaces

(about 110 °). Note that in these conditions, the initial scratches present on the surface may act as nuclei for cavitation and starting sites of electrochemical corrosion, and therefore accelerate the formation of crater structures on Mg-Zr surfaces.

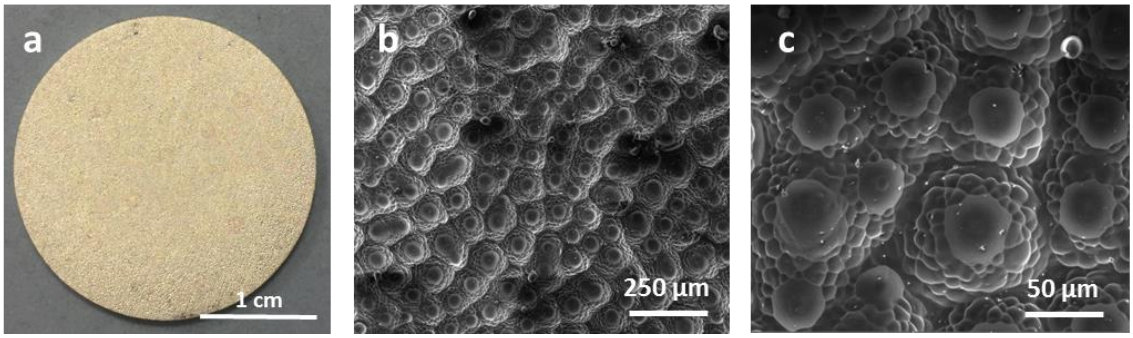

Figure IV-25 Mg-Zr surface treated at 345 kHz, P_{ac}= 40 W, stirring for 1 hour in 0.01 M oxalic acid solution (Ar, 20 °C): a) photo; b) and c) SEM observations.

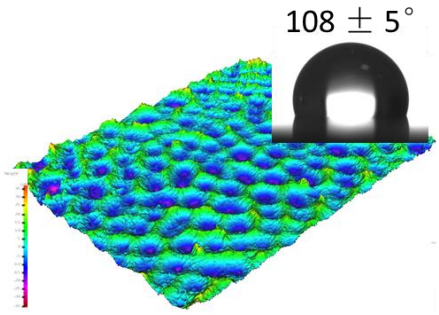

Figure IV-26 3D reconstruction of Mg-Zr surface treated at 345 kHz, P_{ac}= 40 W for 1 hour in 0.01 M oxalic acid solution (Ar, 20 °C). The insert is an image of the water contact angle.

In dilute 0.001 M oxalic acid, Mg-Zr surface modification is slow in agreement with the observation made on pure Mg surface. As shown in **Figure IV-27**, the measured contact angle rapidly decreases in the first 10 minutes and then remains at about 45 ° during approximately 60 minutes. After 75 minutes sonication, Mg-Zr surface contact angle starts to rise again and reaches 80 ° after 2 hours of treatment. This evolution trend again confirms the strong correlation between the formation of craters and surface wettability.

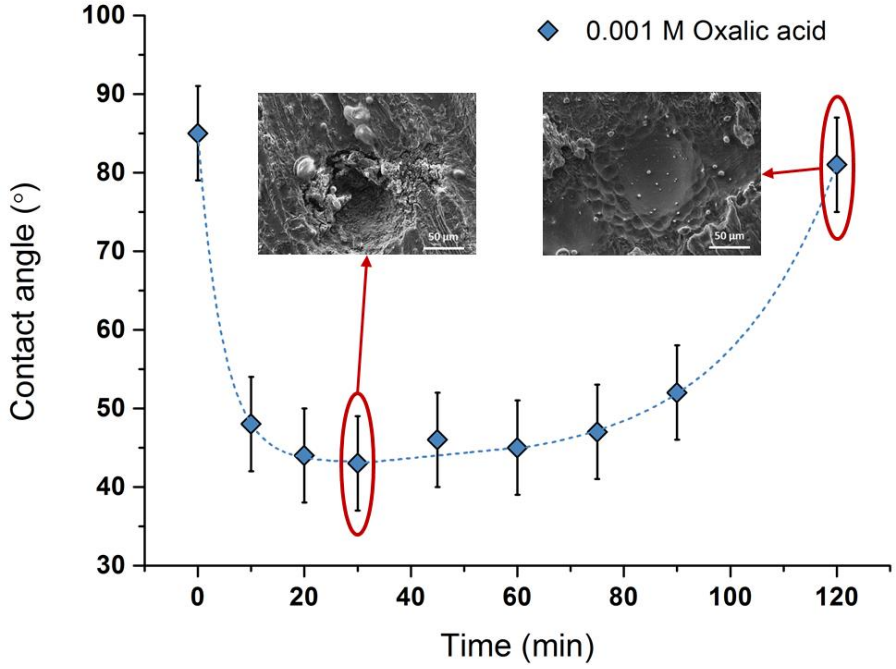

Figure IV-27 Mg-Zr surfaces treated at 100 kHz, P_{ac}= 20 W, stirring, Ar, 20 ℃ for 2 hours in 0.001 M oxalic acid (insert: SEM images at 30 minutes and 2 hours).

IV.2.6.3 Secondary phase

Secondary phases with different sizes and shapes are also found to be distributed on Mg-Zr surface after sonication in agreement with what observed on pure Mg with however different features (**Figure IV-28**). Mg/Zr samples allow the observation of big aggregates around poorly dissolved regions (**Figure IV-28**.a) while regions with high concentration of craters (**Figure IV-28**.b) show the presence of spherical particles having a smaller size (less than 10 µm diameter). The chemical identification of the two SEM images in Figure IV-28, made by EDX analysis, is listed in **Table IV-8**.

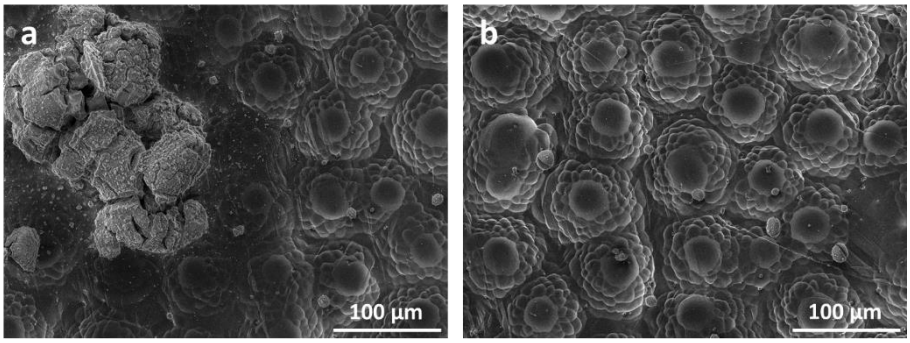

Figure IV-28 Mg-Zr surface treated at 345 kHz, P_{ac}= 40 W for 1 hour in 0.01 M oxalic acid solution, Ar, 20 ℃: a) zone with secondary phase; b) zone without secondary phase.

Table IV-8 Chemical composition of Mg-Zr surface treated at 345 kHz, P_{ac}= 40 W for 1 hour in 0.01 M oxalic acid solution, Ar, 20 ℃, by EDX analysis.

	element	**Mg**	**Zr**	**O**	**C**
wt %	region a	31.3 ± 2.7	2.4 ± 0.3	59.3 ± 4.4	7.0 ± 0.5
	region b	80.7 ± 5.6	0.8 ± 0.1	13.5 ± 2.1	5.0 ± 0.5

In the area of concentrated craters (**Figure IV-28**.b.), the chemical composition is very close to Mg-Zr alloys with a low content of oxygen, which indicates a very limited oxidation of the surface. By contrast the area exhibiting the larger secondary phase (**Figure IV-28**.a.), the oxygen content is much higher and Zr amount is high in this area. It is assumed that localized galvanic corrosion can contribute to the formation of these secondary phases. In this case, Zr may act as a cathode and Mg as an anode.[242] Precipitation, including Mg hydroxides and oxides, can then occur and accumulate at the cathode site where Zr is initially rich.[2, 243] This phenomenon is also involved by ultrasound.

IV.2.6.4 Mg-Zr dissolution

Figure IV-29 compares the evolution of Mg concentration in 0.01 M oxalic acid solution during the sonication at 345 kHz of pure Mg and Mg-Zr surfaces. A much higher Mg initial dissolution is observed compared to **Figure IV-12**, since the acoustic power here is double in comparison to that at 200 kHz with pure Mg surfaces. The total concentration of dissolved Mg in solution after 1 hour sonication is approximately the same for pure Mg and Mg-Zr surfaces, while the dissolution rate during the first 10 minutes is higher for Mg-Zr sample. This can be attributed to the lower oxidation and the initial scratches on Mg-Zr surface which may accelerate Mg corrosion and dissolution in the beginning. However, the galvanic corrosion between Zr-Mg electrical couple does not seem to contribute much to the dissolution of Mg-Zr surface.

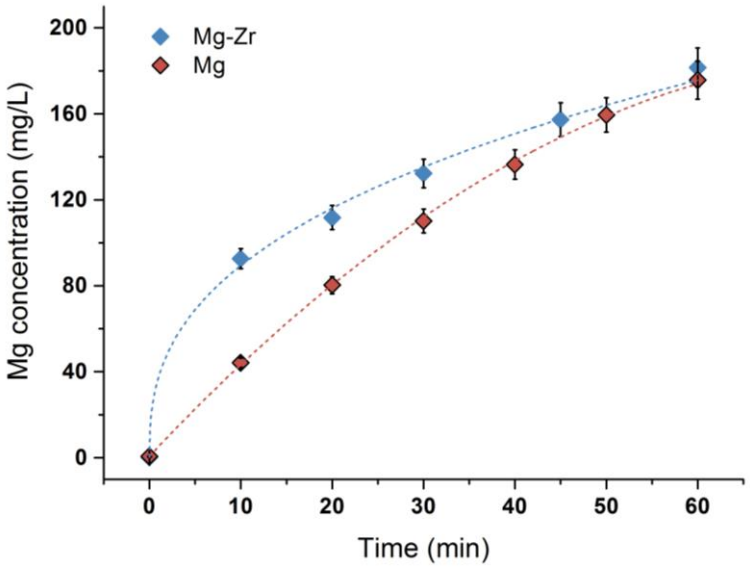

Figure IV-29 Dissolution of pure Mg and Mg-Zr surfaces treated at 345 kHz, P_{ac}= 40 W, stirring, Ar, 20 ℃ for 1 hour in 0.01 M oxalic acid solution.

IV.3 Conclusion

This chapter clearly demonstrates that ultrasound can significantly modify an extended surface and participate, in combination to an appropriate solute, in the formation of an original and unprecedented microstructure. Golf-ball shape microstructures are observed on pure Mg surfaces after sonication at 100 to 345 kHz in dilute oxalic acid, and big holes and undulations channels are present at 20 kHz, while no specific microstructure but a flat surface with grain boundaries appears on surface treated at 1 MHz. The accumulation of Mg^{2+} in solution combined to the generation of H_2 gas during treatment confirm the ultrasound-controlled dissolution of metallic Mg.

An original approach resulting in the 3D reconstruction of sonicated surfaces allows to investigate the formation mechanism of these extended surfaces. The formation of microstructures is convincingly correlated to the chosen acoustic frequency, the proton activity and the nature of the counter ions. Most probably, ultrasound allows the generation of surface defects which are then used as nucleation sites that favor the crater formation. The craters may increase in diameter and depth with sonication time with heterogeneous nucleation. In addition, pitting corrosion is assumed to be involved in the growth of craters. H_2 gas release in the localized area may also be used as nucleation for cavitation. The sonicated surface wettability is also found to be strongly correlated to the formation of craters, and a high hydrophobicity is expected with a surface covered by a homogeneously formed craters.

Dissolution progress is found to be accompanied by the formation of new spherical micrometric structures formed on the Mg surface and attributed to $Mg(OH)_2$. The formation of these secondary

phases is most probably related to local alkalization effect induced by Mg dissolution and is found to be lowered under ultrasound in comparison to conventional dissolution procedure.

Such observations open new routes of investigation for other alloy and metal-based materials and new alternatives of potential interest for applications in many fields including industry, medicine, and nanotechnology. For example, this golf-ball shape structure can be of potential interest for biomedical materials where wettability properties are required to improve the adhesion of surface coatings.

The results observed with Mg-Zr surfaces are very close to that of pure Mg, which indicates that both pure Mg and Mg-Zr alloy can be used probably as good surrogates for reals UNGG claddings. The ultrasonic decontamination effects on the contaminated pure Mg, Mg-Zr alloy and UNGG cladding fragments are investigated and discussed in the next chapter.

In addition, at the frequency of 345 kHz, an inhomogeneous erosion distribution is observed on the sonicated Mg surfaces in repeated experiments. The pattern of the treated surfaces presents a series of concentric pentagons where the crater structures are concentrated in certain areas: either on the corners or on the side of pentagons (see **Figure IV-30**). Such cymatical star shape is very similar to the observations of the standing gravity waves on silicon oil surface by vertically vibrating the container at a very low frequency of 8 Hz.[244] It was found that this specific star shape is dependent on the vibrational amplitude and frequency. It will be of great interest for future study to understand the formation mechanism of this structure by using experimental probes and simulation methods, especially in the case of high frequency ultrasound.

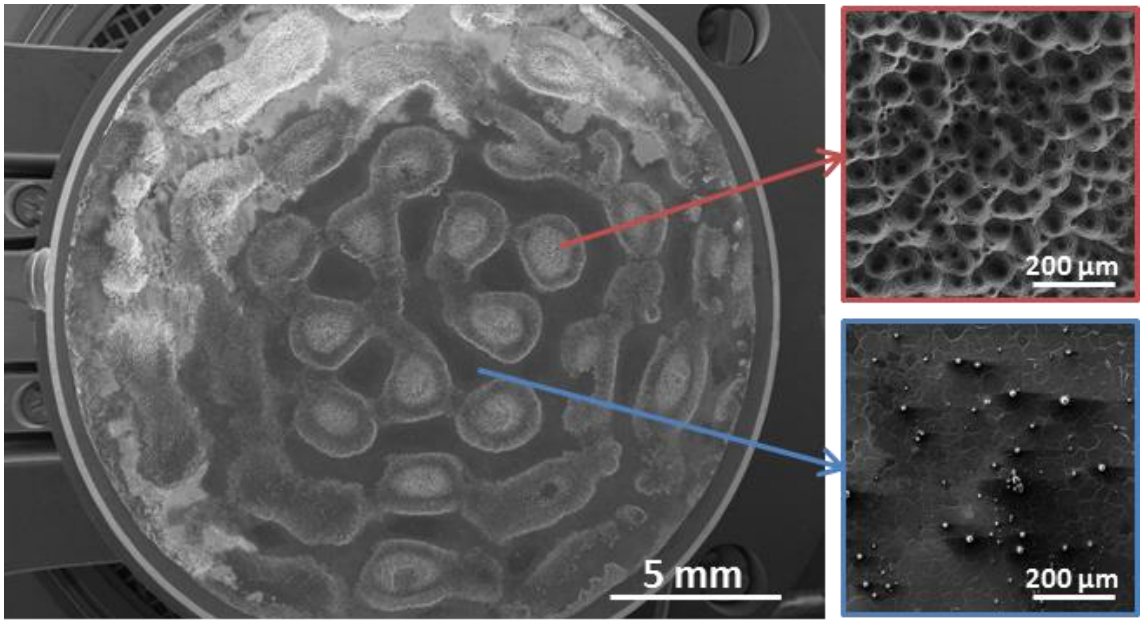

Figure IV-30 SEM observations of Mg surface treated for 1 hour in 0.01 M oxalic acid solution, (Ar/(20 vol.%)O_2, 20 ℃, stirring 100 rpm) at 345 kHz P_{ac}= 40 W.

Chapter V. Metallic surface decontamination by ultrasound

V.1 Introduction

This chapter is dedicated to the application of power ultrasound at 345 kHz in the decontamination of metal surfaces contaminated by uranium. The treatment of two different types of contaminated materials is discussed: i) Mg-based surfaces, including pure Mg, Mg-Zr alloy surrogates and genius but non-irradiated UNGG cladding fragments; ii) stainless steel, which is widely used in nuclear industry, and is here studied to evaluate ultrasonic application in another material field. Uranium contaminants on the as-prepared samples surfaces are characterized by XRD, ATR-FTIR and Raman spectrometry. For Mg-based material, only dilute oxalic acid is used, and the decontamination effect on a complex geometry Mg sample is compared with disc samples. Stainless steel surfaces are treated in both dilute oxalic acid and strong nitric acid. The decontamination effect is determined by the evolution of surface morphology (photos and SEM images) and α radioactivity.

V.2 Mg based material surfaces decontamination by ultrasound

V.2.1 Characterization of UNGG cladding material and the contaminates on Mg based surfaces

V.2.1.1 UNGG cladding material

Figure V-1.a shows both the external fin side and internal graphite side of a non-irradiated UNGG cladding tube fragment that was used during this study. SEM pictures related to the outer side characterization of the cladding tube is present in **Figure V-1**.b. Two distinct grey levels can be noticed on these figures. EDX analyses carried out in the bright zone evidence a local enrichment of Zr up to ~3 wt.% while approximately 0.5 wt.% are measured in the surrounding dark area which is consistent with the literature.[162] The bright zones present elongated shapes that can be attributed to the precipitation of metastable Mg-Zr solid solutions during the controlled annealing in fabrication process.[245] Such structure is believed to improve the ductility of Mg alloys by reducing the nucleation, growth and coalescence of cracks and voids at grain boundaries.[246, 247] A similar morphology was observed on Magnox ZR55 alloys (0.45 - 0.65 wt.% Zr) and aluminum alloys.[148, 248] In general, about 35 wt.% oxygen and 15 wt.% carbon were detected on the Mg substrates possibly indicating a complex oxidation layer composed of MgO, $Mg(OH)_2$ and $MgCO_3$ which is in agreement with the previous EDX analysis of the oxidation layer on pure Mg. The presence of carbon may also come from the exfoliated graphite particles observed on the internal side of the cladding.

On the other side of UNGG cladding tube, a graphite barrier named aquadag (described in Chapter Chapter I) is coated on the inner surface. **Figure V-1**.c allows the observation of graphite particles of black color and irregular shapes distributed on the surface. According to EDX analyses, more than 70 wt.% of carbon is composing the black areas. The less dark surrounding areas, which probably result from the peel off of graphite coating, still contain about 30 - 40 wt.% carbon. The oxidation of the graphite particles (oxygen ~20 wt.%) is not as important as it is observed on the less dark surrounding areas (oxygen ~50 wt.%).

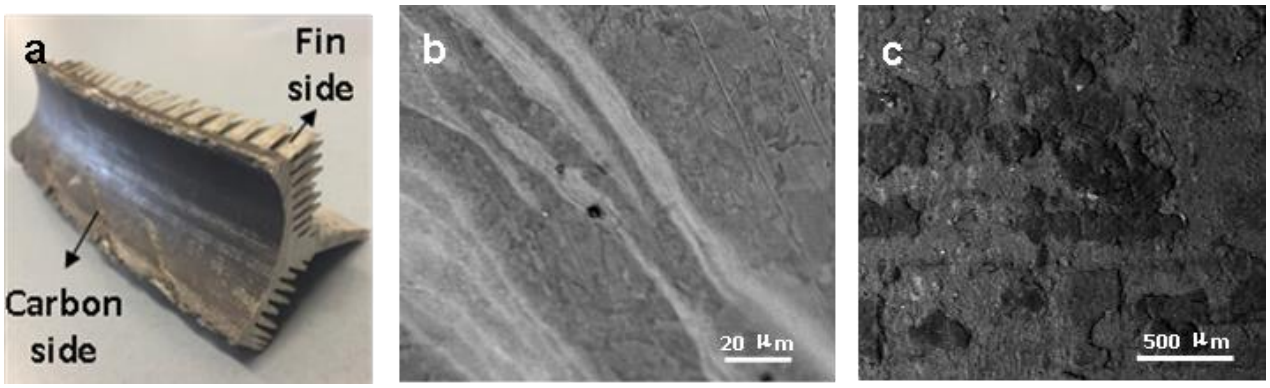

Figure V-1 Non-irradiated UNGG cladding tube fragment: a) photo; SEM BSE images of b) fin side and c) carbon side.

X-ray diffraction, Raman spectroscopy and FTIR spectroscopy were used to verify the observations carried out with SEM and EDX spectroscopy on the UNGG cladding fragments. The analysis results are presented in **Figure V-2** to **Figure V-5**.

According to the XRD pattern showed in **Figure V-2**, it is clear that the fin side surface is mainly composed of magnesium. Several peaks in the pattern can be correlated to MgO and $Mg(OH)_2$ with however a weak intensity though these UNGG cladding material has been stored for decades of years under aerobic atmosphere. This observation evidences the good corrosion resistance of Mg-Zr alloys under ambient environment.

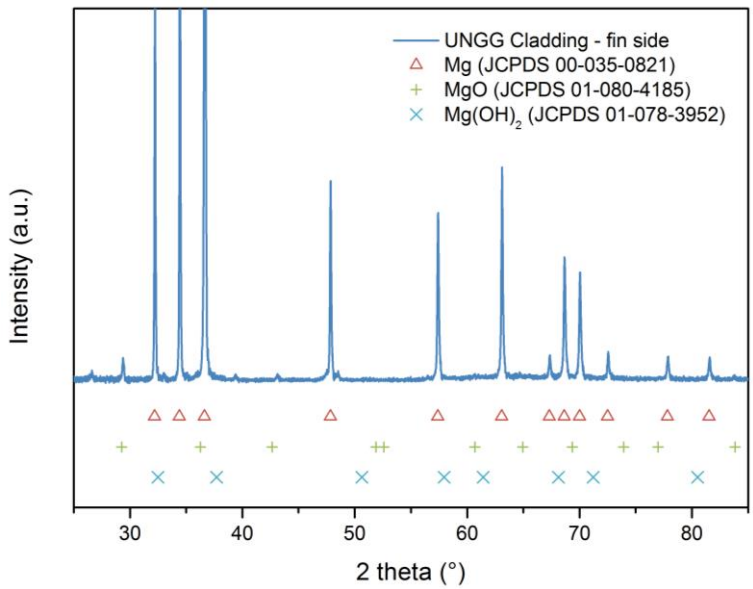

Figure V-2 X-ray diffraction pattern of the outer side (fin side) of a non-irradiated UNGG cladding tube fragment, in comparison with standard patterns of Mg JCPDS 00-035-0821, MgO JCPDS 01-080-4185 and Mg(OH)2 JCPDS 01-078-3952).

XRD investigations shown in **Figure V-3** confirm that the majority of the inner part of the cladding material is covered by carbon and magnesium hydroxides. Most probably, magnesium observation results from the partial stripping of the graphite coating. The hydroxylation of UNGG cladding carbon side is found to be more significant than what observed on the fin side which may be due to the galvanic corrosion between electrical couples of graphite and exposed substrate of Mg on the internal surface.

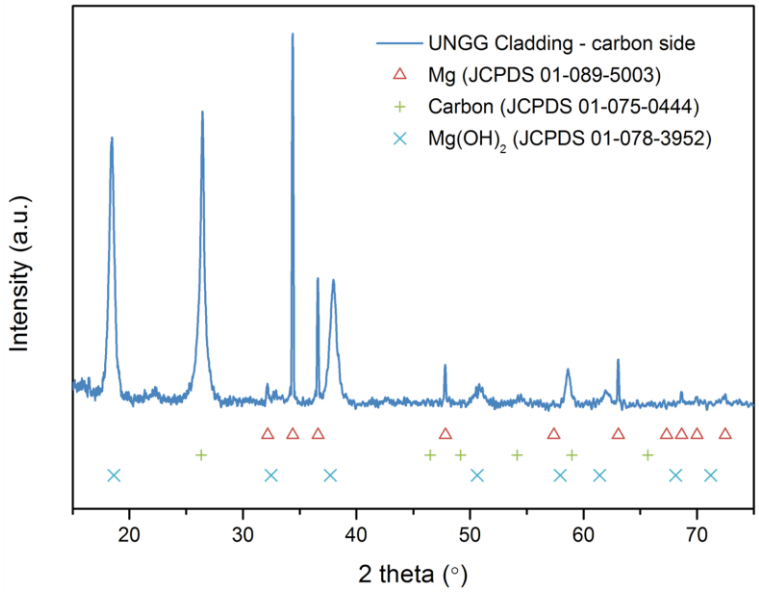

Figure V-3 X-ray diffraction pattern of the inner side (carbon side) of a non-irradiated UNGG cladding tube fragment, in comparison with standard patterns of Mg JCPDS 01-089-5003, carbon JCPDS 01-075-0444 and Mg(OH)2 JCPDS 01-078-3952).

The infrared spectra showed in **Figure V-4** are found to be in agreement with XRD analyses. On the fin side surface, both hydroxyl and organic groups (C-O, C=O and C-O-C), besides Mg-O and Mg-O-C bands exist; while for carbon side, the hydroxyl and Mg-O bands are not observed. Raman spectra presented in **Figure V-5** are in agreement with the observations noticed on XRD patterns and infrared spectra: on the UNGG cladding external fin surface, chemical compositions of metal magnesium and its hydroxides are detected; while only graphite bands are identified by Raman spectrometer on the carbon side (bands information in Appendix I).

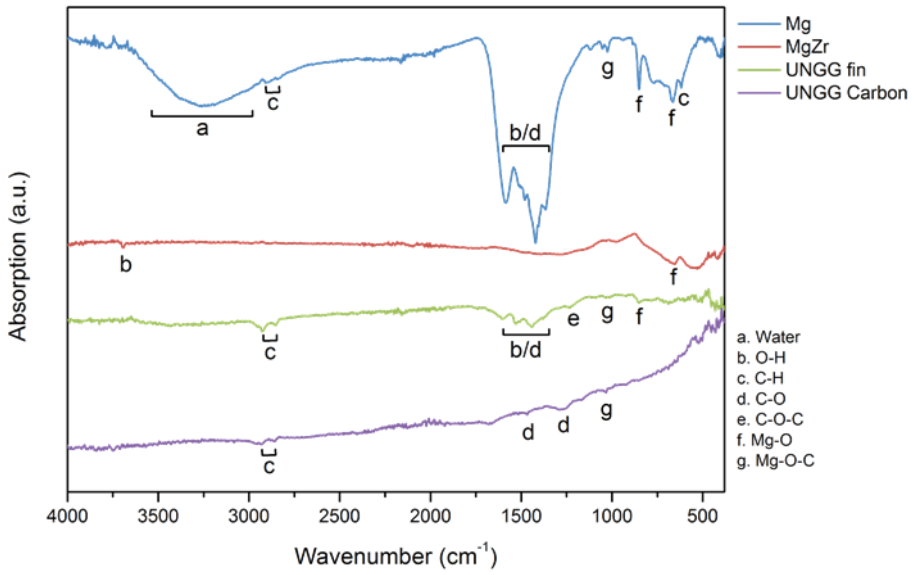

Figure V-4 FTIR spectra of a non-irradiated UNGG cladding tube fragment (fin side and carbon side), and non-contaminated areas of as-prepared pure Mg and Mg-Zr samples

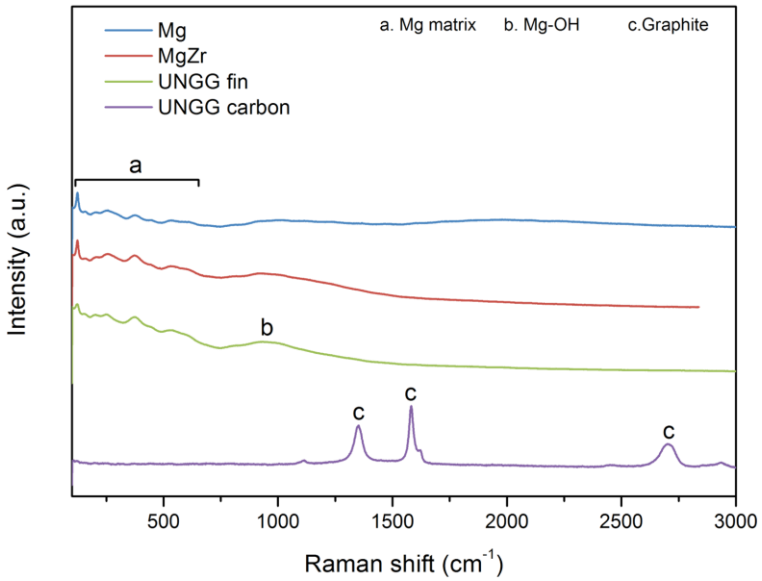

Figure V-5 Raman spectra of a non-irradiated UNGG cladding tube fragment (fin side and carbon side), and non-contaminated area of as-prepared pure Mg and Mg-Zr samples.

To be noted here, the vibration band situated at 1580 cm^{-1} refers to crystalline graphite (G), and the vibration band at 1350 cm^{-1} to crystalline defects or disorder (D) in graphite structure. The ratio between D and G band intensities indicates the degree of disorder in graphite crystals and is found to be inversely proportional to the average graphite crystalline size L_a:[249]

$$L_a = 2.4 \times 10^{-10} \times \lambda_{laser}^4 \times I_G/I_D \quad \text{(V-1)}$$

Where λ_{laser} is the incident laser beam wavelength, I_G and I_D are the intensities of D and G bands. With values of $\lambda_{laser} = 532$ nm and $I_G/I_D = 0.754$, the crystal size of the graphite particles coated on the UNGG cladding internal side can be calculated to be approximately 14.5 nm.

Generally, UNGG cladding fragment shows the chemical compositions of Mg matrix and an oxidations (MgO, $Mg(OH)_2$ and $MgCO_3$) on its external fin side, which is similar to that of the pure Mg and Mg-Zr alloy samples. The internal side is mainly composed of graphite, exposed Mg substrate and the produced oxidation ($Mg(OH)_2$ and $MgCO_3$).

V.2.1.2 Contaminants on Mg based surfaces and UNGG cladding material

Figure V-6 illustrates the morphology of Mg-Zr sample used as an example which was contaminated according to the procedure described in materials and methods. Uranyl contamination is present as large exfoliated and polydispersed micrometric particles (from 20 µm to 500 µm) adhering to the metallic surface. EDX analyses show that these contaminates are mainly composed of magnesium (~35 wt.%), oxygen (~25 wt.%) and uranium (~40 wt.%). It is supposed that a complex non-stoichiometric $Mg_xU_yO_z$ contamination is generated on the prepared surfaces in agreement with the literature.[250]

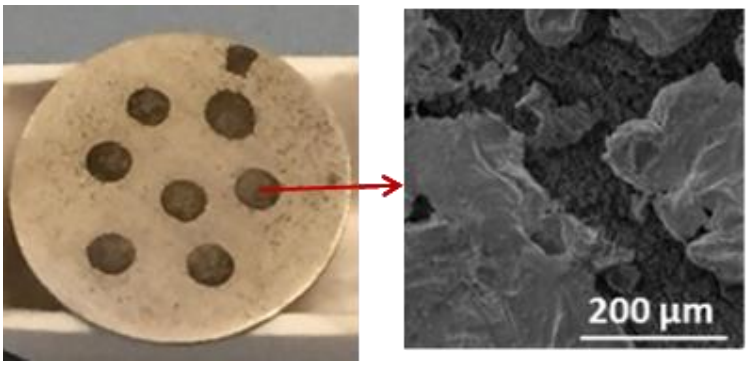

Figure V-6 Contaminated Mg-Zr surface prepared by calcination at 500 ℃ under Ar atmosphere of Mg-Zr surface on which 0.1 M $UO_2(NO_3)_2$ were homogenously deposited. The right side of the figure shows a SEM image of the contamination.

Considering the sample preparation temperature at 500 ℃, the decomposition reaction of $UO_2(NO_3)_2$ may be described by:[251]

$$UO_2(NO_3)_2 \xrightarrow{500\,^{\circ}C} UO_3(\gamma+\beta) + 2NO_2 + 1/2\,O_2 \quad \text{(V-2)}$$

Both β and γ structural forms of UO_3 can exist as decomposition products of $UO_2(NO_3)_2$. However, UO_3 is not stable at high temperature; its transformation into U_3O_8 was reported to begin from 400 ℃, but was found to be not complete until the temperature approaches about 650 ℃.[252] Reaction (V-3) shows the conversion reaction from UO_3 into U_3O_8:

$$3UO_3 \xrightarrow{400-650\,^{\circ}C} U_3O_8 + 1/2\,O_2 \quad \text{(V-3)}$$

As a result, in our sample preparation conditions, both UO_3 and U_3O_8 should exist in the contaminated areas. According to the photos of U_3O_8 and UO_3 powders illustrated in **Figure V-7**, U_3O_8 has an olive green to black color, while UO_3 displays an orange (β-UO_3) or yellow (γ-UO_3) color. Some of our contaminated samples, such as the Mg-Zr surface presented in **Figure V-7**.d, show both the black and orange colors, indicating the presence of both U_3O_8 and UO_3 oxidation products after calcination at 500 ℃ in Ar flow for 2 hours. In addition, the electropositive Mg may also reduce U^{6+} into U^{4+} or U^{3+} and leads to the formation of the non-stoichiometric $Mg_xU_yO_z$ compositions after calcination.[253] It is interesting to note that not all the sample surfaces present both colors (see for example the Mg-Zr sample in **Figure V-6**) which can be attributed to an inhomogeneous heating in the tubular oven.

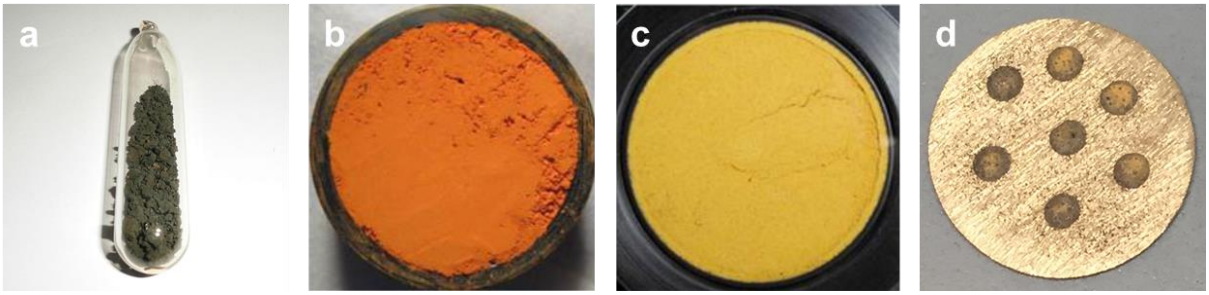

Figure V-7 Photos of: a) U_3O_8 produced by heating ammonium diuranate;[254] b) β-UO_3 powder; c) γ-UO_3 powder[255] and d) as-prepared contaminated Mg-Zr surface (0.1 M $UO_2(NO_3)_2$).

To verify the presence of UO_3, U_3O_8 and non-stoichiometric $Mg_xU_yO_z$ on the contaminated surfaces, X-ray diffraction, FTIR and Raman spectroscopies were applied. To be noticed, no significant difference between the contaminated UNGG cladding fin side, Mg and Mg-Zr alloys surfaces is observed in the XRD patterns, so as their Raman and infrared spectra. So here only the XRD result of contaminated UNGG cladding fin side and the Raman and infrared spectra of contaminated Mg-Zr surfaces are shown and discussed.

Figure V-8 shows the X-ray diffraction pattern observed on a UNGG cladding fin side surface contaminated with 0.1 M $UO_2(NO_3)_2$. The sharp diffraction peaks are attributed to Mg matrix of the non-contaminated area. Several broad peaks can also be observed on the XRD pattern and can refer to

MgU_3O_{10} and UO_3. U_3O_8 standard pattern is not present here, since it is almost coincident with the UO_3 pattern (see **Figure V-23**).

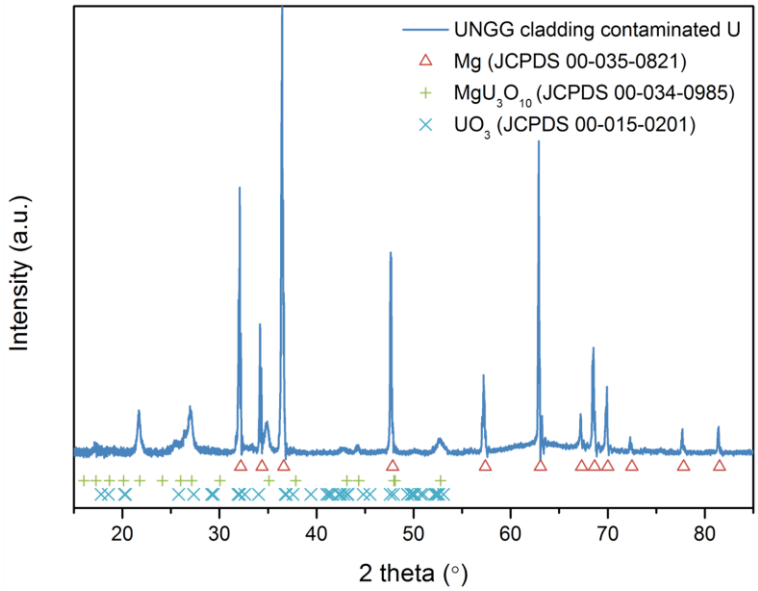

Figure V-8 X-ray diffraction pattern of the fin side of a UNGG cladding tube fragment contaminated with 0.1 M $UO_2(NO_3)_2$ in comparison with standard patterns of Mg (JCPDS 00-035-0821), MgU_3O_{10} (JCPDS 00-034-0985) and UO_3 (JCPDS 00-015-0201).

In fact, XRD is not that sensitive for detecting the phases of UO system and for determining the ratio of U/O.[256] To better identify the black and orange contaminations on surfaces, different spots on surfaces were analyzed by FTIR and Raman spectroscopies (**Figure V-9** and **Figure V-10**).

Figure V-9 shows the FTIR spectra of a contaminated Mg-Zr surface; the low wavenumber region of the spectra (< 2000 cm^{-1}) for the two different color spots on surface consists of several peaks assigned to O-H, C-O, C-O-C, C=O, Mg-O, Mg-O-C, UO_3 and U_3O_8. No vibration band characteristic from UO_3 is observed in the black contaminated spots, while both UO_3 and U_3O_8 bands are noted in the orange spots (bands information in Appendix I).

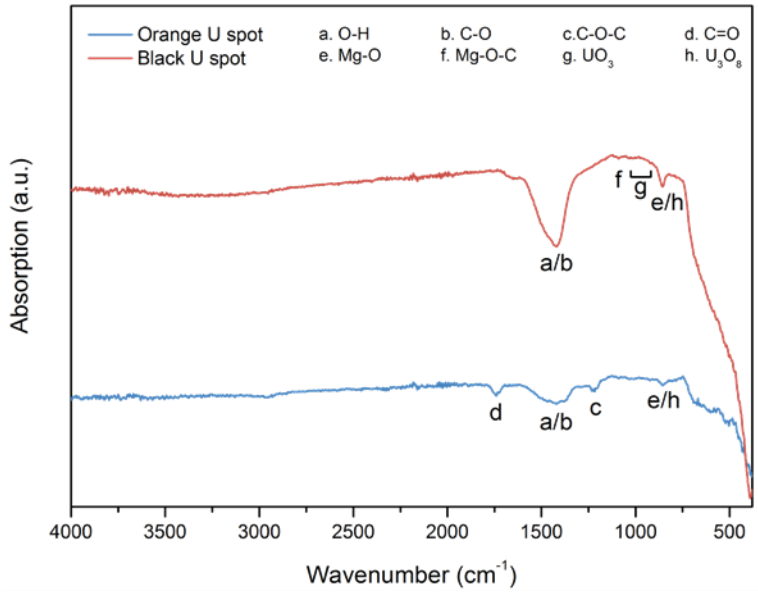

Figure V-9 FTIR spectra of as-prepared contaminated Mg-Zr (0.1 M $UO_2(NO_3)_2$)

According to the Raman spectra presented in **Figure V-10**, the black spot observed on the contaminated Mg-Zr surface exhibits two significant vibration bands at around 125 cm^{-1} and 735 cm^{-1}, which are associated with U_3O_8. The other strong band at 265 cm^{-1} and two weak intensity bands at 360 cm^{-1} and 500 cm^{-1} are related to UO_3 and non-stoichiometric $Mg_xU_yO_z$ or U_xO_y. For the orange contaminant spot, several weak bands indicate a mixture of UO_3, U_3O_8 and non-stoichiometric $Mg_xU_yO_z$ or U_xO_y complex contamination (bands information in Appendix I).

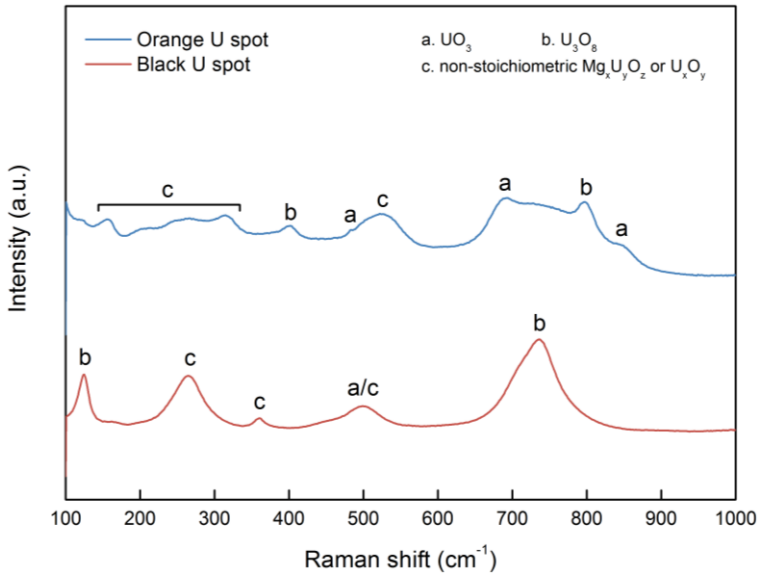

Figure V-10 Raman spectra of as-prepared contaminated Mg-Zr (0.1 M $UO_2(NO_3)_2$)

In summary, Mg based material (pure Mg and Mg-Zr alloy) and UNGG cladding fragment (external surface) contaminated with uranyl nitrate using our experimental conditions (500 ℃ for 2 hours under

Ar atmosphere) allows the observation of a mixture of UO_3, U_3O_8 and non-stoichiometric $Mg_xU_yO_z$ or U_xO_y.

V.2.2 Ultrasonic decontamination results

V.2.2.1 Decontamination of Mg-based surfaces and UNGG cladding material

V.2.2.1.1 Decontamination of Mg-Zr surface

Both Mg and Mg-Zr surfaces contaminated with uranyl nitrate were sonicated by 345 kHz ultrasound in 0.01 M oxalic acid solution with an in-situ stirring of 100 rpm. A decontamination procedure was also applied as reference in similar conditions but without ultrasound. The decontamination kinetics of Mg-Zr surfaces was characterized with α-spectroscopy (an example of the measured α spectra in Appendix J) and SEM microscopy after 90 minutes of treatment. The results obtained under ultrasound and silent conditions are illustrated in **Figure V-11** and 错误!未找到引用源。.

From the pictures given in **Figure V-11**, some residual contamination areas (dark zones) are still visible on the Mg-Zr surface after treatment under silent conditions while ultrasonic treatment visually allows the complete decontamination of the surface. In agreement with the preliminary studies reported for non-contaminated Mg-Zr samples in this manuscript, the oxidation layer of the material is completely removed under sonication. We can also clearly notice the presence of “golf ball” shape craters in agreement with previous observations (with similar shape and size). Under stirring only, it is interesting to note that some residual contaminates are still observed for some areas in addition to the initial oxidation. According to EDX analyses, the ultrasonic decontamination leads to less than 2 wt.% uranium left at the initial contaminated spot after 90 minutes treatment, which is much more efficient than that observed under only stirring in the same conditions (about 35 wt.% uranium residue).

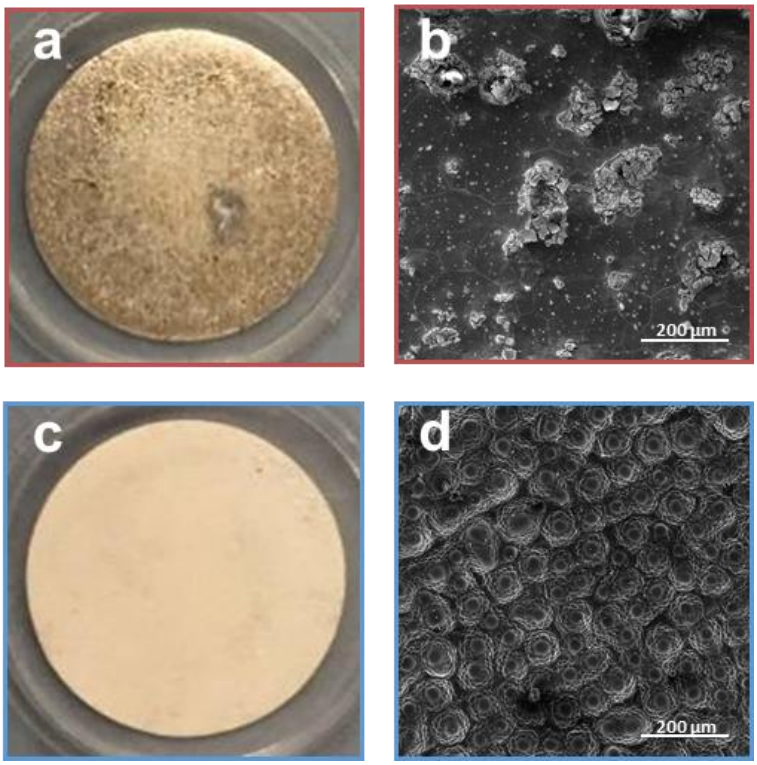

Figure V-11 Photos and SEM images of Mg-Zr surfaces contaminated with U (0.1 M $UO_2(NO_3)_2$) decontaminated under silent conditions (a and b) and by 345 kHz ultrasound, P_{ac}= 40 W (c and d) in 0.01 M oxalic acid, Ar, stirring 100 rpm, 20 ℃, 90 min

According to **Figure V-12**, Mg-Zr surface radiation level decreases linearly under silent conditions with a final DF equals to 3.2. By contrast, ultrasonic decontamination leads to a rapid radioactivity drop within the first 20 minutes with a maximum DF equals to 133 which is 40 times higher than what observed under silent conditions. After 20 min of sonication, a slow increase of the radioactivity can be noticed reaching 5.6 Bq after 90 minutes sonication. The rapid decrease of the surface radioactivity within the first 20 minutes can be attributed to the strong diffusion and mass transfer driven by acoustic cavitation phenomenon at the interface between the contaminated surface and the acidic solution (microjets, shockwaves and microstreaming). Such ultrasonic process is known to significantly accelerate the chemical reaction rates and mechanical damages on the contaminated surfaces, hence improving the decontamination efficiency. Previous decontamination tests performed at Beloyarsk nuclear power plant allowed to observe comparable decontamination effect under ultrasound: the radioactive metal waste with an initial radioactivity of over 4000 $Bq.g^{-1}$ was decontaminated by ultrasonic operation in less than 3 hours to achieve a remarkable high DF of over 17,000. Without ultrasound, more than 110 hours were required to reach a 10 times lower DF of 1700.[169]

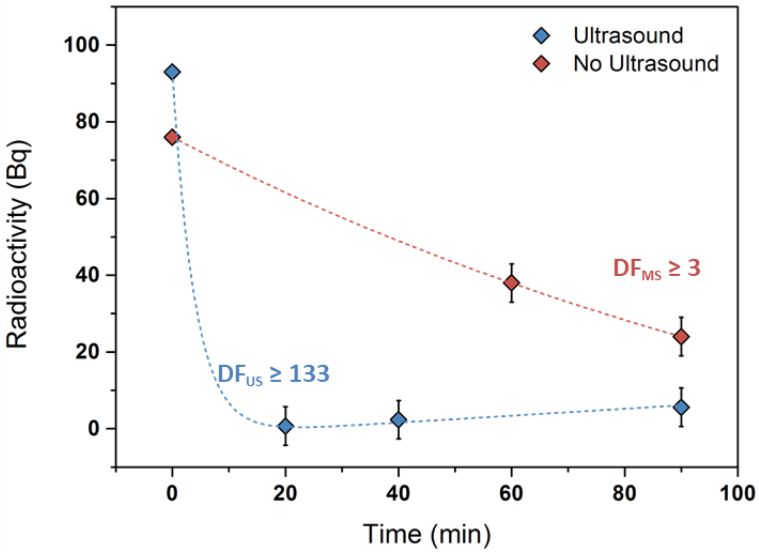

Figure V-12 α-radioactivity evolution of Mg-Zr surfaces contaminated with U (0.1 M $UO_2(NO_3)_2$) decontaminated by 345 kHz ultrasound, P_{ac}= 40 W (blue) and under silent conditions (red) in 0.01 M oxalic acid, Ar, stirring 100 rpm, 20 ℃, 90 min

V.2.2.1.2 Decontamination of Mg ribbon having a complex geometry

In order to simulate a real industrial surface exhibiting a complex shape and structure, an Mg ribbon was contaminated with uranyl nitrate and then rolled into an approximate cylinder shape with the contamination on the internal surface as showed in **Figure V-13**. Ultrasonic decontamination was applied for 90 minutes in 0.01 M oxalic acid by 345 kHz ultrasound with an in-situ stirring. In **Figure V-13**, the ultrasound-assisted decontamination of the internal side of the Mg ribbon is characterized by a metallic bright surface without any visual trace of contaminate or residual oxidation layer. SEM image in **Figure V-** reveals the formation of "golf ball" shape craters on the internal surface of the bent ribbon, which have already been noticed on disc samples, and the craters are more developed at the edge of the Mg ribbon, which indicates that the complex geometry does not prevent cavitation bubble to access to the inner side of the Mg ribbon and to collapse in the vicinity of the surface.

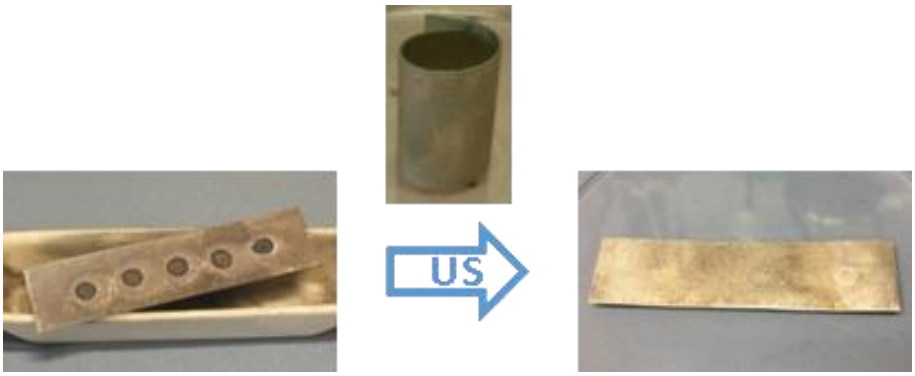

Figure V-13 Photos of a contaminated Mg ribbon (0.1 M $UO_2(NO_3)_2$) wound in a complex geometry before and after 345 kHz sonication (P_{ac}= 40 W) during 90 min in 0.01 M oxalic acid, Ar, stirring 100 rpm, 20 ℃.

According to the corresponding surface α-activity evolution presented in **Figure V-14**, surface activity follows a fast reduction within the first 40 min of sonication before increasing slightly during the rest of the treatment, in agreement with what previously observed on Mg-Zr surfaces. Comparing to disc samples, the decontamination of a complex and geometrical sample takes more time to be achieved. In addition, the lowest radioactivity level characterized by a maximum DF value of 51 in these conditions is less important than what observed on disc samples. These discrepancies can be related to active bubble diffusion difficulty in the complex sample and to a larger sample surface to be treated. However, these observations strengthen the potential of the sonochemical decontamination of industrial metallic samples in comparison to conventional approaches.

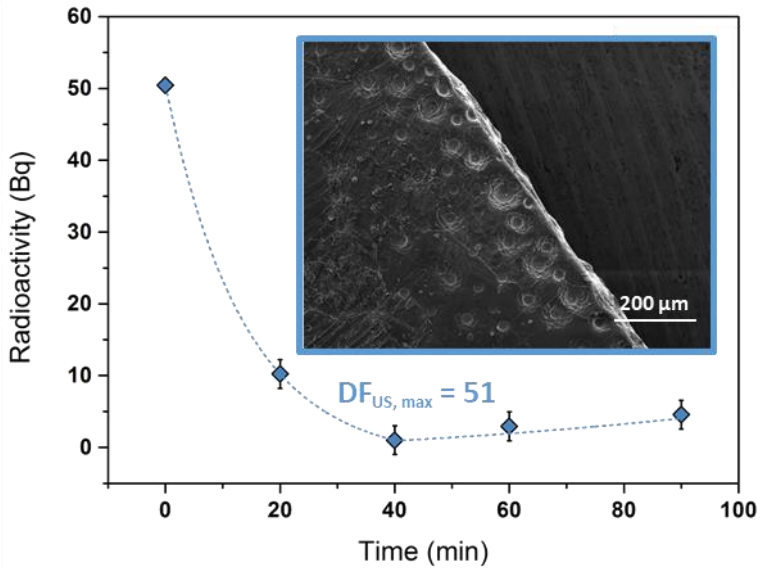

Figure V-14 α-radioactivity evolution of the inner side of a contaminated Mg ribbon (0.1 M $UO_2(NO_3)_2$) wound in a complex geometry sonicated during 90 min at 345 kHz in 0.01 M oxalic acid, Ar, stirring 100 rpm, 20 ℃, P_{ac}= 40 W (insert: SEM image after treatment).

V.2.2.1.3 Decontamination of UNGG cladding material - fin side

The decontamination of the external fin side of a UNGG cladding fragment was implemented in the same conditions. From the pictures in **Figure V-15**, the contaminants appears to have been completely removed and the sample surface is strongly eroded after 90 minutes sonication in oxalic acid. A similar trend of decontamination evolution can indeed be observed in **Figure V-16**. The α-activity of the surface follows a rapid decrease reaching a value of 0.7 Bq after 20 min of sonication. A very slow increase of the activity, reaching a final value of 1.2 Bq after 90 min sonication, can be noticed. After the experiment, the sonicated surface appears very rough without any visual trace of contamination or residual oxidation layer. The SEM image displays an intense concentration of "golf ball" shape craters similarly to what observed on the surrogates and non-contaminated UNGG fin samples (with similar shape and size). EDX analyses confirmed the decontamination effect by measuring a uranium content lower than 2 wt.% (instead of over 40 % before sonication).

To be noted that for UNGG cladding fin sample, the DF value (DF= 82) is relatively lower than that of Mg-Zr disc sample decontamination (DF= 132.8). This may be caused by the sensitivity of the α-spectrometer, which cannot give a precise measurement of surface radioactivity when it is lower than 1 Bq. As a result, the DF value becomes smaller when the initial radiation level is lower.

Figure V-15 Photos of an as-prepared contaminated UNGG cladding fin side sample (0.1 M $UO_2(NO_3)_2$) before and after 345 kHz sonication (P_{ac}= 40 W) during 90 min in 0.01 M oxalic acid, Ar, stirring 100 rpm, 20 ℃.

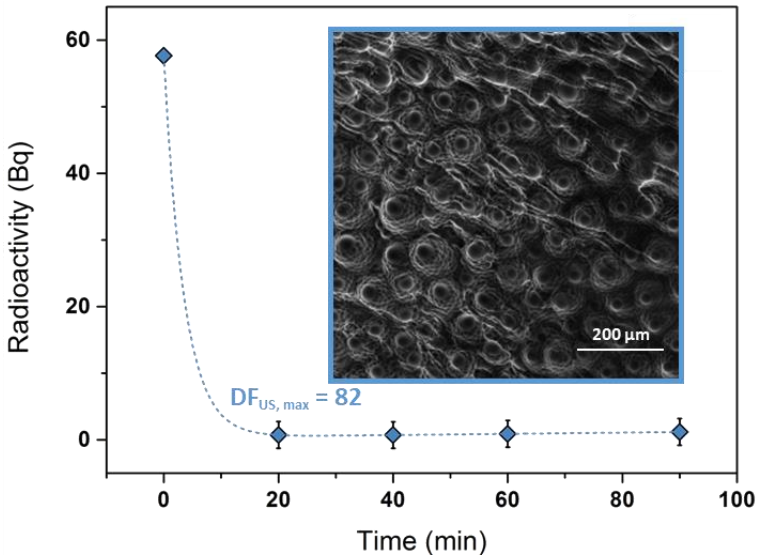

Figure V-16 α-radioactivity evolution of contaminated UNGG cladding fin side sample (0.1 M $UO_2(NO_3)_2$) decontaminated by 345 kHz (P_{ac}= 40 W) during 90 min in 0.01 M oxalic acid, Ar, stirring 100 rpm, 20 ℃ (insert: SEM image after treatment)

V.2.2.1.4 Decontamination of UNGG cladding material - carbon side

Ultrasound treatment of the non-irradiated graphite coating situated on the inner side of UNGG cladding fragment was carried out in similar conditions. Since no radioactive contaminates was deposited on the carbon side, sonication effect was demonstrated by comparison of photos (**Figure V-17**), SEM images (**Figure V-18**) and EDX analyses before and after treatment.

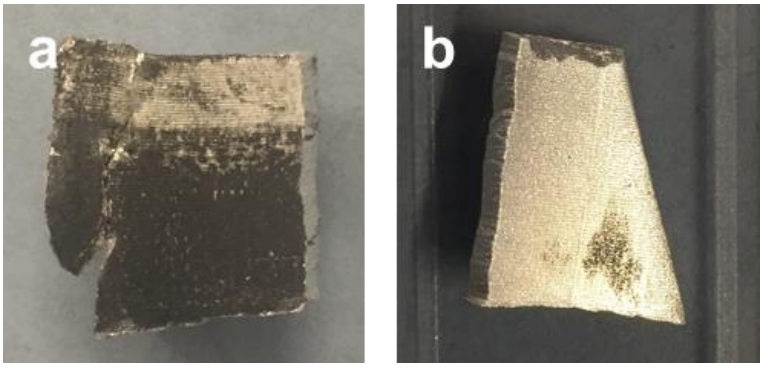

Figure V-17 Photos of the inner side of a UNGG cladding fragment showing the presence of carbon a) before and b) after 1 hour treatment in 0.01 M oxalic acid (345 kHz ultrasound, Ar, stirring 100 rpm, 20 ℃, P_{ac}= 40 W (note: both samples are different).

In these conditions, effective removal of the carbon layer can be clearly observed by naked eye as illustrated in **Figure V-17**. The 1 hour sonicated (345 kHz) sample shows a clean, bright and metallic surface with only a small amount of residual graphite coating. According to EDX analyses performed on areas deprived of graphite residue, the carbon composition decreases as low as 2 wt.% in comparison to the initial state. As shown on **Figure V-18**, it is interesting to notice an initially regular distribution

of parallel grooves on the graphite coated surface. Most probably, these grooves result from the manufacture of the claddings, they probably act as nucleation sites for acoustic cavitation which lead to the formation of a parallel distribution of craters on the sonicated surface. Note that the formation of these craters is once again in agreement with the previous observations made on cladding metallic surrogates (with similar shape and size).

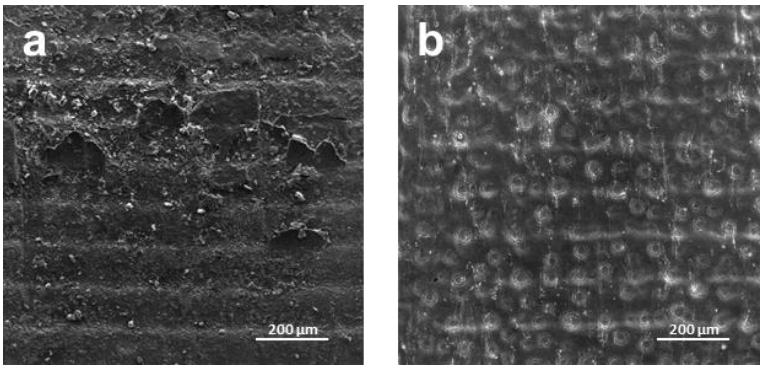

Figure V-18 SEM observations of the inner carbon side of a UNGG cladding fragment a) before and b) after 1 h sonication (345 kHz) in 0.01 M oxalic acid (Ar, stirring 100 rpm, 20 ℃, P_{ac}= 40 W).

V.2.2.2 Secondary phase on decontaminated samples

In agreement with the previous decontamination experiments carried out on Mg-based materials and UNGG cladding fragments, a large amount of secondary phases is generated with the treatment of the different surfaces. As previously described, these secondary phases can be associated to $Mg(OH)_2$. EDX analyses illustrated on **Figure V-19** nevertheless allowed to measure locally high contents of uranium (10 to 20 wt.%) associated with these secondary phases while the surrounding area does not show significant amount of uranium (≤ 2 wt.%).

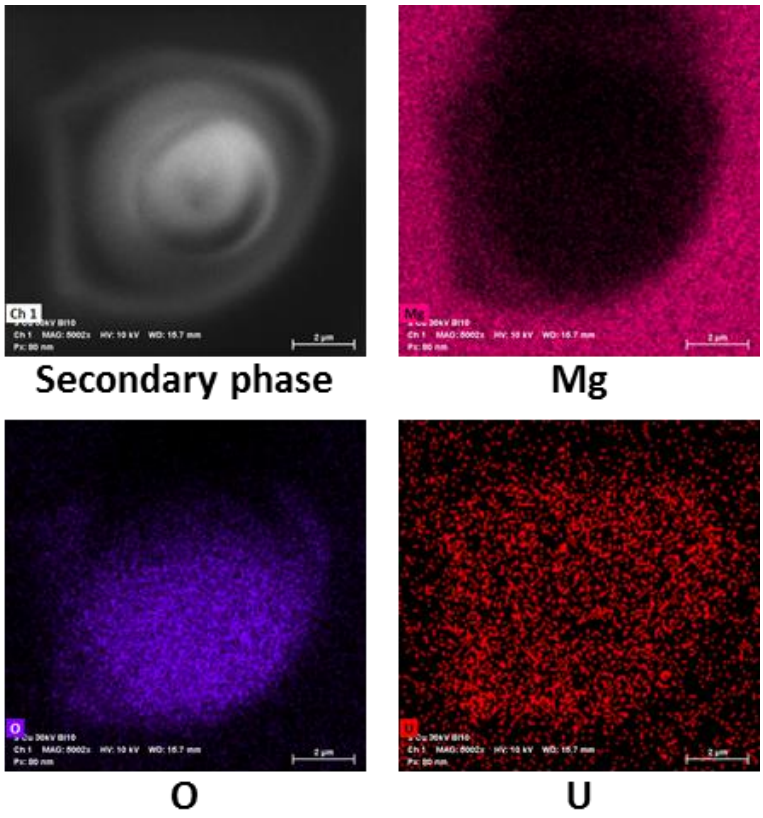

Figure V-19 SEM-EDX analyses of the secondary phases observed on the fin side of a contaminated UNGG cladding fragment (0.1 M $UO_2(NO_3)_2$) sonicated at 345 kHz during 90 min in 0.01 M oxalic acid (Ar, stirring 100 rpm, 20 ℃, P_{ac}= 40 W).

To confirm that this local uranium enrichment does not result from the initial contamination of the surface (residual and non-removed contamination), a non-contaminated Mg surface was sonicated by 345 kHz ultrasound for 30 minutes in 0.01 M oxalic acid before 70 µL of a 0.1 M uranyl nitrate solution was added. Further 30 minutes sonication of this system allowed to observe locally more than 15 wt.% of uranium on the formed secondary phases while the areas without secondary phases generally showed a uranium with 3 wt % in general. Infrared spectra shown in **Figure V-20** confirm the existence of O=U=O bands on the treated Mg surface. As a result, uranium present some affinities with Mg and is preferentially adsorbed in the area presenting $Mg(OH)_2$ secondary phases.

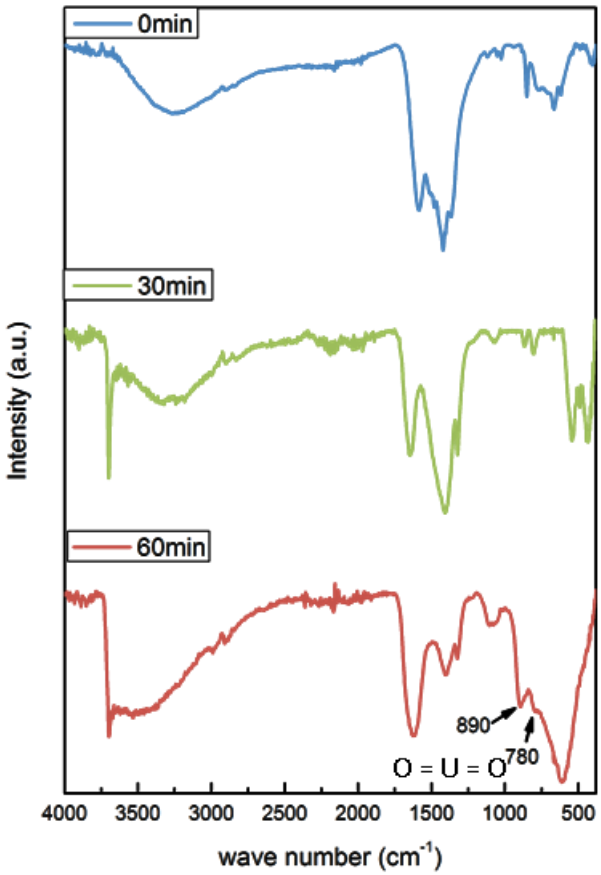

Figure V-20 ATR-FTIR spectra of contaminated Mg surfaces (0.1 M $UO_2(NO_3)_2$) sonicated at 345 kHz during 1 hour in 0.01 M oxalic acid (Ar, stirring 100 rpm, 20 ℃, P_{ac}= 40 W).

Brucite structure can be described as layers of $Mg(OH)_2$ consisting in double-planes of OH groups and a plane of Mg^{2+} sandwiched in between (**Figure V-21**).[257] Due to a weak interlayer force, the space between $Mg(OH)_2$ layers is quite large, leading to a high sorption property of brucite.[258] Previous study published by Pushkaryova et al. proved that brucite can efficiently adsorb metal ions including Cu, Zn, Cd, Co, etc.[259]

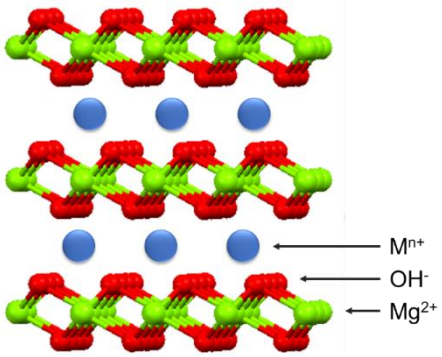

Figure V-21 Schematic representation of metal ions M^{n+} adsorbed in Brucite structure.[257]

Previous study of Cao et al. demonstrated that nano-$Mg(OH)_2$ has an excellent adsorption ability for uranyl in aqueous solutions.[260, 261] Besides, Bochkarev and Pushkareva found that an ultrasonic treatment at low frequency (22 to 35 kHz) can significantly accelerate the diffusion process of metal ions towards the sorbent surface, hence improving the brucite sorption rate of metal ions like copper and nickel.[262, 263]

Therefore, a hypothesis can be proposed concerning the ultrasound decontamination process described in this work. Two principal parameters dominate the surface radioactivity: i) the ultrasound-controlled dissolution of the Mg surface, which efficiently removes the uranium contamination on surfaces; and ii) the formation of $Mg(OH)_2$ which acts as adsorbents for uranyl ions dissolved in solution. During the early stage of ultrasound decontamination (within 20 or 40 minutes), the former parameter is dominant and a rapid reduction of the surface α-activity is observed as already presented in 错误!未找到引用源。, **Figure V-** and **Figure V-**. As the decontamination process continues, the dissolution effect becomes less efficient and the concomitant accumulation of secondary phases at the metallic surface allows the adsorption of uranium from the solution. Note that this process may be reinforced with the consumption of protons in solution and the subsequent solution pH increase which involves the precipitation of more secondary phases on sonicated surface. The adsorption of uranium by brucite may also be accelerated by ultrasound in this case.

V.3 Stainless steel surfaces decontamination by ultrasound

V.3.1 Characterization of stainless steel and the contaminates on stainless steel surfaces

As present in **Figure V-22**, the contaminated stainless steel surface prepared by calcination at 500 ℃ under Ar atmosphere exhibits a dark blue-violet color on the substrate material (the tempering color of a thin oxidation layer on the calcined stainless steel surface),[264] while the uranium areas show an olive-green color (close to the color of U_3O_8). SEM image show some zones with adhering contaminants having a porous structure everywhere.

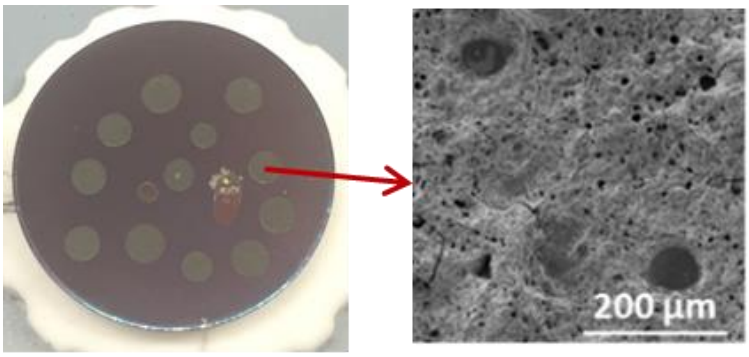

Figure V-22 Contaminated stainless steel surface prepared by calcination at 500 ℃ under Ar atmosphere of a stainless steel surface on which 0.1 M $UO_2(NO_3)_2$ were homogenously deposited. The right side of the figure shows a SEM image of the contamination

The XRD characterization of the contaminated stainless steel surface is illustrated in **Figure V-23**. The diagram shows the presence of UO_3 or U_3O_8 (coincident in XRD pattern), as previously observed on contaminated Mg based materials. A complex compound of $CrFe_7C_{0.45}$ exhibits on contaminated stainless steel surface after 2-hour calcination at 500 ℃. Infrared spectra (**Figure V-24**) also reveal the existence of UO_3 and U_3O_8, as well as Fe_2O_3, Cr_2O_3 and organic bands of C-O and C=O on stainless steel surface. Only UO_3 and U_3O_8 were detected by Raman spectrometry when focusing on the contaminated areas (**Figure V-25**). The non-contaminated area shows Raman bands of metal oxides indicating the existence of Fe_2O_3, $NiFe_2O_4$ and $NiCr_2O_4$ in agreement with the composition of stainless steel. (Bands information in Appendix I)

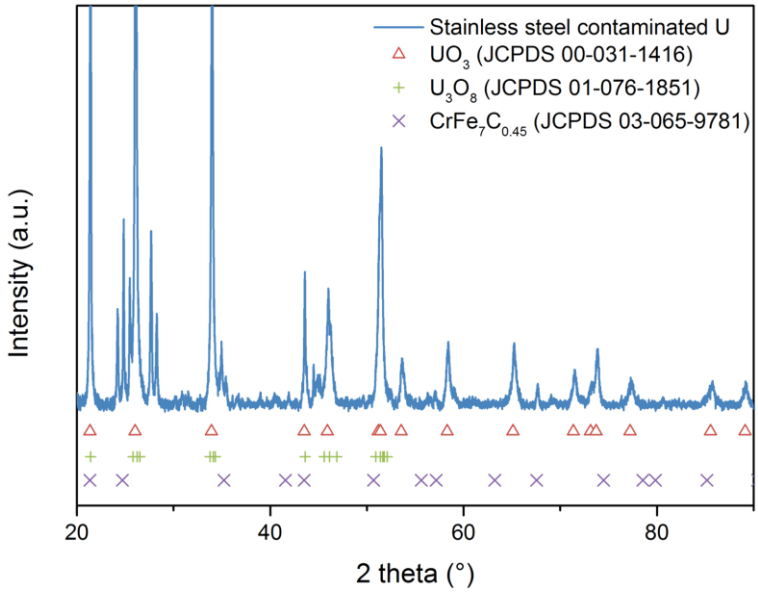

Figure V-23 X-ray diffraction pattern of an as-prepared contaminated stainless steel surface (0.1 M $UO_2(NO_3)_2$) (standard patterns of UO_3 JCPDS 00-031-1416, U_3O_8 JCPDS 01-076-1851 and $CrFe_7C_{0.45}$ JCPDS 03-065-9781).

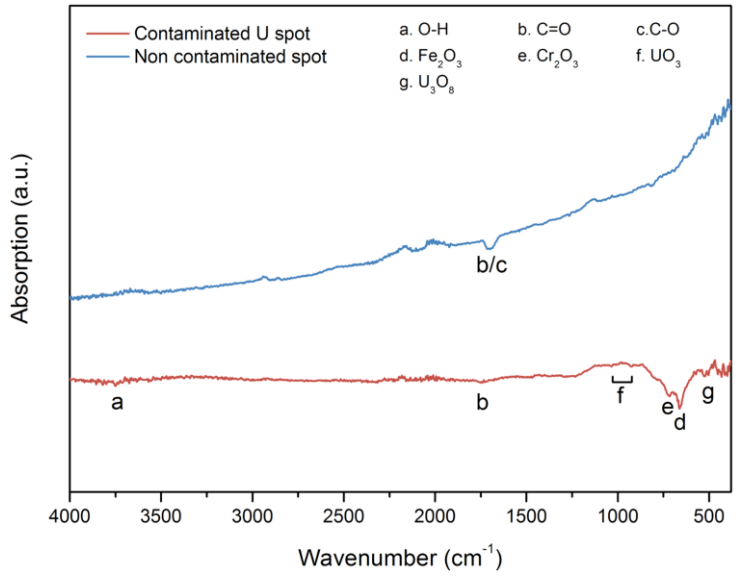

Figure V-24 FTIR spectra of as-prepared contaminated stainless steel surface (0.1 M $UO_2(NO_3)_2$)

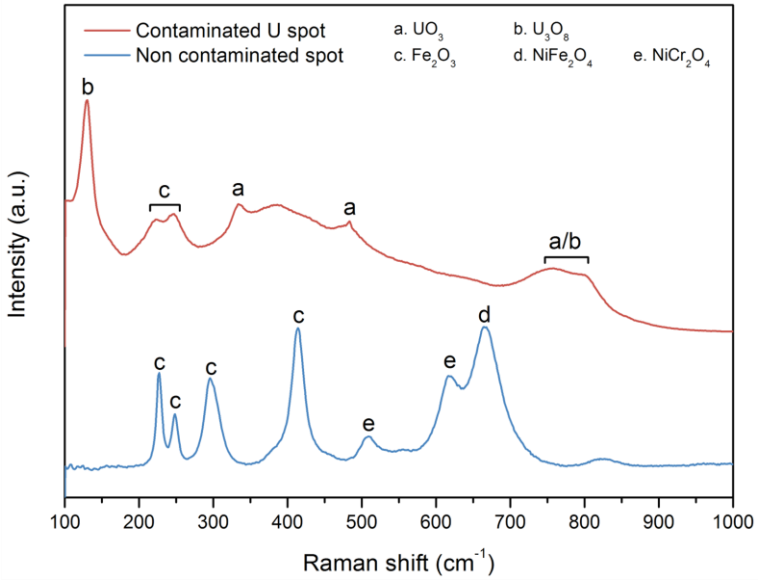

Figure V-25 Raman spectra of as-prepared contaminated stainless steel surface (0.1 M $UO_2(NO_3)_2$)

V.3.2 Ultrasonic decontamination results

Similar experimental conditions used for Mg based surfaces were applied for the decontamination of the prepared stainless steel surfaces. Experiments carried out in the absence of ultrasound (silent conditions) were implemented as references.

According to **Figure V-26**, the decrease of stainless steel surface α-radioactivity in 0.01 oxalic acid present a similar trend to what observed with Mg-Zr surface (see for instance 错误!未找到引用源。). A fast decrease of the surface activity is indeed observed during the first 20 min of sonication, while a lower, but significant and linear, decontamination effect is observed from 20 in to 90 min of treatment.

The DF factor reaches 14.8 in these conditions. A stronger decontamination effect is noted under ultrasound in comparison to silent conditions where contaminants are observed (**Figure V-27**) to strongly remain on the surface after 90 min treatment. The surface activity follows a linear reduction with a DF value of only 1.4 at the end of the experiment. It is important to note that in these conditions, the recontamination of the surface is not observed (opposite to Mg-based materials) even in the case of an extended sonication. Indeed, ultrasonic decontamination carried out during 180 min allowed to reach a surface activity of about 10 Bq (DF= 26.6, in comparison to initial activity of 266 Bq) without any increase of the surface contamination.

In comparison to decontaminated Mg-based samples, the final radiation level measured on the treated stainless steel surfaces is higher whatever the treatment conditions. This is in agreement with the photos and SEM observations illustrated in **Figure V-27**. Whatever the conditions, the color of the substrate remains blue-violet which can be attributed to the good corrosion resistance of stainless steel material. Under silent condition, no obvious change of the contaminants is observed; the initial porous structure is still observed after treatment. For the surface treated under ultrasound, uranium contaminants are found to be strongly damaged with the formation of intensive pits grown from the initial pores, but not yet completely removed. No crater structure is produced in the contaminated or non-contaminated areas.

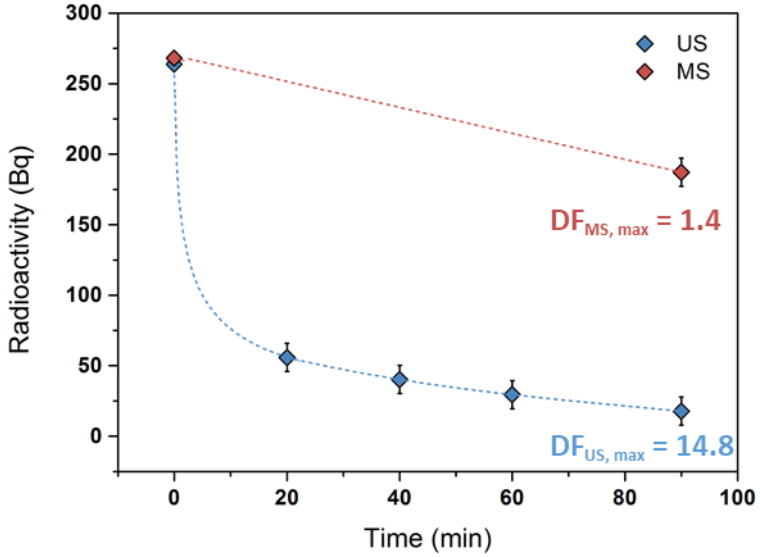

Figure V-26 Radioactivity evolution of contaminated stainless steel surfaces (0.1 M $UO_2(NO_3)_2$) treated in 0.01 M oxalic acid, Ar, stirring 100 rpm, 20 ℃, for 90 minutes under silent condition (red) and by 345 kHz ultrasound, P_{ac}= 40 W (blue).

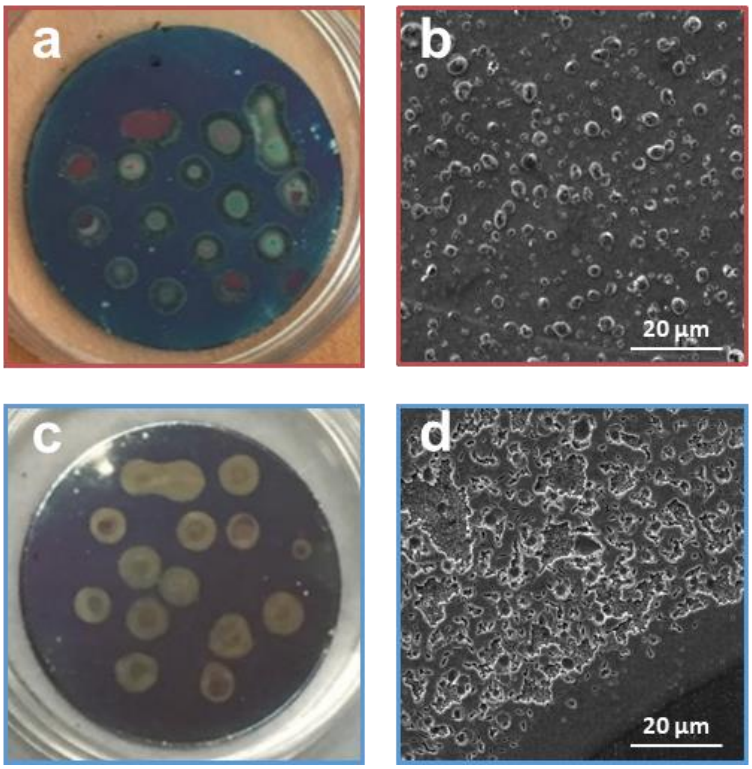

Figure V-27 Photos and SEM images of stainless steel surfaces contaminated with U (0.1 M $UO_2(NO_3)_2$) treated under silent conditions (a and b) and by 345 kHz ultrasound, P_{ac}= 40 W (c and d) in 0.01 M oxalic acid, Ar, stirring 100 rpm, 20 ℃, 90 min

Considering the lower reactivity of stainless steel material and the apparently better adhesion of uranium contaminant on its surface, 1 M nitric acid was chosen as decontamination medium. In 1 M nitric acid, **Figure V-28** shows that the stainless steel surface activity decreases to about 10 Bq after 90 min treatment in both silent and ultrasonic decontaminations. Comparing to 0.01 M oxalic acid, especially in the case of silent treatment, a stronger decontamination effect is observed in 1 M nitric acid which can be attributed to the higher concentration of protons in solution and the stronger corrosive property of this acid. Ultrasound irradiation does not improve significantly the final DF result (DF value of 28.8 in comparison to 23.4 under silent condition) although the ultrasonic acceleration effect is still obvious in the first 10 minutes.

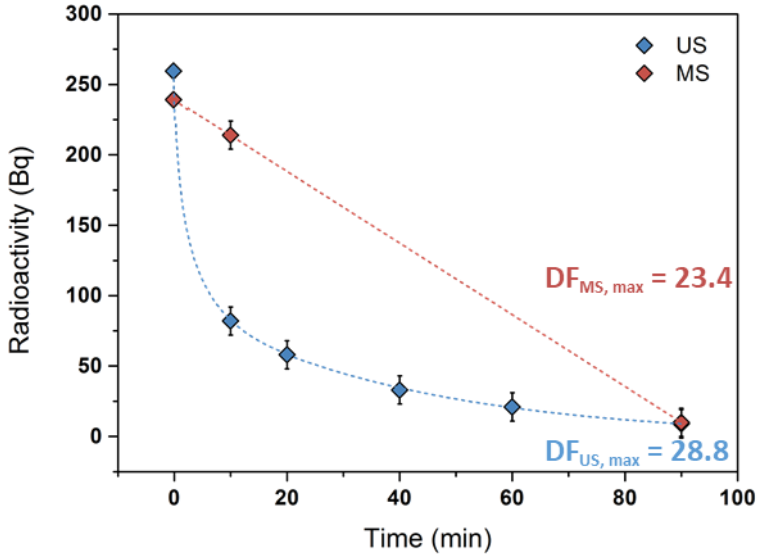

Figure V-28 Radioactivity evolution of contaminated stainless steel surfaces (0.1 M $UO_2(NO_3)_2$) treated in 1 M nitric acid, Ar, stirring 100 rpm, 20 ℃, for 90 minutes under silent condition (red) and by 345 kHz ultrasound, P_{ac}= 40 W (blue)

From **Figure V-29**, it is obvious that the color of the metallic substrate changes from dark blue-violet to a burnished metallic color for both treatment conditions, which is close to the original stainless steel color observed before calcination and indicates the removal of the thin oxidation layer on stainless steel surface. Though the contamination areas can still be observed, a much more eroded morphology can be noticed for the contaminants with SEM investigations.

Generally, stainless steel has a good corrosion resistance to organic acid like oxalic acid. But in a concentrated nitric acid, stainless steel erosion is efficient and the contamination besides oxidation layer is significantly removed. Again, ultrasound here accelerates the decontamination process (in the first 10 to 20 minutes) in both oxalic acid and nitric acid. Therefore, for stainless steel and similar corrosion resistant metal materials, an efficient ultrasonic decontamination is necessary to carry out in a strongly acidic solution, such as concentrated nitric acid.

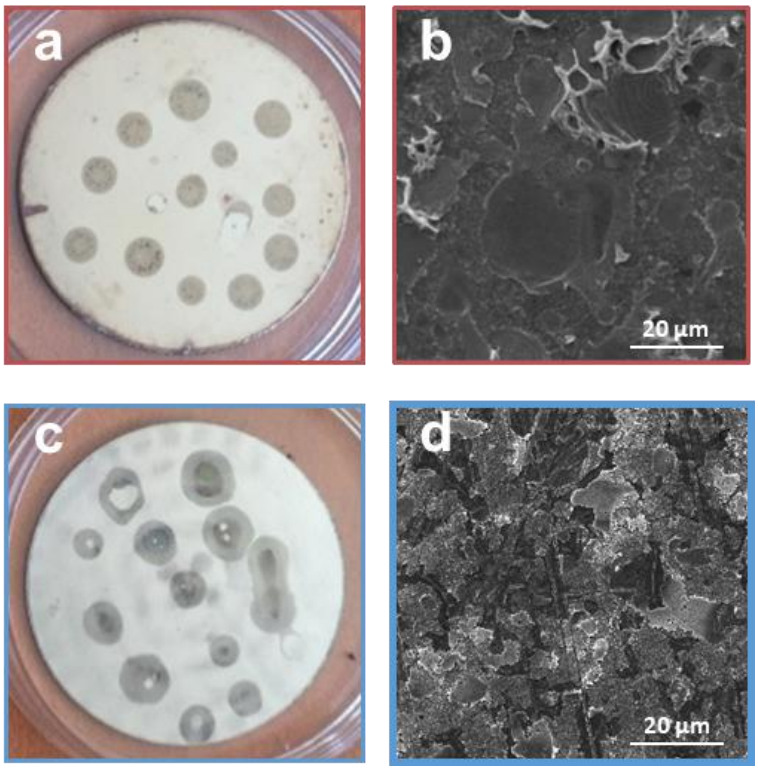

Figure V-29 Photos and SEM images of stainless steel surfaces contaminated with U (0.1 M $UO_2(NO_3)_2$) decontaminated under silent conditions (a and b) and by 345 kHz ultrasound, P_{ac}= 40 W (c and d) in 1 M nitric acid, Ar, stirring 100 rpm, 20 ℃, 90 min

V.4 Conclusion

In this chapter, ultrasonic treatment at 345 kHz is found efficient for the decontamination of Mg-based surfaces, including pure Mg, Mg-Zr alloy surrogates and non-irradiated UNGG cladding fragments, which can be carried out in dilute 0.01 M oxalic acid at room temperature. Contaminants on the as-prepared Mg surfaces are in agreement with UO_3, U_3O_8 and non-stoichiometric $Mg_xU_yO_z$. In comparison to silent conditions, 345 kHz ultrasound in oxalic acid significantly accelerates the decontamination process of Mg during the first 20 to 40 minutes, even for the surfaces having a complex geometry such as the Mg ribbon sample. Simultaneously, the “golf ball” shape craters are created on the Mg-based surfaces and a very low residual activity is observed on the surfaces evidencing the good decontamination conditions selected in this study. Nevertheless, a low recontamination phenomenon is observed after the surface radioactivity reaches its minimum. This observation is attributed to the adsorption of uranium by the formed brucite structures at the surface of the samples, which phenomenon is in good agreement with the observation made on Mg surrogate samples (so as the organized crater formations). The evolution of the surface radioactivity is function of the balance between ultrasonic dissolution of Mg accompanying the decontamination of uranium and the adsorption of uranium in solution by the formed brucite on the sonicated surface. Such balance is to be correlated to the proton

concentration and pH of solution. Meantime, the graphite coating on the inner side of UNGG cladding samples, which is problematic during storage, can be successfully removed by ultrasound in oxalic medium. Contaminants on the as-prepared stainless steel surfaces only present UO_3 and U_3O_8. The efficient ultrasonic decontamination of stainless steel surfaces can also be observed in 1 M nitric acid. No recontamination process is monitored during stainless steel surface decontamination; however, it is found that a stronger and more concentrated nitric acid solution is required for efficient decontamination of this metallic surface. Also, the ultrasound formation of structures is not observed for this material, probably because of its lower reactivity and higher strength.

General Conclusion

In general, this thesis is divided into 3 major axes: 1) a fundamental study of sonochemistry and sonoluminescence in aqueous solution submitted at 100 kHz ultrasound followed by the characterization of the acoustic cavitation field in the vicinity of an extended solid surface; 2) the study of the behavior and structuring of Mg-based surfaces under ultrasonic irradiation; 3) the ultrasonic treatment of radioactive Mg-based materials contaminated with natural uranium as surrogates for UNGG claddings.

The first section of this study is dedicated on sonochemistry and sonoluminescence at 100 kHz. It is shown that the characteristics of acoustic cavitation at intermediate frequencies are in between those at low- and high-frequency ultrasound. H_2O_2 yield in water under Ar regularly increases with ultrasonic frequency from 20 kHz to 362 kHz. On the one hand, the shape of the SL spectrum at 100 kHz is similar to that at 20 kHz. On the other hand, the rovibronic temperatures of OH ($A^2\Sigma^+$) radicals in the non-equilibrium sonochemical plasma produced by 100 kHz ultrasound are closer to high frequency rather than to 20 kHz. A 20% O_2 addition to Ar leads to higher H_2O_2 yield at all frequencies, and to higher SL intensity at intermediate and high frequencies. This discrepancy was traced back to their higher collapse energy that enables O_2 dissociation and subsequent formation of more excited species, while at 20 kHz O_2 mostly has a quenching effect on SL. Cavitation bubbles at 100 kHz also share the ability of high frequency ones to dissociate N_2 molecules, which requires a high energy. Thus, from spectroscopic and chemical points of view, 100 kHz can be seen as a transition between low and high frequency.

Then, the impact of the presence of a solid surface on SL and SCL was studied in luminol and NaCl solutions. With close proximity to the solid surface, a higher ratio between Na* and continuum emission intensity is observed from the MBSL spectrum of the NaCl solution, which is due to the asymmetrical collapses of cavitation bubbles in the vicinity of the stainless steel plate. This effect seems quite localized in a very short distance (≤1.5 mm) under the solid plate. Reflection of the ultrasonic wave leads to the formation of a standing wave in liquid and it is found that SL and SCL (thus sonochemical activity) distribution and intensity are strongly dependent on the position of the reflective surface: a well-defined distance (resonant mode) between solid surface and transducer leads to brighter SCL photos and stronger SL emissions. When a chemically active Mg surface is used as a reflector, no direct reflection is observed since the produced hydrogen bubbles form a gas layer below the solid surface which interfere with the formation of a standing wave in the solution.

The next section focuses on the sonication of Mg-based surfaces. It is found that ultrasound can activate extended surfaces and participate, in combination to an appropriate solute, to the formation of original and unprecedented microstructures. “Golf-ball” shape microstructuration is observed on pure Mg and Mg-Zr alloy surfaces after sonication in dilute oxalic acid at 100 to 345 kHz at 20 ℃. The tuning of the

applied acoustic frequency in combination to a relevant solute can lead to dramatic changes at the material surface. Big holes and undulation channels can be observed on Mg surface treated at 20 kHz, while no specific microstructure but flat surface and grain boundaries appear on a surface treated at 1 MHz.

The accumulation of Mg^{2+} in solution combined to the generation of H_2 gas during the treatment confirms the ultrasound-controlled dissolution of metallic Mg. An original approach resulting in the 3D reconstruction of sonicated surfaces allowed to investigate the formation mechanism of these extended surfaces. Most probably, ultrasound allows the generation of surface defects which are then used as nucleation sites that favor the crater formation. The crater increases in diameter and depth with sonication time due to the heterogeneous nucleation of cavitation bubbles, accompanying the pitting corrosion which accelerates the growth of craters. H_2 gas release in the localized area may also serve as nucleation of cavitation. The surface wettability is also found to be strongly correlated to the formation of craters, and a high hydrophobicity is expected with a surface of homogeneously formed craters. This property can be of potential interest for industrial applications, for instance for biomedical materials, where wettability properties are required to improve the adhesion of surface coatings. Mg surface dissolution progress is found to be accompanied by the formation of new spherical micrometric structures formed at the Mg surface and attributed to $Mg(OH)_2$. The formation of these secondary phases is related to local alkalization effect induced by Mg dissolution and is found to be lowered under ultrasound in comparison to conventional dissolution procedure.

These observations open new routes of investigation for other alloy and metal-based materials and new alternatives of potential interest for applications in many fields including industry, medicine, and nanotechnology.

Ultrasonic decontamination of Mg-based materials contaminated with uranium (and stainless steel surfaces in a less extent) was investigated in the last chapter of this thesis. The ultrasonic frequency fixed at 345 kHz is found to be very efficient though rarely used in conventional ultrasonic cleaning. The ultrasonic decontamination effect is highly different whether it is performed on Mg-based materials or stainless steel surfaces. Mg-based materials can be efficiently decontaminated leading to surface activities lower than 1 Bq within 20 minutes in dilute oxalic acid solution within the experimental domain studied. Although significant, stainless steel surfaces require a stronger and more concentrated acid solution (HNO_3) which leads to a remaining radioactivity of about 10 Bq after 3 hours sonication. A slow recontamination process is observed during the decontamination of Mg-based surfaces after 20 minutes treatment which is explained by the adsorption of uranium ions by the formed $Mg(OH)_2$ on the surface. Such layer structures are known to exhibit excellent ability in adsorption of heavy ions like uranyl. The successful decontamination of Mg standing in a complex geometry can also be achieved

under ultrasound irradiation thus confirming the potential of sonochemistry for the treatment of such kind of materials.

The various investigations confirmed that Mg and Mg-Zr samples used in this study can be considered as good surrogates to study the behavior of UNGG cladding samples. The homogeneous “golf-ball” shape structuration and efficient decontamination of this material can indeed be observed under ultrasound in similar conditions. Moreover, a remarkable removal of the graphite coating situated on the inner side of UNGG cladding sample strengthen the possibility of using high-frequency ultrasound as a tool for Mg cladding wastes decontamination in France.

References

1. DEN. *Technical report. Etat d'avancement de la caractérisation des déchets MAVL produits avant 2015 - Programmes d'étude du conditionnementdes déchets* 2015. CEA. CEA Saclay.
2. Chartier, D., Muzeau, B., Stefan, L., Sanchez-Canet, J., and Monguillon, C., *Magnesium alloys and graphite wastes encapsulated in cementitious materials: Reduction of galvanic corrosion using alkali hydroxide activated blast furnace slag.* Journal of Hazardous Materials, 2017. **326**: p. 197-210.
3. Chen, D., Sharma, S.K., and Mudhoo, A., eds. *Handbook on applications of ultrasound : Sonochemistry for sustainability*. 2012, CRC Press: Boca Raton, FL.
4. Thompson, L.H. and Doraiswamy, L.K., *Sonochemistry: Science and engineering.* Industrial & Engineering Chemistry Research, 1999. **38**(4): p. 1215-1249.
5. Leong, T., Ashokkumar, M., and Kentish, S., *The fundamentals of power ultrasound - a review.* Acoustics Australia, 2011. **39**(2): p. 54-63.
6. Wu, T.Y., Guo, N., The, C.Y., and Wen Hay, J.X., *Advances in ultrasound technology for environmental remediation*. SpringerBriefs in Molecular Science. 2012, Netherlands: Springer.
7. Harkin, A., Nadim, A., and Kaper, T.J., *On acoustic cavitation of slightly subcritical bubbles.* Physics of Fluids, 1999. **11**(2): p. 274-287.
8. Yasui, K., *Acoustic cavitation and bubble dynamics*. 2018: Springer international publishing.
9. Suslick, K.S. *Sonoluminescence and sonochemistry*. in *1997 IEEE Ultrasonics symposium proceedings*. 1997. Toronto, Ont., Canada: IEEE. p. 523-532.
10. Ashokkumar, M., Lee, J., Kentish, S., and Grieser, F., *Bubbles in an acoustic field: An overview.* Ultrasonics Sonochemistry, 2007. **14**(4): p. 470-475.
11. Vinatoru, M., Mason, T.J., and Calinescu, I., *Ultrasonically assisted extraction (UAE) and microwave assisted extraction (MAE) of functional compounds from plant materials.* Trends in analytical chemistry : TRAC, 2017. **97**: p. 159-178.
12. Suslick, K.S., Doktycz, S.J., and Flint, E.B., *On the origin of sonoluminescence and sonochemistry.* Ultrasonics, 1990. **28**(5): p. 280-290.
13. Louisnard, O. and González-García, J., *Acoustic cavitation*, in *Ultrasound technologies for food and bioprocessing*, H. Feng, G. Barbosa-Canovas, and J. Weiss, Editors. 2011, Springer: New York. p. 13-64.
14. Van Wijngaarden, L., *Mechanics of collapsing cavitation bubbles.* Ultrasonics Sonochemistry, 2016. **29**: p. 524-527.
15. Suslick, K.S., Hammerton, D.A., and Cline, R.E., *The sonochemical hot-spot.* Journal of the American Chemical Society, 1986. **108**(18): p. 5641-5642.
16. Suslick, K.S., *Sonochemistry.* Science, 1990. **247**(4949): p. 1439-1445.

17. Suslick, K.S., McNamara, W.B., and Didenko, Y., *Hot spot conditions during multi-bubble cavitation*, in *Sonochemistry and sonoluminescence*, L.A. Crum, et al., Editors. 1999, Springer: Dordrecht. p. 191-204.

18. Didenko, Y.T., McNamara, W.B., and Suslick, K.S., *Hot spot conditions during cavitation in water.* Journal of the American Chemical Society, 1999. **121**(24): p. 5817-5818.

19. Cairos, C. and Mettin, R., *Simultaneous high-speed recording of sonoluminescence and bubble dynamics in multibubble fields.* Physical Review Letters, 2017. **118**(6): p. 064301.1-064301.5.

20. Ndiaye, A.A., Pflieger, R., Siboulet, B., Molina, J., Dufreche, J.F., and Nikitenko, S.I., *Nonequilibrium vibrational excitation of OH radicals generated during multibubble cavitation in water.* Journal of Physical Chemistry A, 2012. **116**(20): p. 4860-4867.

21. Pflieger, R., Ouerhani, T., Belmonte, T., and Nikitenko, S.I., *Use of NH (A^3P-X^3S^-) sonoluminescence for diagnostics of nonequilibrium plasma produced by multibubble cavitation.* Physical Chemistry Chemical Physics, 2017. **19**(38): p. 26272-26279.

22. Nikitenko, S.I. and Pflieger, R., *Toward a new paradigm for sonochemistry: Short review on nonequilibrium plasma observations by means of MBSL spectroscopy in aqueous solutions.* Ultrasonics Sonochemistry, 2017. **35**(B): p. 623-630.

23. Pflieger, R., Ndiaye, A.A., Chave, T., and Nikitenko, S.I., *Influence of ultrasonic frequency on Swan band sonoluminescence and sonochemical activity in aqueous tert-butyl alcohol solutions.* The Journal of Physical Chemistry B, 2015. **119**(1): p. 284-290.

24. Brujan, E.A., Keen, G.S., Vogel, A., and Blake, J.R., *The final stage of the collapse of a cavitation bubble close to a rigid boundary.* Physics of Fluids, 2002. **14**(1): p. 85-92.

25. Bremond, N., Arora, M., Dammer, S.M., and Lohse, D., *Interaction of cavitation bubbles on a wall.* Physics of Fluids, 2006. **18**(12): p. 150501-150510.

26. Mason, T. and Lorimer, J.P., *Applied sonochemistry: The uses of power ultrasound in chemistry and processing*. 2002, Weinheim: Wiley VCH.

27. Lauterborn, W. and Bolle, H., *Experimental investigations of cavitation-bubble collapse in neighborhood of a solid boundary.* Journal of Fluid Mechanics, 1975. **72**(2): p. 391-399.

28. Sugimoto, Y., Yamanishi, Y., Sato, K., and Moriyama, M., *Measurement of bubble behavior and impact on solid wall induced by fiber-holmium: YAG laser.* Journal of Flow Control, Measurement & Visualization, 2015. **Vol.03**(No.04): p. 135-143.

29. Lauterborn, W., Kurz, T., Mettin, R., and Ohl, C.D., *Experimental and theoretical bubble dynamics*, in *Advances in Chemical Physics*, P. I. and R.S. A., Editors. 1999. p. 295-380.

30. Supponen, O., Obreschkow, D., Kobel, P., Tinguely, M., Dorsaz, N., and Farhat, M., *Shock waves from nonspherical cavitation bubbles.* Physical Review Fluids, 2017. **2**(9): p. 360101-360120.

31. Young, F.R., *Sonoluminescence*. 2004: CRC Press.

32. Virot, M., Chave, T., Nikitenko, S.I., Shchukin, D.G., Zemb, T., and Mohwald, H., *Acoustic cavitation at the water-glass interface.* Journal of Physical Chemistry C, 2010. **114**(30): p. 13083-13091.

33. Reuter, F. and Mettin, R., *Mechanisms of single bubble cleaning.* Ultrasonics Sonochemistry, 2016. **29**: p. 550-562.

34. Brujan, E.A., Ikeda, T., and Matsumoto, Y., *On the pressure of cavitation bubbles.* Experimental Thermal and Fluid Science, 2008. **32**(5): p. 1188-1191.

35. Philipp, A. and Lauterborn, W., *Cavitation erosion by single laser-produced bubbles.* Journal of Fluid Mechanics, 1998. **361**: p. 75-116.

36. Piercy, J.E. and Lamb, J., *Acoustic streaming in liquids.* Proceedings of the Royal Society of London. Series A. Mathematical and Physical Sciences, 1954. **226**(1164): p. 43-50.

37. Karlsen, J.T., Qiu, W., Augustsson, P., and Bruus, H., *Acoustic Streaming and Its Suppression in Inhomogeneous Fluids.* Physical Review Letters, 2018. **120**(5): p. 054501.1-054501.6.

38. Legay, M., Gondrexon, N., Le Person, S., Boldo, P., and Bontemps, A., *Enhancement of heat transfer by ultrasound: Review and recent advances.* International Journal of Chemical Engineering, 2011. **2011**(2): p. 1-17.

39. Trinh, E.H. and Gopinath, A. *Acoustic streaming and heat and mass transfer enhancement*. in *Third Microgravity Fluid Physics Conference*. 1996. p. 791-796.

40. Brennen, C., *Cavitation and bubble dynamics*. Vol. 44. 1995, New York: Oxford University Press.

41. Richards, W.T. and Loomis, A.L., *The chemical effects of high frequency sound waves I. A preliminary survey.* Journal of the American Chemical Society, 1927. **49**(12): p. 3086-3100.

42. Pokhrel, N., Vabbina, P.K., and Pala, N., *Sonochemistry: Science and engineering.* Ultrasonics Sonochemistry, 2016. **29**: p. 104-128.

43. Lepoint, T. and Mullie, F., *What Exactly is Cavitation Chemistry.* Ultrasonics Sonochemistry, 1994. **1**: p. S13-S22.

44. Wood, R.J., Lee, J., and Bussemaker, M.J., *A parametric review of sonochemistry: Control and augmentation of sonochemical activity in aqueous solutions.* Ultrasonics Sonochemistry, 2017. **38**: p. 351-370.

45. Ji, R., Pflieger, R., Virot, M., and Nikitenko, S.I., *Multibubble sonochemistry and sonoluminescence at 100 khz: The missing link between low- and high-frequency ultrasound.* Journal of Physical Chemistry B, 2018. **122**(27): p. 6989-6994.

46. Ouerhani, T., Pflieger, R., Ben Messaoud, W., and Nikitenko, S.I., *Spectroscopy of sonoluminescence and sonochemistry in water saturated with N_2-Ar mixtures.* Journal of Physical Chemistry B, 2015. **119**(52): p. 15885-15891.

47. Hagenson, L.C. and Doraiswamy, L.K., *Comparison of the effects of ultrasound and mechanical agitation on a reacting solid-liquid system.* Chemical Engineering Science, 1998. **53**(1): p. 131-148.

48. Serpone, N. and Colarusso, P., *Sonochemistry I. Effects of Ultrasounds On Heterogeneous Chemical Reactions - a Useful Tool To Generate Radicals and To Examine Reaction Mechanisms.* p. 635-679.

49. Dooher, J., Genberg, R., Moon, S., Gilmartin, B., Jakatt, S., Skura, J., and Wright, D., *Combustion studies of water-oil emulsion on a commercial boiler using number 2 oil and low and high sulfur number 6 oil.* Fuel, 1980. **59**(12): p. 883-892.

50. Shchukin, D.G., Skorb, E., Belova, V., and Mohwald, H., *Ultrasonic cavitation at solid surfaces.* Advanced Materials, 2011. **23**(17): p. 1922-1934.

51. Mason, T.J., *Ultrasonic cleaning: An historical perspective.* Ultrasonics Sonochemistry, 2016. **29**: p. 519-523.

52. Banerjee, S., Kumar, R., and Gandhi, K.S., *Analysis of ultrasonically enhanced hydrogen evolution for Zn-$NiCl_2$ system.* Chemical Engineering Science, 1995. **50**(15): p. 2409-2418.

53. Domingos, R.N., Vollet, D.R., and Bucalon, A.J., *Structural changes induced by ultrasound during aging of the boehmite phase.* Ultrasonics Sonochemistry, 1997. **4**(4): p. 321-323.

54. Mason, T.J., Lorimer, J.P., and Walton, D.J., *Sonoelectrochemistry.* Ultrasonics, 1990. **28**(5): p. 333-337.

55. Compton, R.G., Eklund, J.C., and Marken, F., *Sonoelectrochemical processes: A review.* Electroanalysis, 1997. **9**(7): p. 509-522.

56. Brotchie, A., Grieser, F., and Ashokkumar, M., *Effect of power and frequency on bubble-size distributions in acoustic cavitation.* Physical Review Letters, 2009. **102**(8): p. 084302.1-084302.4.

57. Babgi, B., Zhou, M.F., Aksu, M., Alghamdi, Y., and Ashokkumar, M., *Initial growth of sonochemically active and sonoluminescence bubbles at various frequencies.* Ultrasonics Sonochemistry, 2016. **29**: p. 55-59.

58. Dake. *Sonoluminescence*. 2005 [cited 2015 November 03]; Available from: https://fr.wikipedia.org/wiki/Sonoluminescence.

59. Hatanaka, S., Yasui, K., Kozuka, T., Tuziuti, T., and Mitome, H., *Influence of bubble clustering on multibubble sonoluminescence.* Ultrasonics, 2002. **40**(1-8): p. 655-660.

60. Krefting, D., Mettin, R., and Lauterborn, W., *High-speed observation of acoustic cavitation erosion in multibubble systems.* Ultrasonics Sonochemistry, 2004. **11**(3-4): p. 119-123.

61. Brenner, M.P., Hilgenfeldt, S., and Lohse, D., *Single-bubble sonoluminescence.* Reviews of Modern Physics, 2002. **74**(2): p. 425-484.

62. Matula, T.J., Roy, R.A., Mourad, P.D., McNamara Iii, W.B., and Suslick, K.S., *Comparison of multibubble and single-bubble sonoluminescence spectra.* Physical Review Letters, 1995. **75**(13): p. 2602-2605.

63. Didenko, Y.T. and Pugach, S.P., *Spectra of water sonoluminescence.* Journal of Physical Chemistry, 1994. **98**(39): p. 9742-9749.

64. Abe, S. and Choi, P.K., *Spatiotemporal separation of Na-atom emission from continuum emission in sonoluminescence.* Japanese Journal of Applied Physics, 2009. **48**(7): p. 07GH02.1-07GH02.3.

65. Hayashi, Y. and Choi, P.K., *Effects of rare gases on sonoluminescence spectrum of the K atom.* Journal of Physical Chemistry B, 2012. **116**(27): p. 7891-7897.

66. Choi, P.K., *Sonoluminescence and acoustic cavitation.* Japanese Journal of Applied Physics, 2017. **56**(7): p. 07JA01.1-07JA01.9.

67. Xu, H. and Suslick, K.S., *Molecular emission and temperature measurements from single-bubble sonoluminescence.* Physical Review Letters, 2010. **104**(24): p. 244301.1-244301.4.

68. Xu, H., Glumac, N.G., and Suslick, K.S., *Temperature Inhomogeneity during Multibubble Sonoluminescence.* Angewandte Chemie International Edition, 2010. **49**(6): p. 1079-1082.

69. Flannigan, D.J. and Suslick, K.S., *Temperature Nonequilibration during Single-Bubble Sonoluminescence.* Journal of Physical Chemistry Letters, 2012. **3**(17): p. 2401-2404.

70. McNamara, W.B., Didenko, Y.T., and Suslick, K.S., *Sonoluminescence temperatures during multi-bubble cavitation.* Nature, 1999. **401**(6755): p. 772-775.

71. Merouani, S., Ferkous, H., Hamdaoui, O., Rezgui, Y., and Guemini, M., *A method for predicting the number of active bubbles in sonochemical reactors.* Ultrasonics Sonochemistry, 2015. **22**: p. 51-58.

72. Laborde, J.L., Bouyer, C., Caltagirone, J.P., and Gerard, A., *Acoustic cavitation field prediction at low and high frequency ultrasounds.* Ultrasonics, 1998. **36**(1-5): p. 581-587.

73. Ashokkumar, M., Lee, J., Iida, Y., Yasui, K., Kozuka, T., Tuziuti, T., and Towata, A., *Spatial distribution of acoustic cavitation bubbles at different ultrasound frequencies.* Chemphyschem, 2010. **11**(8): p. 1680-1684.

74. Beckett, M.A. and Hua, I., *Impact of ultrasonic frequency on aqueous sonoluminescence and sonochemistry.* Journal of Physical Chemistry A, 2001. **105**(15): p. 3796-3802.

75. Tronson, R., Ashokkumar, M., and Grieser, F., *Comparison of the effects of water-soluble solutes on multibubble sonoluminescence generated in aqueous solutions by 20- and 515-kHz pulsed ultrasound.* Journal of Physical Chemistry B, 2002. **106**(42): p. 11064-11068.

76. Asakura, Y., Nishida, T., Matsuoka, T., and Koda, S., *Effects of ultrasonic frequency and liquid height on sonochemical efficiency of large-scale sonochemical reactors.* Ultrasonics Sonochemistry, 2008. **15**(3): p. 244-250.

77. Yusof, N.S.M. and Ashokkumar, M., *Sonochemical synthesis of gold nanoparticles by using high intensity focused ultrasound.* Chemphyschem, 2015. **16**(4): p. 775-781.

78. Kanthale, P., Ashokkumar, M., and Grieser, F., *Sonoluminescence, sonochemistry (H_2O_2 yield) and bubble dynamics: Frequency and power effects.* Ultrasonics Sonochemistry, 2008. **15**(2): p. 143-150.

79. Cum, G., Galli, G., Gallo, R., and Spadaro, A., *Role of frequency in the ultrasonic activation of chemical reactions.* Ultrasonics, 1992. **30**(4): p. 267-270.

80. Petrier, C., Jeunet, A., Luche, J.L., and Reverdy, G., *Unexpected frequency-effects on the rate of oxidative processes induced by ultrasound.* Journal of the American Chemical Society, 1992. **114**(8): p. 3148-3150.

81. Portenlänger, G. and Heusinger, H., *The influence of frequency on the mechanical and radical effects for the ultrasonic degradation of dextranes.* Ultrasonics Sonochemistry, 1997. **4**(2): p. 127-130.

82. Mason, T.J., Cobley, A.J., Graves, J.E., and Morgan, D., *New evidence for the inverse dependence of mechanical and chemical effects on the frequency of ultrasound.* Ultrasonics Sonochemistry, 2011. **18**(1): p. 226-230.

83. Whillock, G.O.H. and Harvey, B.F., *Ultrasonically Enhanced Corrosion of 304L Stainless Steel: 2. The Effect of Frequency, Acoustic Power and Horn to Specimen Distance.* Ultrasonics Sonochemistry, 1997. **4**(1): p. 33-38.

84. Pflieger, R., Chave, T., Vite, G., Jouve, L., and Nikitenko, S.I., *Effect of Operational Conditions on Sonoluminescence and Kinetics of H_2O_2 Formation during the Sonolysis of Water in the Presence of Ar/O_2 Gas Mixture.* Ultrasonics Sonochemistry, 2015. **26**: p. 169-175.

85. Cairos, C., Schneider, J., Pflieger, R., and Mettin, R., *Effects of argon sparging rate, ultrasonic power, and frequency on multibubble sonoluminescence spectra and bubble dynamics in NaCl aqueous solutions.* Ultrasonics Sonochemistry, 2014. **21**(6): p. 2044-2051.

86. Yasui, K., *Influence of ultrasonic frequency on multibubble sonoluminescence.* Journal of the Acoustical Society of America, 2002. **112**(4): p. 1405-1413.

87. Merouani, S., Hamdaoui, O., Rezgui, Y., and Guemini, M., *Effects of Ultrasound Frequency and Acoustic Amplitude on the Size of Sonochemically Active Bubbles - Theoretical Study.* Ultrasonics Sonochemistry, 2013. **20**(3): p. 815-819.

88. Gutierrez, M. and Henglein, A., *Chemical action of pulsed ultrasound - observation of an unprecedented intensity effect.* Journal of Physical Chemistry, 1990. **94**(9): p. 3625-3628.

89. Sivakumar, M. and Gedanken, A., *Insights into the sonochemical decomposition of $Fe(CO)_5$: theoretical and experimental understanding of the role of molar concentration and power density on the reaction yield.* Ultrasonics Sonochemistry, 2004. **11**(6): p. 373-378.

90. Didenko, Y.T., Gordeychuk, T.V., and Koretz, V.L., *The effect of ultrasound power on water sonoluminescence.* Journal of Sound and Vibration, 1991. **147**(3): p. 409-416.

91. Lee, H.B. and Choi, P.K., *Acoustic power dependences of sonoluminescence and bubble dynamics.* Ultrasonics Sonochemistry, 2014. **21**(6): p. 2037-2043.

92. Sunartio, D., Ashokkumar, M., and Grieser, F., *The influence of acoustic power on multibubble sonoluminescence in aqueous solution containing organic solutes.* Journal of Physical Chemistry B, 2005. **109**(42): p. 20044-20050.

93. Ashokkumar, M., Mulvaney, P., and Grieser, F., *The effect of pH on multibubble sonoluminescence from aqueous solutions containing simple organic weak acids and bases.* Journal of the American Chemical Society, 1999. **121**(32): p. 7355-7359.

94. Okitsu, K., Suzuki, T., Takenaka, N., Bandow, H., Nishimura, R., and Maeda, Y., *Acoustic multibubble cavitation in water: A new aspect of the effect of a rare gas atmosphere on bubble temperature and its relevance to sonochemistry.* Journal of Physical Chemistry B, 2006. **110**(41): p. 20081-20084.

95. Pflieger, R., Gravier, L., Guillot, G., Ashokkumar, M., and Nikitenko, S.I., *Inverse effects of the gas feed positioning on sonochemistry and sonoluminescence.* Ultrasonics Sonochemistry, 2018. **46**: p. 10-17.

96. Yasui, K., Iida, Y., Tuziuti, T., Kozuka, T., and Towata, A., *Strongly interacting bubbles under an ultrasonic horn.* Physical Review E, 2008. **77**(1): p. 016609.1-016609.10.

97. Entezari, M.H. and Kruus, P., *Effect of frequency on sonochemical reactions II. Temperature and intensity effects.* Ultrasonics Sonochemistry, 1996. **3**(1): p. 19-24.

98. Nikitenko, S.I., Le Naour, C., and Moisy, P., *Comparative study of sonochemical reactors with different geometry using thermal and chemical probes.* Ultrasonics Sonochemistry, 2007. **14**(3): p. 330-336.

99. Calvisi, M.L., Lindau, O., Blake, J.R., and Szeri, A.J., *Shape stability and violent collapse of microbubbles in acoustic traveling waves.* Physics of Fluids, 2007. **19**(4): p. 047101.1-047101.15.

100. Lee, J., Ashokkumar, M., Yasui, K., Tuziuti, T., Kozuka, T., Towata, A., and Iida, Y., *Development and optimization of acoustic bubble structures at high frequencies.* Ultrasonics Sonochemistry, 2011. **18**(1): p. 92-98.

101. Kauer, M., Belova-Magri, V., Cairos, C., Schreier, H.J., and Mettin, R., *Visualization and optimization of cavitation activity at a solid surface in high frequency ultrasound fields.* Ultrasonics Sonochemistry, 2017. **34**: p. 474-483.

102. Thangavadivel, K., Okitsu, K., Owens, G., Lesniewski, P.J., and Nishimura, R., *Influence of sonochemical reactor diameter and liquid height on methyl orange degradation under 200 kHz indirect sonication.* Journal of Environmental Chemical Engineering, 2013. **1**(3): p. 275-280.

103. De La Rochebrochard, S., Suptil, J., Blais, J.F., and Naffrechoux, E., *Sonochemical efficiency dependence on liquid height and frequency in an improved sonochemical reactor.* Ultrasonics Sonochemistry, 2012. **19**(2): p. 280-285.

104. Tuziuti, T., Yasui, K., Kozuka, T., and Towata, A., *Influence of liquid-surface vibration on sonochemiluminescence intensity.* Journal of Physical Chemistry A, 2010. **114**(27): p. 7321-7325.

105. Kim, E., Cui, M., Jang, M., Park, B., Son, Y., and Khim, J., *Investigation of sonochemical activities at a frequency of 334 kHz: The effect of geometric parameters of sonoreactor.* Ultrasonics Sonochemistry, 2014. **21**(4): p. 1504-1511.

106. Bussemaker, M.J. and Zhang, D., *A phenomenological investigation into the opposing effects of fluid flow on sonochemical activity at different frequency and power settings. 1. Overhead stirring.* Ultrasonics Sonochemistry, 2014. **21**(1): p. 436-445.

107. Kaltsa, O., Gatsi, I., Yanniotis, S., and Mandala, I., *Influence of ultrasonication parameters on physical characteristics of olive oil model emulsions containing xanthan.* Food and Bioprocess Technology, 2014. **7**(7): p. 2038-2049.

108. Falleh, H., Ksouri, R., Lucchessi, M.E., Abdelly, C., and Magne, C., *Ultrasound-assisted extraction: Effect of extraction time and solvent power on the levels of polyphenols and antioxidant activity of mesembryanthemum edule l. Aizoaceae shoots.* Tropical Journal of Pharmaceutical Research, 2012. **11**(2): p. 243-249.

109. Leong, S.X., Mayorga-Martinez, C.C., Sofer, Z., Luxa, J., Tana, S.M., and Pumera, M., *A study of the effect of sonication time on the catalytic performance of layered WS_2 from various sources.* Physical Chemistry Chemical Physics, 2017. **19**(4): p. 2768-2777.

110. Zhao, Y., Bao, C., Feng, R., and Li, R., *A new method of etching ABS plastic for plating by ultrasound.* Plating and Surface Finishing, 1998. **85**(9): p. 98-100.

111. Suslick, K.S. and Price, G.J., *Applications of ultrasound to materials chemistry.* Annual Review of Materials Science, 1999. **29**(1): p. 295-326.

112. Suslick, K.S., Casadonte, D.J., Green, M.L.H., and Thompson, M.E., *Effects of high-intensity ultrasound on inorganic solids.* Ultrasonics, 1987. **25**(1): p. 56-59.

113. Cobley, A. and Mason, T., *The evaluation of sonochemical techniques for sustainable surface modification in electronic manufacturing.* Circuit World, 2007. **33**(3): p. 29-34.

114. Cobley, A., Mason, T., and Robinson, J., *Sonochemical surface modification: A route to lean, green and clean manufacturing?* Journal of Applied Surface Finishing, 2008. **3**(4): p. 190-196.

115. Skorb, E.V., Shchukin, D.G., Mohwald, H., and Andreeva, D.V., *Ultrasound-driven design of metal surface nanofoams.* Nanoscale, 2010. **2**(5): p. 722-727.

116. Hutli, E., Nedeljkovic, M.S., Bonyar, A., Radovic, N.A., Llic, V., and Debeljkovic, A., *The ability of using the cavitation phenomenon as a tool to modify the surface characteristics in micro- and in nano-level.* Tribology International, 2016. **101**: p. 88-97.

117. Skorb, E.V., Mohwald, H., and Andreeva, D.V., *Effect of cavitation bubble collapse on the modification of solids: Crystallization aspects.* Langmuir, 2016. **32**(43): p. 11072-11085.

118. Zhou, Y.K. and Hammitt, F.G., *Cavitation erosion incubation period.* Wear, 1983. **86**(2): p. 299-313.

119. Rivas, D.F., Verhaagen, B., Seddon, J.R.T., Zijlstra, A.G., Jiang, L.M., van der Sluis, L.W.M., Versluis, M., Lohse, D., and Gardeniers, H., *Localized removal of layers of metal, polymer, or biomaterial by ultrasound cavitation bubbles.* Biomicrofluidics, 2012. **6**(3): p. 034114.1-034114.20.

120. Verdan, S., Burato, G., Comet, M., Reinert, L., and Fuzellier, H., *Structural changes of metallic surfaces induced by ultrasound.* Ultrasonics Sonochemistry, 2003. **10**(4-5): p. 291-295.

121. Kollath, A., Cherepanov, P.V., and Andreeva, D.V., *Controllable manipulation of crystallinity and morphology of aluminium surfaces using high intensity ultrasound.* Applied Acoustics, 2016. **103**: p. 190-194.

122. Zhukova, Y., Ulasevich, S.A., Dunlop, J.W.C., Fratzl, P., Mohwald, H., and Skorb, E.V., *Ultrasound-driven titanium modification with formation of titania based nanofoam surfaces.* Ultrasonics Sonochemistry, 2017. **36**: p. 146-154.

123. Skorb, E.V., Fix, D., Shchukin, D.G., Mohwald, H., Sviridov, D.V., Mousa, R., Wanderka, N., Schaferhans, J., Pazos-Perez, N., Fery, A., and Andreeva, D.V., *Sonochemical formation of metal sponges.* Nanoscale, 2011. **3**(3): p. 985-993.

124. Saadi, N.S., Hassan, L.B., and Karabacak, T., *Metal oxide nanostructures by a simple hot water treatment.* Scientific Reports, 2017. **7**(1): p. 7158.

125. Bulat, T.J., *Macrosonics in industry .3. Ultrasonic cleaning.* Ultrasonics, 1974. **12**(2): p. 59-68.

126. Crum, L.A. and Ferrell, G.W., *The role of acoustic cavitation in megasonic cleaning.* Acustica, 1996. **82**(S): p. 132-132.

127. Fuchs, F.J., *Ultrasonic cleaning and washing of surfaces*, in *Power ultrasonics*, J.A. Gallego-Juárez and K.F. Graff, Editors. 2015, Woodhead Publishing: Oxford. p. 577-609.

128. Barbara, K. and Ed, K. *Ultrasonics vs megasonics*. [cited 2018 April 19]; Available from: https://electroiq.com/2002/07/ultrasonics-vs-megasonics/.

129. Sonosys. *MEMS (microelectromechanical systems) / LIGA technology*. [cited 2015 Octorber 15]; Available from: https://sonosys.de/en/mems-liga-technology.html.

130. Li, Y.L., *Ultrasonic cleaning principle and application.* Cleaning World, 2006. **22**(7): p. 31-35.

131. Yusof, N.S.M., Babgi, B., Alghamdi, Y., Aksu, M., Madhavan, J., and Ashokkumar, M., *Physical and chemical effects of acoustic cavitation in selected ultrasonic cleaning applications.* Ultrasonics Sonochemistry, 2016. **29**: p. 568-576.

132. Galy, N., *Behavior of 14C in irradiated nuclear graphite : effects of irradiation and decontamination by steam reforming*. 2016, Université de Lyon.

133. Vende, L., *Nuclear graphite waste's behaviour under disposal conditions : Study of the release and repartition of organic and inorganic forms of carbon 14 and tritium in alkaline media*. 2012, Ecole des Mines de Nantes.

134. ANZIEU, p., BONIN, B., and Pradel, P., *Gas-cooled nuclear reactors*. 2006: CEA Saclay; Groupe Moniteur.

135. Cannes, C., *Matrices de confinement pour les déchets nucléaires : corrosion des métaux dans les conditions de stockage*. 2018, CS IPNO: Orsay, Paris, France.

136. Barre, B., Anzieu, P., Lenain, R., and Thomas, J.-B., *Nuclear reactor systems - a technical, historical and dynamic approach*. 2016, Les Ulis (France): EDP Sciences.

137. Pageot, J., *Study of a nuclear graphite waste ^{14}C decontamination process by CO_2 gasification*. 2014, Université Paris Sud - Paris XI.

138. Caillat, R. and Darras, R. *Technical report. Corrosion du magnésium et de certains de ses alliages dans les piles refroidies par gaz* 1958. CEA Saclay.

139. Azevedo, C.R.F., *Selection of fuel cladding material for nuclear fission reactors.* Engineering Failure Analysis, 2011. **18**(8): p. 1943-1962.

140. Pugh, S.F., Harris, J.E., Raraty, L.E., Wareing, J., Burras, G.A., Antill, J.E., Mott, B.W., and Busk, R.S., *Magnesium alloy cladding for nuclear fuels.* Journal of the British Nuclear Energy Society, 1972. **11**(4): p. 313-330.

141. Neelameggham, R., *Primary production of magnesium*, in *Fundamentals of Magnesium Alloy Metallurgy*, M.O. Pekguleryuz, K.U. Kainer, and A. Arslan Kaya, Editors. 2013, Woodhead Publishing. p. 1-32.

142. Juers, C., *Corrosion and surface treatments for magnesium alloys used for aeronautical applications*. 2008, Université Henri Poincaré - Nancy 1.

143. Polmear, I., StJohn, D., Nie, J.-F., and Qian, M., *Magnesium alloys*, in *Light alloys (fifth edition)*, I. Polmear, et al., Editors. 2017, Butterworth-Heinemann: Boston. p. 287-367.

144. Mordike, B.L. and Ebert, T., *Magnesium - properties - applications - potential.* Materials Science and Engineering A, 2001. **302**(1): p. 37-45.

145. Caillat, R., Herenguel, J., Salesse, M., and Stohr, J., *Raisons du choix de l'alliage Mg-Zr pour le gainage des éléments combustibles.* Journal of Nuclear Materials, 1963. **8**(1): p. 1-2.

146. Gu, J., *Grain refinement of Mg-Zn and Mg-Mn alloys by SiC inoculation*. 2017, Clausthal University of Technology.

147. Rendu, M. *Sicral F1 graphite-core fuel element behavior in power reactors* 1987. CEA. CEA Cadarache.

148. Hallam, K.R., Minshall, P.C., Heard, P.J., and Flewitt, P.E.J., *Corrosion of the alloys Magnox AL80, Magnox ZR55 and pure magnesium in air containing water vapour.* Corrosion Science, 2016. **112**: p. 347-363.

149. Gregson, C.R., Goddard, D.T., Sarsfield, M.J., and Taylor, R.J., *Combined electron microscopy and vibrational spectroscopy study of corroded Magnox sludge from a legacy spent nuclear fuel storage pond.* Journal of Nuclear Materials, 2011. **412**(1): p. 145-156.

150. Song, G.L., *Corrosion electrochemistry of magnesium (Mg) and its alloys*, in *Corrosion of magnesium alloys*. 2011, Woodhead Publishing. p. 3-65.

151. Zeng, R.C., Zhang, J., Huang, W.J., Dietzel, W., Kainer, K.U., Blawert, C., and Ke, W., *Review of studies on corrosion of magnesium alloys.* Transactions of Nonferrous Metals Society of China, 2006. **16**: p. S763-S771.

152. Joyce, M., *Radioactive waste management and disposal*, in *Nuclear engineering: A conceptual introduction to nuclear power*, M. Joyce, Editor. 2018, Butterworth-Heinemann. p. 357-378.

153. Efremenkov, V.M., *Radioactive waste management at nuclear power plants.* International Atomic Energy Agency Bulletin, 1989. **31**(4): p. 37-42.

154. Atkins, M. and Glasser, F.P., *Application of portland cement-based materials to radioactive waste immobilization.* Waste Management, 1992. **12**(2): p. 105-131.

155. Fairhall, G.A. and Palmer, J.D., *The encapsulation of Magnox Swarf in cement in the United Kingdom.* Cement and Concrete Research, 1992. **22**(2): p. 293-298.

156. Rooses, A., Lambertin, D., Chartier, D., and Frizon, F., *Galvanic corrosion of Mg-Zr fuel cladding and steel immobilized in Portland cement and geopolymer at early ages.* Journal of Nuclear Materials, 2013. **435**(1-3): p. 137-140.

157. Strasser, A., Santucci, J., Lindquist, K., Yario, W., Stern, G., Goldstein, L., and Joseph, L. *Evaluation of stainless steel cladding for use in current design LWRs. Final report* 1982. EPRI. New York (USA).

158. Abe, A., Giovedi, C., Gomes, D., and Silva, A., *Revisiting stainless steel as pwr fuel rod cladding after fukushima daiichi accident.* Journal of Power and Energy Engineering, 2013. **1**(6): p. 323-329.

159. Pino, E., Abe, A., and Giovedi, C., *The quest for safe and reliable fuel cladding materials*, in *2015 International nuclear atlantic conference*. 2015, Associacao Brasileira de Energia Nuclear (ABEN): São Paulo, SP, Brazil. p. 4847-4854.

160. Leontyev, A., *Laser decontamination and cleaning of metal surfaces : modelling and experimental studies*. 2011, Université Paris Sud - Paris XI.

161. ANDRA. *Intermediate-level waste (ILW-LL)*. [cited 2018 January 17]; Available from: http://www.radioactivity.eu.com/site/pages/ML_LLW.htm.

162. Lambertin, D., Frizon, F., and Bart, F., *Mg-Zr alloy behavior in basic solutions and immobilization in Portland cement and Na-geopolymer with sodium fluoride inhibitor.* Surface & Coatings Technology, 2012. **206**(22): p. 4567-4573.

163. Agullo, J.L., Alain., *Etude de la faisabilité du traitement et du confinement des effluents issus de la dissolution dans l'acide nitrique des déchets magnésiens*. 2018: CEA Marcoule.

164. OTND, *Étude de faisabilité du procédé de dissolution carbonique sur des déchets magnésiens du dégainage - définition du procédé de dissolution carbonique*. 2015: CEA Marcoule.

165. NEA. *Decontamination techniques used in decommissioning activities* 1999. N.T. Group. Belgium.

166. Kaul, A. and Lasch, M., *Decontamination*, in *Radiological Protection*, A. Kaul and D. Becker, Editors. 2005, Springer: Berlin, Heidelberg. p. 259-294.

167. Kinnunen, P. *ANTIOXI - Decontamination techniques for activity removal in nuclear environments* 2008. VTT. Finland.

168. Moser, T. and Carr, T. *Pressurized Water Reactor Fuel Cleaning Using Advanced Ultrasonics* 2000. E.P.R.I. (EPRI). United States.

169. Lebedev, N., Krasilnikov, D., Vasiliev, A., Dubinin, G., and Yurmanov, V. *Development and application of the ultrasonic technologies in nuclear engineering*. in *NPC 2012: Nuclear Plant Chemistry Conference, International Conference on Water Chemistry of Nuclear Reactor Systems*. 2012. France.

170. Kumar, A., Bhatt, R.B., Behere, P.G., and Afzal, M., *Ultrasonic decontamination of prototype fast breeder reactor fuel pins.* Ultrasonics, 2014. **54**(4): p. 1052-1056.

171. Wells, H., *Radioactive decontamination by ultrasonics.* Ultrasonics, 1966. **4**(1): p. 29-34.

172. Cerre, P., Mestre, E., and de Kerdelleau, J. *Decontamination of Surfaces by Ultrasonics* 1962. CEA.

173. Courtault, J., de Kerdelleau, J., and Mestre, E. *The ultrasonic copper and brass decontamination study* 1965. CEA.

174. Borioli, E., Bregani, F., and Garofalo, A. *Effectiveness of different decontamination techniques on metallic scraps arising from decommissioned power plants* 1998. IAEA.

175. Hong, Y.-H., Park, S.-R., Han, S.-W., and Kim, B.-J., *Smart decontamination device for small-size radioactive scrap metal waste : Using abrasion pin in rotating magnetic field and ultrasonic wave cleaner.* Journal of Nuclear Fuel Cycle and Waste Technology, 2014. **12**(1): p. 79-88.

176. Vasilyev, A.P., Lebedev, N.M., Savkin, A.E., and Karlina, I.E. *Experimental Tests of Ultrasonic Decontamination of Metal Radioactive Waste*. in *2009 Waste Management Symposium - WM2009/WM'09: HLW, TRU, LLW/ILW, Mixed, Hazardous Wastes and Environmental Management - Waste Management for the Nuclear Renaissance*. 2009. United States.

177. Rosman, K.J.R. and Taylor, P.D.P. *Isotopic compositions of the elements 1997* 1998. IUPAC. United Kingdom.

178. Jaffe, H. and Berlincourt, D.A., *Piezoelectric transducer materials.* Proceedings of the IEEE, 1965. **53**(10): p. 1372-1386.

179. Wells, P.N.T., Bullen, M.A., Follett, D.H., Freundlich, H.F., and James, J.A., *The dosimetry of small ultrasonic beams.* Ultrasonics, 1963. **1**(2): p. 106-110.

180. Gong, C.L. and Hart, D.P., *Ultrasound induced cavitation and sonochemical yields.* Journal of the Acoustical Society of America, 1998. **104**(5): p. 2675-2682.

181. Dalodiere, E., Virot, M., Moisy, P., and Nikitenko, S.I., *Effect of ultrasonic frequency on H2O2 sonochemical formation rate in aqueous nitric acid solutions in the presence of oxygen.* Ultrasonics Sonochemistry, 2016. **29**: p. 198-204.

182. Amelinckx, S., Dyck, D.v., Landuyt, J.v., and Tendeloo, G.v., eds. *Handbook of microscopy. Applications in materials, science, solid-state physics and chemistry*. Food / Nahrung. 1997, VCH Verlagsgesellschaft mbH: Weinheim.

183. Epp, J., *X-ray diffraction (XRD) techniques for materials characterization*, in *Materials Characterization Using Nondestructive Evaluation (NDE) Methods*, G. Hübschen, et al., Editors. 2016, Woodhead Publishing. p. 81-124.

184. Quéré, D., *Rough ideas on wetting.* Physica A: Statistical Mechanics and its Applications, 2002. **313**(1): p. 32-46.

185. Wenzel, R., *Resistance of Solid Surfaces to Wetting by Water.* Industrial & Engineering Chemistry, 1936. **28**(8): p. 988-994.

186. Demir, A.G., Furlan, V., Lecis, N., and Previtali, B., *Laser surface structuring of AZ31 Mg alloy for controlled wettability.* Biointerphases, 2014. **9**(2): p. 029009.1-029009.10.

187. Sigmund, W.M. and Hsu, S.-H., *Cassie–Baxter Model*, in *Encyclopedia of Membranes*, E. Drioli and L. Giorno, Editors. 2016, Springer Berlin Heidelberg: Berlin, Heidelberg. p. 310-311.

188. Shimanovich, D.L., Vorobjova, A.I., Tishkevich, D.I., Trukhanov, A.V., Zdorovets, M.V., and Kozlovskiy, A.L., *Preparation and morphology-dependent wettability of porous alumina membranes.* Beilstein Journal of Nanotechnology, 2018. **9**: p. 1423-1436.

189. Aina, A., *In situ monitoring of pharmaceutical crystallisation*. 2012, University of Nottingham.

190. Brotchie, A., Grieser, F., and Ashokkumar, M., *Characterization of acoustic cavitation bubbles in different sound fields.* Journal of Physical Chemistry B, 2010. **114**(34): p. 11010-11016.

191. Merouani, S., Hamdaoui, O., Rezgui, Y., and Guemini, M., *Sensitivity of free radicals production in acoustically driven bubble to the ultrasonic frequency and nature of dissolved gases.* Ultrasonics Sonochemistry, 2015. **22**: p. 41-50.

192. Koda, S., Kimura, T., Kondo, T., and Mitome, H., *A standard method to calibrate sonochemical efficiency of an individual reaction system.* Ultrasonics Sonochemistry, 2003. **10**(3): p. 149-156.

193. Mark, G., Tauber, A., Rudiger, L.A., Schuchmann, H.P., Schulz, D., Mues, A., and von Sonntag, C., *OH-radical formation by ultrasound in aqueous solution - part II: Terephthalate and fricke dosimetry and the influence of various conditions on the sonolytic yield.* Ultrasonics Sonochemistry, 1998. **5**(2): p. 41-52.

194. Suslick, K.S., Didenko, Y., Fang, M.M., Hyeon, T., Kolbeck, K.J., McNamara, W.B., Mdleleni, M.M., and Wong, M., *Acoustic cavitation and its chemical consequences.* Philosophical Transactions of the Royal Society A: Mathematical, Physical and Engineering Sciences, 1999. **357**(1751): p. 335-353.

195. Price, G.J., Harris, N.K., and Stewart, A.J., *Direct observation of cavitation fields at 23 and 515 kHz.* Ultrasonics Sonochemistry, 2010. **17**(1): p. 30-33.

196. Yasui, K., Tuziuti, T., Kozuka, T., Towata, A., and Iida, Y., *Relationship between the bubble temperature and main oxidant created inside an air bubble under ultrasound.* Journal of Chemical Physics, 2007. **127**(15): p. 154502.1-154502.9.

197. Slanger, T.G. and Copeland, R.A., *Energetic oxygen in the upper atmosphere and the laboratory.* Chemical Reviews, 2003. **103**(12): p. 4731-4766.

198. Tuziuti, T., Hatanaka, S., Yasui, K., Kozuka, T., and Mitome, H., *Influence of dissolved oxygen content on multibubble sonoluminescence with ambient-pressure reduction.* Ultrasonics, 2002. **40**(1-8): p. 651-654.

199. Arakeri, V.H. and Nishad, K.P., *Influence of argon content on intensity of multibubble sonoluminescence*, in *IEEE 3rd International conference on communication software and networks*. 2011, IEEE Xi'an, China. p. 353-355.

200. Kanthale, P., Ashokkumar, M., and Grieser, F., *Sonoluminescence, Sonochemistry (H_2O_2 Yield) and Bubble Dynamics: Frequency and Power Effects.* Ultrasonics Sonochemistry, 2008. **15**: p. 143-150.

201. Laux, C.O., Spence, T.G., Kruger, C.H., and Zare, R.N., *Optical diagnostics of atmospheric pressure air plasmas.* Plasma Sources Science & Technology, 2003. **12**(2): p. 125-138.

202. Ndiaye, A.A., Pflieger, R., Siboulet, B., and Nikitenko, S.I., *The origin of isotope effects in sonoluminescence spectra of heavy and light water.* Angewandte Chemie-International Edition, 2013. **52**(9): p. 2478-2481.

203. Thiemann, A., Holsteyns, F., Cairos, C., and Mettin, R., *Sonoluminescence and dynamics of cavitation bubble populations in sulfuric acid.* Ultrasonics Sonochemistry, 2017. **34**: p. 663-676.

204. Zhou, J., Tada, Y., Kato, Y., Nagatsu, Y., Yasui, K., Sakaguchi, Y., Takebayashi, R., and Iwata, K., *Effects of Reflection Plate on Ultrasonic Reaction in a Sonoreactor.* JOURNAL OF CHEMICAL ENGINEERING OF JAPAN, 2009. **42**(8): p. 570-575.

205. Ashokkumar, M., Lee, J., Iida, Y., Yasui, K., Kozuka, T., Tuziuti, T., and Towata, A., *The detection and control of stable and transient acoustic cavitation bubbles.* Physical Chemistry Chemical Physics, 2009. **11**(43): p. 10118-10121.

206. Tuziuti, T., Yasui, K., Kozuka, T., Towata, A., and Iida, Y., *Suppression of Sonochemiluminescence Reduction at High Acoustic Amplitudes by the Addition of Particles.* The Journal of Physical Chemistry A, 2007. **111**(48): p. 12093-12098.

207. Lindström, O., *Physico-Chemical Aspects of Chemically Active Ultrasonic Cavitation in Aqueous Solutions.* The Journal of the Acoustical Society of America, 1955. **27**(4): p. 654-671.

208. Sunartio, D., Yasui, K., Tuziuti, T., Kozuka, T., Iida, Y., Ashokkumar, M., and Grieser, F., *Correlation between Na* emission and "chemically active" acoustic cavitation bubbles.* Chemphyschem, 2007. **8**(16): p. 2331-2335.

209. Liu, L., Yang, Y., Liu, P., and Tan, W., *The influence of air content in water on ultrasonic cavitation field.* Ultrasonics Sonochemistry, 2014. **21**(2): p. 566-571.

210. Isselin, J.C., Alloncle, A.P., and Autric, M., *On laser induced single bubble near a solid boundary: Contribution to the understanding of erosion phenomena.* Journal of Applied Physics, 1998. **84**(10): p. 5766-5771.

211. Vogel, A., Busch, S., and Parlitz, U., *Shock wave emission and cavitation bubble generation by picosecond and nanosecond optical breakdown in water.* Journal of the Acoustical Society of America, 1996. **100**(1): p. 148-165.

212. Hammitt, F.G. and De, M.K., *Cavitation erosion of aluminum considering bubble collapse, pulse-height spectra and cavitation erosion efficiency.* Wear, 1979. **55**(2): p. 221-234.

213. Rao, B.C.S. and Buckley, D.H., *Erosion of Aluminum 6061-T6 under Cavitation Attack in Mineral-Oil and Water.* Wear, 1985. **105**(2): p. 171-182.

214. Chen, H.S., Li, J., Chen, D.R., and Wang, J.D., *Damages on Steel Surface at the Incubation Stage of the Vibration Cavitation Erosion in Water.* Wear, 2008. **265**(5-6): p. 692-698.

215. Virot, M., Pflieger, R., Skorb, E.V., Ravaux, J., Zemb, T., and Mohwald, H., *Crystalline Silicon under Acoustic Cavitation: From Mechanoluminescence to Amorphization.* Journal of Physical Chemistry C, 2012. **116**(29): p. 15493-15499.

216. Skorb, E.V. and Mohwald, H., *Ultrasonic Approach for Surface Nanostructuring.* Ultrasonics Sonochemistry, 2016. **29**: p. 589-603.

217. Fotea, C., Callaway, J., and Alexander, M.R., *Characterisation of the surface chemistry of magnesium exposed to the ambient atmosphere.* Surface and Interface Analysis, 2006. **38**(10): p. 1363-1371.

218. Ogawa, S., Niwa, H., Nakanishi, K., Ohta, T., and Yagi, S., *Influence of CO_2 and H_2O on Air Oxidation of Mg Nanoparticles Studied by NEXAFS.* Journal of Surface Analysis, 2011. **17**(3): p. 319-323.

219. Wang, Y., Wang, W., Zhong, L., Wang, J., Jiang, Q., and Guo, X., *Super-hydrophobic surface on pure magnesium substrate by wet chemical method.* Applied Surface Science, 2010. **256**(12): p. 3837-3840.

220. Mitrovicscepanovic, V. and Brigham, R.J., *Localized corrosion initiation on magnesium alloys.* Corrosion, 1992. **48**(9): p. 780-784.

221. Berziou, C., Remy, K., Billard, A., and Creus, J., *Corrosion behaviour of dc magnetron sputtered $Fe_{1-x}Mg_x$ alloy films in 3 wt% NaCl solution.* Corrosion Science, 2007. **49**(11): p. 4276-4295.

222. Lide, D.R., *CRC Handbook of Chemistry and Physics*. 84th ed. 2003: Taylor & Francis.

223. Hauptmann, M., Struyf, H., De Gendt, S., Glorieux, C., and Brems, S., *Importance of bubble size control in ultrasonic surface cleaning by pulsed high-frequency sound fields.* Electrochemical Society Journal of Solid State Science and Technology, 2014. **3**(1): p. N3032-N3040.

224. Jain, R. and Pitchumani, R., *Fractal model for wettability of rough surfaces.* Langmuir : the ACS journal of surfaces and colloids, 2017. **33**(28): p. 7181-7190.

225. Chave, T., Navarro, N.M., Pochon, P., Perkas, N., Gedanken, A., and Nikitenko, S.I., *Sonocatalytic degradation of oxalic acid in the presence of oxygen and Pt/TiO_2.* Catalysis Today, 2015. **241**: p. 55-62.

226. Dükkancı, M. and Gündüz, G., *Ultrasonic degradation of oxalic acid in aqueous solutions.* Ultrasonics Sonochemistry, 2006. **13**(6): p. 517-522.

227. *CRC Handbook of Chemistry and Physics*. 86th Edition ed. Journal of the American Chemical Society, ed. D.R. Lide. Vol. 128. 2006, Boca Raton: American Chemical Society. 5585.

228. Hasty, E., *Chemistry, The Central Science*. Third Edition ed. Journal of Chemical Education, ed. T.L.L. Brown, Eugene, Jr. Vol. 64. 1987: American Chemical Society. A173.

229. Drelich, J. and Chibowski, E., *Superhydrophilic and Superwetting Surfaces: Definition and Mechanisms of Control.* Langmuir, 2010. **26**(24): p. 18621-18623.

230. Nogita, K., Ockert, S., Pierce, J., Greaves, M.C., Gourlay, C.M., and Dahle, A.K., *Engineering the Mg-Mg2Ni eutectic transformation to produce improved hydrogen storage alloys.* International Journal of Hydrogen Energy, 2009. **34**(18): p. 7686-7691.

231. Zainal Abidin, N.I., Atrens, A.D., Martin, D., and Atrens, A., *Corrosion of High Purity Mg, $Mg_2Zn_{0.2}Mn$, ZE41 and AZ91 in Hank's Solution at 37 °C.* Corrosion Science, 2011. **53**(11): p. 3542-3556.

232. Jung, H.S., Lee, J.K., Kim, J.Y., and Hong, K.S., *Crystallization Behaviors of Nanosized MgO Particles from Magnesium Alkoxides.* Journal of Colloid and Interface Science, 2003. **259**(1): p. 127-132.

233. Valouma, A., Verganelaki, A., Maravelaki-Kalaitzaki, P., and Gidarakos, E., *Chrysotile Asbestos Detoxification with a Combined Treatment of Oxalic Acid and Silicates Producing Amorphous Silica and Biomaterial.* Journal of Hazardous Materials, 2016. **305**: p. 164-170.

234. Rozalen, M. and Huertas, F.J., *Comparative Effect of Chrysotile Leaching in Nitric, Sulfuric and Oxalic Acids at Room Temperature.* Chemical Geology, 2013. **352**: p. 134-142.

235. Chen, H.S. and Liu, S.H., *Inelastic Damages by Stress Wave on Steel Surface at the Incubation Stage of Vibration Cavitation Erosion.* Wear, 2009. **266**(1-2): p. 69-75.

236. Frankel, *Pitting corrosion of metals: A review of the critical factors.* Journal of the Electrochemical Society, 1998. **145**(6): p. 2186-2197.

237. Zhang, R., Qiu, Y., Qi, Y., and Birbilis, N., *A closer inspection of a grain boundary immune to intergranular corrosion in a sensitised Al-Mg alloy.* Corrosion Science, 2018. **133**: p. 1-5.

238. Benjamin, T.B. and Ellis, A.T., *The Collapse of Cavitation Bubbles and Pressures Thereby Produced Against Solid Boundaries.* Philosophical Transactions of the Royal Society of London Series a-Mathematical and Physical Sciences, 1966. **260**(1110): p. 221-240.

239. Tinguely, M., *The Effect of Pressure Gradient on the Collapse of Cavitation Bubbles in Normal and Reduced Gravity*, in *Faculté des sciences et techniques de l'ingénieur*. 2013, École polytechnique fédérale de Lausanne EPFL.

240. Borkent, B.M., Gekle, S., Prosperetti, A., and Lohse, D., *Nucleation Threshold and Deactivation Mechanisms of Nanoscopic Cavitation Nuclei.* Physics of Fluids, 2009. **21**(10): p. 1-9.

241. Belova, V., Krasowska, M., Wang, D.Y., Ralston, J., Shchukin, D.G., and Mohwald, H., *Influence of Adsorbed Gas at Liquid/Solid Interfaces on Heterogeneous Cavitation.* Chemical Science, 2013. **4**(1): p. 248-256.

242. Lambertin, D., Rooses, A., and Frizon, F., *Galvanic Corrosion of Mg-Zr Alloy and Steel or Graphite in Mineral Binders*, in *Magnesium Technology 2013*, N. Hort, et al., Editors. 2016, Springer International Publishing: Cham. p. 153-155.

243. Su, Y., Lin, J., Su, Y., Zai, W., Li, G., and Wen, C., *Investigation on composition, mechanical properties, and corrosion resistance of Mg-0.5Ca-X(Sr, Zr, Sn) biological alloy.* Scanning, 2018. **2018**: p. 1-10.

244. Rajchenbach, J., Clamond, D., and Leroux, A., *Observation of Star-Shaped Surface Gravity Waves.* Physical Review Letters, 2013. **110**(9): p. 094502.

245. Brady, M.P., Ievlev, A.V., Fayek, M., Leonard, D.N., Frith, M.G., Meyer, H.M., Ramirez-Cuesta, A.J., Daemen, L.L., Cheng, Y., Guo, W., Poplawsky, J.D., Ovchinnikova, O.S., Thomson, J., Anovitz, L.M., Rother, G., Shin, D., Song, G.-L., and Davis, B., *Rapid Diffusion and Nanosegregation of Hydrogen in Magnesium Alloys from Exposure to Water.* ACS Applied Materials & Interfaces, 2017. **9**(43): p. 38125-38134.

246. Sun Fangfang, L.N.G., Li Qunying, Liu Enzuo, He Chunnain, Shi Chunsheng, Zhao Naiqin, *Effect of Sc and Zr additions on microstructures and corrosion behavior of Al-Cu-Mg-Sc-Zr alloys.* Journal of Materials Science & Technology, 2017. **33**(9): p. 1015-1022.

247. Wen, L.H., Ji, Z.S., Hu, M.L., and Ning, H.Y., *Microstructure and mechanical properties of Mg–3.0Nd–0.4Zn–0.4Zr magnesium alloy.* Journal of Magnesium and Alloys, 2014. **2**(1): p. 85-91.

248. Mikhaylovskaya, A.V., Mochugovskiy, A.G., Levchenko, V.S., Tabachkova, N.Y., Mufalo, W., and Portnoy, V.K., *Precipitation behavior of L12 Al3Zr phase in Al-Mg-Zr alloy.* Materials Characterization, 2018. **139**: p. 30-37.

249. Cançado, L., Takai, K., Enoki, T., Endo, M., Kim, Y., Mizusaki, H., Jorio, A., Coelho, L., Paniago, R., and Pimenta, M., *General equation for the determination of the crystallite size L_a of nanographite by raman spectroscopy.* Applied Physics Letters, 2006. **88**(16): p. 163106.1-163106.3.

250. Haag, R.M. and MUNCY, C.R., *Studies in the system $MgUO_3$—$MgUO_4$.* Journal of the American Ceramic Society, 1964. **47**(1): p. 34-36.

251. Ondrejcin, R.S. and Garrett, T.P., *The thermal decomposition of anhydrous uranyl nitrate and uranyl nitrate dihydrate1.* The Journal of Physical Chemistry, 1961. **65**(3): p. 470-473.

252. Thein, S.M. and Bereolos, P.J. *Thermal stabilization of $^{233}UO_2$, $^{233}UO_3$ and $^{233}U_3O_8$* 2000. United States.

253. Rodden, C.J., *Uranium*. 1964: Technical Information Center, Oak Ridge, TN (United States); New Brunswick Lab., AEC, N.J. (United States). Medium: ED.

254. Leiem. *Triuranium octoxide*. 2014 [cited 2018 May 24]; Available from: https://en.wikipedia.org/wiki/Triuranium_octoxide.

255. Sweet, L.E., Reilly, D.D., Abrecht, D.G., Buck, E.C., Meier, D.E., Su, Y.-F., Brauer, C.S., Schwantes, J.M., Tonkyn, R.G., Szecsody, J.E., Blake, T.A., and Johnson, T.J. *Spectroscopic studies of the several isomers of UO3*. in *SPIE Security + Defence*. 2013. SPIE. p. 7.

256. Faêda, K.C.M., Machado, G.C., and Lameiras, F.S., *Characterization of UO_2 by infrared spectroscopy*, in *2011 International Nuclear Atlantic Conference - INAC 2011*. 2011, Associao Brasileira De Energia Nuclear - Aben: Belo Horizonte,MG, Brazil.

257. Nakagaki, S., Mantovani, K., Sippel Machado, G., Dias de Freitas Castro, K., and Wypych, F., *Recent Advances in Solid Catalysts Obtained by Metalloporphyrins Immobilization on Layered Anionic Exchangers: A Short Review and Some New Catalytic Results.* Molecules, 2016. **21**(3): p. 291.

258. Makkos, E., Kerridge, A., Austin, J., and Kaltsoyannis, N., *Ionic adsorption on the brucite (0001) surface: A periodic electrostatic embedded cluster method study.* The Journal of Chemical Physics, 2016. **145**(20): p. 204708.1-204708.36.

259. Pushkaryova, G.I., *Sorption extraction of metals from mono- and multicomponent solutions using brucite.* Journal of Mining Science, 1999. **35**(6): p. 660-663.

260. Cao, Q., Huang, F., Zhuang, Z., and Lin, Z., *A study of the potential application of nano-Mg(OH)2 in adsorbing low concentrations of uranyl tricarbonate from water.* Nanoscale, 2012. **4**(7): p. 2423-2430.

261. Chen, Z., Zhuang, Z., Cao, Q., Pan, X., Guan, X., and Lin, Z., *Adsorption-Induced Crystallization of U-Rich Nanocrystals on Nano-Mg(OH)2 and the Aqueous Uranyl Enrichment.* ACS Applied Materials & Interfaces, 2014. **6**(2): p. 1301-1305.

262. Bochkarev, G.R. and Pushkareva, G.I., *Intensification of sorption properties of brucite.* Journal of Mining Science, 2005. **41**(4): p. 380-384.

263. Pushkareva, G.I. and Bobyleva, S.A., *Influence of Ultrasound on the Sorption Properties of Brucite.* Journal of Mining Science, 2003. **39**(6): p. 616-620.

264. Higginson, R.L., Jackson, C.P., Murrell, E.L., Exworthy, P.A.Z., Mortimer, R.J., Worrall, D.R., and Wilcox, G.D., *Effect of thermally grown oxides on colour development of stainless steel.* Materials at High Temperatures, 2015. **32**(1-2): p. 113-117.

265. Levin, D.A., Laux, C.O., and Kruger, C.H., *A General Model for the Spectral Calculation of OH Radiation in the Ultraviolet.* Journal of Quantitative Spectroscopy & Radiative Transfer, 1999. **61**(3): p. 377-392.

266. *Hydrogen Peroxide Ultraviolet Absorption Spectrum*. [cited 2018 January 18]; Available from: http://www.h2o2.com/technical-library/physical-chemical-properties/radiation-properties/default.aspx?pid=65.

267. Zhu, Y., Wu, G., Zhang, Y.-H., and Zhao, Q., *Growth and characterization of Mg(OH)2 film on magnesium alloy AZ31.* Applied Surface Science, 2011. **257**(14): p. 6129-6137.

268. Bera, M., Chandravati, Gupta, P., and Maji, P.K., *Facile One-Pot Synthesis of Graphene Oxide by Sonication Assisted Mechanochemical Approach and Its Surface Chemistry.* Journal of Nanoscience and Nanotechnology, 2018. **18**(2): p. 902-912.

269. Gourley, J.T. and Runciman, W.A., *Multiphonon infrared absorption spectra of MgO and CaO.* Journal of Physics C: Solid State Physics, 1973. **6**(3): p. 583-592.

270. Wozniak, N., *Spectroscopic Signatures of Uranium Speciation for Forensics*. 2017, University of Nevada. p. 238.

271. Poncet, F., Valdivieso, F., Gibert, R., and Pijolat, M., *In situ infrared spectroscopic study on uranium oxides during UO3 carboreduction.* Materials Chemistry and Physics, 1999. **58**(1): p. 55-57.

272. Nicholas, W., *Spectroscopic signatures of uranium speciation for forensics*, in *Chemistry and Biochemistry*. 2017, University of Nevada.

273. Honda, K., Atake, T., and Saito, Y., *Infrared spectra of oxide films on SUS430 stainless steel formed at temperatures between 473 and 1073 K.* Journal of Materials Research, 2016. **7**(1): p. 80-84.

274. Braterman, P.S. and R., C.T., *Vibrational spectroscopy of brucite: A molecular simulation investigation.* American Mineralogist, 2006. **91**(7): p. 1188-1196.

275. Merlen, A., Buijnsters, J., Gerardus, and Pardanaud, C., *A guide to and review of the use of multiwavelength raman spectroscopy for characterizing defective aromatic carbon solids: From graphene to amorphous carbons.* Coatings, 2017. **7**(10): p. 1-55.

276. Kawashima, Y. and Katagiri, G., *Fundamentals, overtones, and combinations in the Raman spectrum of graphite.* Physical Review B, 1995. **52**(14): p. 10053-10059.

277. Palacios, M.L. and Taylor, S.H., *Characterization of Uranium Oxides Using in Situ Micro-Raman Spectroscopy.* Applied Spectroscopy, 2000. **54**(9): p. 1372-1378.

278. Allen, G.C., Butler, I.S., and Nguyen Anh, T., *Characterisation of uranium oxides by micro-Raman spectroscopy.* Journal of Nuclear Materials, 1987. **144**(1): p. 17-19.

279. Allen, G.C. and Griffiths, A.J., *Vibrational spectroscopy of alkaline-earth metal uranate compounds.* Journal of the Chemical Society, Dalton Transactions, 1979(2): p. 315-319.

280. Thierry, D., Persson, D., Leygraf, C., Boucherit, N., and Hugot-le Goff, A., *Raman spectroscopy and XPS investigations of anodic corrosion films formed on FeMo alloys in alkaline solutions.* Corrosion Science, 1991. **32**(3): p. 273-284.

281. Maslar, J.E., Hurst, W.S., Jr., W.J.B., and Hendricks, J.H., *In Situ Raman Spectroscopic Investigation of Stainless Steel Hydrothermal Corrosion.* CORROSION, 2002. **58**(9): p. 739-747.

Appendixes

Appendix A: Calorimetric results

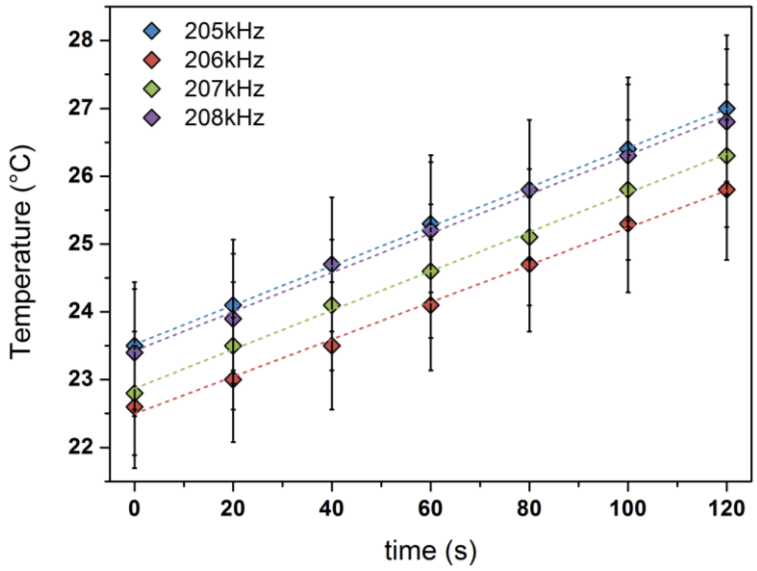

Appendix figure 1 Calorimetry of 200 kHz transducer: temperature vs. time (LP = 50 W, 250 mL water, Ar, 100 rpm stirring)

Appendix table 1 Calorimetry results of 200 kHz transducer (LP = 50 W, effective acoustic surface 25 cm2, 250 mL water, stirring 100 rpm)

Ultrasound frequency (kHz)	Load power, LP (W)	Slope dT/dt (K s^{-1})	Absorbed acoustic power P_{ac} (W)	Volumetric acoustic power $P_{v,ac}$ (W L^{-1})	Acoustic intensity I_{ac} (W cm^{-2})
205	50	0.029	29.99	119.97	1.20
206		0.028	28.84	115.37	1.15
207		0.029	29.99	119.97	1.20
208		0.029	29.89	119.55	1.20

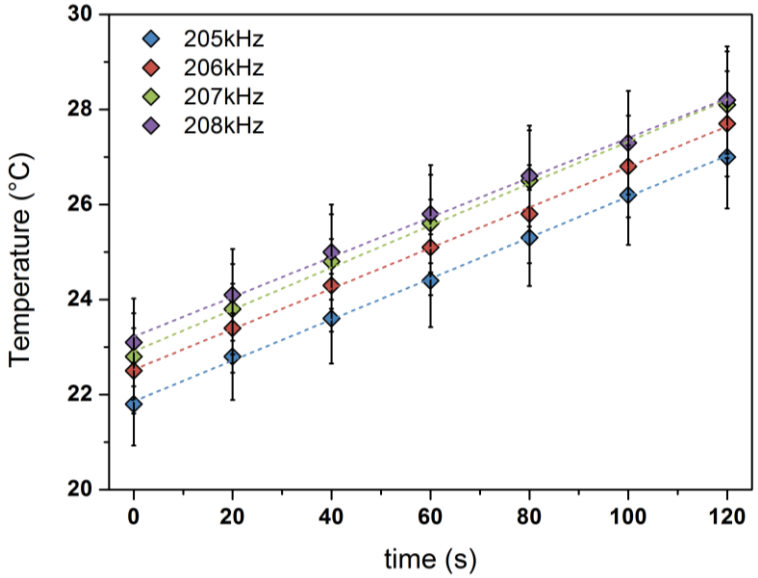

Appendix figure 2 Calorimetry of 200 kHz transducer: temperature vs. time (LP = 73 W, 250 mL water, Ar, 100 rpm stirring)

Appendix table 2 Calorimetry results of 200 kHz transducer (LP = 73 W, effective acoustic surface 25 cm2, 250 mL water, stirring 100 rpm)

Ultrasound frequency (kHz)	Load power, LP (W)	Slope dT/dt (K s^{-1})	Absorbed acoustic power P_{ac} (W)	Volumetric acoustic power $P_{v,ac}$ (W L^{-1})	Acoustic intensity I_{ac} (W cm^{-2})
205	73	0.043	45.14	180.58	1.81
206		0.043	44.52	178.07	1.78
207		0.043	45.35	181.41	1.81
208		0.041	42.43	169.71	1.70

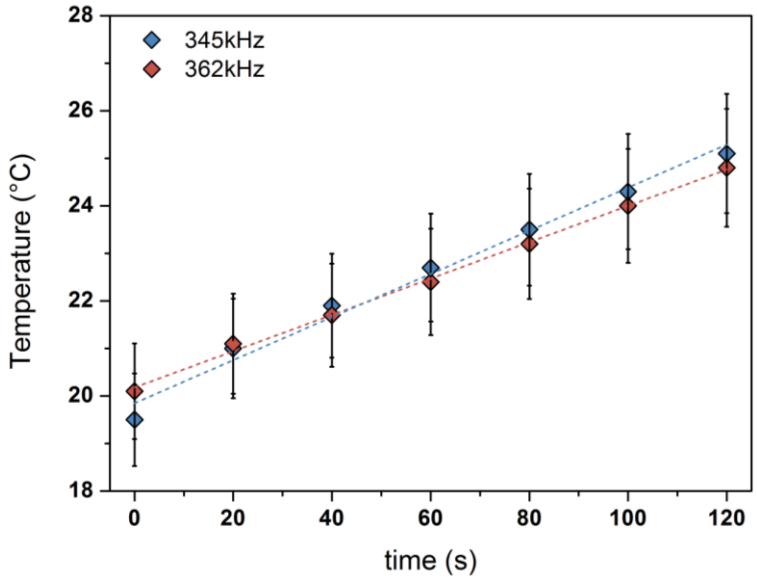

Appendix figure 3 Calorimetry of 300 kHz transducer: temperature vs. time (LP = 55 W for 345 kHz and LP = 60 W for 362 kHz, 250 mL water, Ar, 100 rpm stirring)

Appendix table 3 Calorimetry results of 300 kHz transducer: temperature vs. time (LP = 55 W for 345 kHz and LP = 60 W for 362 kHz, 250 mL water, Ar, 100 rpm stirring)

Ultrasound frequency (kHz)	Load power, LP (W)	Slope dT/dt ($K\ s^{-1}$)	Absorbed acoustic power P_{ac} (W)	Volumetric acoustic power $P_{v,ac}$ ($W\ L^{-1}$)	Acoustic intensity I_{ac} ($W\ cm^{-2}$)
345	55	0.045	46.61	186.43	1.86
362	60	0.037	38.67	154.66	1.55

Appendix B: Molar extinction coefficient ε determination

The molar extinction coefficient ε for the prepared $TiOSO_4$ solution is determined by mixing an equal volume of $TiOSO_4$ solution with a commercial H_2O_2 standard solution (diluted from 0 to $5 \cdot 10^{-3}$ M) and then calibrating with its UV-Visible absorption spectra.

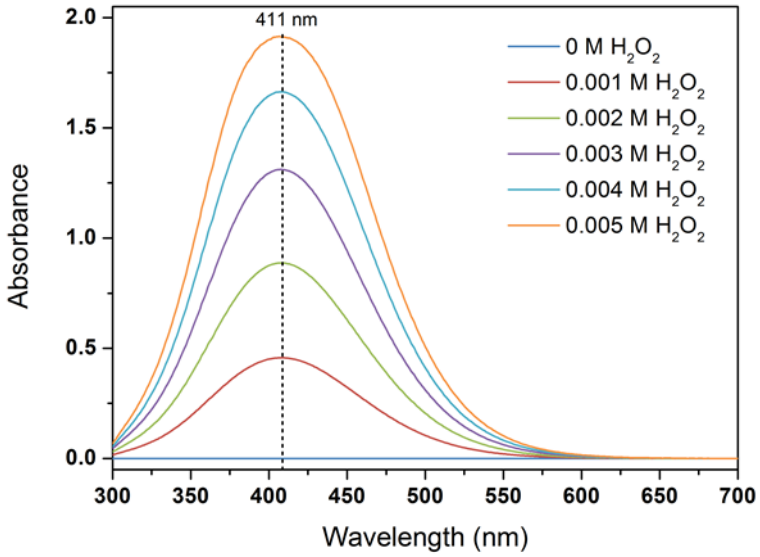

Appendix figure 4 UV-vis absorption spectra of the peroxotitanium(IV) complex formed by mixing sonicated dilute standard H_2O_2 solutions with $TiOSO_4$ solution.

The maximum absorbance at 411 nm is selected and multiplied by 2 to plot **Appendix figure 5**. By fitting the points, the slope of the linear line equals to 814.34.

$$\varepsilon = \frac{A}{l \times C} = \frac{dA}{d(l \times C)} = \frac{dA}{l \times dC}$$

Since l = 1 cm in our case, so $\varepsilon = 814.34\ mol^{-1}\ L\ cm^{-1}$.

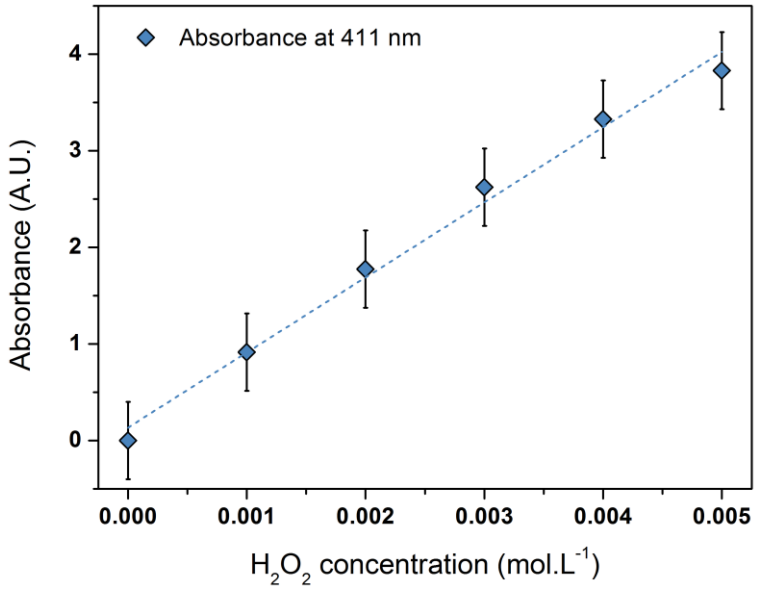

Appendix figure 5 Calibration curve for the determination of molar extinction coefficient ε.

Appendix C: H_2 formation determination during MS measurement

The relation between mass spectrometer measurement and the concentration of H_2 in gas flow (Ar) is calibrated with standard Ar and Ar/(500 ppm)H_2 gases in **Appendix table 4**, and the coefficient slope k is calculated to be 1718.

Appendix table 4 calibration of H_2 measurement in mass spectrometer

H_2 (ppm)	0	500
H_2/Ar	$7.3 \cdot 10^{-2}$	0.291

The hydrogen generation rate C_{H_2} (mol/s) is given by:

$$C_{H_2} = kRQ \times 10^{-6}/V_m$$

Where R is the measured H_2/Ar ratio by mass spectrometer, Q is the Ar gas volumetric flow rate (L/s) calculated from the volumetric flowmeter measurement and V_m is the gas molar volume (here we assume it equals 24 L/mol, as an ideal gas at 1 atmosphere at 25 ℃).

Appendix D: Spectral wavelength calibration and quantum efficiencies of gratings and CCD

Wavelength correction (10th of Nov 2017):

1st grating 600 blz 300: $\lambda_{corr} = 0.99948 * \lambda_{meas} - 5.36914$

2nd grating 150 blz 500: $\lambda_{corr} = 0.99866 * \lambda_{meas} - 3.10182$

3rd grating 1200 blz 300: $\lambda_{corr} = 0.99959 * \lambda_{meas} - 1.16526$

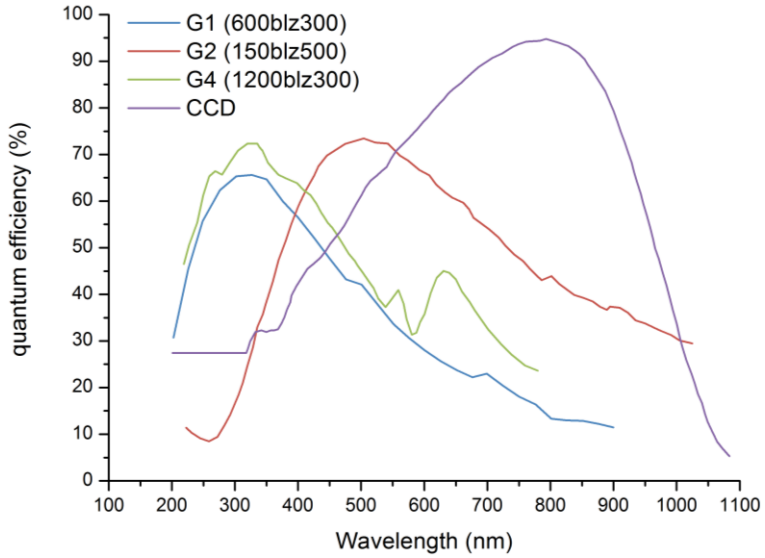

Appendix figure 6 Official quantum efficiencies of gratings (G1 600blz300, G2 150blz500 and G4 1200blz300) and CCD.

Appendix E: Simulation of SL spectra with Specair software

Emissions from excited species OH ($A^2\Sigma^+$) and NH ($A^3\Pi$) were simulated by the spectroscopy code Specair.[201] The simulation input parameters vibrational temperature T_v, rotational temperature T_r and pressure p were manually varied and optimized to fit experimental spectra as well as possible. A user defined measured slit function is introduced in Specair to calculate the experimental spectral resolution (150blz500 grating with slit of 0.12 mm, FWHM = 3.9 nm; 600blz300 grating with slit of 0.05 mm, FWHM = 1.63 nm; 1200blz300 grating with slit of 0.09 mm, FWHM = 0.30 nm and with slit of 0.12 mm, FWHM = 0.37 nm).

Due to the low SL intensity and unavoidable noise, besides the relatively low spectral resolution, all the parameters concerned have to be modified manually and the automatic fitting function

is not usable. For example, for OH the relative intensities of the two peaks at about 307 and 309 nm depend on T_r and p; the spectrum shape at wavelengths between 310 and 315 nm is sensitive to both T_r and T_v (contributions from both 0-0 and 1-1 transitions). The pressure also decides the broadness of the transition lines.[265] As discussed recently[201] in SL spectra the pressure is not the only parameter determining the broadening of the emissions, but strong Stark effects also occur. Unfortunately, they are not taken into account in existing spectroscopy software. Thus, the pressure value was increased to reproduce the broadening, and this parameter should be considered as an "effective pressure" combining pressure and Stark effects.

Appendix F: SL emission absorption by H_2O_2

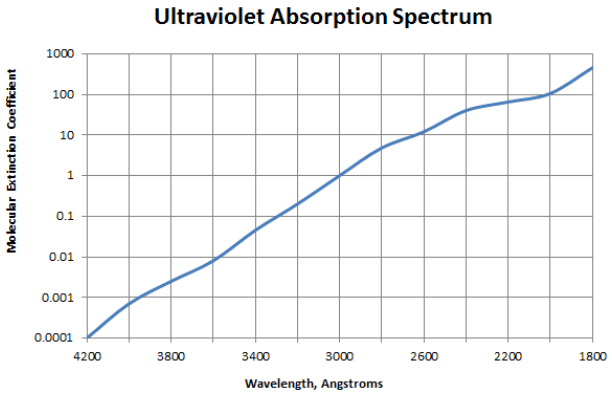

Appendix figure 7 H_2O_2 absorption spectrum.[266]

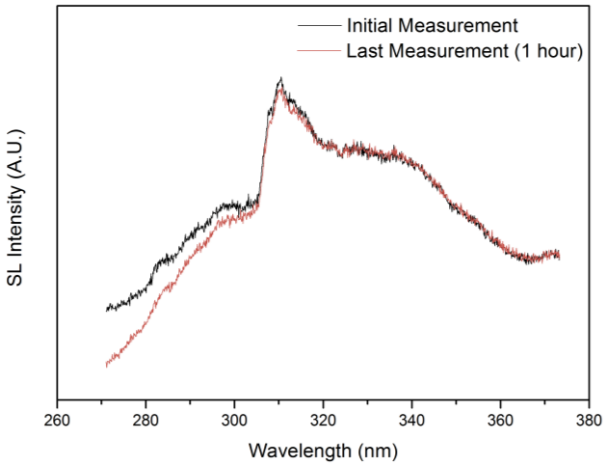

Appendix figure 8 H_2O_2 absorption effect: comparison of the first and last measurements of H_2O SL spectra at 362 kHz ultrasound (43W, 18 ℃) under 100 mL.min-1 Ar-20%O_2 flow.

Appendix figure 7 and **Appendix figure 8** show that the SL emission absorption by H_2O_2 accumulation is important after certain duration (1 hour). This absorption decreases the SL emission. Thus the

simulations of vibrational and rotational temperatures are biased and affected by an error, especially in solution saturated by Ar-20%O_2 and at high frequency.

Appendix G: Mg surface topography treated at 665 kHz

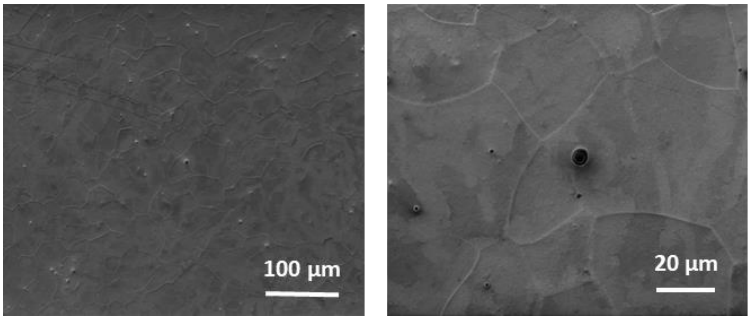

Appendix figure 9 SEM observations of Mg surface treated for 1 hour in 0.01 M oxalic acid solution, (Ar, 18 ℃, stirring 100 rpm) at 665 kHz P_{ac}= 40 W.

Appendix H: SCL photos

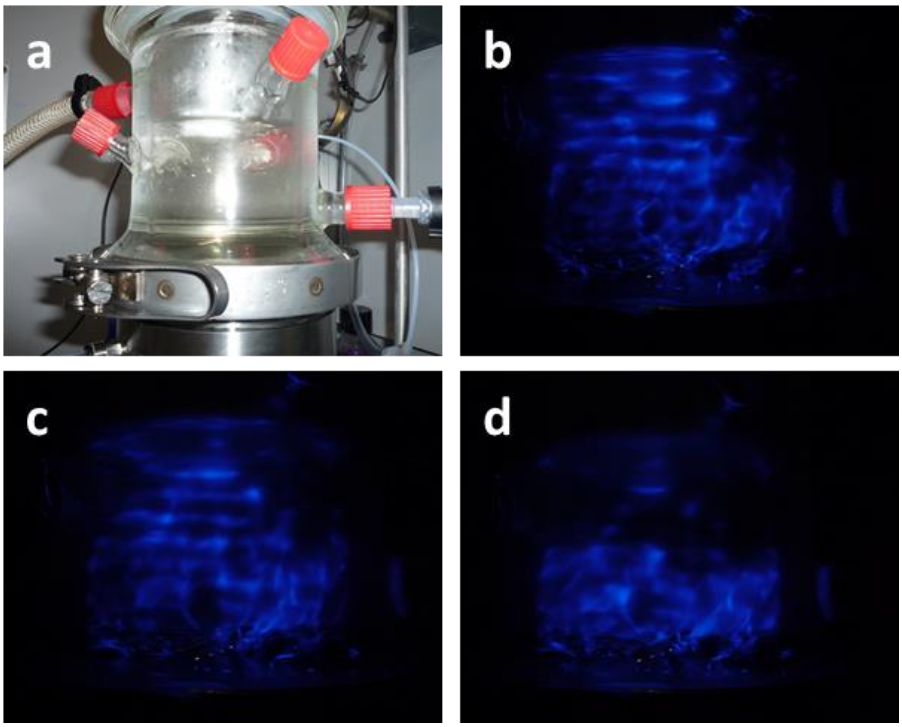

Appendix figure 10 Photographs of 0.01 M luminol solution (pH = 11, Na_2CO_3) submitted to 100 kHz (P_{ac}= 20 W) in the presence of the sample holder under 100 mL.min-1 Ar/(20 vol.%)O_2 flow, at 17 ℃, exposure 60 s: a) experimental set-up; b) non stirring; c) stirring 100 rpm and d) stirring 200 rpm.

Appendix I: Infrared and Raman bands

Appendix table 5 FTIR bands and peaks.

band	peak (cm^{-1})	reference
water	1630, 3400 (broad)	[232, 267]
O-H	3700	[232, 267]
C-H	2800	[232]
C-O	1225, 1450	[232, 268]
C=O	1735	[268]
C-O-C	1250	[268]
Mg-O	846	[269]
Mg-O-C	1050	[232]
UO_3	931	[270, 271]
U_3O_8	520, 850	[272]
Fe_2O_3	660	[273]
Cr_2O_3	730	[273]

Appendix table 6 Raman bands and peaks.

band	peak (cm^{-1})	reference
Mg-OH	700 - 1000	[274]
C=C	1350, 1580	[275, 276]
UO_3	846	[277]
U_3O_8	342, 412, 483, 738, 798	[277, 278]
non-stoichiometric $Mg_xU_yO_z$	250, 282, 365, 525, 535, 747	[279]
Fe_2O_3	225, 247, 299	[280]
$NiFe_2O_4$	665, 1345	[281]
$NiCr_2O_4$	512, 616	[281]

Appendix J: Alpha spectra of Mg-Zr surface decontamination

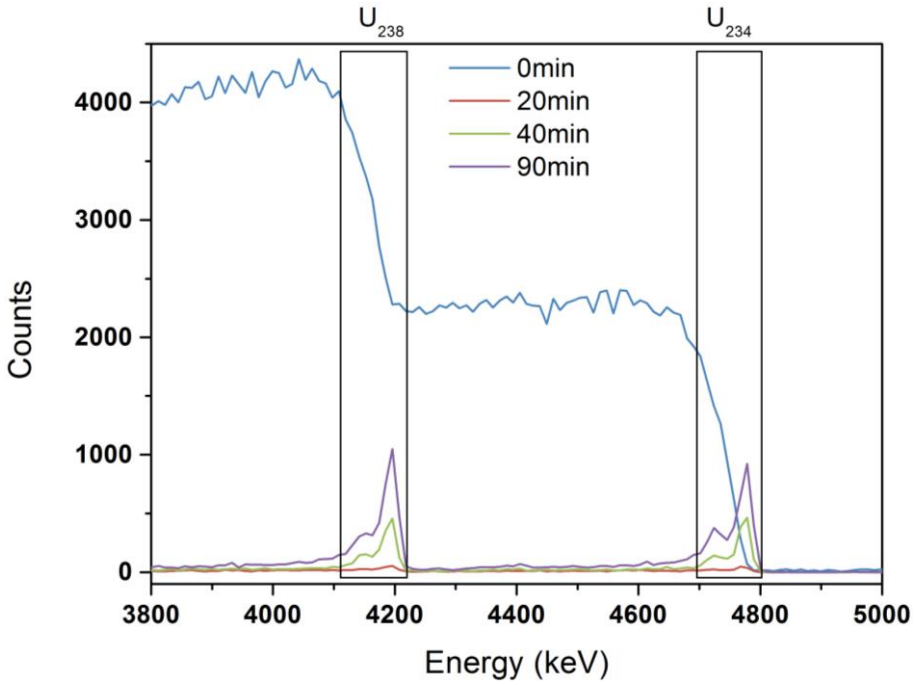

Appendix Figure 11 α spectra of Mg-Zr surfaces contaminated with U (0.1 M $UO_2(NO_3)_2$) decontaminated by 345 kHz ultrasound, P_{ac}= 40 W in 0.01 M oxalic acid, Ar, stirring 100 rpm, 20 ℃, from 0 min to 90 min